



Analytical Formulations for Systematic Design of Dual-/Tri-Frequency Impedance Transformation Networks Required in Software-Defined Radios (SDRs) and Energy Harvesting Applications

by
Md Ayatullah Maktoomi

Under the Supervision of Dr. Mohammad S. Hashmi

Indraprastha Institute of Information Technology Delhi
July, 2016



Analytical Formulations for Systematic Design of Dual-/Tri-Frequency Impedance Transformation Networks Required in Software-Defined Radios (SDRs) and Energy Harvesting Applications

by
Md Ayatullah Maktoomi

Submitted
in partial fulfillment of the requirements for the degree of
Doctor of Philosophy

to the

Indraprastha Institute of Information Technology Delhi
July, 2016

Certificate

This is to certify that the thesis titled “*Analytical Formulations for Systematic Design of Dual-/Tri-Frequency Impedance Transformation Networks Required in Software-Defined Radios (SDRs) and Energy Harvesting Applications*” being submitted by Md Ayatullah Maktoomi to the Indraprastha Institute of Information Technology Delhi, for the award of the degree of Doctor of Philosophy, is an original research work carried out by him under my supervision. In my opinion, the thesis has reached the standards fulfilling the requirements of the regulations relating to the degree.

The results contained in this thesis have not been submitted in part or full to any other university or institute for the award of any degree/diploma.

July, 2016
Dr. Mohammad S. Hashmi

Department of Electronics & Communication Engineering
Indraprastha Institute of Information Technology Delhi
New Delhi 110 020

Acknowledgements

This thesis would not have been possible without immense support from my supervisor, family, friends, and colleagues.

I would like to thank my advisor *Dr. Mohammad Hashmi* for giving me the opportunity to work on this thesis. Like all the prospective students I dropped emails to many professors, but very few replied! So, thanks for replying to my first email to you! Not only did you help improve my writing skills, but you kept me encouraging always and especially during the days of despair (well, as a PhD student you despair when your works get rejected one after the other!). As a result, at this juncture when I compare my CV with the one I had before joining your group, I see awesome changes— indeed; it has been a wonderful journey together. To be able to work independently is the most rewarding consequence of joining your group; I would join your group again if I ever wanted to get another PhD.

Another PhD? Well, I know my wife *Zeba* would never allow it! Or maybe she would, she has always been a wonderful support; constantly encouraging me during all my endeavors. I got married to her just after joining PhD program, but it was as if she had married to do sacrifices— spending a *forced bachelor life*, as Dr. Hashmi puts it, discontinuing her studies for me and our kid *Rayyan's* sake— you have done so much! I would never be able to match and would wonder if anyone else could be. *Thanks! You are the best!* No more forced bachelor life, let us be together now!

Despite having no formal education, my mother always wanted me to get well educated. And, despite a very weak financial background, my parents never hesitated to spend on my education. My parents have been very special to me— each time I planned to begin something; I would always call them to get their blessings (*Duas*). Whatever I am today, it's because of their blessings- May God grant them best in this world and in the life to come. Thanks are also due to my siblings, especially for my eldest brother *M. N. Haidri* for his endless support. I also wish to extend my sincere thanks to my father-in-law for his constant encouragements.

Thanks are due to *Rahul Gupta* (RAGU, in short! wow!), *the lab engineer*, and also a friend for helping me during preparation of many papers. Thanks are also due to *Manoj Gulati* for sharing his insights during prototype fabrication.

Sincere thanks also goes to my colleagues at IIIT Delhi, especially to the guys in PhD Lab (old)- *Hemanta, Hemant, Wazir, Naushad, Shiju*, and *TS*; Thanks are due to *Naveen Gupta*- It is wonderful to go for a tea!

I would like to give a special thanks to a very *down-to-the-earth person* (happy now!), a long time friend *Quamr Niyaz*, Utoledo, USA for always being with me. And thanks to one and only *Junaid Ahmad Ansari*! And thanks to friends and teachers at Aligarh Muslim University, especially to *Dr. S. A. Rahman* and *Dr. Ekram Khan*.

I would like to give a special thanks to *Dr. Fadhel Ghannouchi* for supporting and hosting me in his iRadio Lab, University of Calgary, Canada. Immense thanks are due to *Dr. M. Akbarpour, Dr. R. Darraji, Dr. Andrew Kwan, Dr. Farid, Abulhasan, Mohsin, Amir Vaezi, Yulong Zhao, Dongming Wang*, and all friends in the iRadio Lab. I wish to especially acknowledge *Dr. M. Akbarpour* and *Amir Vaezi* for many long hours of interesting technical discussions.

Special thanks to my friend *Wei Wei Zhang*- man, you are so energetic, keep it up and don't forget to fund my research when you build an enterprise!

To be born in a remote village of India, having elementary education from the village itself and coming this far would not have been possible without great help from friends and well-wishers. It is not possible to mention all the names, but your help has been indispensable and thanks to all of you. Thanks are due *M. Prem Pyari* and her wonderful family.

I want to thank *Dr. S. Deb* and *Dr. V. A. Bohara* for serving on my Ph.D. supervisory committee. I would also grab this opportunity to thank *Dr. Pankaj Jalote*, the director, IIIT Delhi for his endless encouragement and immense support to the PhD students and especially for granting me the Overseas Research Fellowship.

Finally, I appreciate much help from the IIIT Delhi administrative staffs, especially from Room A-109– the best office!

Abstract

The proliferation of multi-band and multi-standard wireless systems are well known but very little is known about the challenges associated in the design and development of such systems. For example, the RF front-ends in such systems require operation of all of the system components optimally functioning at more than one carrier frequency at a time. Traditional solution to address the above problem is to use multiple RF front-ends for each different standard. However, this essentially leads to large board size, higher power consumption along with other technical issues. This scenario has led to an extensive research in the devices and systems which are capable of operating at multiple frequencies concurrently. Such multi-frequency RF components have numerous advantages over the traditional narrow band components. For example, a dual-band power amplifier (PA) not only simplifies the hardware complexity but also provides higher reconfigurability and hence makes it a front runner for deployment in multi-band wireless transceiver architectures.

In addition, the concept of multi-frequency components is also crucial for simultaneous energy harvesting from more than one RF radiation sources. Distance of the harvester from RF energy source has profound impact on the amount of available power. Since, RF to DC conversion efficiency is not uniform over the entire input power levels; concurrent RF energy harvesting from multiple RF sources is envisaged as a means to enhance the conversion efficiency over a wider range of the available input power.

Impedance transformation circuit is a *sine qua non* to the many RF front-end blocks and energy harvesting systems. Design of RF/Microwave components such as amplifiers, mixers, oscillators, antennas, and power dividers/combiners require impedance matching as a key component. Conventionally, quarter-wavelength/single-/double-stub impedance transformers have been used for this purpose. But, the ever growing interest in multi-frequency RF/Microwave devices necessitates that the age-old theory of impedance transformation circuits must be now investigated to come up

with new multi-frequency transformation circuits, in general, and dual- and tri-frequency impedance transformation circuits, in particular.

In this thesis, novel and advanced techniques for dual- and tri-frequency impedance matching networks have been explored. Specifically, since the limited frequency- and transformation-ratio ails state-of-the-art of dual-frequency matching networks, therefore, the first part of this thesis presents design techniques to mitigate these limitations. Moreover, applications of the proposed techniques have been demonstrated for advanced dual-frequency components such as power dividers and couplers with significantly enhanced performance.

The current state-of-the-art of tri-frequency impedance matching network is still in its infancy. Therefore, a novel systematic and analytical design technique to implement them has been introduced.

The concept of DC-feed as applied in RF/microwave amplifiers is a special kind of impedance matching network where the idea is to establish infinite input impedance at the frequency of interest. In this thesis, a streamlined synthesis procedure for DC-feeds has been proposed to cater to the multi-frequency amplifier requirements.

List of the Relevant Publications

Patents:

- [1]. M. A. Maktoomi and M. S. Hashmi, "Generic tri-frequency impedance transformation network for RF/microwave active and passive circuits, components and systems," *Indian Patent Pending (Application No: 201611022038)*.
- [2]. M. A. Maktoomi and M. S. Hashmi, " A method and system for multi-frequency DC-feed network," *Indian Patent Pending (Application No: 201611028802)*.

Peer-Reviewed Published Journal Articles:

- J[1]. M. A. Maktoomi, M. Akbarpour, M. S. Hashmi, and F. M. Ghannouchi, " On the dual-frequency impedance/admittance characteristic of multi-section commensurate transmission-line," *IEEE Transactions on Circuits and Systems II: Express Briefs*, 2016 (Accepted, available online in the IEEExplore).
- J[2]. M. A. Maktoomi, M. S. Hashmi, and F. M. Ghannouchi, "Improving load range of dual-band impedance matching networks using novel load-healing concept," *IEEE Transactions on Circuits and Systems II: Express Briefs*, 2016 (Accepted, available online in the IEEExplore).
- J[3]. M. A. Maktoomi, M. Akbarpour, M. S. Hashmi, and F. M. Ghannouchi, "A theorem for multi-frequency DC-feed network design," *IEEE Microwave Wireless Components Letters*, , vol. 26, no. 9, pp. 648–650, Sept. 2016.
- J[4]. M. A. Maktoomi, M. S. Hashmi, and F. M. Ghannouchi, "Systematic design technique for dual-band branch-line coupler using T- and Pi-networks and a novel wide band-ratio crossover," *IEEE Transactions on Components, Packaging and Manufacturing Technology*, vol. 6, no. 5, pp. 784–795, Apr. 2016.
- J[5]. M. A. Maktoomi, M. S. Hashmi, A. P. Yadav, and V. Kumar, "A generic tri-band matching network," *IEEE Microwave Wireless Components Letters*, vol. 26, no. 5, pp. 316–318, Apr. 2016.
- J[6]. M. A. Maktoomi, M. S. Hashmi, and V. Panwar, "A dual-frequency matching network for FDCLs using dual-band $\lambda/4$ -lines," *Progress In Electromagnetics Research L*, vol. 52, pp. 23–30, 2015.

- J[7]. M. A. Maktoomi and M. S. Hashmi, "A coupled-line based l-section DC-isolated dual-band real to real impedance transformer and its application to a dual-band T-junction power divider," *Progress In Electromagnetics Research C*, vol. 55, pp. 95–104, 2014.
- J[8]. M. A. Maktoomi, M. S. Hashmi, and F. M. Ghannouchi, "A T-section dual-band matching network for frequency-dependent complex loads incorporating coupled line with DC-block property suitable for dual-band transistor amplifiers," *Progress In Electromagnetics Research C*, vol. 54, pp.75–84, 2014.

Articles Published in Conference Proceedings

- C[1]. M. A. Maktoomi, M. H. Maktoomi, Ajay P. Yadav, M. S. Hashmi, and F. M. Ghannouchi, "Dual-frequency admittance property of two sections transmission-line and application," in *IEEE 59th Midwest Symposium on Circuits and Systems (MWSCAS2016)*, Abu Dhabi, UAE, October 2016.
- C[2]. M. A. Maktoomi, R. Gupta, and M. S. Hashmi, "A dual-band impedance transformer for frequency-dependent complex loads incorporating an L-type network," in *Asia-Pacic Microwave Conference (APMC)*, Nanjing, China, December 2015.
- C[3]. M. A. Maktoomi, V. Panwar, M. S. Hashmi, and F. M. Ghannouchi, "A dual-band matching network for frequency-dependent complex loads suitable for dual-band RF Amplifiers," in *IEEE MTT-S International Microwave and RF Conference (IMaRC)*, Bangalore, India, December 2014.

Under-Review Articles:

- UR[1]. M. A. Maktoomi, M. S. Hashmi, and F. M. Ghannouchi, "A dual-band port extended branch-line coupler and mitigation of the band-ratio and power division limitations," *IEEE Transactions on Components, Packaging and Manufacturing Technology*. (Revision Submitted).
- UR[2]. M. A. Maktoomi, A. P. Yadav, M. S. Hashmi, and F. M. Ghannouchi, "Performance enhancement of dual-frequency impedance matching networks using dual-frequency property of two-section transmission-line terminated

into a real impedance," *IET Microwaves, Antennas and Propagation*.
(Revision Submitted).

UR[3]. M. A. Maktoomi and M. S. Hashmi, "A novel enhanced band-ratio dual-band Wilkinson power divider with option of partial port extension," *IEEE Transactions on Microwave Theory and Techniques*. (Revision Submitted).

Key Contributions

- Discovery of dual-frequency admittance properties of single, dual- and multi-section transmission lines terminated into real impedance.
- Performance Improvement of dual-frequency impedance matching networks and related components.
- Systematic and analytical design technique for tri-frequency impedance matching networks.
- Theorem for the synthesis of multi-frequency DC-feed networks.

Contents

Acknowledgements	iii
Abstract	v
List of the Relevant Publications.....	vii
Key Contributions	x
Chapter 1	1
Introduction	1
1.1 Introduction and Motivation.....	1
1.1.1 Impedance Matching Circuits.....	1
1.1.2 Applications of Matching Networks.....	2
1.2 Recent Interests	5
1.3. Major Contributions and Scope of this Thesis	8
1.3.1 Dual-frequency Impedance Transforming Circuits.....	8
1.3.2 Tri-frequency Impedance Transforming Circuits.....	9
1.3.3 Scope of This Work.....	9
1.4. Organization and Presentation of the Thesis	10
Chapter 2	13
Literature Review	13
2.1 Dual-Frequency Impedance Matching Networks.....	14
2.1.1 Dual-Frequency Matching Networks for Real Load Impedances	14
2.1.2 Dual-Frequency Matching Networks for Complex Load Impedances.....	17
2.2 Tri-Frequency Impedance Matching Networks.....	25
2.3 Multi-Frequency Impedance Matching Networks.....	27
2.4 Conclusion.....	29
Chapter 3	30
Admittance Property of Single Section Transmission line.....	30
3.1 Dual-Frequency Admittance Property of Single Section Transmission Line.....	30
3.2 Dual-Frequency Matching Networks	34
3.2.1 Design of Section A.....	35
3.2.2 Design of Section B.....	36
3.2.3 Design of Section C: The L-network.....	37
3.3 Dual-Frequency Wilkinson Power Divider with Improved Performance	40
3.3.1 Dual-Frequency Behavior of WPD Core.....	42
3.3.2 The Proposed WPD	45
3.3.3 Design Equations for the Input/ Output Side Matching Networks: Equating the real-parts	46
3.3.4 Design Equations for the Input/ Output Side Matching Networks: Cancelling the imaginary-parts.....	47
3.3.5 Simulation and Experimental Verifications.....	49

3.4. Conclusions	57
Chapter 4	58
Dual-Frequency Matching using Quarter Wavelength Blocks.....	58
4. 1 The Proposed Matching Network: Basic Idea	59
4.2 Implementation of the Proposed Scheme	60
4.2.1 Design of section A	61
4.2.2 Design of section B.....	61
4.2.3 Design of section C.....	62
4.3 Simulation and Experimental Verification	64
4.4 Conclusion.....	69
Chapter 5	70
Coupled Lines based DC-isolated Dual-Frequency Impedance Transformers	70
5. 1 Dual-Frequency Admittance Property of Coupled lines Terminated into a Real Impedance.....	71
5.2 DC-Isolated Dual-Frequency Impedance Transformer for Real Load Impedance.....	75
5.2.1 Analysis of Configuration-I.....	75
5.2.2 Analysis of Configuration-II	78
5.2.3 Design Procedure.....	78
5.2.4 Results and Discussions.....	80
5.3 DC Isolated Dual-Frequency Impedance Matching Network for Complex Impedance... 88	
5.3.1 Design of Section A.....	89
5.3.2 Design of Section B.....	89
5.3.3 Design of Section C	90
5.3.4 Design Steps	91
5.3.5 Simulation and Experimental Validation.....	91
5.4 Conclusion.....	96
Chapter 6	98
Admittance Property of Two-Sections Transmission line.....	98
6.1 Dual-Frequency Admittance Property of TSTL Terminated into a Real Impedance	98
6.2 The Monzon Two-sections Transformer	102
6.3 Limitation of Previous Designs	103
6.4 Proposed Impedance Transformers Employing TSTL.....	104
6.4.1 Proposed Dual-Frequency L-type Networks Employing TSTL.....	104
6.4.2 Proposed Dual-Frequency T-type Network Employing TSTL.....	107
6.5 Generic Nature of the Proposed Transformers	109
6.6 Design Steps for the Proposed Transformers	109
6.7 Simulation and Discussion	110
6.8 Prototype and Measurement	118
6.9 Application in Port-Extended Branch-Line Coupler	119
6.9.1. The BLC Core	121

6.9.2. Conventional Coupler from Riblet's View-point.....	122
6.9.3 Limitation of the Conventional Approach.....	124
6.9.4 The Proposed Dual-Frequency Port Extended Coupler.....	125
6.9.5 Design Steps.....	128
6.9.6 Simulation and Discussion.....	129
6.10 Conclusion.....	139
Appendix.....	140
Chapter 7.....	142
Load Healing in Dual-Frequency Matching Networks.....	142
7.1 Proposed Scheme: Analysis and Design.....	143
7.1.1 The Load-Healer.....	144
7.1.2 Design of Section A.....	146
7.1.3 Design of Section B.....	146
7.1.4. Design of Section C.....	147
7.1.5. Design Procedure.....	149
7.2 Design Examples, Prototypes and Measurement Results.....	149
7. 3 Discussion.....	153
7.4 Conclusion.....	154
Chapter 8.....	155
Dual-Frequency Admittance Property of Multi-Section Commensurate Transmission Lines.....	155
8.1 The Property and its Proof.....	155
8.2 Application of the Property.....	158
8.2.1 Proposed Tri-Section Dual-Frequency Transformer.....	159
8.2.2 Generic Multi-Section Transformer Design.....	161
8.2.3 Simulation and Discussion.....	161
8.2.4 Prototypes and Measurement Results.....	163
8.3 Conclusion.....	165
Chapter 9.....	166
Tri-Frequency Matching Network.....	166
9.1 Proposed Tri-Frequency Matching Network.....	166
9.2 Design Procedure.....	170
9.3 Design Examples.....	170
9.3.1 Design Example-I with type-I DBIT.....	170
9.3.2 Design Example-II with type-II DBIT.....	171
9.4. Conclusion.....	173
Appendix.....	174
Chapter 10.....	175
A Theorem for Multi-Frequency DC-Feed Network Design.....	175
10.1 The Statement of the Theorem.....	175

10.2 Proof of the Theorem.....	177
10.2.1. Proof of the Lemma.....	177
10.2.2 Proof of the theorem.....	178
10.3 CAD Assisted Design Methodology	179
10.4 Design and Comparison	180
10.5 Conclusion.....	182
Conclusion and Future Directions	184
Bibliography	189
Biography and Curriculum Vitae	196

Chapter 1

Introduction

1.1 Introduction and Motivation

1.1.1 Impedance Matching Circuits

Impedance matching or impedance transforming circuits (networks) are one of the most ubiquitous blocks in a host of RF/microwave components and systems. One of the motivations to use impedance matching networks comes from the *maximum power transfer theorem*. A voltage source V_s with its source resistance connected to the load R_L is shown in Fig. 1.1(a). Variation of the power delivered to the load, P_L is shown in Fig. 1.1(b). It is evident from Fig. 1.1(b) that P_L is maximum when $R_L=R_s$. This result is known as the condition for maximum power transfer. If the source and the load were a complex quantity, $R_L=R_s^*$ holds true, where asterisk denotes a complex conjugate quantity [1].

Since, in general, in RF/microwave components such as in amplifier, the impedance looking into the gain device is different than the source impedance; a matc-

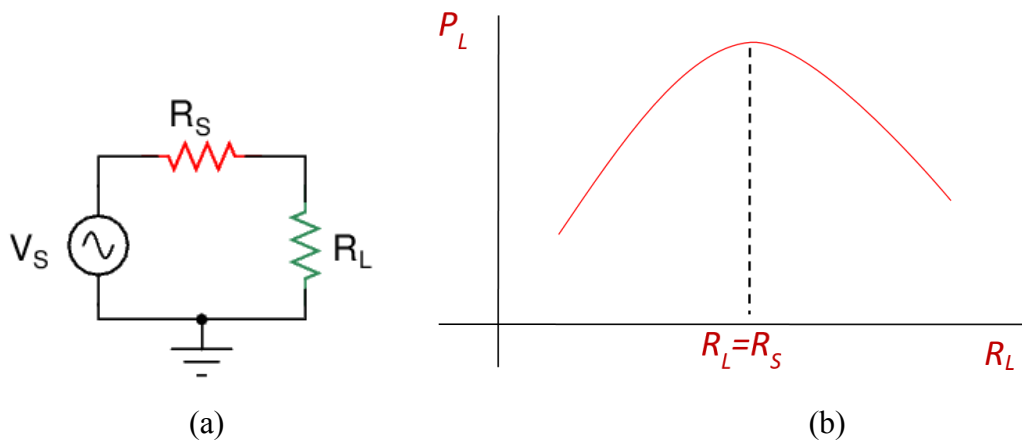


Figure 1.1 (a) Voltage source connected to a load (b) Power delivered to the load versus the load value.

hing network is required to transfer maximum power from the source side to the load side. Two points must be noted in this context. First, need of matching is not always motivated from the maximum power transfer theorem. Sometimes, such as in low-noise amplifiers or in wideband amplifiers, matching (other than conjugate) is used to trade-off among noise, bandwidth and gain requirements [2-3]. Second, amplifiers are not the only devices where a matching circuit is required. In fact, matching network is such a ubiquitous block in RF/Microwave devices and systems that it would be no exaggeration to say that “*they are everywhere*”. Some applications of matching networks in RF/microwave devices are highlighted in the next few paragraphs.

1.1.2 Applications of Matching Networks

Power Dividers: A Wilkinson power divider is shown in Fig. 1.2(a). This configuration is used for splitting power equally or for power combining. It may not be apparent if the concept of matching has to do anything here. For this purpose, even-mode equivalent circuit of the Wilkinson divider is shown in Fig. 1.2(b). It is evident now that the idea in such a situation is to *match* a real load impedance of Z_0 to $2Z_0$ using a quarter-wave line [4]. It is a fact that the characteristic impedance of the quarter-wave line must be $\sqrt{(Z_0*2Z_0)}= \sqrt{2} Z_0$ and that is exactly shown in the Wilkinson power divider of Fig. 1.2(a) [2].

Very Flat Coupler: A conventional branch-line coupler uses quarter-wave transmission lines due to which the achievable bandwidth is limited. In 1978, Riblet pr-

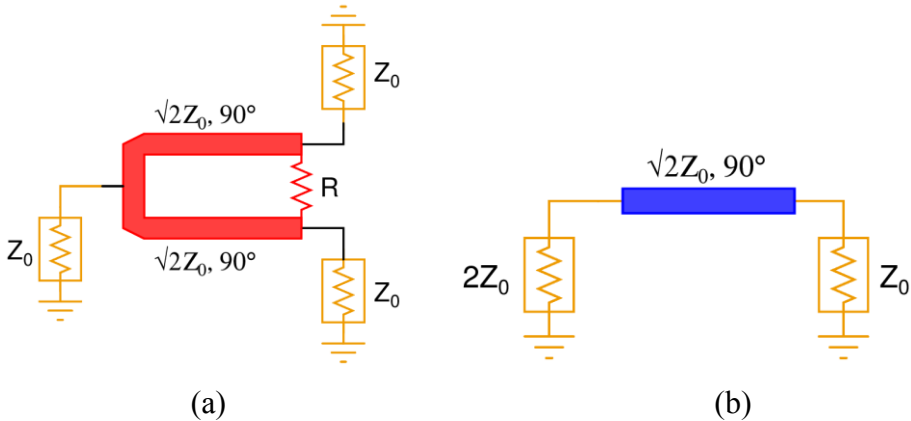


Figure 1.2 (a) A Wilkinson power divider and its (b) even-mode half circuit.

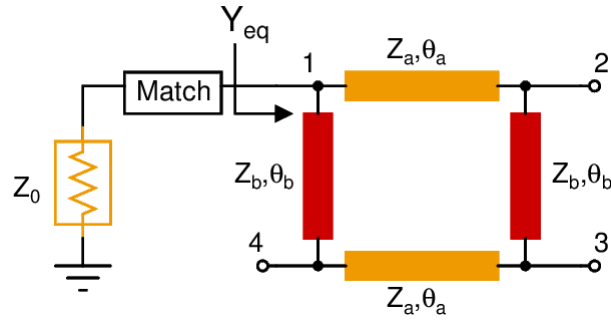


Figure 1.3 Very flat coupler topology. Not shown for brevity, but identical matching networks are required at all the four ports.

posed the formula of equivalent admittance, Y_{eq} , of a generalized branch-line coupler [5-6]. Furthermore, he reported the concept of port-matching network at all four ports of the coupler to match Y_{eq} with Z_0 to achieve a coupler with very flat response and excellent bandwidth performance. The scheme is illustrated in Fig. 1.3.

Antenna Feed Line: A patch antenna is shown in Fig. 1.4. The feed lines can be attached as shown in figure [7]. As one moves away from the center of the antenna, the impedance looking into the antenna also varies. Thus, to couple maximum power from the power amplifier (PA, serving as a source to the antenna with Z_0 as the source impedance) to the antenna, the impedance of PA and the antenna must be matched. Moreover, if the impedance level at the patch edge is matched to Z_0 , it results into very thin feed lines. Therefore, an inset feed is often used [7].

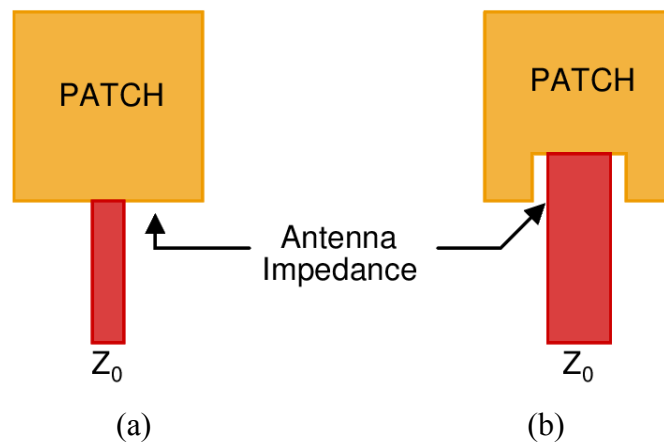


Figure 1.4 Patch antenna with feed lines. (a) edge-feed (b) inset feed.

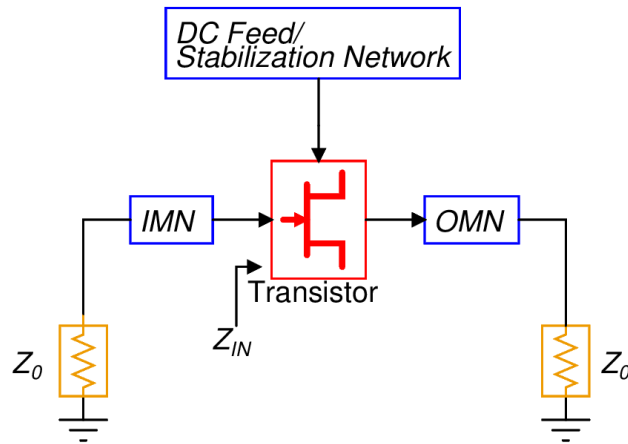


Figure 1.5 RF/Microwave single stage amplifier. Input and output matching networks (IMN/OMN) are essential blocks.

RF Amplifiers: As mentioned earlier, input and output matching networks (IMN/OMN) are required in RF/microwave amplifier to match a complex load (such as Z_L) to the port impedance, Z_0 . This situation is depicted in Fig. 1.5. Similarly, other passive components such as Baluns etc. and active devices such as mixers and oscillators etc. are required to have proper matching networks [2-3].

Energy Harvesting: There has been immense interest in RF energy harvesting systems. This essentially entails extraction of energy from cell phone towers or other ambient RF radiations. The motivation is to supply power to the low-energy wireless sensor nodes and wearable electronic devices whose manual maintenance would be very challenging [8-11]. Fig. 1.6 shows a typical block diagram of an RF energy harvesting system.

It is obvious that an antenna would capture the ambient RF energy and pass it to a non-linear device, normally a Shottky diode, followed by a filter to suppress the ripples. This part of the system is usually termed as *rectenna*. The load includes a power mana-

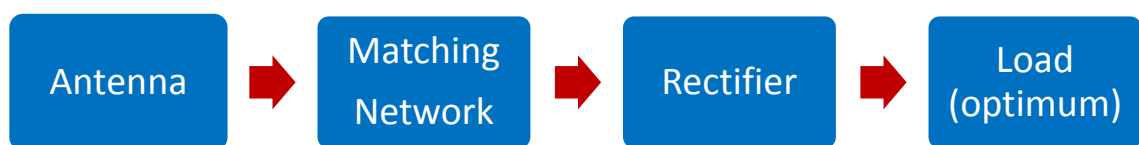


Figure 1.6 Block diagram for RF energy scavenging system.

gement module (PMM) that would be required to store the energy. However, a very crucial block is the impedance matching network. Its purpose is to match the complex input impedance of the rectifier to the 50Ω impedance of antenna for maximum power transfer. Design of an energy harvesting system essentially involves design of the rectifier and associated matching networks.

1.2 Recent Interests

An unprecedented recent growth in wireless communication technologies has resulted in numerous challenges due to ever increasing complexity of radio terminal infrastructure. A typical modern mobile handset needs to support multiple wireless standards like GSM, UMTS, Bluetooth, GPS, WLAN, as well as FM. Each of these standards is specified at different frequencies and moreover standards such as GSM and UMTS themselves are specified for different frequency bands in different regions of the world [12-14]. This requires a handset to be capable of supporting multiple radio frequencies [15-16]. For example, the RF front-ends in such systems require concurrent operation of all of the system components optimally functioning at more than one carrier frequency. In the traditional handsets, multiple radios are supported by dedicated hardware for each radio as depicted in Fig. 1.7 [15].

Specifically, Fig. 1.7 depicts a simplified front-end block diagram of current state-of-the-art radio terminal supporting multiple standards making use of multiple components for various RF inputs. For example, support for three standards necessitat-

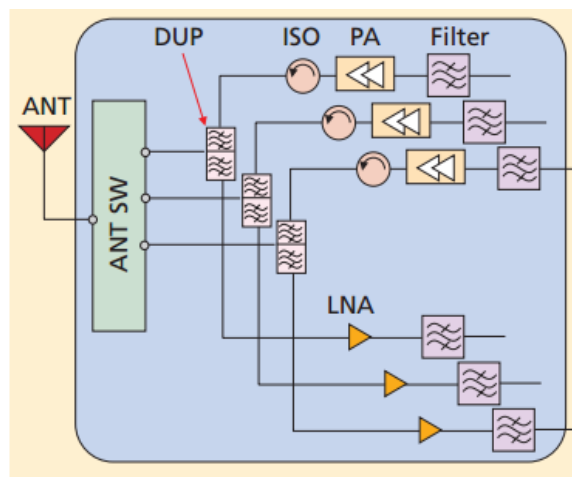


Figure 1.7 Conventional radio terminal: multiple devices for various RF inputs [15].

es the use of three distinct isolators, three distinct power amplifiers (PAs), and three distinct filter blocks, etc. Apparently, this is a suboptimal solution in terms of power consumption, area, and cost [12]. This type of architecture also puts considerably burden while designing band-select filters and requires careful frequency planning due to high number of interferers [13]. In order to address such a situation, a possible alternative architecture makes use of the multi-frequency circuit components [15-16]. As shown in Fig. 1.8, the idea is to just utilize one set of circuit components but each possessing frequency dependent characteristics. So, rather than having, say, three distinct PAs, one needs just single PA capable of operating at the three distinct frequencies concurrently. Precisely speaking, each of these multi-frequency components is required to show similar characteristics around the different central frequencies. Apparently impedance matching is central to each of the components in the RF front-end shown in Fig. 1.8 and, therefore, it is important that the classical theory of single frequency impedance matching techniques now must be modified and replaced with multi-frequency impedance matching techniques.

At the outset, it should be noted that the wideband circuits are more suitable for multi-band/multi-standard radio terminal design. However, most of the required components are severely limited due to severe constraints in achieving wideband matching. Specifically, the Bode-Fano criterion dictates that arbitrary load impedance cannot be matched to a pure resistive source over the whole frequency spectrum or even at all frequencies within a finite frequency band [17-19]. However, it is definitely possible that matching can be established at desired number of frequencies provided the

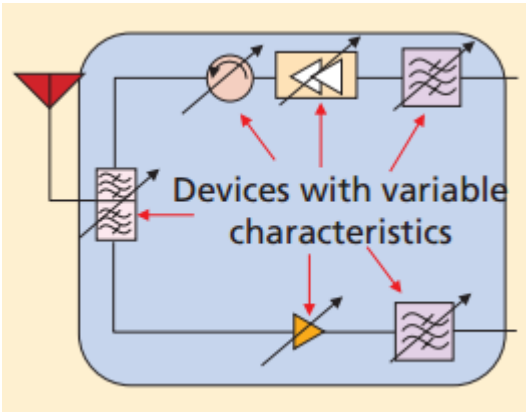


Figure 1.8 Multi-band RF front-ends incorporating multi-frequency components [15].

required impedances have finite resistive components at those frequencies [2, 13]. For example, a wideband PA design needs optimal loads to be seen over entire bandwidth. Any mismatch from the optimal loads can severely affect efficiency and linearity of the transmitter. This mismatch generally occurs due to the bandwidth limitation of matching network imposed by Bode-Fano criterion. As a consequence, the design of wideband matching, a pre-requisite for obtaining optimum efficiency and linearity over the specified band from non-linear components such as PA, is not practically possible for the situation when the intended bandwidth covers two distinct communication standards far apart in terms of their carrier frequencies. In such situations, dual-frequency/multi-frequency matching could be extremely useful considering that they can provide optimum solution over a limited range of bandwidth around the chosen carrier frequencies of operation [13]. For example, to get a dual-frequency amplifier, the single frequency amplifier depicted earlier in Fig. 1.5 must be modified and specifically the required input and the output matching networks (IMN/OMN) now must be replaced by dual- frequency IMN/OMN as shown in Fig. 1.9. Similarly, dual-frequency matching is required for the Wilkinson power divider shown earlier in Fig. 1.2 to ensure a dual-frequency behavior.

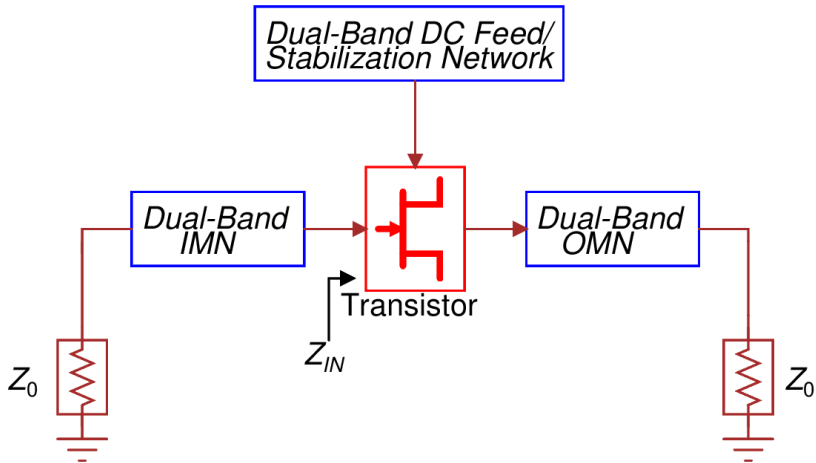


Figure 1.9 Schematic of a dual-frequency single stage amplifier.

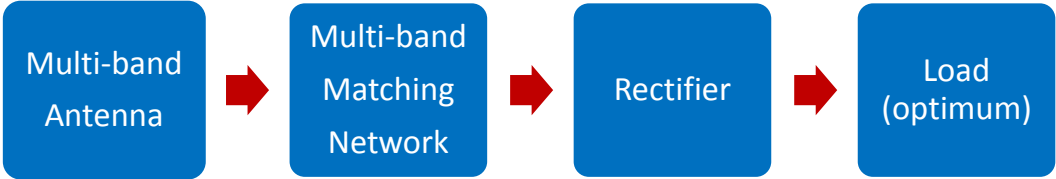


Figure 1.10 Block diagram for RF energy scavenging system for multiple RF sources.

Furthermore, energy available from the ambient RF radiations is very low, and even a good energy harvesting system having RF-DC conversion efficiency of 80% or higher may not be that helpful [8, 11]. The low levels of ambient RF energy are normally distributed in multiple frequency bands. Very recently, there has been a proposal of concurrent energy scavenging from multiple RF sources operating at different frequencies [8-11]. In a city, multiple RF radiation would come from, say, GSM900 BTS, DTV towers, Bluetooth and WiFi (although energy from the latter two would be very small). As shown in Fig. 1.10, again the concept of multi-frequency matching networks becomes critical. RF energy from multiple sources is passed through a multi-band/wideband antenna to a rectifier which necessitates incorporation of a multi-frequency matching network.

1.3. Major Contributions and Scope of this Thesis

After an extensive research survey on impedance transformation circuits, presented in the next chapter, it was identified that the existing state-of-art has severe limitations. It is, therefore, extremely important to investigate and propose novel solutions to address those limitations in the existing design approaches. This thesis has been pursued to contribute into this direction and to address some of the concerns. The scope, objectives, and the contributions of this thesis are briefly outlined below.

1.3.1 Dual-frequency Impedance Transforming Circuits

Many of the reviewed dual-frequency circuits were found to be limited in one or the other aspect. For example, design of most of the circuits capable of operating at two frequencies concurrently rely on design equations that are either too complex or need extensive optimization. Similarly, some reported techniques are simple but they are limited in terms of the achievable frequency ratio or by the range of impedances that could be matched. Furthermore, some of them are unable to provide features, such as DC isolation, which in turn necessitates the requirement of coupling capacitor in amplifier designs. Thus, the first part of this doctoral research work provides the following solutions:

- Analytical formulations with closed-form and simple design equations for dual-frequency matching networks.

- Dual-frequency matching strategy that caters to the wider range of load impedances.
- Design of dual-frequency matching techniques, supported with simple formulations, to achieve enhanced features such as DC isolation.
- Application of the developed dual-frequency matching approaches in the design of novel dual-frequency components such as couplers, dividers etc.

1.3.2 Tri-frequency Impedance Transforming Circuits

It is extremely important to note that the work on tri-frequency impedance transformation and associated circuits and components are still in its infancy. Not many works have been reported in this direction. Therefore, as part of the doctoral research, effort has been put to carry out the work in this direction to achieve the following objective:

- To develop a systematic approach to realize generalized tri-band impedance matching technique to address wider impedance mismatch scenarios.

1.3.3 Scope of This Work

With regard to the scope and limitations of this thesis, few important points must be borne in mind. Firstly, the impedance matching networks presented in this thesis are intended for establishing matching at fundamental frequencies. Passive components, such as the Wilkinson power divider, shown earlier in Fig. 1.2, or the branch-line coupler, shown earlier in Fig. 1.3, require matching at fundamental frequencies. The power amplifiers, especially the high efficiency PAs, however, require proper matching at harmonic frequencies as well. Fortunately, as reported in [20], the fundamental matching network could always be designed independent of the required harmonic terminations and, therefore, the techniques discussed in this thesis would also be of significant interests to the PA designers.

Secondly, the seasoned engineers would be taken aback by not finding even a single Smith Chart in this thesis. We do not deny the importance of the Smith Chart, but the analytical approach taken in this thesis are mainly intended for computer aided design program [21].

Thirdly, the bandwidths of matching networks are not emphasized as is customary in the literature of multi-frequency matching network. The reason is that the notion of bandwidth is a vague idea when the loads become frequency dependent. And, more importantly, this figure of merit is not that crucial in multi-frequency design as it is in wide-band design. If the same bandwidth performance is sought from a multi-frequency circuit as it is mandated in wideband design then there is no need to go for multi-frequency design in the first place. It is perhaps this reason that the reported multi-frequency designs have as low as 30MHz bandwidth [22-23]. Nevertheless, this thesis has made an important contribution by providing an intuitive explanation of relative bandwidth [24].

Finally, it must be noted as well that the impedance matching network prototypes shown in this thesis are essentially one-port devices terminated into the considered loads. Therefore, only the measured return-losses, that is, reflection in terms of S_{11} or Gamma have been depicted for them. The insertion-losses have not been shown as they are not accessible for one-port networks. It should also be noted that insertion loss is direct function of the return loss assuming that no radiation/conductive/dielectric losses exist in structure. These losses are often negligible at low RF frequencies and for transmission line based structures built properly in low loss dielectric substrate. As discussed in chapter 8, a good return-loss in these one-port devices causes very small insertion-loss when manufactured using high-quality and frequency stable dielectric materials.

1.4. Organization and Presentation of the Thesis

This thesis can be broadly organized into three parts. The first and, in fact, the major part delves into the analysis and design of dual-frequency impedance transformation networks. This part is further divided into eight chapters.

Chapter 2 presents a review of various dual-, tri-, and multi-frequency impedance matching networks. A clear distinction is made among the contribution and design strategies of various reported works. We have also elaborated upon the strengths and weaknesses of each related work. It must be emphasized that a major contribution of this thesis is to report multi-frequency devices, such as dual-frequency directional

coupler, divider etc. Since, these devices are shown as applications of impedance matching network; their reviews have been presented in the same chapters where they have been discussed.

Chapter 3 presents interesting dual-frequency admittance properties of single section transmission lines terminated into real impedance. Advantages of using this discovered property is also discussed along with its application in the design of the Wilkinson power divider.

Chapter 4 delves upon the use of dual-frequency quarter wavelength blocks in dual-frequency impedance matching networks. It is demonstrated that making use of multitudes of the existing dual-frequency quarter wavelength blocks in the literature comes very handy in the matching network design.

In Chapter 5, use of coupled lines to create DC isolated matching networks are discussed. A clear analytical approach to design dual-frequency matching network that caters to a wider range of load impedances are presented for real as well as frequency dependent complex impedances.

Afterwards, Chapter 6 focuses on the properties of two sections transmission line based transformers. Specifically, admittance properties of two section transmission line when terminated into real impedance are discussed and their applications in design of directional couplers are shown.

In Chapter 7, the concept of load-healing as applied to dual-frequency matching networks are discussed. It is shown through analysis aided with a number of design cases that the novel concept of load-healing could be very useful in extending transformation ratio.

In Chapter 8, the concept of single section and two section transmission lines terminated into real impedances are generalized to multi-section scenario. Again, the advantage of using multiple-sections to improve the transformation ratio is demonstrated. This chapter closes the part 1 of this thesis.

Chapter 9 is the second part of this thesis. It reports a systematic design methodology for tri-frequency matching network. In essence, this technique uses dual-

frequency matching networks in conjunction with a dual-to-tri-frequency transformer to implement the functionality.

A very easy way to synthesize a multi-frequency DC-feed network is discussed in Chapter 10 as third and the last part of this thesis. A DC-feed network is used to feed DC bias signal as well as to stop DC-RF interaction. A DC-feed network can be thought as a special case of impedance matching network where the task is to create infinite input impedance at the frequencies of interest. Therefore, this chapter aptly fits into this thesis work.

Afterwards, conclusion is presented in the end that highlights the achievements of this thesis and some future possibilities of research in this area.

Finally, a note about the presentation style is in order: Few formulas and design equations would seem reoccurring many times during the entire thesis; this has been done intentionally. The motivation is to help readers easily grab the concept without having to bother about browsing back to previous pages in this extensive thesis. This does increase the page count, but definitely not much- the total excess page count does not exceed by ten or so.

Chapter 2

Literature Review

As pointed out in the previous chapter, impedance matching network is one of the most ubiquitous blocks of many RF/Microwave circuits/systems. For example, they are very crucial in design of amplifier, mixer, oscillator and antenna, and also find extensive use in power dividers/combiners. Some conventional matching topologies like quarter-wavelength/single-/double-stub impedance transformers are routinely used for this purpose [2-3, 25-26]. Early researchers have focused on wideband matching networks and their limitations [17-19, 27-29]. However, as outlined in the Chapter 1, in recent years there is huge interest in dual-frequency/multi-frequency circuits and systems, which has resulted into new design challenges [13] including in the design of matching networks. Thus, researchers have responded to this challenge and have reported numerous dual-frequency impedance transformers, few tri- and very few multi-frequency matching circuits during this decade and vast interest in such circuits is still evident [21-23, 30-56].

Three types of matching networks are of interest to the circuit designers:

- 1) Real impedance to real impedance transformer,
- 2) Complex impedance to real impedance transformer, and
- 3) Complex impedance to complex impedance transformer.

For example, a real to real impedance transformer is useful in power dividers [30], a complex to real impedance transformer is useful in amplifiers [31], and a complex to complex impedance transformer is useful in multi-stage amplifiers for inter-stage matching [32].

In the following sections, an extensive review of literature on multi-frequency impedance matching networks is presented.

2.1 Dual-Frequency Impedance Matching Networks

Since, the vast majority of recent works on impedance matching circuits are aimed at dual-frequency applications; therefore, this subsection reviews these works in details. Specifically, the following two subsections discuss the works on the first two categories of the load impedance—real and complex loads. The third category involving complex load as well as the complex source impedance scenario is of relatively lesser interest to the researchers, there are very few works on them if at all, and therefore their review has been combined with the second category.

2.1.1 Dual-Frequency Matching Networks for Real Load Impedances

One of the most common network configurations to match a real load impedance (Z_L) to a real source impedance (Z_S) is a two sections transmission line network shown in Fig. 2.1. A matching network working at fundamental and its first harmonic based on two section of $1/3$ -wavelength was reported by Chow et al. [33]. The idea in this Chow's transformer is to transform $Z_L = Z_0 = 50 \Omega$ to $Z_S = KZ_0$, where K is a constant called **transformation ratio**. Input impedance Z_{inB} shown in Fig. 2.1 is forced to be real and equal to KZ_0 and this result into total four transcendental equations. A particular case is solved for $K=2$ using CAD and it is deduced that the solution is satisfied by a choice $Z_B=K^{2/3}Z_L$, $Z_A=K^{1/3}Z_L$, and $\theta_A = \theta_B = \lambda/6$ (total length= $\lambda/3$). This solution is only approximate and it is found that the imaginary part of Z_{inB} is close to zero and the real part is close to Z_0 for K up to 6. The major limitation of this work is that it is neither exact nor analytical and the second frequency cannot be selected arbitrarily.

A small, arbitrary dual-frequency transformer to match real source and load impedances was reported by Monzon [34]. It was very well received by the community as it solved both the problems of Chow's transformer. The structure of this configuration is similar to that of Chow's except that θ_A and θ_B are no more fixed at $1/3$ -wavelength. Monzon assumes that $\theta_A = \theta_B = \theta$ and thereby reduces the number of variables. It leads to few simple design equations (2-1) to (2-3):

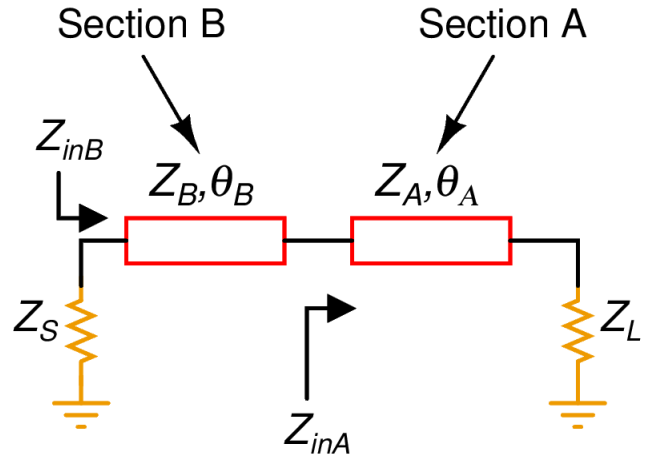


Figure 2.1 Two sections dual-frequency transformer.

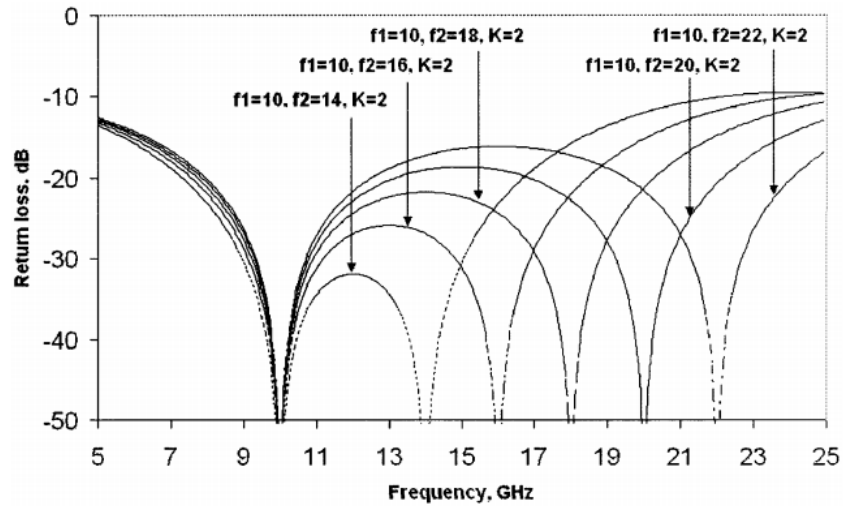


Figure 2.2 Return loss of Monzon's two sections dual-frequency transformer for a fixed f_1 and K , and varying f_2 [34].

$$Z_B = \sqrt{\frac{Z_s(Z_L - Z_s)}{2\alpha} + \sqrt{\left(\frac{Z_s(Z_L - Z_s)}{2\alpha}\right)^2 + Z_L Z_s^3}} \quad (2-1)$$

$$Z_A = \frac{Z_s Z_L}{Z_B} \quad (2-2)$$

$$\alpha = \tan^2 \theta \quad (2-3)$$

The value of θ depends on the ratio, $r = f_2/f_1$, of the two arbitrary frequencies. The parameter r is usually termed as the **band-ratio** or **frequency-ratio**. While Monzon presented the electrical length in terms of β (the propagation constant) but it can be shown after little algebraic manipulations that θ can also be written as follows:

$$\theta = \pi / (1 + r) \quad (2-4)$$

No doubt the Monzon transformer with simple design equations has become a de facto dual-frequency transformer for real impedances. It works for different cases as shown in Fig. 2.2. However, the explanation to arrive at (2-4) is not very intuitive and is a brute-force solution. Moreover, this work does not take the limited characteristic impedance $20\Omega - 150\Omega$ that could only be fabricated in simple microstrip technology. Also, it is not clear as what happens when more than two section are used. It will be demonstrated in the later chapters that the achievable transformation-ratio from the Monzon transformer is also limited.

A two section dual-frequency Chebyshev impedance transformer reported in [35] demonstrates that the Monzon transformer is a special case of two section Chebyshev dual-frequency transformer. Moreover, the two section transformer of [35] is more general in that it showed a tradeoff between the out of band reflection coefficient and the achievable bandwidth. A more generic dual-frequency Chebyshev transformer proposed in [36] utilizes even number of sections.

L-type network has traditionally been used extensively for single-frequency applications [2]. An L-type network for dual-frequency applications reported in [30] is shown in Fig. 2.3. It is more flexible physically in that the stub could either be placed on the right or left side of the horizontal transmission line section (TL-section) having

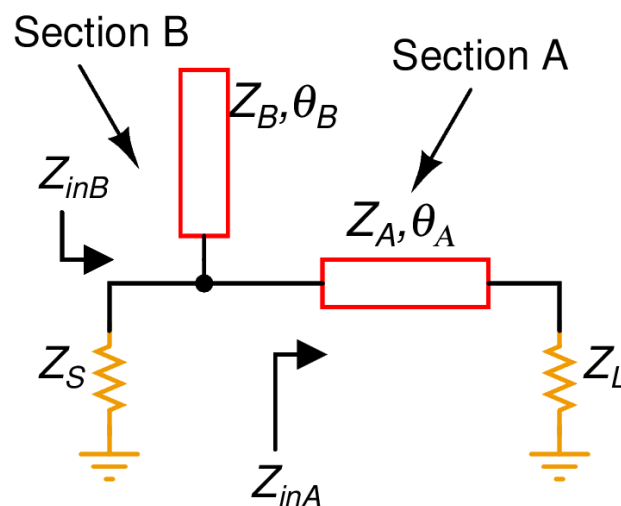


Figure 2.3 L-type network for dual-frequency matching application [30].

the characteristic impedance Z_A . Besides, the stub could itself be either short or open circuited. These different possibilities give this impedance transformer a great deal of flexibility as it can address many impedance environments. Despite all this different flavors of the L-type transformer, its frequency-ratio (r) and transformation ratio (K) is highly limited as compared to the Monzon transformer. Moreover, quite like the Monzon transformer, this work also fails to give insightful working of the transformer. It will be shown in the next chapters how the discovered admittance property of multi-section transmission line provides a better solution and understanding.

2.1.2 Dual-Frequency Matching Networks for Complex Load Impedances

Impedance transforming networks reviewed in the previous subsections were applicable for real-to-real impedance transformation. A further challenge in dual-frequency amplifier or energy harvesting network design is that the load impedance has two distinct complex values at the two frequencies. Fig. 2.4 (top) shows a simulation setup to access the input impedance of a two-port network from S-parameter data of any device— here a transistor. The Fig. 2.4 (bottom) shows how the real and the imaginary parts of the transistor vary with frequency. It is apparent that the input impedance is complex as well as frequency dependent. Therefore, now the problem essentially is to match $Z_L=R_1+jX_1 @f_1$ and $Z_L=R_2+jX_2 @f_2$ to Z_0 , concurrently.

An intriguing question would be about not considering frequency dependent real impedance in the previous sub-section. The reason for assuming a fixed real impedance $Z_L=R_1 @f_1$ and $Z_L=R_1 @f_2$ comes from possible application of such transformers. For example, consider the design of dual-frequency Wilkinson power divider [Chap. 1, Fig. 1.2]. It is apparent from Fig. 1.2 that this design involves matching of $Z_L=Z_0 @f_1$ and $Z_L=Z_0 @f_2$ to $2Z_0$. This is the most common scenario where the load impedance in such problems is fixed and, therefore, there is very little interest in frequency dependent real impedance.

Many dual-frequency impedance transforming networks have been proposed to cater to frequency-dependent complex load impedance. Perhaps, the first attempt reported in [37] which uses multiple sections and two parallel stubs as shown in Fig. 2.5 requires a CAD based approximation besides needing solution of a fourth degree equation. More-

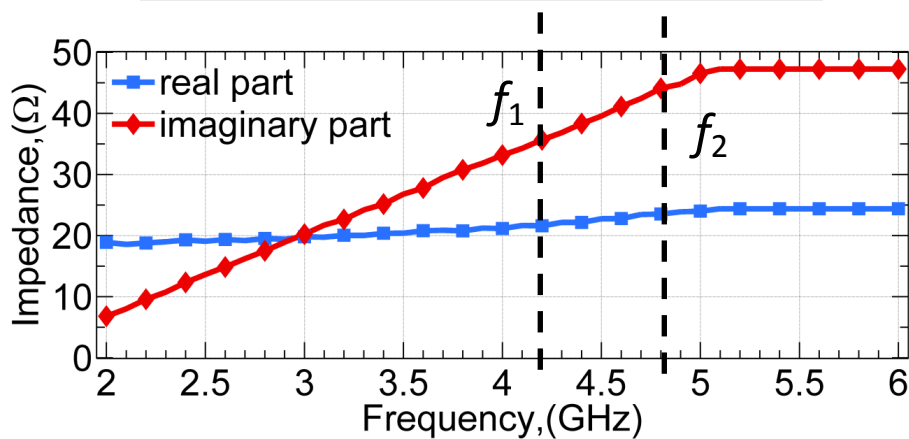
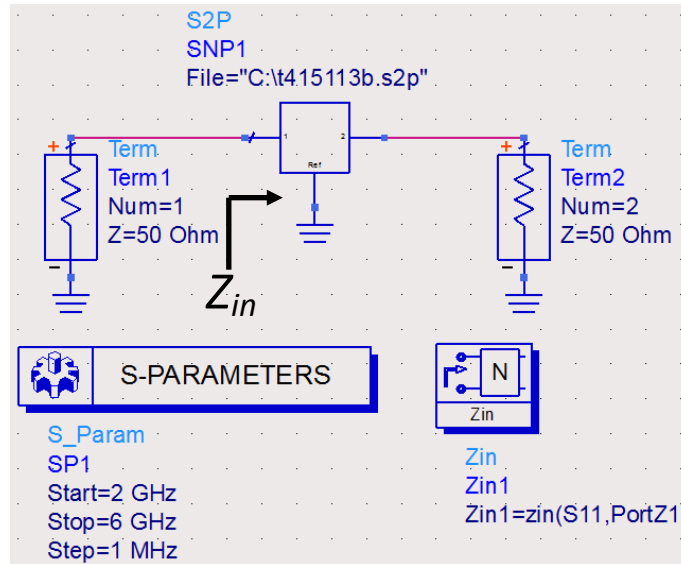


Figure 2.4 Variation of the input impedance of a transistor with frequency. The impedance is frequency dependent and complex: $Z_L=R_1+jX_1 @f_1$ and $Z_L=R_2+jX_2 @f_2$.

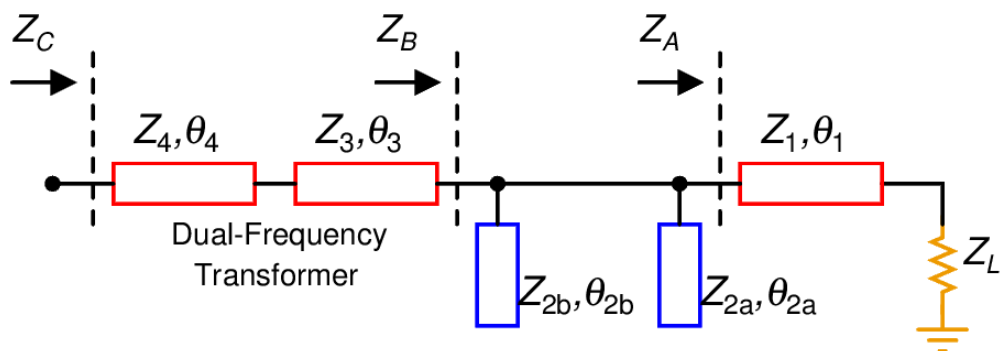


Figure 2.5 A transformer for frequency-dependent complex load impedance [37].

over, this work can be considered as a more appropriate wideband transformation network rather than a dual-frequency transformer. A more general matching network in this context is shown in Fig. 2.6 (top) [38]. It considered complex source impedance as

well as complex load impedance. The design methodology is based on fully analytical equations, although a bit involved, and performs well under different load/source conditions (Fig. 2.6, bottom). However, this type of transformer is highly limited in use since it does not consider a frequency dependent nature of the load [39].

A three section transformer, depicted in Fig. 2.7 (top), can also be used to match a frequency-dependent complex load to a real source impedance [40]. In this, the third section (Z_3) is used to transform $Z_L=R_1+jX_1 @f_1$ and $Z_L=R_2+jX_2 @f_2$ to an intermediate impedance $Z_{L2}=R+jX @f_1$ and $Z_{L2}=R-jX @f_2$. Then, the remaining two sections are used to match the complex conjugate impedances to Z_0 . This impedance transformer is based on complete analytical equations and its ideal response is shown in Fig. 2.7 (bottom). However, the design equations are complicated as it necessitates solution of a

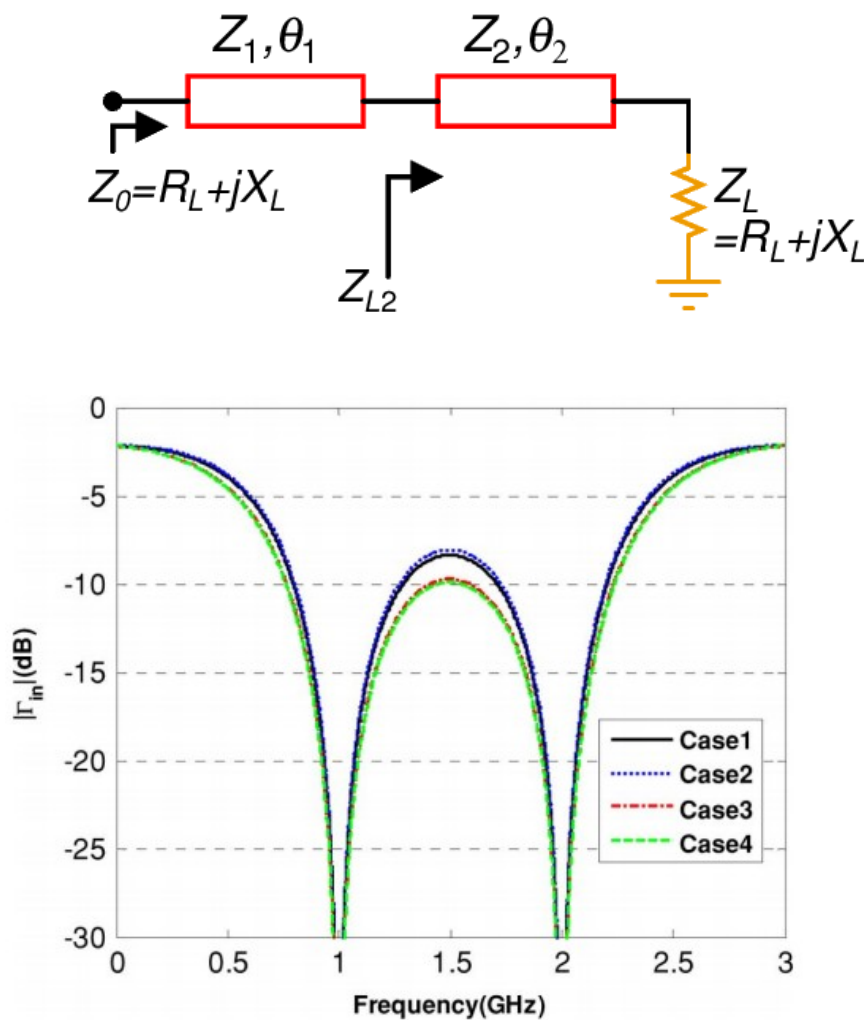


Figure 2.6 A two section transformer for complex load and source impedances [38].

fourth order polynomial. Furthermore, it is also not apparent as to why the latter two sections are able to match a complex conjugate related impedances to a real impedance.

Later a more generalized impedance transformer, shown in Fig. 2.8 (top), was reported in [41]. Here, the load as well as the source was assumed to be complex and frequency dependent. The idea is similar to the three-section transformer with an additional section to turn the source impedance into complex conjugate related impedance Z_{in} and then the two middle sections match the same to Z_{out} . Fig. 2.8 (bottom) shows the response of this transformer for load/source impedance shown in Fig. 2.8 (middle). This transformer has the same limitations as that of the three-section transformer [40].

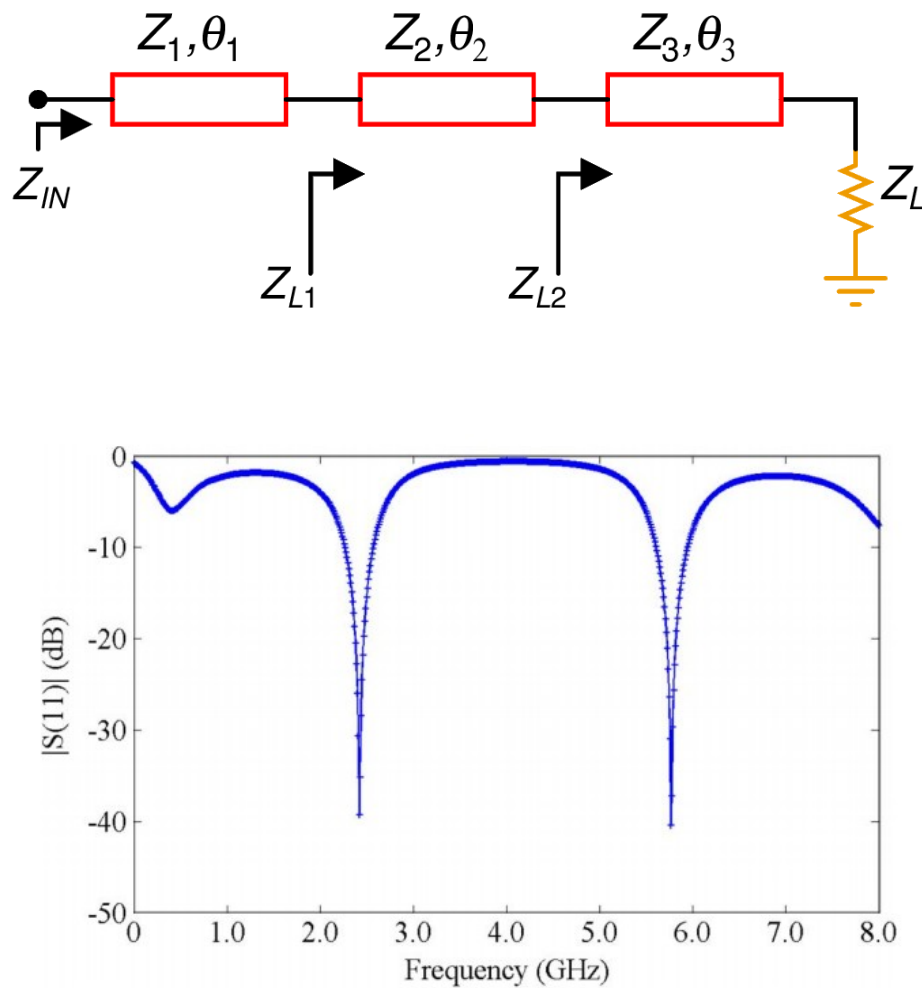


Figure 2.7 A three-section transformer for complex frequency-dependent load impedance (top) and its ideal performance (bottom) [40].

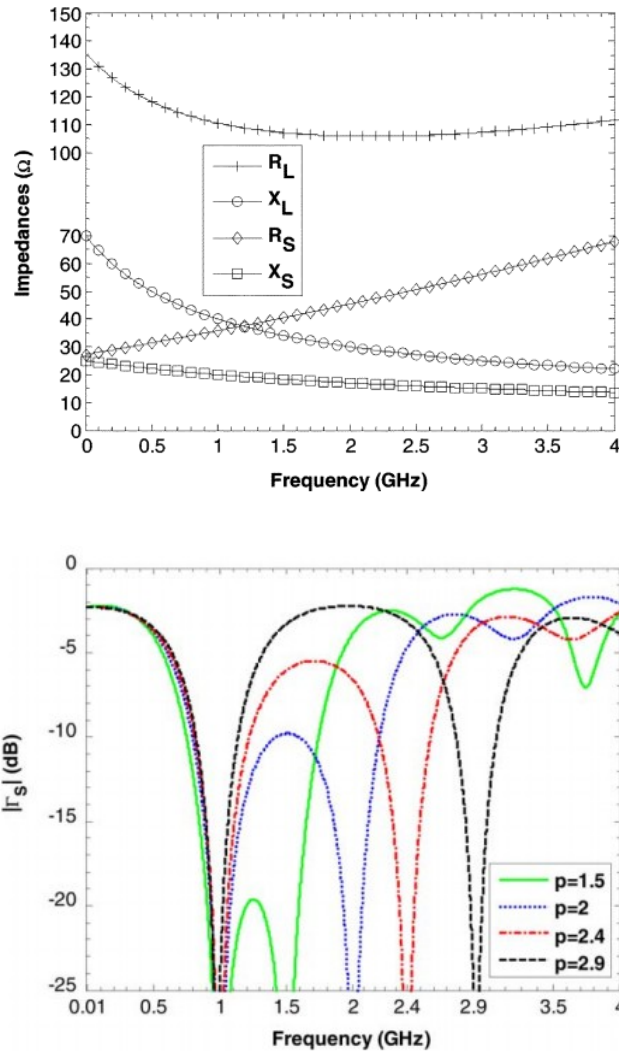
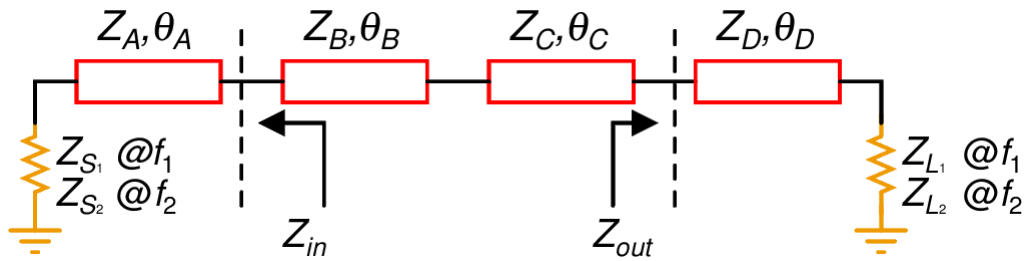


Figure 2.8 A generic dual-frequency transformer for complex frequency-dependent load as well as source impedance and the corresponding performance [41].

Chuang [42] reported a two-section transformer incorporating shunt stubs. But, the design equations are transcendental and could be solved only through some optimization algorithm/numerically.

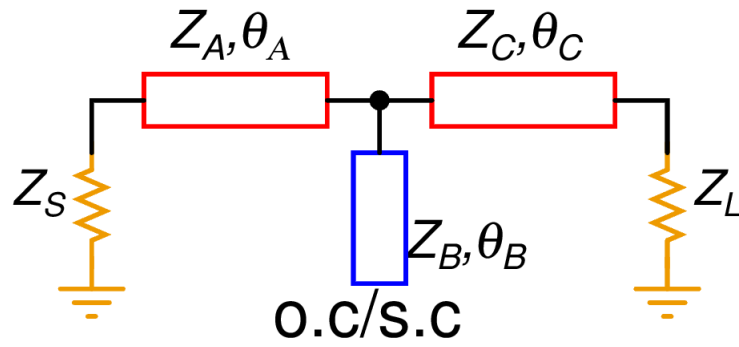


Figure 2.9 A T-type transformer for complex frequency-dependent load impedance [43].

A very simple and elegant design, shown in Fig. 2.9, utilizes a T-section network for dual-frequency matching [43]. The idea is to use the formulation reported in [40] to design a complex conjugate related Y_{right} , and match the real part of the same to real part of Y_{left} . The remaining imaginary part is cancelled using a dual frequency stub. The major limitation of this approach is its failure to achieve a wider transformation ratio. This solution does not work in many situations as the transformer may not be physically realizable. A **load-healing** concept will be discussed in this context in the later chapters as a way to improve the transformation ratio. Similarly, a Pi-section transformer shown in Fig. 2.10 was reported very recently [23] but again it also provides only iteration based solution.

A dual-frequency transformer using dual-frequency phase offset line with different characteristic impedances, reported in [22], also showed their application in a dual-frequency power amplifier. This transformer needed graphical solution and has a slightly complex layout.

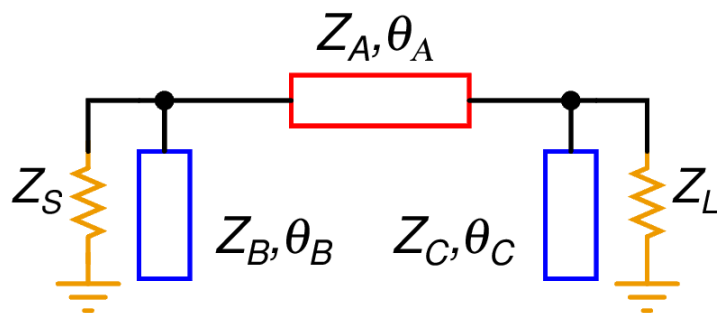


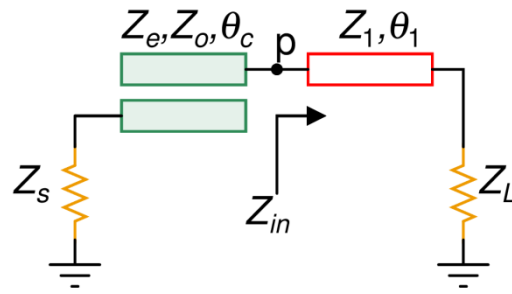
Figure 2.10 A Pi-type transformer for complex frequency-dependent load impedance [23].

Use of pi-section dual-frequency network along with shunt stub was shown in [44] but it has limitation of putting 'too much burden' on the Pi-network. A modified T-network type impedance transformer, reported in [45], utilizes Monzon's transformer as of its arm. However, the use of Monzon's transformer limits the usefulness of this modified transformer. Using smith chart to convert two distinct loads into complex conjugate values then using a filter prototype to transform them into Z_0 is also not very helpful as there is no analytical method to work this out [46]. Besides, it is also not possible to achieve wideband matching using this technique as claimed and a large board area is consumed by the overall structure. Later, an analytical approach to this method was presented in [21] but again the designs equations are involved. Moreover, the transformation ratio/frequency ratio of this network is still limited.

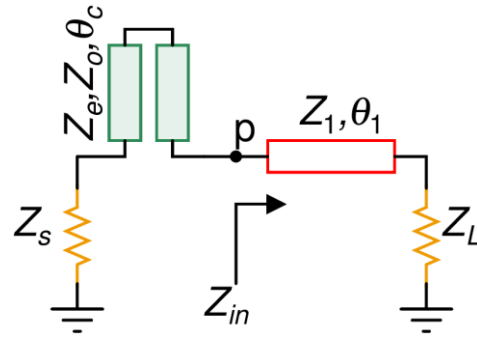
Applications of coupled line in matching complex load were reported in [47-49]. The motivations to use coupled lines are that they are most often compact, and they have an added degree of design freedom due to availability of two characteristic impedances corresponding to the two different modes. Moreover, a parallel coupled line is also DC isolated that is very useful in the design of amplifiers as it discards the need of the coupling capacitors.

An inherent DC block coupled line dual-frequency matching network was reported in [47] and a T-junction power divider using coupled line based matching circuit was discussed in [48]. In both of these designs, shown in Fig. 2.11, one has to guarantee matching both for real as well as for imaginary parts of Z_{in} at the coupled line-transmission line common node (p), that too, at two distinct frequencies which is often difficult. It is especially difficult with microstrip coupled line having unequal even/odd mode phase velocities.

A miniaturized dual-frequency matching network reported in [49] is shown in Fig. 2.12. The idea is to load the other two terminals of the coupled lines with stubs that are usually kept open or short circuited. This results into a compact structure with DC isolation. However, this transformer works only at relatively close operating frequencies.



(a)



(b)

Figure 2.11 Coupled line based matching networks (a) [47] (b) [48].

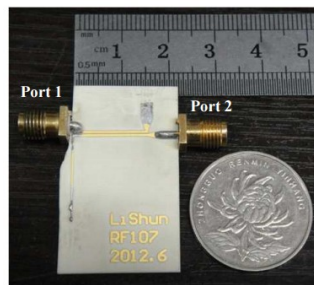
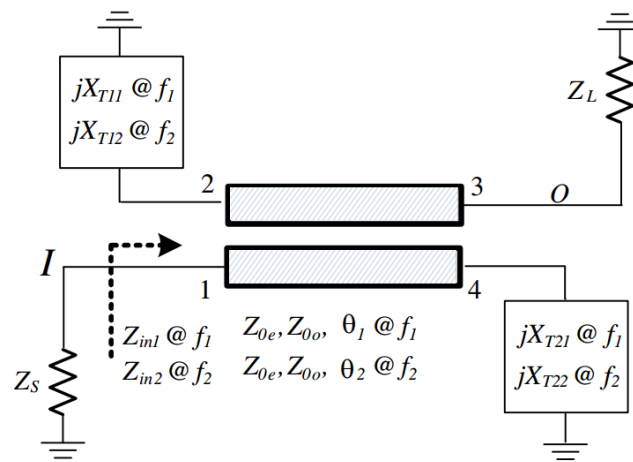


Figure 2.12 Dual-frequency matching network (top) and its prototype (bottom) for very close operating frequencies [49].

Finally, lumped component based dual-frequency matching networks are also found in literature such as in [50]. However fabrication of lumped component, that too an ideal one, is difficult at higher frequencies. Besides, maintaining their value over wide frequency range is also difficult [32].

2.2 Tri-Frequency Impedance Matching Networks

As is evident from the above section, there have been numerous research reports on dual-frequency impedance matching networks. However, only few tri-frequency impedance matching networks have been reported. A three section tri-frequency impedance transformer, reported in [51], is specific to Wilkinson power divider besides being only an approximate result based on curve fitting. The LC resonators based tri-frequency transformer shown in Fig. 2.13 [52] is limited due to the use of lumped components. Moreover, the design technique is based on hit-and-trial rather on analytical equations.

A compact tri-frequency matching network shown in Fig. 2.14 (top) was reported in [53]. It also works at fourth frequency, but is a function of the lower three frequencies, and therefore the fourth frequency cannot be arbitrary or uncorrelated. It utilizes C-type coupled lines in cascade and in essence is a two section transformer.

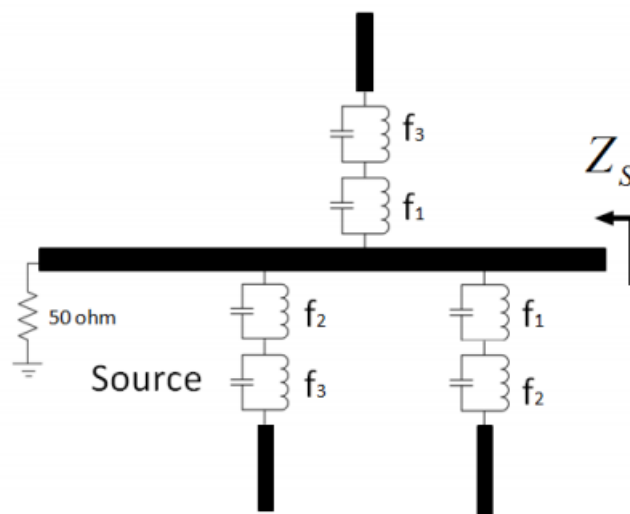


Figure 2.13 Resonators based tri-frequency matching network [52].

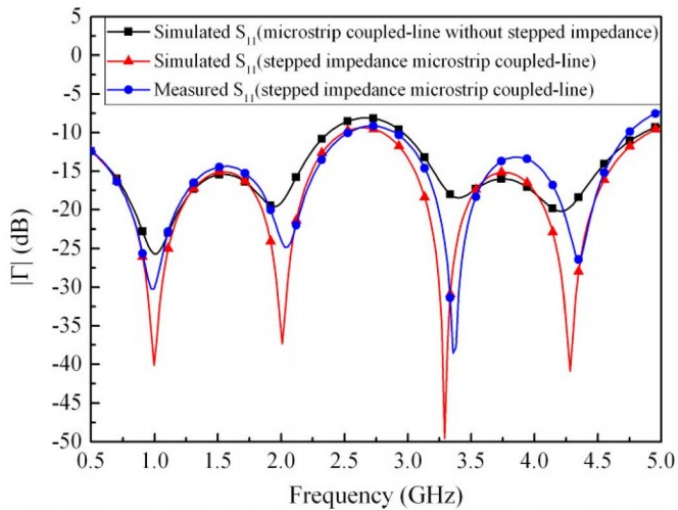
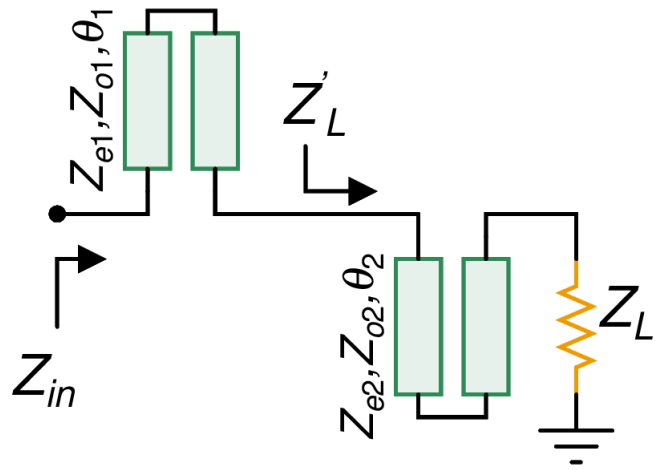


Figure 2.14 Coupled line two-section tri-frequency matching network (top) and the corresponding response (bottom) [53].

The design methodology is fully analytical and shows good performance in strip-line technology. The performance gets degraded in microstrip due to unequal even-odd velocities and thus would require compensation. In addition, the technique is only limited to real load impedance.

Another variant of this network shown in Fig. 2.15 [54] utilizes two C-type coupled lines. However, one of the coupled lines basically works as a stub. Thus, it is essentially an L-type transformer for real loads. It has similar limitations as the previous one. In addition, the layout is complicated and apparently would be difficult to incorporate in many scenarios. The multiband impedance inverter network (IIN) used in [55] can be used for real to real impedance transformation but is not capable of wor-

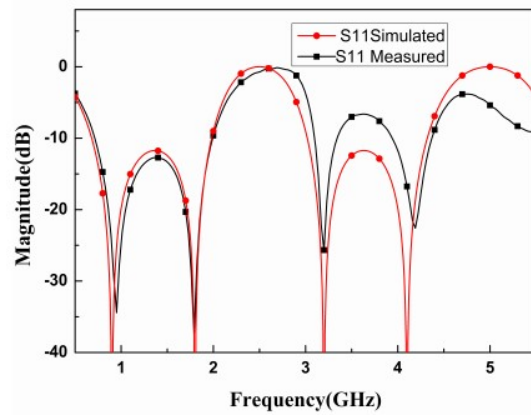
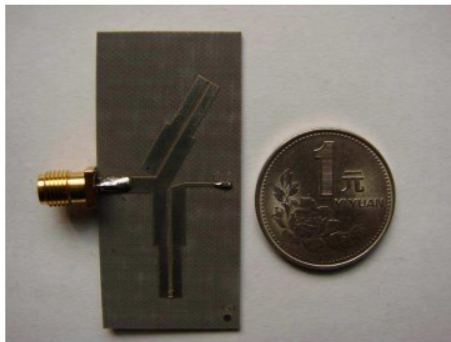
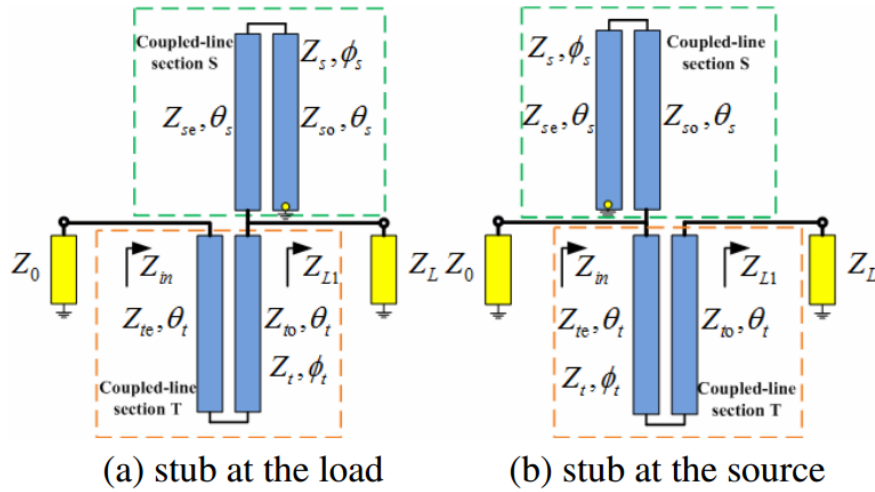


Figure 2.15 Coupled line L-type tri-frequency matching network [54].

king at any uncorrelated chosen frequencies. There is unfortunately no systematic design technique for tri-frequency matching networks, especially, considering complex load impedance.

2.3 Multi-Frequency Impedance Matching Networks

Very few works have been reported on multi-frequency matching networks, where in principle there is no limitation on the number of frequencies over which a load could be matched to source impedance. For example, Nallam [12] utilized the concept of filter transformation method to report a lumped-element realization of multi-frequency matching network as shown in Fig. 2.16. Its performance, when implemented on FR4 substrate is shown in Fig. 2.17 for dual-frequency case. On the positive side, this methodology is generic. However, it is only applicable to the lumped component mat-

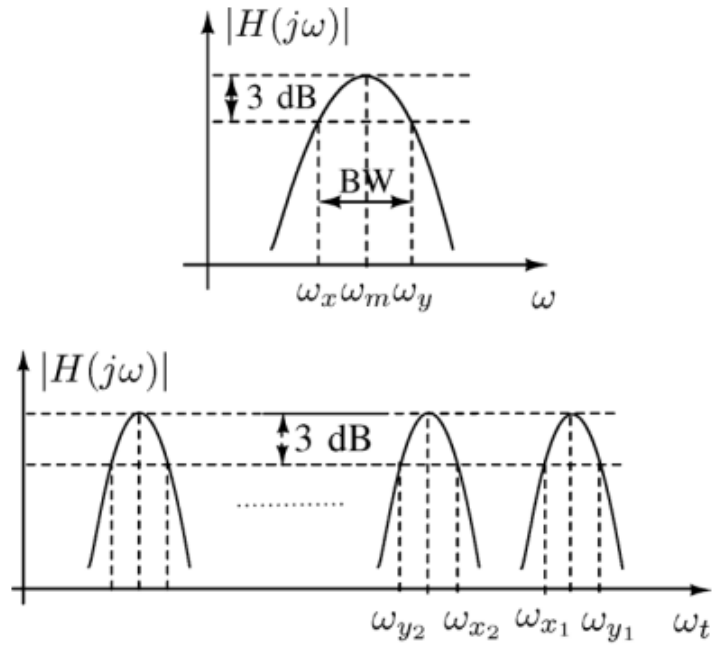


Figure 2.16 Multi-frequency impedance matching network using filter transformation method [12].

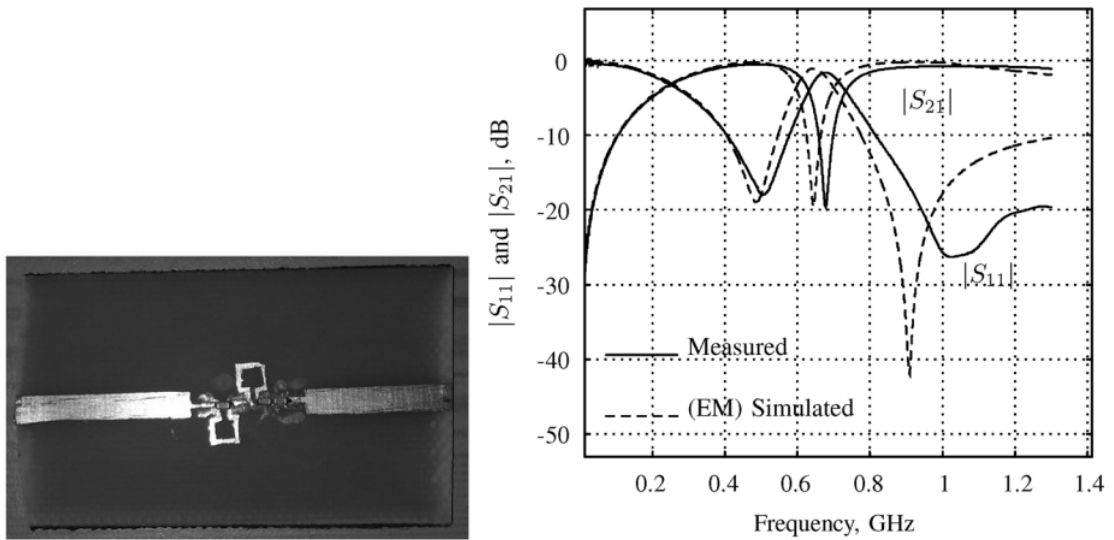


Figure 2.17 A dual-frequency matching network prototype and its performance [12].

hing network which is not that useful at high frequencies. Moreover, this approach does not seem scalable considering that the order of polynomial to be solved increases proportionally with the increase in the number of design frequencies. For example, a six-frequency match would require solution of a six-order polynomial.

The multi-frequency matching network reported in [56] is more useful at higher frequencies considering that they are completely transmission line based. However, a major limitation of this design methodology is the requirement of search algorithm to arrive at realizable design. Even a dual-frequency design using this technique requires intensive algorithm runs.

2.4 Conclusion

In summary, the art and science of multi-frequency impedance matching is largely limited to dual-frequency scenario. The vast majorities of dual-frequency matching networks reported in literature are interesting but are limited in one or the other aspects with the major limitation being their low achievable frequency-ratio and transformation-ratio. For example, there are few circuits that provide matching at two frequencies concurrently. However, most of these rely on design equations that are either too complex or need extensive optimization. Similarly, some reported matching circuits are simple but they are limited in terms of the achievable frequency ratio or by the transformation. Furthermore, some of them are unable to provide DC isolation which in turn necessitates the requirement of coupling capacitor in amplifier designs. It is extremely important to note that the work on tri-band impedance transformation and associated circuits and components are in its infancy. Moreover, multi-frequency matching networks are either limited to lumped element realization with proportional increase in complexity as the number of frequency increases or are optimization and search algorithm based. The algorithm based matching network designs are unsystematic and may have convergence issues.

Chapter 3

Admittance Property of Single Section Transmission line

Single section of transmission line has been widely used in dual-frequency matching networks, such as the L-type networks discussed in previous sections. However, as pointed out earlier, their usage is based on brute-force approach rather than on any concrete theoretical premise and clear insight into their behavior. In this chapter, an analytical approach has been taken to demonstrate an interesting dual-frequency behavior of a single section of transmission line terminated into a real impedance [57-58]. Moreover, the derived properties have been applied in matching networks and Wilkinson power divider (WPD) for their performance enhancement.

3.1 Dual-Frequency Admittance Property of Single Section Transmission Line

A single section transmission line (TL) is shown in Fig.1. Here Z_1 and θ_1 are the characteristic impedance and electrical length of the TL section while Z_s is the real load impedance into which the TL section is terminated. The input admittance looking to the right is denoted as Y_A .

The input impedance, Y_A , for a transmission line can be expressed as follows:

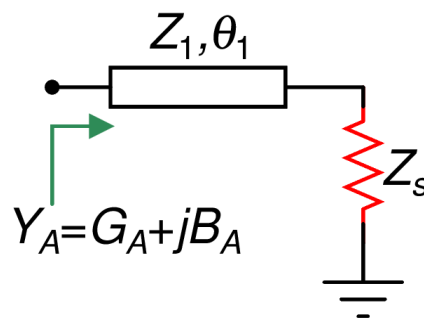


Figure 3.1 A TL section terminated into a real impedance.

$$Y_A = 1 / \left(Z_1 \frac{Z_s + jZ_1 \tan \theta_1}{Z_1 + jZ_s \tan \theta_1} \right) = G_A + jB_A \quad (3-1)$$

with,

$$G_A = \frac{Z_s (1 + \tan^2 \theta_1)}{Z_s^2 + Z_1^2 \tan^2 \theta_1} \quad (3-2)$$

$$B_A = \frac{(Z_s^2 - Z_1^2) \tan \theta_1}{Z_1 (Z_s^2 + Z_1^2 \tan^2 \theta_1)} \quad (3-3)$$

A quick look at the above expression reveals that if θ_1 is replaced by $m\pi - \theta_1$, where $m \in \text{integer}$, then G_A remains the same. However, in such a situation the sign of B_A gets changed. Therefore, if θ_1 is the electrical length assigned to the TL section at the first frequency, f_1 , and it is chosen in such a manner that the corresponding electrical length at the second frequency, f_2 , is $m\pi - \theta_1$, then $Y_A = |G_A| + j|B_A| @f_1$ and $Y_A = |G_A| - j|B_A| @f_2$ and vice-versa. To ensure this behavior, the corresponding value of θ_1 is given by (3-4) [59].

$$\theta_1 = \frac{m\pi}{1+r} \quad (3-4)$$

where, m is an integer and $r = f_2/f_1$ is the band-ratio or frequency-ratio.

To summarize:

"if θ_1 is chosen as defined by (3-4), then the input admittance looking into a transmission line terminated into a purely real impedance is complex conjugate of each other at the two frequencies."

The plots of Y_A in Fig. 3.2 illustrate this behavior. To begin with, complex conjugate property of admittance Y_A whose real and imaginary parts are given by (3-2) and (3-3) are verified by assuming $Z_s = 50\Omega$ and $f_1 = 1\text{GHz}$. Variation of G_A is shown in Fig. 3.2(a) for arbitrarily selected $Z_1 = 40\Omega$ and $r = 2, 3$ and 4 . These values of r corresponds to $f_2 = 2\text{GHz}, 3\text{GHz}$ and 4GHz respectively. It is apparent that for $r=2$, G_A has the same value at $f_1 = 1\text{GHz}$ and $f_2 = 2\text{GHz}$. This is also valid for other values of r as shown in the same figure.

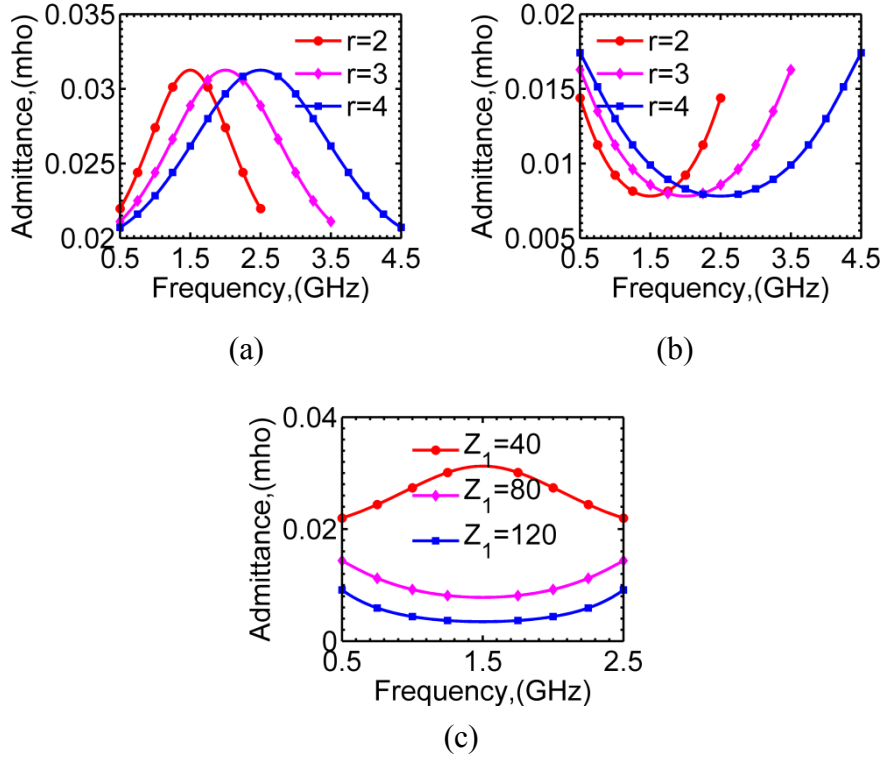


Figure 3.2 Real part, G_A of the input admittance of TL terminated into a real impedance for (a) $Z_1=40\Omega$ and $r=2, 3$ and 4 (b) $Z_1=80\Omega$ and $r=2, 3$ and 4 (c) $r=2$ and $Z_1=40\Omega, 80\Omega$ and 120Ω . G_A remains the same at $f_1=1\text{GHz}$ and rf_2 , as θ_1 is chosen according to (3-4).

The same observation is made in Fig. 3.2(b) obtained by just changing the value of Z_1 to 80Ω . It is also observed that G_A has maxima at $f_0=(f_1+f_2)/2$ (which corresponds to $\theta_1 = \pi/2$ with $m=1$) for one value of Z_1 , while it is minima for other value of Z_1 . This observation can be justified analytically as follows:

$$\frac{dG_A}{dt_1} = \frac{2Z_s t_1 (Z_s^2 - Z_1^2)}{(Z_s^2 + Z_1^2 t_1^2)^2}, t_1 = \tan \theta_1 \quad (3-5)$$

It is apparent from (3-5) that:

$$\Rightarrow \frac{dG_A}{dt_1} = 0 \quad \text{as } t_1 \rightarrow \infty \quad (3-6)$$

And thus, it proves that G_A has either maxima or minima at f_0 . Moreover, since:

$$\frac{d^2G_A}{dt_1^2} = \frac{2Z_s (Z_s^2 - Z_1^2)(Z_s^2 + Z_1^2 t_1^2)(Z_s^2 - 3Z_1^2 t_1^2)}{(Z_s^2 + Z_1^2 t_1^2)^4} \quad (3-7)$$

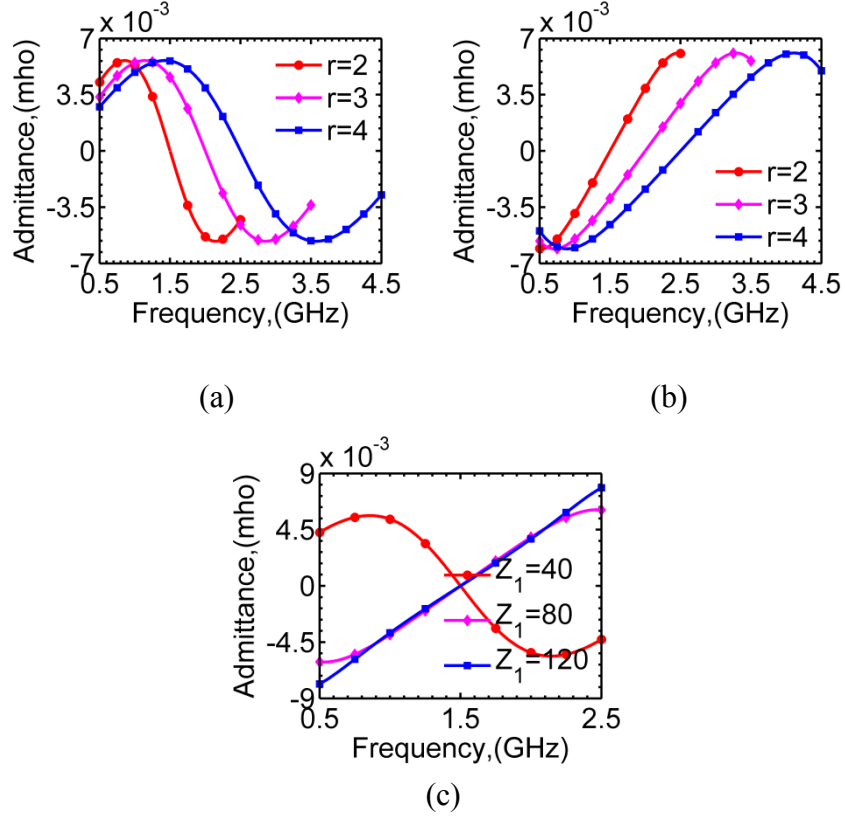


Figure 3.3 Imaginary part B_A of the input admittance of TL terminated into a real impedance for (a) $Z_1=40\Omega$ and $r=2, 3$ and 4 (b) $Z_1=80\Omega$ and $r=2, 3$ and 4 (c) $r=2$ and $Z_1=40\Omega, 80\Omega$ and 120Ω . Only the sign of B_A gets changed as plunges from $f_1=1\text{GHz}$ to rf_2 , as far as θ_1 is chosen according to (3-4).

$$\Rightarrow \frac{d^2 G_A}{dt_1^2} = \frac{2Z_s(Z_s^2 - Z_1^2)(Z_1^2 t_1^2)(-3Z_1^2 t_1^2)}{(Z_s^2 + Z_1^2 t_1^2)^4} \quad \text{as } t_1 \rightarrow \infty \quad (3-8)$$

Therefore, the sign of the second derivative depends on $(Z_s^2 - Z_1^2)$. If $Z_1 < Z_s$, then $\frac{d^2 G_A}{dt_1^2} < 0$ and a maxima occurs for G_A as can be seen in Fig. 3.2(a), otherwise a minima occurs as shown in Fig. 3.2(b).

Next keeping r fixed at 2, the value of Z_1 is swept from 40Ω to 120Ω in steps of 40Ω . As shown in Fig. 3.2(c), again, G_A has the same value at $f_1=1\text{GHz}$ and $f_2=2\text{GHz}$.

Similarly, the imaginary part of Y_A is plotted in Figs. 3.3(a)-3.3(c). It is clear that only the sign of B_A changes while going from f_1 to f_2 . Thus, as proved theoretically in

the previous section, irrespective of the value of r and Z_1 , the complex conjugate relation of Y_A at the two frequencies is ensured if θ_1 is selected according to (3-4).

The discovered dual-frequency admittance property is extremely interesting and useful property and its application in a novel port extended WPD will be demonstrated in section 3.3. This property was utilized in the intuitive design of dual-frequency impedance transformer [57].

3.2 Dual-Frequency Matching Networks

The observed admittance behavior of single section TL can be utilized in the design of dual-frequency matching networks [57]. For this purpose, Fig. 3.4 can be considered as a generic and intuitive scheme to transform a complex and frequency dependent load (Z_L) into a real impedance (Z_S) at two distinct frequencies [57]. The first step in such a design is to transform the two arbitrary and unrelated load impedances, namely $Z_L = R_1 + jX_1 @f_1$ and $Z_L = R_2 + jX_2 @f_2$, into a conjugate pair admittances, $Y_{inA} = G_{inA} - jB_{inA} @f_1$ and $Y_{inA} = G_{inA} + jB_{inA} @f_2$, using the section A. Since the admittances in parallel sums at a node, the role of section B is to cancel out the imaginary part of Y_{inA} at the two frequencies, and thus $Y_{inB} = +jB_{inA} @f_1$ and $Y_{inB} = -jB_{inA} @f_2$. Finally, since Z_{inBC} , the impedance looking into the combination of section A and section B, is

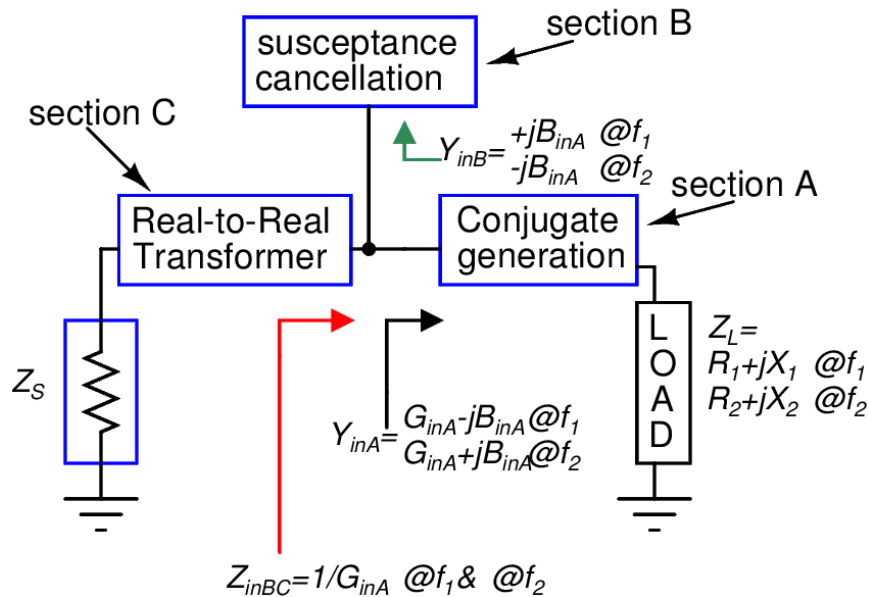


Figure 3.4 A generic scheme for dual-frequency impedance transformation.

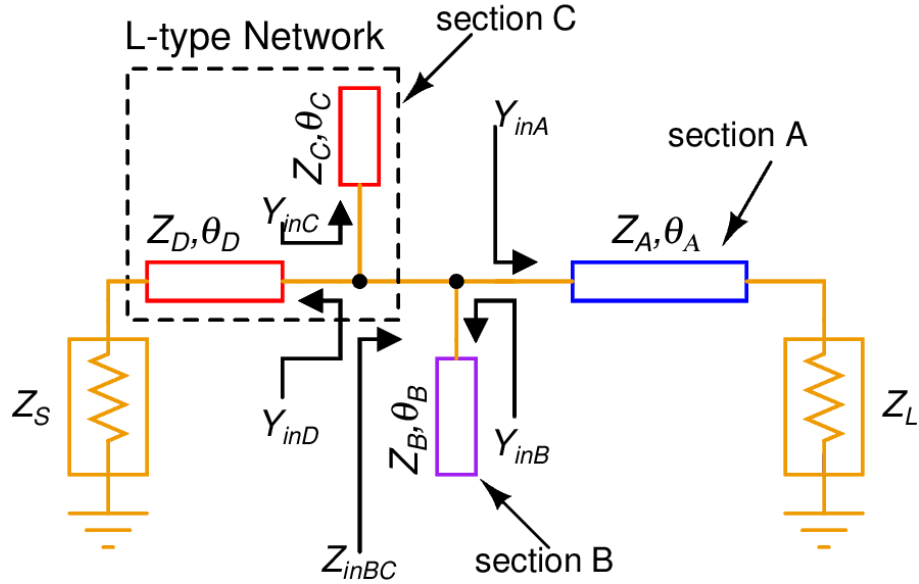


Figure 3.5 Implementation of the proposed scheme using L-type network [57].

now real ($= 1/G_{inA}$, both @ f_1 and @ f_2), the section C is aptly used for a real to real impedance transformation.

One possible implementation of the proposed transformer is shown in Fig. 3.5. Section A consists of a transmission line with characteristics impedance Z_A and electrical length θ_A . Section B consists of a stub with characteristics impedance Z_B and stub length θ_B which can either be an open circuit or a short circuit or a combination thereof. An L-type network, that makes section C, consists of a transmission line section Z_D with length θ_D and a stub having characteristics impedance Z_C and stub length θ_C (again, open/short/combo). Design and analysis of the various sections are discussed in the next section. The defined electrical lengths of all the sections are at the first frequency of f_1 .

3.2.1 Design of Section A

The section A of the proposed matching network is designed using the following design equations [40]:

$$Z_A = \sqrt{R_1 R_2 + X_1 X_2 + \frac{X_1 + X_2}{R_2 - R_1} (R_1 X_2 - R_2 X_1)} \quad (3-9)$$

$$\theta_A = \frac{p\pi + \arctan\left(\frac{Z_1(R_1 - R_2)}{R_1X_2 - R_2X_1}\right)}{1+r}, \quad \text{where: } p \in \mathbb{I}, r = f_2/f_1 \text{ with } r \geq 1 \quad (3-10)$$

Design of the section A using these formula guarantees that the impedance looking into section A are complex conjugate of each other at the two frequencies, that is $Z_{inA}|_{f_1} = (Z_{inA}|_{f_2})^*$, where $Z_{inA} = 1/Y_{inA}$ in Fig. 3.5. If $Z_{inA} = 1/Y_{inA} = R_{inA} + jX_{inA} @ f_1$ then $Z_{inA} = 1/Y_{inA} = R_{inA} - jX_{inA} @ f_2$, where the values of R_{inA} and X_{inA} are given as follows [59]:

$$R_{inA} = \frac{R_1 Z_A^2 [1 + \tan^2 \theta_A]}{Z_A^2 - 2Z_A X_1 \tan \theta_A + (R_1^2 + X_1^2) \tan^2 \theta_A} \quad (3-11)$$

$$X_{inA} = \frac{(Z_A^2 - R_1^2 - X_1^2) Z_A \tan \theta_A + Z_A^2 X_1 [1 - \tan^2 \theta_A]}{Z_A^2 - 2Z_A X_1 \tan \theta_A + (R_1^2 + X_1^2) \tan^2 \theta_A} \quad (3-12)$$

In addition, $Y_{inA} = G_{inA} - jB_{inA} @ f_1$ and $Y_{inA} = G_{inA} + jB_{inA} @ f_2$ may also be obtained by inverting and simplifying Z_{inA} :

$$G_A = R_{inA} / (R_{inA}^2 + X_{inA}^2) \quad (3-13)$$

$$B_A = X_{inA} / (R_{inA}^2 + X_{inA}^2) \quad (3-14)$$

3.2.2 Design of Section B

The dual-frequency susceptance [22] has limitations due to complex structure and unclosed form design equations. In the proposed design, owing to the use of section A, very simple dual-frequency susceptance using an open circuit or a short circuit stub or a combination thereof can be designed [59-60]. Since, the function of section B is to cancel out the imaginary part of Y_{inA} at the two frequencies, and thus $Y_{inB} = +jB_{inA} @ f_1$ and $Y_{inB} = -jB_{inA} @ f_2$. Now, suppose an open stub is to be used then the following two equations must be satisfied:

$$B_{inA} = \tan(\theta_B)/Z_B \quad (3-15)$$

$$-B_{inA} = \tan(r\theta_B)/Z_B \quad (3-16)$$

Equations (3-15)-(3-16) are solved simultaneously which results into (3-17)-(3-18).

$$Z_B = \tan(\theta_B) / B_{inA} \quad (3-17)$$

$$\theta_B = (1 + m) / (1 + r), m \in \text{integer} \quad (3-18)$$

More details of this dual-frequency stub design appear in [60], and will be discussed in later chapters.

3.2.3 Design of Section C: The L-network

After cancelling the imaginary parts of Y_{inA} with the help of Y_{inB} , what is left is a real impedance $Z_{inBC} = 1/G_{inA}$ both @ f_1 and @ f_2 . This real impedance can easily be matched using dual-frequency L-network [30]. Since the original explanation of the L-network was limited in intuition, this network is again explained here using the dual-frequency admittance property identified in the previous section. It is apparent that the TL section with characteristics impedance Z_D terminated into real impedance Z_S in Fig. 3.5 resembles with the network of Fig. 3.1. Therefore, again, if θ_D is selected as given in (3-4) then Y_{inD} will have a complex conjugate relationship at the two frequencies. Thus, matching this to Z_{inBC} , which is real, requires cancellation of the imaginary parts of Y_{inD} . This can be done using dual-frequency susceptance and, this is exactly what the stub with characteristic impedance Z_C in Fig. 3.5 provides. Therefore, the design equations for Section C can be found after a little algebraic manipulation:

$$Z_D = \sqrt{\left[\frac{Z_s (1 + \tan^2 \theta_D)}{Z_{inBC}} - Z_s^2 \right] \frac{1}{\tan^2 \theta_D}} \quad (3-19)$$

It is reemphasized that the value of θ_D is selected as given in (3-4). After finding Z_D using (3-19), the imaginary part of Y_{inD} can be found by suitable application of (3-3), which in turn leads to the design of the stub of Section C. It must be noted that the design of this dual-frequency stub proceeds in the same manner as that of the Section B. This explanation of dual-frequency L-network design is much more intuitive.

At this juncture, the readers would be wondering as to how the network shown in Fig. 3.5 differs from that reported in [43]. To understand it, firstly, it is to be seen that there are only three transmission line parameters in [43], and all of them are well-

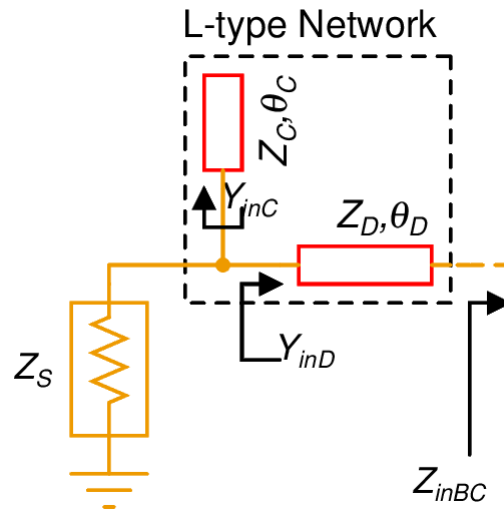


Figure 3.6 Implementation of the proposed scheme using an inverted L-type network.

defined. However, since there are four transmission lines in Fig. 3.5, one of the lines could be chosen independently and this gives the network of [57] more flexibility. Secondly, the network of [43] has only one configuration. However, it can be readily seen that the L-network used in Fig. 3.5 could be reversed by placing the stub towards Z_s as shown in Fig. 3.6. The design equation remains the same, except that the terms Z_{inBC} and Z_s are interchanged in (3-19).

To show the proper working of the proposed impedance transformer, arbitrarily varying load impedance is considered as shown in Fig. 3.7. This load is utilized to crea-

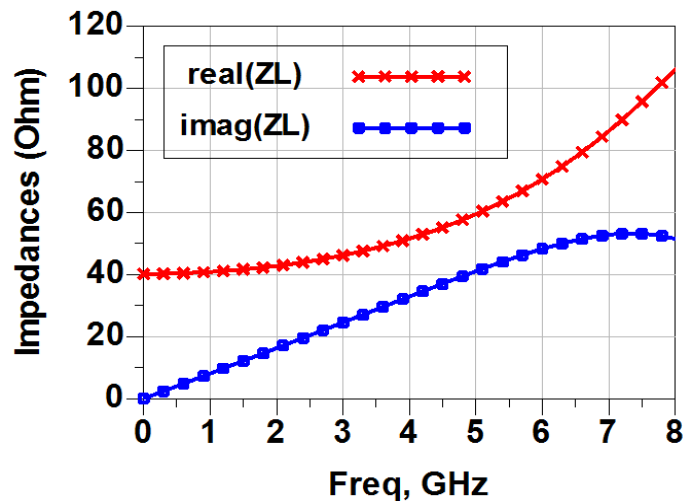
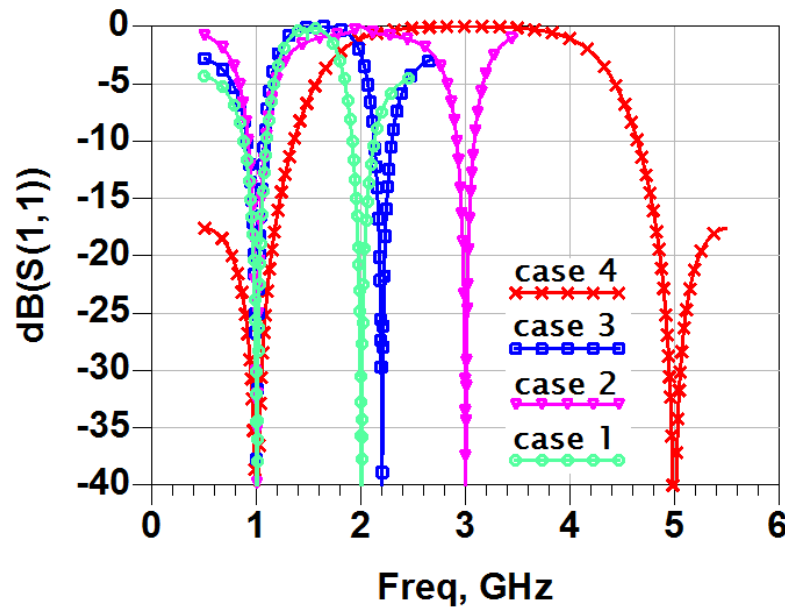


Figure 3.7 Variation of considered load impedance.

Table 3-1 Case Studies on the Proposed Dual-Frequency Matching Network

Case	Frequency (GHz)		Characteristic Impedance (Ω)				Electrical Length (deg)				Stub Type	
	f_1	f_2	Z_A	Z_B	Z_C	Z_D	θ_A	θ_B	θ_C	θ_D	Z_B	Z_C
1	1	2	76.41	115.53	145.99	83.07	51.71	120	120	60	Short	Short
2	1	3	76.92	134.74	22.46	25.22	36.69	45	45	45	Open	Short
3	1	2.2	76.93	73.62	93.46	83.87	47.95	112.50	112.50	56.25	Short	Short
4	1	5	76.38	64.50	102.80	75.93	21.64	30	30	30	open	open

**Figure 3.8** Simulated return-losses for the cases listed in TABLE 3-1.

te the design cases mentioned in TABLE 3-1. The first frequency is fixed whereas the second one is varying. The calculation of the parameters of the various transmission lines are done according to the design equations derived in the previous section. The simulated results of all the cases of TABLE 3-1 are shown in Fig. 3.8. It is apparent that the proposed impedance transformer works properly for arbitrary design cases.

To experimentally verify the working of the proposed transformer, a prototype is designed and implemented corresponding to the first entry in TABLE 3-1. RO4350B substrate (substrate with height 1.524mm and 35um copper) from Rogers is used to implement the PCB. The fabricated device is shown in Fig. 3.9 and the corresponding EM simulation and the measured results are shown in Fig. 3.10. The measurement result shows better than 15dB return loss at both the design frequencies. A small shift around the design frequencies are attributed to in-home fabrication of the prototype.

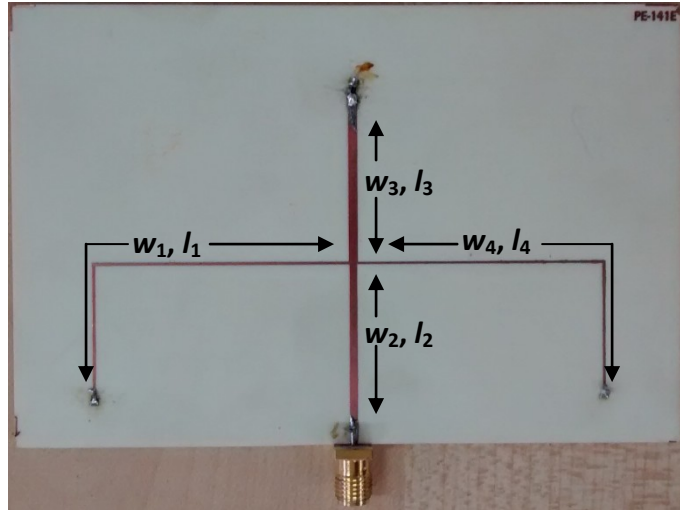


Figure 3.9 Implementation of the proposed network on RO4350B substrate [57].
 Dimensions (mils): $w_1=21.2$, $l_1=2564$, $w_2=51.26$, $l_2=1231$, $w_3=61.4$, $l_3=1055$, $w_4=13.8$,
 $l_4=2520$.

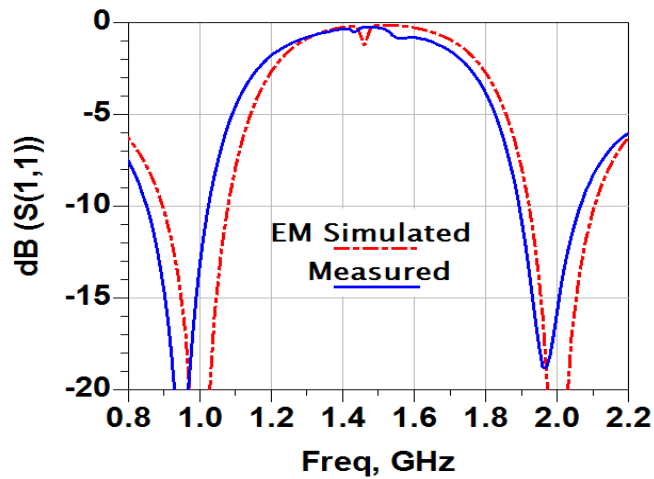


Figure 3.10 EM simulated and the measurement results [57].

The EM simulated results resemble quite well with the measured results and this verifies and confirms the proposed theory.

3.3 Dual-Frequency Wilkinson Power Divider with Improved Performance

The Wilkinson power divider (WPD) is one of the most popular and useful power divider/combiner structures for advanced RF/Microwave communication and instrumentation systems. They are indispensable part of many sophisticated blocks such as Doherty power amplifier, phased array antennas, I/Q vector modulators, balanced

mixer and frequency multipliers [61-62]. As explained in Chapter 1, rapid developments in the field of multi-frequency/multi-standard wireless communication systems have profound impact on how the state-of-the-art circuits and systems are developed and designed. Therefore, requirement of advanced RF/Microwave components possessing identical characteristics at two or more frequencies, in general, and that of the WPD in particular has emerged [63]. Numerous designs of dual-frequency WPD have been reported in the literature [64]-[84]. Many of these designs [64]-[66] have topologies utilizing R , L and C lumped components in their isolation networks which provides more flexibility in the design. For example, a very wide band-ratio WPD was reported in [66]. However, these designs have limited use at high frequencies due to inherent parasitics associated with lumped components [32]. Moreover, although the composite-right/left-hand (CRLH) material based WPD [67] has advantage of miniaturization, but their utilization at higher frequency is again limited due to the similar reason. On the other hand, replacement of quarter wavelength line by equivalent dual-frequency quarter wave-length line [68] is a simple approach but they have limited band-ratio. Some other techniques [69]-[74], such as shifting the output ports [71] have also been reported. Some of the researchers have also focused on miniaturization, and, therefore coupled lines are incorporated into their reported designs [75]-[81] to achieve this through an additional inherent degree of freedom. However, in planar microstrip technology, these designs are difficult to realize as they require compensation for even-odd mode velocities. It is often relatively difficult to achieve the desired performance at two different frequencies concurrently.

Finally, port matching technique [5] is a very simple and intuitive technique for performance enhancement of couplers/dividers that is essentially based on impedance matching concept. Recently, port matching concept was used in dual-band WPD reported in [82]. A major limitation in this design is the need of the isolation resistor being continuous function of the band-ratio. In fact, this ails many other non-port extended designs as well, as listed later in TABLE 3.5. However, the commercially available lumped components are found only in discrete values, therefore, in practice such designs will work perfectly only at discrete frequencies. In addition, the design technique reported in [82] is very involved as it necessitates solution of an 8th-order polynomial.

It must be noted that the dual-band WPDs of [82] mandatorily needs port-extension by a series transmission line at all the three ports. Very recently, another dual-band port-extended technique was reported in [83] for application to tri-frequency WPD. Owing to the utilization of only stubs at all the three ports, the ports do not get extended physically, additional networks that extend the ports physically is required for tri-frequency operation. However, the band-ratio of dual-band WPD of [83] is very limited, which ultimately sets major limitation on the performance of the resulting tri-band WPD.

In this section, the dual-frequency properties of the single transmission-line section terminated into a real impedance is utilized to overcome some of the above mentioned limitations of the port-matched WPD. The proposed port-extended WPD [58] has the following advantages as compared to the other designs based on port matching technique:

- 1) *Isolation resistor independent of the band-ratio:* a key contribution of the proposed technique is that it makes the isolation resistor independent of the band-ratio.
- 2) *The port-extension is required only at the input port in normal circumstance:* it is demonstrated that in most of the cases the port extension (through a series TL section) is required only at the input side, that is, the port-extension is only partial. In situations, where a physically realizable WPD cannot be designed, it is proposed that the full port extension technique can be used to realize the same.
- 3) *Use of single resistor:* In addition, while majority of WPDs in the current state-of-the-art makes use of more than one lumped elements in so called complex isolation architectures which are normally difficult to handle at higher frequencies, the proposed design approach utilizes only one resistor.

3.3.1 Dual-Frequency Behavior of WPD Core

A WPD core structure shown in Fig. 3.11 has two identical TL sections and an isolation resistor, R . Z_2 and θ_2 are characteristic impedance and electrical length of the TL sections. The input and output admittances of the conventional WPD are given by (3-20)-(3-21) [83]:

$$Y_{eq,in} = \frac{R}{Z_2^2 \sin^2 \theta_2} - j \frac{2}{Z_2 \tan \theta_2} = Y_{eqR,in} + jY_{eqI,in} \quad (3-20)$$

$$Y_{eq,out} = \frac{2}{R} - j \frac{1}{Z_2 \tan \theta_2} = Y_{eqR,out} + jY_{eqI,out} \quad (3-21)$$

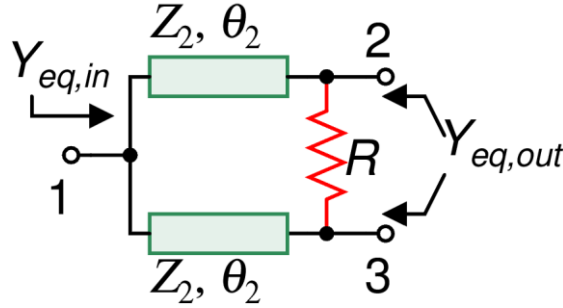


Figure 3.11 Conventional equal power division WPD core structure.

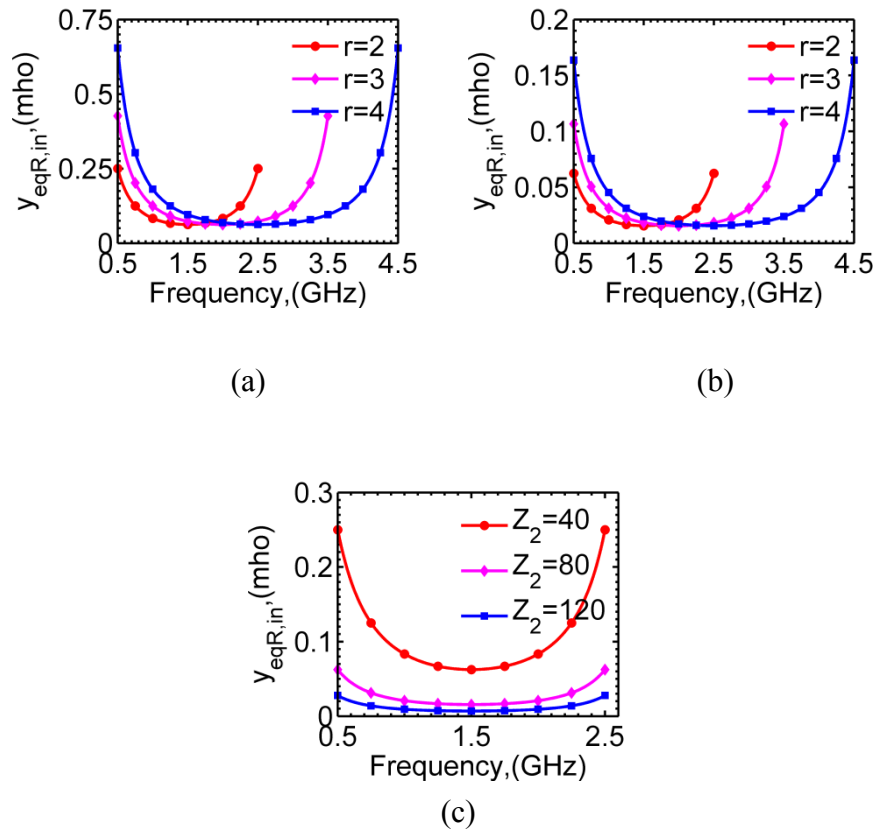


Figure 3.12 Real part , $Y_{eqR,in}$ of the input admittance of WPD for (a) $Z_2=40\Omega$ and $r=2,3$ and 4, (b) $Z_2=80\Omega$ and $r=2,3$ and 4 and (c) $r=2$ and $Z_2=40\Omega, 80\Omega$ and 120Ω .

$Y_{eqR,in}$ remains the same at $f_1=1\text{GHz}$ and rf_2 , as θ_2 is chosen according to (3-22).

The terms $Y_{eqR,in}$ and $Y_{eqI,in}$ are the real and imaginary parts of the input admittance, whereas $Y_{eqR,out}$ and $Y_{eqI,out}$ are the real and imaginary parts of the output admittance. As discovered in the previous subsection, a careful look at (3-20) and (3-21) reveals complex conjugate relation; that is $Y_{eq,in}|_{f_1} = Y_{eq,in}^*|_{f_2}$ and $Y_{eq,out}|_{f_1} = Y_{eq,out}^*|_{f_2}$, if θ_2 is chosen as:

$$\theta_2 = \frac{n\pi}{1+r} \quad (3-22)$$

where, r is the frequency-ratio and n is an integer.

The dual-frequency property of input admittance of conventional WPD as given by (3-20)-(3-22) is illustrated as follows. R is fixed at $2Z_0$, Z_2 is assumed to be 40Ω , and θ_2 is selected as per (3-22). Variation of $Y_{eqR,in}$ is shown in Fig. 3.12(a) for $r=2, 3$ and 4 . It is evident from the plots that $Y_{eqR,in}$ is unchanged as frequency flips from $f_1=1\text{GHz}$ to $f_2=rf_1$. This property of $Y_{eqR,in}$ remains valid even if the value of Z_2 is changed to 80Ω as

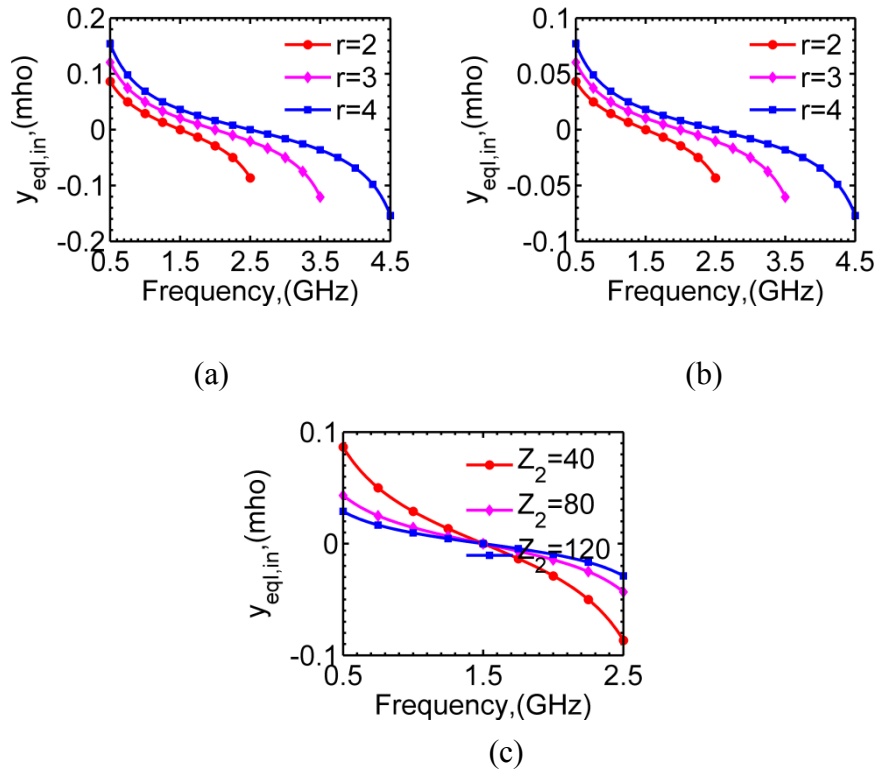


Figure 3.13 Imaginary part, $Y_{eqI,in}$ of the input admittance of WPD for (a) $Z_2=40\Omega$ and $r=2,3$ and 4 , (b) $Z_2=80\Omega$ and $r=2,3$ and 4 and (c) $r=2$ and $Z_2=40\Omega, 80\Omega$ and 120Ω . $Y_{eqR,in}$ remains the same at $f_1=1\text{GHz}$ and rf_2 , as θ_2 is chosen according to (3-22).

shown in Fig. 3.12(b). Moreover, as depicted in Fig. 3.12(c), $Y_{eqR,in}$ has the same value at $f_1=1\text{GHz}$ and $f_2=2\text{GHz}$ while keeping r fixed at 2 and sweeping Z_2 from 40Ω to 120Ω in steps of 40Ω . The same behavior as that of $Y_{eqR,in}$ is also exhibited by $Y_{eqI,in}$ except for a change of sign as shown in Fig. 3.13. And therefore, as proved earlier, the complex conjugate relation of $Y_{eq,in}$ at the two frequencies holds true if θ_2 is chosen according to (3-22).

For brevity, $Y_{eq,out}$ is not plotted but complex conjugate relation is easy to visualize since,

- 1) $Y_{eqR,out} = 2/R$ is a fixed quantity for a given R and hence its value at any two frequency is always the same.
- 2) $Y_{eqI,out} = -1/Z_2 \tan\theta_2$ is only the scaled version of $Y_{eqI,in}$, hence the two have similar behavior.

3.3.2 The Proposed WPD

Next, the proposed dual-frequency WPD is shown in Fig. 3.14. It is comprised of a conventional WPD core consisting of TL sections having characteristic impedance Z_m and electrical length θ_m and an isolation resistor R , and the three matching networks at

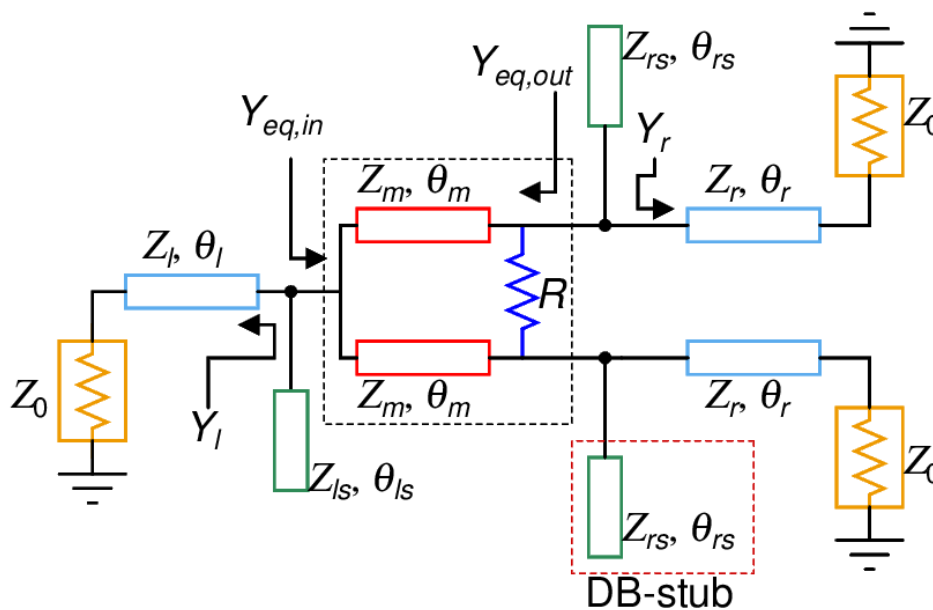


Figure 3.14 The proposed dual-band WPD with port extensions. Short or open circuited dual-band (DB) stubs are required at all the three ports.

each of the three ports. The input side matching network consists of the TL section with characteristic impedance Z_l and electrical length θ_l and a dual-frequency stub, either open or short circuited, having characteristic impedance Z_{ls} and electrical length θ_{ls} . In this equal split divider, the two output side matching networks are identical and consist of the TL section having characteristic impedance Z_r and electrical length θ_r and dual-frequency stub, again, either open or short circuited, having characteristic impedance Z_{rs} and electrical length θ_{rs} . Thus, the input port of conventional WPD is extended by an amount of θ_l in the proposed dual-frequency WPD, whereas the output ports are extended by θ_r . However, it shall be proved later that output ports may not need to be extended, partial extension case. Z_0 is the port termination impedance.

The matching in the proposed WPD is established as follows: at the input side, the real part of $Y_{eq,in}$ is equated to the real part of Y_l and the algebraic sum of their leftover imaginary parts, that is, the imaginary part of $(Y_{eq,in} + Y_l)$ is cancelled using the dual-frequency stub. Similar steps are repeated at the output side. Having outlined the working plan of the proposed dual-frequency WPD, the required design equations are derived in the next sub-sections.

3.3.3 Design Equations for the Input/ Output Side Matching Networks:

Equating the real-parts

Referring to Fig. 3.14, since $\text{Re}(Y_{eq,in}) = \text{Re}(Y_l)$ where $\text{Re}(X)$ denotes the real-part of X ; the following equations can be obtained using (3-2) and (3-20):

$$\frac{R}{Z_m^2 \sin^2 \theta_m} = \frac{Z_0(1 + \tan^2 \theta_l)}{Z_0^2 + Z_l^2 \tan^2 \theta_l} \quad (3-23)$$

$$\Rightarrow Z_l = \sqrt{\frac{Z_0 [Z_m^2 \sin^2 \theta_m (1 + \tan^2 \theta_l) - RZ_0]}{R \tan^2 \theta_l}} \quad (3-24)$$

Similarly, invoking $\text{Re}(Y_{eq,out}) = \text{Re}(Y_r)$ for the output side yields:

$$\frac{2}{R} = \frac{Z_0(1 + \tan^2 \theta_r)}{Z_0^2 + Z_r^2 \tan^2 \theta_r} \quad (3-25)$$

$$\Rightarrow Z_r = \sqrt{\frac{Z_0 [R(1 + \tan^2 \theta_r) - 2Z_0]}{2 \tan^2 \theta_r}} \quad (3-26)$$

It may come as a surprise that Z_l depends on Z_m whereas Z_r is independent of the same. However, it must be noted that the whole matching network also consists of a stub and it will be shown shortly that the characteristic impedance of output stubs, Z_{rs} do depend on Z_m . The electrical lengths θ_l and θ_r have the same expression as it appears in (3-4) and (3-22), where the integer is usually selected as unity to achieve compact size. Moreover, R and Z_m are free variables in (3-24) as well as in (3-26), which can be chosen to get a physically realizable WPD.

Although, R is an independent variable but setting $R=2Z_0$ is an interesting choice. It is apparent from (3-26) that with this choice, one can obtain $Z_r = Z_0$, that is, the output ports are matched without port extension. However the stubs would still be required at the output ports to cancel the imaginary part of WPD output admittance, $Y_{eqI,out}$. Therefore, θ_r could be of any length for SMA connection not necessarily given by (3-4). Thus, with this fixed choice of R , the port extension in the proposed dual-frequency WPD is only partial.

3.3.4 Design Equations for the Input/ Output Side Matching Networks:

Cancelling the imaginary-parts

Having equated the real parts, the next step in the matching is to cancel the remaining imaginary parts at the two frequencies. The remaining imaginary parts at the input side is given by:

$$\text{Im}(Y_{eq,in} + Y_l) = (Y_{eqI,in} + B_{Al}) @ f_1 \quad (3-27)$$

$$= -(Y_{eqI,in} + B_{Al}) @ f_2 \quad (3-28)$$

The term B_{Al} is imaginary part of Y_l and is obtained using (3-3) by substituting $Z_s=Z_0$, $Z_l=Z_l$, and $\theta_l=\theta_l$. If an open stub with characteristic impedance Z_{ls} and electrical length θ_{ls} is to be used to cancel this imaginary part, then the following equations must be satisfied [60]:

$$-(Y_{eqI,in} + B_{Al}) = \tan \theta_{ls} / Z_{ls} @ f_1 \quad (3-29)$$

$$\text{and, } (Y_{eqI,in} + B_{Al}) = \tan(r\theta_{ls}) / Z_{ls} @ f_2 \quad (3-30)$$

where, the fact that the electrical length is proportional to frequency has been utilized, and therefore, θ_{ls} defined at f_1 becomes $r\theta_{ls}$ at f_2 .

Solving (3-29) and (3-30) yields:

$$Z_{ls} = -\tan \theta_{ls} / (Y_{eqI,in} + B_{Al}) \quad (3-31)$$

$$\text{and, } \theta_{ls} = p\pi / (1+r) \quad (3-32)$$

with p being an integer, often either equal to 1 or 2. Since, Z_{ls} , a characteristic impedance, is always positive, the value of p must be selected equal to unity if $(Y_{eqI,in} + B_{Al})$ is negative, otherwise $p=2$. Moreover, if a short stub is to be used instead then its design expressions are still given by (3-31) to (3-32) but instead of the tangent function, a cotangent function without minus sign needs to be used in (3-31). More details about these dual-frequency stub designs are given in [60] and will be discussed in the later parts of this thesis.

Similarly, the remaining imaginary parts at the output side is given by:

$$\text{Im}(Y_{eq,out} + Y_r) = (Y_{eqI,out} + B_{Ar}) @ f_1 \quad (3-33)$$

$$= -(Y_{eqI,out} + B_{Ar}) @ f_2 \quad (3-34)$$

Again, B_{Ar} is imaginary part of Y_r and is obtained using (3-3) by substituting $Z_s=Z_0$, $Z_1=Z_r$ and $\theta_1=\theta_r$. Moreover,

$$Z_{rs} = -\tan \theta_{rs} / (Y_{eqI,out} + B_{Ar}) \quad (3-35)$$

$$\text{and, } \theta_{rs} = q\pi / (1+r) \quad (3-36)$$

where q is an integer. It must be kept in mind that if $R=2Z_0$ is used then $B_{Ar} = 0$. Moreover, since $Y_{eqI,out}$ depends on Z_m , so does Z_{rs} .

3.3.5 Simulation and Experimental Verifications

The variation of line impedance of input side matching network elements, for three values of $Z_m = 40\Omega$, 80Ω , and 120Ω , is shown in Fig. 3.15. It is apparent that changing the value of Z_m changes the range of band-ratio over which a physically realizable input matching network could be obtained. For instance, setting $Z_m = 40\Omega$ results in $r \in (1, 1.65)$, whereas setting $Z_m = 120\Omega$ causes r to begin from 1.25 and to go beyond 4. Similarly, variation of the elements of the output matching network is depicted in Fig. 3.16, again for the three different values of $Z_m = 40\Omega$, 80Ω , and 120Ω . It must be noted that the band-ratio over which the proposed WPD could be physically realized is the minimum value of r as obtained from Figs. 3.15 and 3.16. For example, when $Z_m = 120\Omega$, the range of r begins from 1.95 ($=\min\{1.25, 1.95\}$), and goes beyond 4.

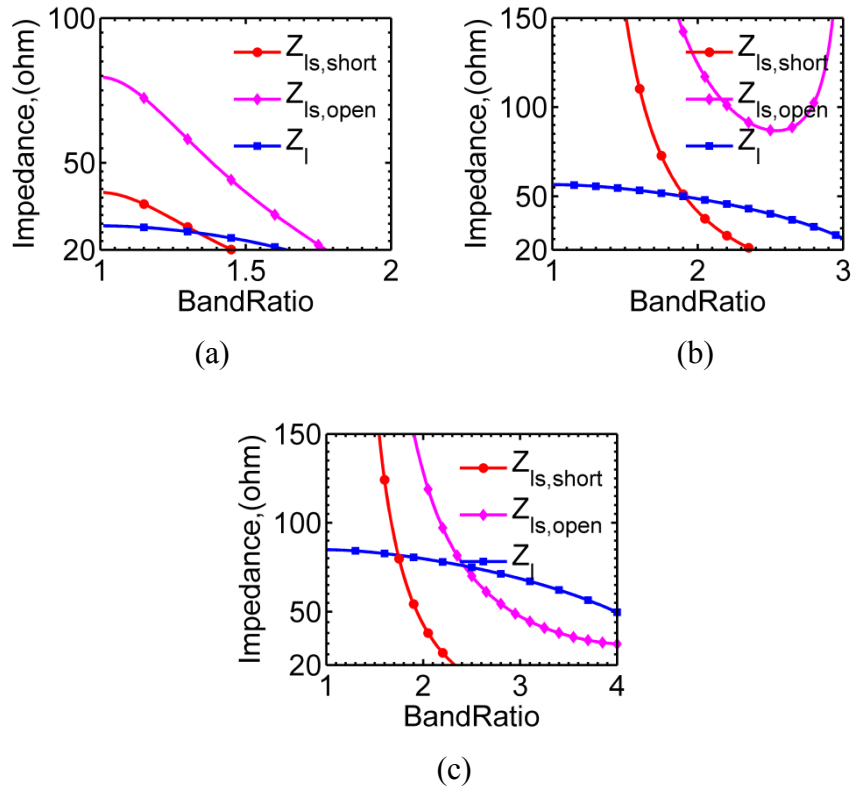


Figure 3.15 Variation of characteristic impedances of input side matching network with band-ratio for (a) $Z_m = 40\Omega$, (b) $Z_m = 80\Omega$, and (c) $Z_m = 120\Omega$. $Z_{ls,short}$ and $Z_{ls,open}$ denotes the characteristic impedance of short and open circuited stubs of input matching network.

To study the impact of Z_m on bandwidth around each frequency of the proposed WPD, design parameters of four examples are listed in TABLE 3-2 corresponding to $r=2$ and $Z_m=50\Omega$, 70.7Ω , 90Ω and 120Ω . The S-parameters of these designs are plotted in Fig. 3.17. 15dB return loss and isolation and 1dB for transmission are taken as reference for bandwidth. It is apparent that bandwidth does change with Z_m and in the present case $Z_m=70.7\Omega$ gives the best performance in terms of bandwidth. An intuitive explanation of bandwidth in dual-band context was reported in [24] and will be discussed in later chapters. Furthermore, although $r=2$ is a convenient value to work with, but to prove that the proposed design technique is versatile and scalable for other values of r , design parameters of another example with $r=2.8$ is listed in TABLE 3-3 and the corresponding simulation result is shown in Fig. 3.18.

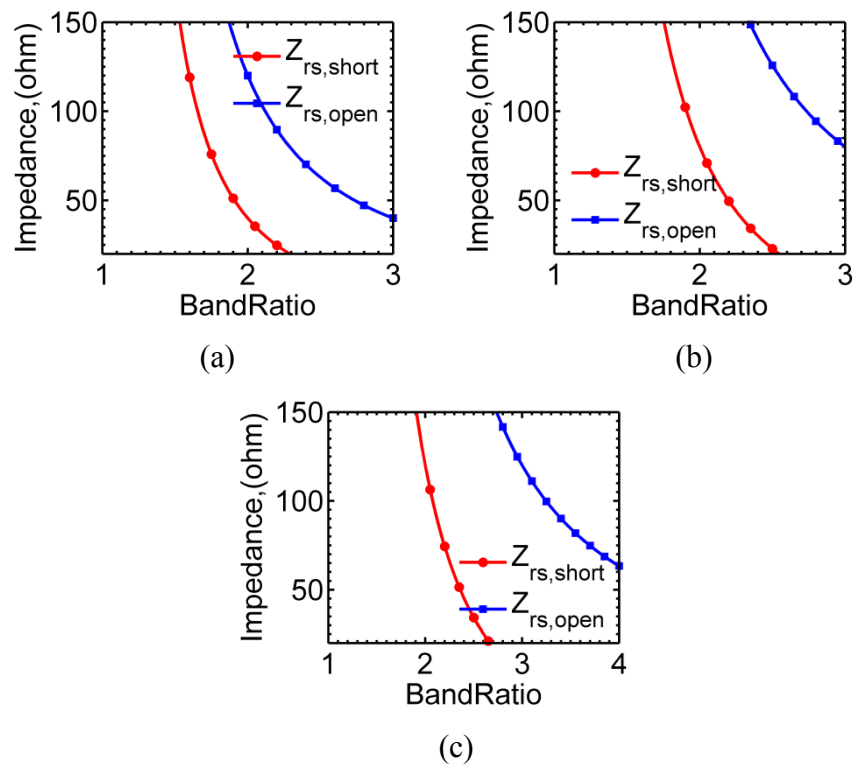


Figure 3.16 Variation of characteristic impedances of output side matching network with band-ratio for (a) $Z_m=40\Omega$, (b) $Z_m=80\Omega$, and (c) $Z_m=120\Omega$. $Z_{rs,short}$ and $Z_{rs,open}$ denotes the characteristic impedance of short and open circuited stubs of output matching network.

Table 3-2 Design Parameters for Four Different Values of Z_m

Case	$Z_m (\Omega), \theta_m$	$Z_l (\Omega), \theta_l$	Stubs (short type)	
			$Z_{ls} (\Omega), \theta_{ls}$	$Z_{rs} (\Omega), \theta_{rs}$
1	50, 60°	20.4, 60°	24, 60°	50, 120°
2	70.7, 60°	40.8, 60°	49.7, 120°	70.7, 120°
3	90, 60°	56.7, 60°	39.5, 120°	90, 120°
4	120, 60°	79.8, 60°	42.7, 120°	120, 120°

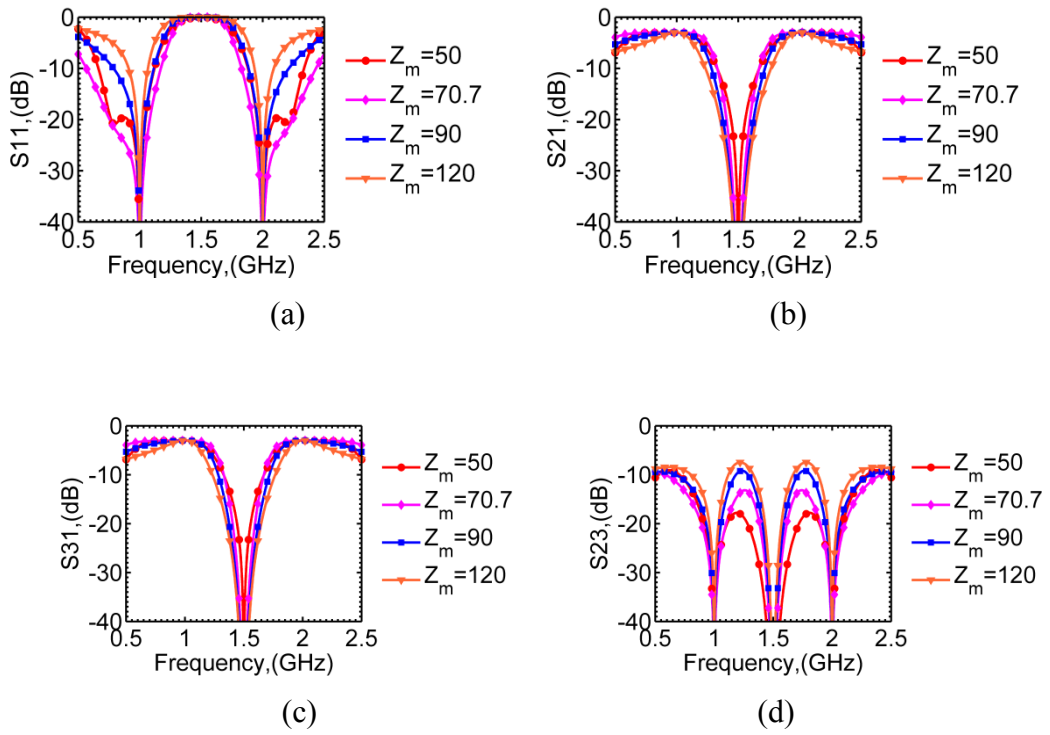


Figure 3.17 S-parameters of the four design examples with $r=2$ and $f_1=1\text{GHz}$ for $Z_m=50\Omega, 70.7\Omega, 90\Omega$ and 120Ω . (a) S_{11} (b) S_{21} (c) S_{31} , and (d) S_{41} . In all these, $Z_m=70.7\Omega$ is apparently the most suitable from bandwidth viewpoint.

Table 3-3 Design Parameters for Example with Band-ratio =2.8

$Z_m (\Omega), \theta_m$	$Z_l (\Omega), \theta_l$	Stubs (open type)	
		$Z_{ls} (\Omega), \theta_{ls}$	$Z_{rs} (\Omega), \theta_{rs}$
120, 47.37°	71.28, 47.37°	54.39, 47.37°	141.6, 47.37°

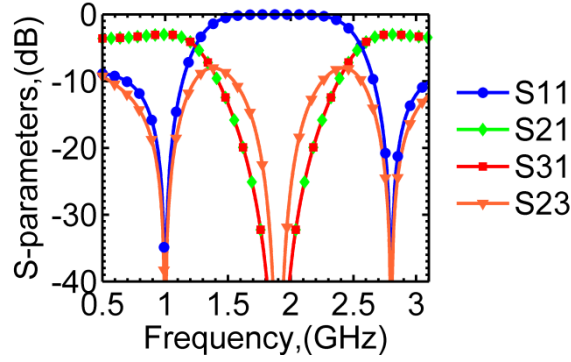


Figure 3.18 S-parameters of the four design examples with $f_1=1\text{GHz}$ and $r= 2.8$ ($f_2=2.8\text{GHz}$). Design parameters are given in TABLE 3-3.

Going back, it can be recalled that Figs. 3.15 and 3.16 were valid for $R=2Z_0$, which requires extension only at the input port, i.e. partial extension. It is seen by comparing Figs. 3.15 and 3.16 that the proposed WPD with partial port extension for $r=1.5$ cannot yield physically realizable design parameters. A remedy to solve this issue is to use port extension on both the sides, but at the cost of increased board area. It allows choice of R to any other convenient value, other than $2Z_0$, that results into a physically realizable design. In full extension case, Z_m and R are two independent design variables that a designer can use to achieve the required performance. One possible set of the design parameters of the final example ($r =1.5$) is listed in TABLE 3-4 to illustrate this situation. The simulated results are plotted in Fig. 3.19 and that exhibit proper working of the design.

In light of the above discussions, an effective design procedure using the proposed technique is outlined in Fig. 3.20. There may be many switching back and forth between designing the input and output matching networks as, in general, Z_m and R are the two independent design variables that can be tuned to achieve a realizable WPD.

Table 3-4 Design Parameters for Example with Band-ratio=1.5

$Z_m(\Omega), \theta_m$	$Z_l(\Omega), \theta_l$	Stubs (short type)		$Z_r(\Omega), \theta_r$
		$Z_{ls}(\Omega), \theta_{ls}$	$Z_{rs}(\Omega), \theta_{rs}$	
80, 72°	78.33, 72°	131.33, 144°	57, 72°	33.44, 72°

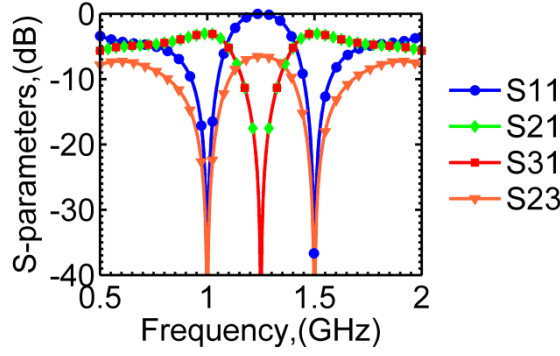


Figure 3.19 S-parameters of the four design examples with $f_1=1\text{GHz}$ and $r=1.5$ ($f_2=1.5\text{GHz}$). Design parameters are given in TABLE 3-4.

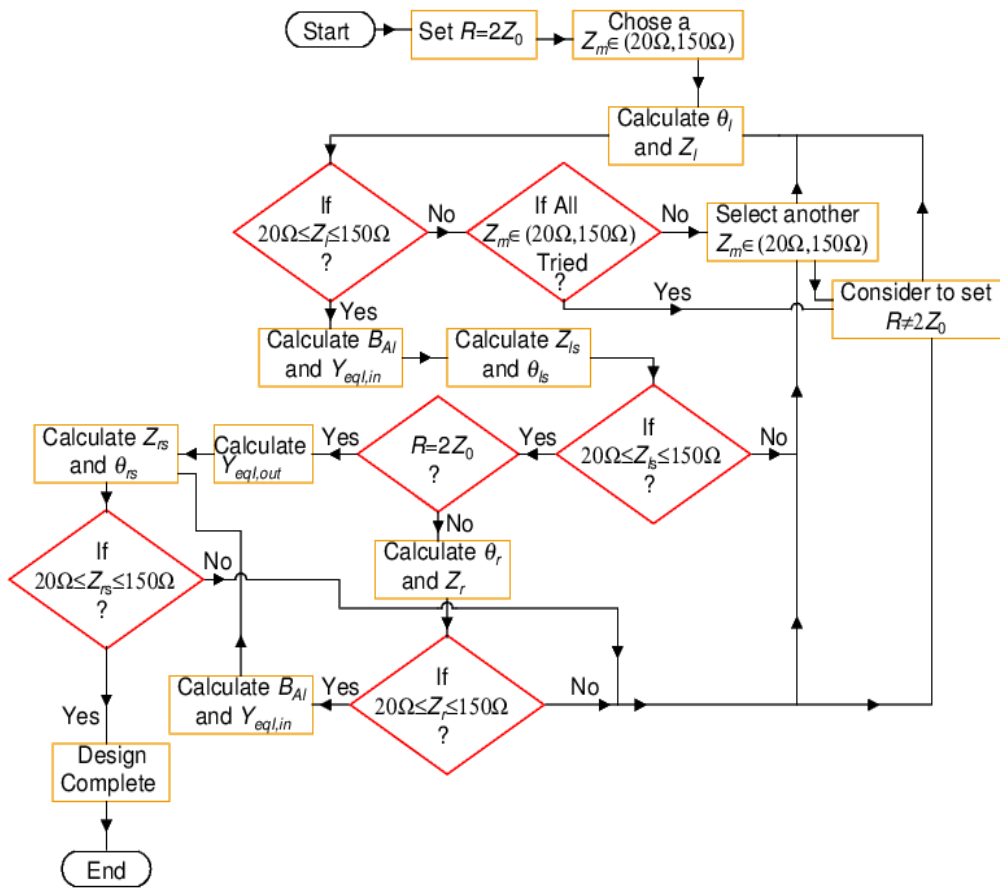


Figure 3.20 Flowchart for the design using the proposed technique. Due to the presence of two design variables Z_m and R , great flexibility is evident. 20Ω to 150Ω range is assumed to be the realizable value of characteristic impedance in microstrip technology.

For demonstration purpose, a prototype, for partial port extension, is designed and fabricated on Roger's RO4350B substrate with dielectric constant of 3.66 and thickness of 1.524mm having copper cladding of 35 μ m. The design frequencies are arbitrarily selected as $f_1=1$ GHz and $f_2=2$ GHz. The corresponding design parameters are given in TABLE 3-5. Resistor used in the prototype is Vishay-Dale CRCW series 100 Ω , 0603 size SMD package. Various dimensions of the prototype are marked in Fig. 3.21 and the fabricated prototype is shown in Fig. 3.22. In terms of the stubs size and type, this example represents the worst case scenario since all the required stub are two time longer than the normal size and all of them are short-circuited type requiring via to the ground.

Table 3-5 Design Parameters of the Prototype

$Z_m (\Omega), \theta_m$	$Z_l (\Omega), \theta_l$	Stubs (short type)	
		$Z_{ls} (\Omega), \theta_{ls}$	$Z_{rs} (\Omega), \theta_{rs}$
70.7, 60°	40.8, 60°	49.7, 120°	70.7, 120°

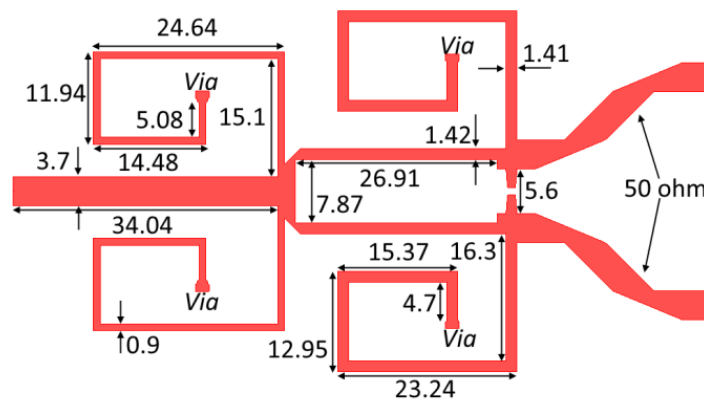


Figure 3.21 Various dimensions of the designed example for prototyping. All dimensions are in mm.

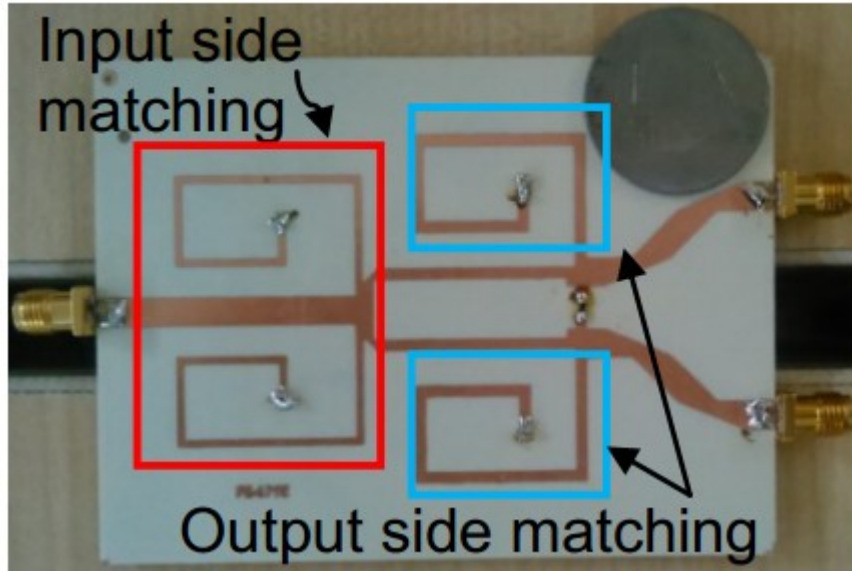
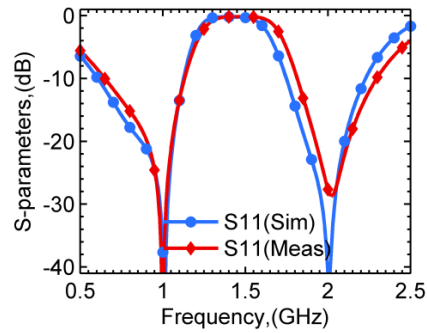
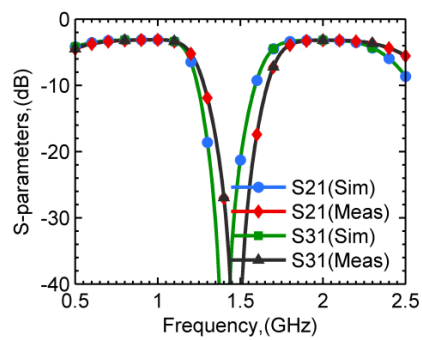


Figure 3.22 The fabricated WPD component [58].

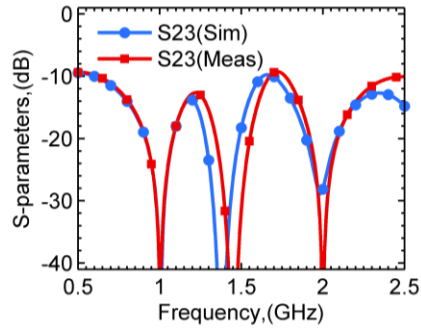
The EM simulated and the measurement results are shown in Fig. 3.23. It is important to mention that the structure was designed to be symmetric about the horizo-



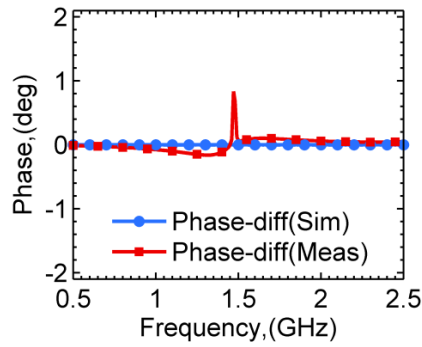
(a)



(b)



(c)



(d)

Figure 3.23 The EM simulated and the measured (a) return loss, S11 (b) power division, S21 and S31 (c) isolation, S23 and (d) the differential phase.

Table 3-6 Comparison with Some Previous Works [58]

<i>Ref.</i>	<i>Year</i>	<i>Technique</i>	<i>Solution</i>	<i>Isolation Elements</i>	Isolation Continuous Function of Band-ratio	<i>Band-ratio (r)</i>
[68]	2007	Dual-band 90° TLs	Analytical	1 Resistor	No	2-2.7
[70]	2008	T-type TLs	Analytical	1 Resistor	No	1.7- 2.5
[82]	2008	Port Extension	Analytical	1 Resistor	Yes	1-3
[74]	2011	Two section coupled line	Analytical	2 Resistor	Yes	1-3
[80]	2011	Two-way two section	Analytical	2 Resistors	Yes	1-3
[71]	2014	Shifted output ports	Graphical	1 Resistor	Yes	2.2-5
[66]	2014	Port extension with complex isolation	Analytical	1 Resistor, 1 Capacitor 1 Inductor	No	> (1-10)
[65]	2015	Two section coupled line with complex isolation	Analytical	1 Resistor, 1 Capacitor 1 Inductor	Yes	1-3.5
This Work	2015	Port extension	Analytical	1 Resistor	No	> (1.5-4)

ntal axis and therefore the single stub at the input side was bifurcated into two parts that is up and down. The utmost care for having a symmetrical design gives the prototype the phase difference very close to the ideal value of 0° as can be seen in Fig. 3.23 (d). The amplitude imbalance is not more 0.3dB and phase-imbalance is also within 0.2° . Apparently, all the results in Figs. 3.23 (a)-d) demonstrate a good agreement between the simulation and the measurement results. In the end, comparison with some of the previously reported designs is given in TABLE 3-6. It is evident from this comparison that the proposed design is capable of solving some of the problems, especially, pertaining to the isolation resistor, and has fairly good band-ratio.

3.4. Conclusions

This chapter started by proposing interesting complex conjugate admittance property of a transmission line terminated into a real impedance. This analytical derivation has been verified graphically as well. Application of this property into intuitive design methodology for dual-frequency impedance matching network was also shown. In addition, a novel equal split dual-frequency WPD utilizing port extension technique has been discussed. Then using these properties, a very simple and effective design technique of proposed WPD has been presented. The design procedure has been outlined through a flowchart and many examples have been used to show the capabilities of the proposed technique. Without using any reactive components, the proposed technique has been shown to possess a great deal of flexibility, owing mainly to the presence of one or more free design variables.

Chapter 4

Dual-Frequency Matching using Quarter Wavelength Blocks

Impedance matching based on quarter wavelength transmissions has been studied extensively in the context of single frequency or wideband matching problem [2, 84]. In addition, most of these reports have focused on matching real load impedances to real source impedances. A quarter wavelength block consists of several distributed/lumped elements and its electrical parameters, e.g. ABCD, are equivalent to that of a quarter wavelength transmission line at a frequency. As per requirement of multi-frequency applications, a large number of dual-frequency quarter wavelength blocks have been reported as well [85-91]. For example, a dual-frequency quarter wavelength block based on Pi-type structure was analysed in [85], whereas in [86] a T-type structure was used to implement the same. In addition, a composite right/left-handed [87] based quarter wavelength block could be used for miniaturized implementation. Stepped impedance lines [88] and slow-wave structures [89] could also be used for the realization of quarter wavelength block. Moreover, dual-frequency quarter wavelength block could also be synthesized with the help of coupled lines [90-91].

Thus, it is evident that the current state-of-the-art in dual-frequency component design is replete with applications of numerous types of dual-frequency quarter wavelength blocks. A pertinent question then arises that if a dual-frequency quarter wavelength transmission block could be used for impedance matching purposes, that too for frequency dependent complex loads (FDCLs). Another important aspect of this discussion is that a quarter wavelength transmission line is a symmetric network. What happens to this symmetry when dual-frequency quarter wavelength blocks are synthesized from seemingly asymmetric structures? Moreover, while requirement of bandwidth is not that critical in multi-frequency applications but it would be instructive

to get some intuitive feeling about this. This chapter [24, 92] of the thesis aims at providing answer to these important questions.

4.1 The Proposed Matching Network: Basic Idea

A conventional quarter wavelength transmission line is used for matching real load impedances to real source impedances. It implies that incorporating the same for FDCL matching could be done in the same manner shown in Fig. 3.4 and redrawn in Fig. 4.1. The only change being the presence of a dual-frequency quarter wavelength block instead of the real-to-real transformer block in Fig. 3.4. The FDCL is assumed to have values as $Z_L=R_1+jX_1 @f_1$ and $Z_L=R_2+jX_2 @f_2$. Once again Y_{in1} is the admittance looking into section A, Y_{in2} is the admittance looking into section B, and Z_{in3} is the impedance looking into the combination of sections A and B.

It is apparent from Fig. 4.1 that the transformer A converts the FDCL to Y_{in1} such that $Y_{in1}|_{f_1}=Y_{in1}^*|_{f_2}$, that is, if $Y_{in1}|_{f_1}=G-jB$ then $Y_{in1}|_{f_2}=G+jB$. The Section B, which is primarily a dual-frequency susceptance, cancels out the imaginary parts of Y_{in1} at the two specified frequencies. Thus, as a last step there is a need to match $Z_{in3}=1/G$ to Z_0 at the two frequencies. It is well known that a real impedance, such as Z_{in3} , can be mat-

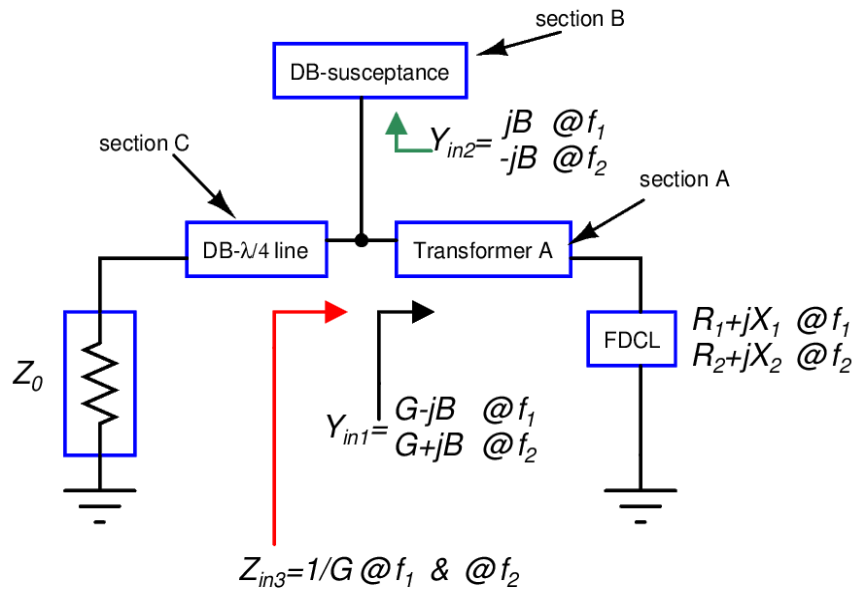


Figure 4.1 Pictorial illustration of the proposed matching scheme (DB: Dual-Band).

ched to another real impedance, such as Z_0 , using a $\lambda/4$ line; the only additional requirement in the present case is to have a dual-frequency $\lambda/4$ line, which is what the section C essentially is.

It must be noted at this juncture that most of the previously reported schemes have used sections A and B in the same manner as being used here. The main aspect of the proposed scheme is the incorporation of section C, the dual-frequency $\lambda/4$ line, into the conventional structure. The strength and uniqueness of the proposed impedance network, therefore, is the flexibility of choosing any dual-frequency $\lambda/4$ -line from a variety of those reported in the literature to suit specific applications.

4.2 Implementation of the Proposed Scheme

One possible implementation of the proposed matching network is shown in Fig. 4.2. Section A, adjacent to the FDCL, $Z_L = R_1 + jX_1$ at f_1 and $R_2 + jX_2$ at f_2 , is a transmission line having characteristic impedance Z_1 and electrical length θ_1 . Section B is either a short or open stub having characteristic impedance Z_2 and electrical length θ_2 whereas section C is an L-shaped dual-frequency $\lambda/4$ -line. The term Z_{Tr_in} is the input impedance that the load sees into the transformer, and we will return to its significance later.

Comparing Figs. 3.5 and 4.2, it should be apparent that the design of Sections A and B must be identical for both of these two networks. Therefore, the equations for the

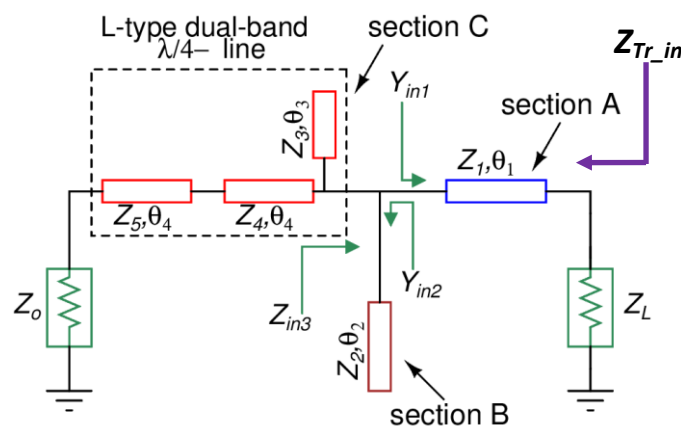


Figure 4.2 Implemented dual-frequency matching network based on the scheme shown in Fig. 4.1.

sections A and B described for Fig. 3.5 are to be utilized and are reproduced here for the sake of completeness.

4.2.1 Design of section A

The required values of Z_1 and θ_1 and the resulting values of G and B given in following expressions are referenced from results given in [40, 59]:

$$Z_1 = \sqrt{R_1 R_2 + X_1 X_2 + \frac{X_1 + X_2}{R_2 - R_1} (R_1 X_2 - R_2 X_1)} \quad (4-1)$$

$$\theta_1 = \frac{p\pi + \arctan\left(\frac{Z_1(R_1 - R_2)}{R_1 X_2 - R_2 X_1}\right)}{1 + r} \quad (4-2)$$

where: $p \in \mathbb{I}$, $r = f_2 / f_1$ with $r \geq 1$

The above expressions can be simplified to obtain:

$$G = R_{in1} / (R_{in1}^2 + X_{in1}^2) \quad (4-3)$$

$$B = X_{in1} / (R_{in1}^2 + X_{in1}^2) \quad (4-4)$$

where,

$$R_{in1} = \frac{R_1 Z_1^2 [1 + \tan^2 \theta_1]}{Z_1^2 - 2Z_1 X_1 \tan \theta_1 + (R_1^2 + X_1^2) \tan^2 \theta_1} \quad (4-5)$$

$$X_{in1} = \frac{(Z_1^2 - R_1^2 - X_1^2) Z_1 \tan \theta_1 + Z_1^2 X_1 [1 - \tan^2 \theta_1]}{Z_1^2 - 2Z_1 X_1 \tan \theta_1 + (R_1^2 + X_1^2) \tan^2 \theta_1} \quad (4-6)$$

As analytically proved in [40], if the section A is designed according to (4-1)-(4-2), then the values of Y_{in1} has a complex conjugate relationship at the two specified frequencies.

4.2.2 Design of section B

For an open stub to work at two frequencies, the following set of equations must be satisfied:

$$jB = j(1/Z_2) \tan \theta_2 \quad (4-7)$$

$$-jB = j(1/Z_2)\tan(r\theta_2) \quad (4-8)$$

The values of Z_2 and θ_2 can be obtained by solving (4-7) and (4-8) simultaneously and the solution is given by:

$$\theta_2 = \frac{s\pi}{1+r}, \quad s \in I \quad (4-9)$$

$$Z_2 = \tan \theta_2 / B \quad (4-10)$$

A short stub may also be shown to work at two frequencies, similar to the way an open stub was shown to work in dual-frequency mode, with design equations similar to (4-9) and (4-10) except that tangent in (4-10) needs to be replaced by cotangent along with a minus sign.

After the cancellation of the imaginary terms of Y_{in1} by using Y_{in2} , the impedance looking into the combination of sections A and B, and the load Z_L , is real given by:

$$Z_{in3} = 1/G @ f_1 \text{ and } @ f_2 \quad (4-11)$$

4.2.3 Design of section C

To match Z_{in3} to Z_0 , the characteristic impedance of the required $\lambda/4$ line is given by $Z_{DB-\lambda/4} = \sqrt{Z_0 Z_{in3}}$ [2]. The underlying concept can be illustrated by utilizing an L-type stepped impedance $\lambda/4$ block for dual-frequency functionality [68]. However, it is reemphasized that there are other dual-frequency $\lambda/4$ blocks reported in literature [85-91]. Interestingly, this particular choice makes the implemented circuit look like that discussed in [45]. However, the two implementations emanate from altogether different

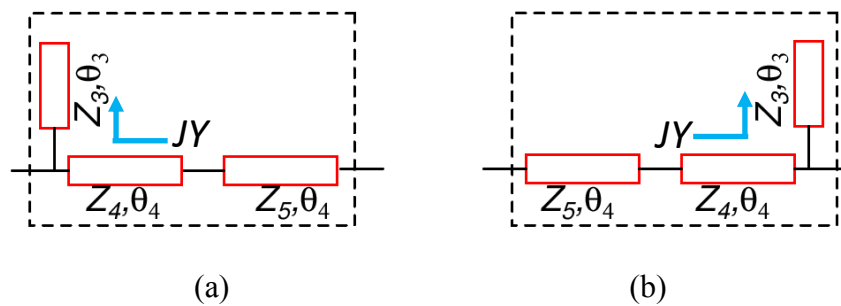


Figure 4.3 (a) Section C and (b) and its mirror image.

working principles. A distinguishing feature of the proposed scheme is its ability of utilizing the mirror image of section C, shown in Fig. 4.3, without any change in the design parameters. In contrast, the Monzon transformer used in [45] cannot be replaced with its mirror image.

To derive the design equations, Figure 4.3(a) is considered. This network is a modified form of the network discussed in [68], with $\alpha = \beta = \theta_4$, $Z_T = Z_{DB-\lambda/4}$, $Z_A = Z_4$, and $Z_B = Z_5$. With the modification of equations (6) to (8) reported in [68], the following design equations can be obtained to suit the present case:

$$Z_4 = Z_{DB-\lambda/4} \cot \theta_4 \quad (4-12)$$

$$Z_5 = Z_{DB-\lambda/4} \tan \theta_4 \quad (4-13)$$

$$Y = \frac{\cos 2\theta_4}{Z_{DB-\lambda/4} \cos^2 \theta_4} \quad (4-14)$$

Therefore for network of Fig. 4.3(a) to work as a dual-frequency $\lambda/4$ line, the electrical length θ_4 needs to be selected as follows:

$$\theta_4 = \frac{m\pi}{1+r}, \quad m \in \mathbb{I} \quad (4-15)$$

Now, the remaining task is to design a dual band susceptance, Y , which can be easily designed using the methodology discussed in section 4.2.2. The final expressions for section C comes out to be:

$$Z_{3,OC} = Z_{DB-\lambda/4} \frac{\cos^2 \theta_4}{\cos 2\theta_4} \tan \theta_3, \quad Z_{3,SC} = -Z_{DB-\lambda/4} \frac{\cos^2 \theta_4}{\cos 2\theta_4} \cot \theta_3 \quad (4-16)$$

$$\theta_3 = \frac{n\pi}{1+r}, \quad n \in \mathbb{I} \quad (4-17)$$

Where $Z_{3,OC}$ and $Z_{3,SC}$ are the required characteristic impedances of open circuit stub and short circuit stub respectively. The integer p , s , m , and n are chosen by keeping in perspective the compact size and realizable values of various transmission line sections.

To prove the original claim that network of Fig.4.3(a) can be substituted by its mirror image shown in Fig.4.3(b), one can consider the ABCD parameter of network of Fig.4.3(b) given by:

$$[ABCD]_{4.3(b)} = \begin{bmatrix} \cos \theta_4 & jZ_5 \sin \theta_4 \\ \frac{j \sin \theta_4}{Z_5} & \cos \theta_4 \end{bmatrix} \begin{bmatrix} \cos \theta_4 & jZ_4 \sin \theta_4 \\ \frac{j \sin \theta_4}{Z_4} & \cos \theta_4 \end{bmatrix} \begin{bmatrix} 1 & 0 \\ jY & 1 \end{bmatrix} \quad (4-18)$$

$$= \begin{bmatrix} \cos^2 \theta_4 - \frac{Z_5}{Z_4} \sin^2 \theta_4 - \frac{Y}{2} (Z_4 + Z_5) \sin 2\theta_4 & \frac{1}{2} (Z_4 + Z_5) \sin 2\theta_4 \\ j \left[\left(\frac{1}{Z_4} + \frac{1}{Z_5} \right) \frac{\sin 2\theta_4}{2} + Y \left(\cos^2 \theta_4 - \frac{Z_4}{Z_5} \sin^2 \theta_4 \right) \right] & \cos^2 \theta_4 - \frac{Z_4}{Z_5} \sin^2 \theta_4 \end{bmatrix} \quad (4-19)$$

Substitutions of the values of Z_4 , Z_5 and Y from (4-12)-(4-14) in the above expression results into following:

$$[ABCD]_{4.3(b)} = \begin{bmatrix} 0 & jZ_{DB-\lambda/4} \\ j \frac{1}{Z_{DB-\lambda/4}} & 0 \end{bmatrix} \quad (4-20)$$

The matrix in (4-20) represents [ABCD] parameter of a quarter wavelength transmission line having characteristic impedance $Z_{DB-\lambda/4}$. This clearly justifies the claim that section C of Fig. 4.2 can be replaced by its mirror image and the design will work without altering the performance at the specified frequencies.

This finding should not come as a surprise considering that it is a highly intuitive result. The procedure to show some network to be equivalent to a $\lambda/4$ -line involves equating the network's ABCD parameter to that of the $\lambda/4$ -line. Since, the quarter-wave line is symmetric, i.e., have the same ABCD parameter to that of its mirror image, the resulting network is also symmetric.

4.3 Simulation and Experimental Verification

To test the proposed idea, the two frequencies are kept fixed and load is varied arbitrarily, in the first set of simulations, as mentioned in TABLE 4-1. The parameters of the proposed impedance transformer are calculated based on the analytical results of the previous Section. Simulation results are shown in Fig. 4.4(a), which confirms the design formulas. Next, an arbitrarily chosen frequency dependent complex load as given by following function is considered with $a_1=70$, $a_2=5E-9$, $a_3=1E9$, $b_1=2E-18$, $b_2=1E-9$ and $b_3=7$:

Table 4-1 The Variation of the Load Impedance

Frequency (GHz)	$Z_L(\Omega)$		
	Case 1	Case 2	Case 3
$f_1 = 1$	$30 - j25$	$80 + j15$	$50 + j60$
$f_2 = 2.5$	$45 + j55$	$90 + j30$	$20 - j30$

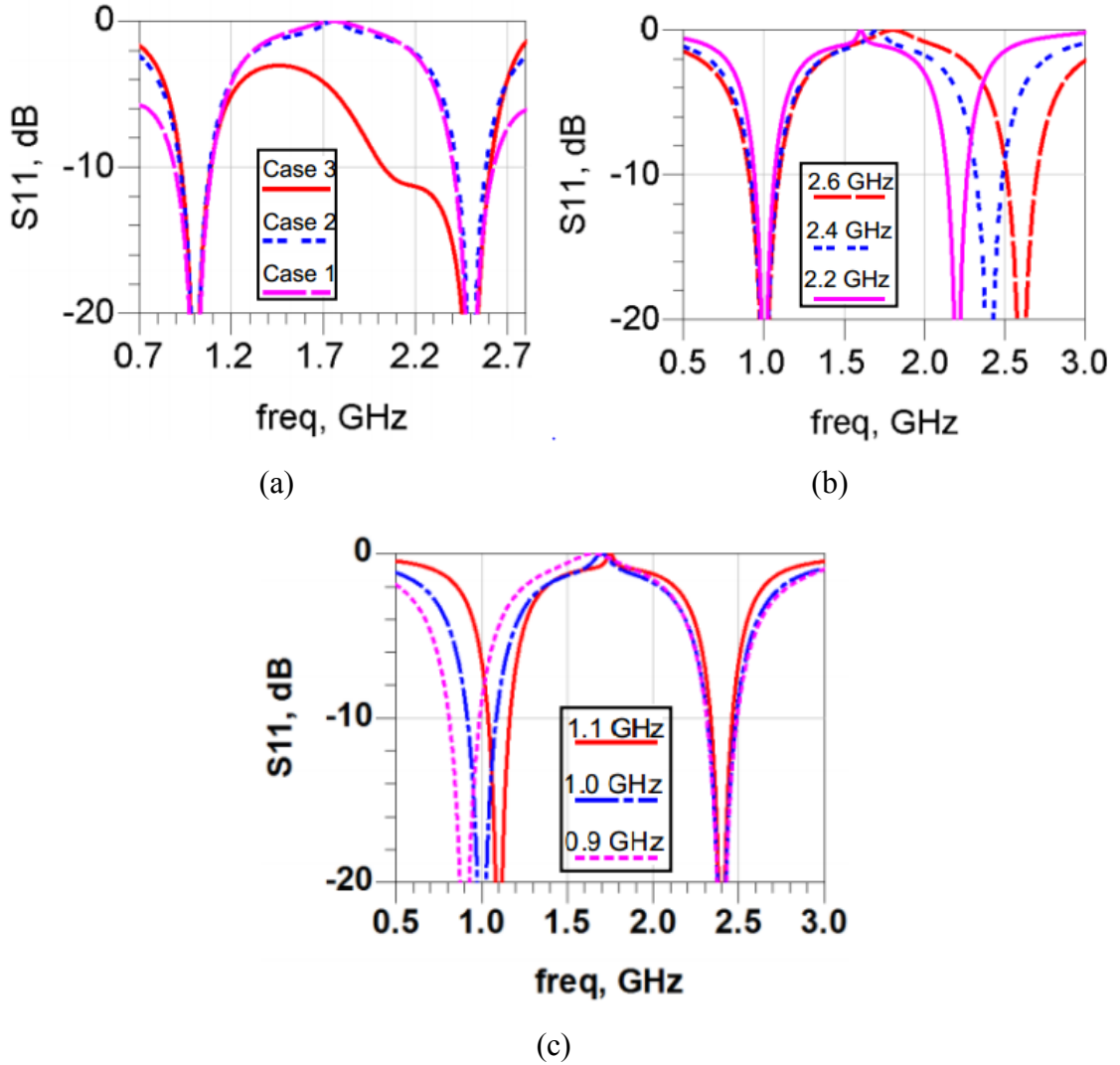


Figure 4.4 Simulation results (a) Load varying but the frequencies fixed (b) Distinct loads as well as frequencies, f_1 fixed f_2 varying, and (c) f_2 fixed f_1 varying.

$$Z_L(f) = [a_1 + a_2(f - a_3)] + j[b_1 f^2 + b_2 f + b_3], \Omega \quad (4-21)$$

With this load, design of the proposed network is carried out for three distinct values of $f_2 = 2.2$ GHz, 2.4 GHz and 2.6 GHz while f_1 is fixed at 1GHz. The simulated results are

depicted in Fig. 4.4(b). In this example, the value of r appears to be very limited; L-type dual-frequency $\lambda/4$ block was shown in [68] to work for $2 \leq r \leq 2.75$. It also emphasizes the flexibility of the proposed scheme that wherever a relatively wider range of r is required, T-type, Pi-type, or other types of dual-band $\lambda/4$ blocks [13] can be used. As a next example, with the load still defined by (4-21), design is carried out by fixing $f_2 = 2.4\text{GHz}$, and taking three distinct values for $f_1 = 0.9\text{GHz}$, 1GHz and 1.1GHz . The results obtained from simulations are shown in Fig. 4.4(c). Thus, it is apparent from the different successful design examples shown in Fig. 4.4 that the presented scheme is indeed suitable for dual-frequency matching problems. The limited frequency-ratio could be increased by considering some other dual-frequency $\lambda/4$ -block. The idea of incorporating a different dual-frequency $\lambda/4$ -block is similar to what has been discussed here, and also reported in [92] where coupled lines based blocks were used.

A figure of merit for a matching network is the bandwidth around the centre frequencies. A 10dB return-loss is considered here as reference for the bandwidth determination. However, it is hard to evaluate the same for the case of FDCLs as the bandwidth hugely depends on how the load varies with frequency. It is also evident from (12-17) that once the value of r and the load at the two frequencies are known, the design parameters of the matching network are fixed. Here comes the role of Z_{Tr_in} , the input impedance that the load sees into the transformer. It effectively regulates what kind of load variation can give higher bandwidth. It is important to remember that for complex conjugate matching, $\text{Re}(Z_{Tr_in}) = \text{Re}(Z_L)$ and $\text{Im}(Z_{Tr_in}) = -\text{Im}(Z_L)$, and therefore the wider the frequency span over which these two conditions are satisfied together, the wider is the bandwidth.

To illustrate and emphasize this point, case 1 and case 3 of the TABLE 4-1 are reconsidered. For the case 1, Fig. 4.5(a) shows the variation of the real part of Z_L and that of Z_{Tr_in} with frequency whereas the variation of the imaginary parts of Z_L and that of Z_{Tr_in} with frequency is shown in the Fig. 4.5(b). For the case 3, the corresponding plots appear in Figs. 4.5(c) and 4.5(d). It can be observed from these plots that the variations in the real and imaginary parts at f_2 in case 3 are slower as compared to the corresponding variations in case 1 at both the frequencies and in case 3 at f_1 . This is

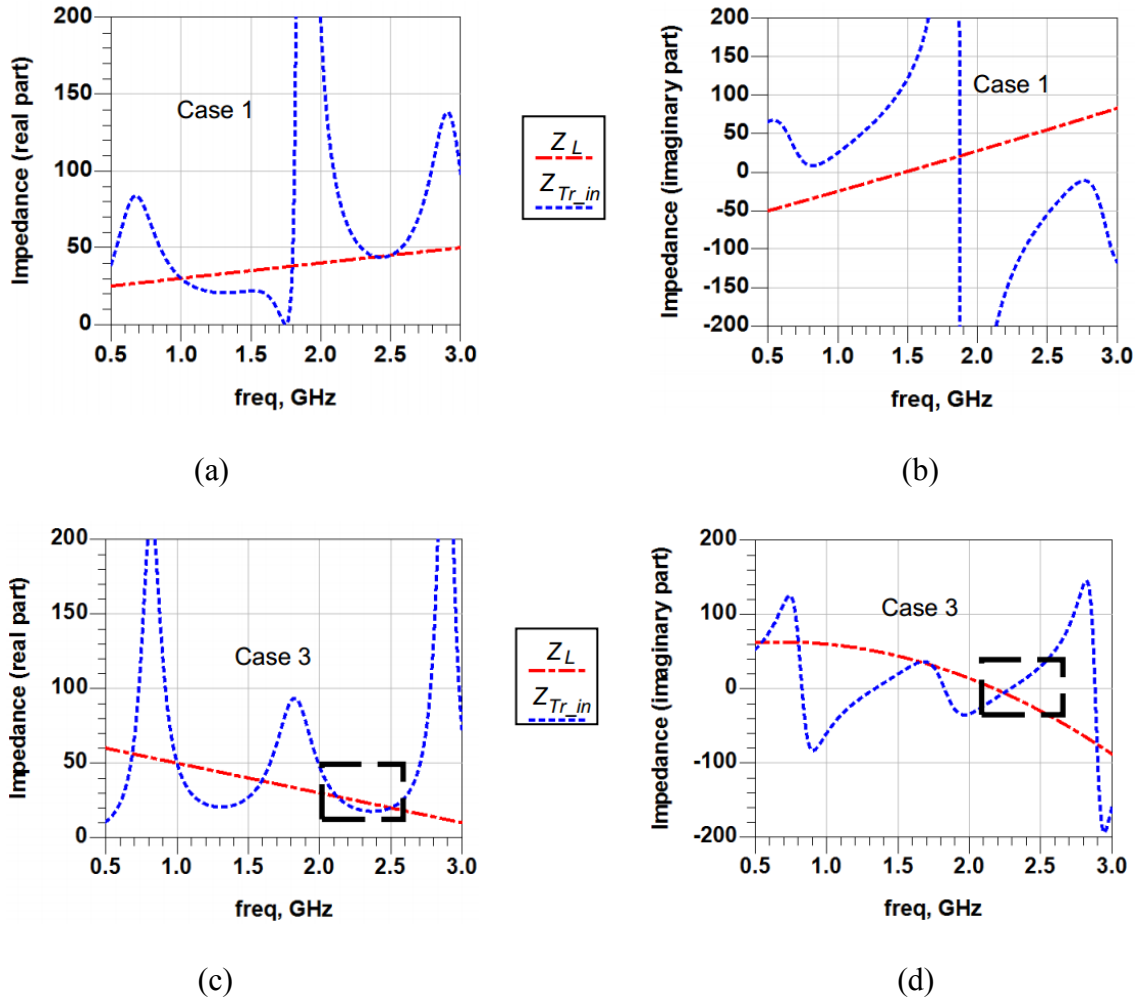


Figure 4.5 Variation of Z_L and Z_{Tr_in} with frequency for (a) Real part, case 1 (b) Imaginary part, case 1 (c) Real part, case 3 (d) Imaginary part, case 3. $f_1=1\text{GHz}$ and $f_2=2.5\text{GHz}$. All impedances are in Ω .

highlighted through the dotted boxes. This eventually leads to enhanced bandwidth in the case 3 at frequency f_2 .

To show the usefulness of the proposed transformer further, the input impedance to be used as Z_L is obtained from measured S-parameter data of a commercial transistor. The computed values are $Z_L(\Omega) = 19.465 + j1.482 @ f_1$ and $20.466 + j18.792 @ f_2$, where $f_1 = 1\text{GHz}$ and $f_2 = 2.42\text{GHz}$. Subsequently, Z_L is realized with the help of Vishay-Dale CRCW-series SMD resistors of 19.6Ω and 20.5Ω and lengths of transmission to obtain the inductive part. The proposed matching network is implemented on an FR-4 substrate ($\epsilon_r = 4.7$, thickness = 1.5mm) with 35um copper cladding. Fig. 4.6(a) shows both the fabricated prototypes. It is important to keep in

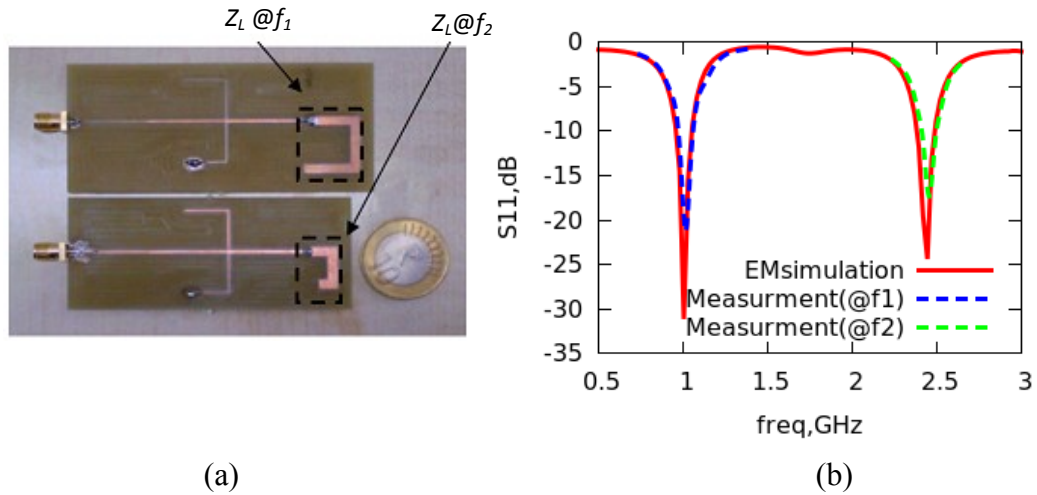


Figure 4.6 (a) Manufactured prototypes of the network shown in Fig.4. 2.
 (b) Simulated and measured results.

Table 4-2 Comparison with Some Existing Designs

Technique/ Ref. No	Type of Load	Experiment	Design Equations
2-Series lines [34]	Real	No	Simple
Chebyshev function [35]	Real	No	Simple
L-type network[30]	Real	Yes	Simple
3-Series lines[40]	FDCL	No	Simple
3-section lines + stubs[42]	FDCL	Yes	Complex ¹
1-section+ stubs+ Monzon's Transformer ² [45]	FDCL	Yes	Simple
This work 1-section+ stubs+ DB- $\lambda/4$ line ³	FDCL	Yes	Simple

¹Need some tool for optimization.

²Some variables are free.

³No unique structure

mind that transformer part is the same in both the prototypes considering that it is a dual-frequency structure whereas the loads are changing with frequency. The simulated and measured results are shown in Fig. 4.6(b). Measurements for both the prototypes were carried out around their respective centre frequencies. There seems to be a bit shift from the designed frequencies which is possibly due to slight inaccuracy in the model of the lumped resistor and fabrication errors/tolerances. Also, it may be noted

that during the prototyping the loss due to the SMA connectors have not been accounted for. Usually, the loss due to SMA at these low frequencies is not significant. Nevertheless, it is evident from the plots that the proposed network is working as a dual-frequency transformer with good performance. A comparison with some state-of-the-art techniques appears in TABLE 4-2. It is apparent that the proposed scheme reported initially in [24, 92] presented a simple technique to realize matching networks for frequency dependent complex loads.

4.4 Conclusion

A novel, simple and successful design methodology for realizing a dual-frequency matching network has been presented. It has been demonstrated that any dual-frequency quarter wavelength block could be utilized for realizing a dual-frequency impedance transformation for frequency dependent complex loads (FDCLs). The reported design also enables the use of mirror image of dual-frequency blocks and this can potentially aid in achieving simpler board layout. Finally, an intuitive explanation of relative bandwidth of different matching networks has also been provided.

Chapter 5

Coupled Lines based DC-isolated Dual-Frequency Impedance Transformers

As the name suggests, a coupled transmission line system comprises of two unshielded transmission lines kept in close proximity such that some amount of power gets coupled from one to another due to electromagnetic field interactions. Coupling may be undesirable such as crosstalk or it may be desirable such as in coupled line couplers. Coupled transmission lines can take many shapes as shown in Fig. 5.1. Coupled lines generally consist of two transmission lines but may also contain more than two. The lines can be symmetrical i.e., both conductors have the same dimensions or asymmetrical [93]. Coupled lines are used in numerous components and directional couplers, filters, baluns, impedance transformer networks, resonators, inductors, interdigital capacitors, dc blocks, and others, of which impedance matching is the subject of this chapter.

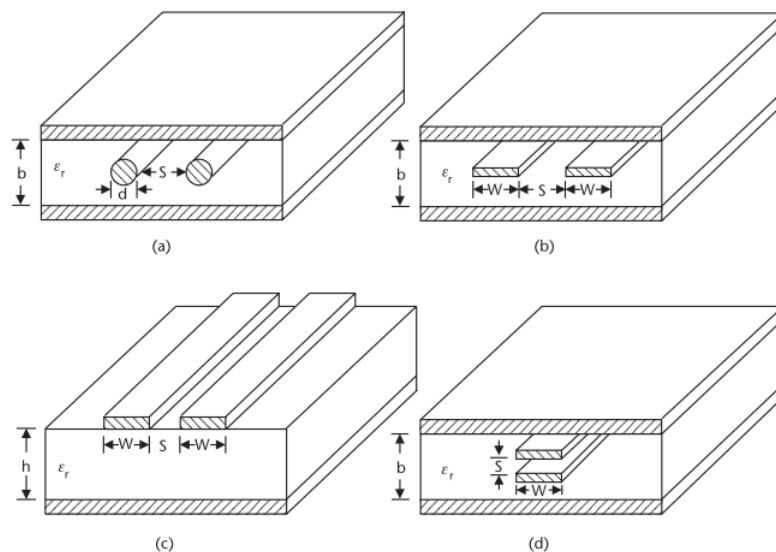


Figure 5.1 Coupled transmission lines: (a) coaxial lines, (b) striplines, (c) microstrip lines, and (d) broadside striplines [93].

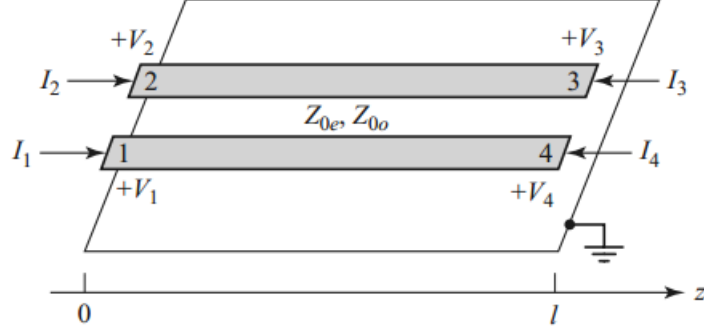


Figure 5.2 A parallel coupled line section with port voltage and current definitions [2].

With the port defined as per Fig. 5.2, the Z-matrix of this parallel coupled line section can be written as follows [2]:

$$Z_{11} = Z_{22} = Z_{33} = Z_{44} = \frac{-j}{2} (Z_{0e} + Z_{0o}) \cot \theta \quad (5-1)$$

$$Z_{12} = Z_{21} = Z_{34} = Z_{43} = \frac{-j}{2} (Z_{0e} - Z_{0o}) \cot \theta \quad (5-2)$$

$$Z_{13} = Z_{31} = Z_{24} = Z_{42} = \frac{-j}{2} (Z_{0e} - Z_{0o}) \csc \theta \quad (5-3)$$

$$Z_{14} = Z_{41} = Z_{23} = Z_{32} = \frac{-j}{2} (Z_{0e} + Z_{0o}) \csc \theta \quad (5-4)$$

It must be noticed that the Z-matrix as defined by (5-1)-(5-4) is that of the four-port symmetrical network shown in Fig. 5.2. It is possible, and in fact is a more common scenario, to terminate two of the four ports with open or short circuit. Such networks are commonly used in filters.

In the next section, a dual-frequency property of parallel coupled lines terminated into a real impedance pertaining to input admittance will be discussed. In addition, applications of this property in advanced dual-frequency impedance matching networks will be demonstrated [59-60].

5. 1 Dual-Frequency Admittance Property of Coupled lines Terminated into a Real Impedance

A one-port network, shown in Fig. 5.3 is considered, to derive the dual-frequency admittance property of coupled lines terminated with a real impedance. It must be noti-

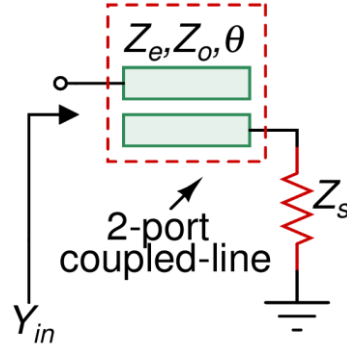


Figure 5.3 A coupled-line section terminated into a real impedance, Z_s .

ced that this network has been obtained by terminating two of the ports by open circuit and one of the ports with a real impedance, Z_s , of the four-port network shown in Fig. 5.2. Thus, the network comprises of a two-port parallel coupled-line section having even- and odd-mode characteristic impedances of Z_e and Z_o respectively with the electrical length of θ . The objective is to deduce dual-frequency behavior of the input admittance, Y_{in} , of this one-port network. To that end, (5-1) - (5-4) can be utilized to obtain the ABCD parameter of the 2-port coupled-line given below:

$$\begin{bmatrix} A & B \\ C & D \end{bmatrix} = \begin{bmatrix} c_{11} & c_{12} \\ c_{21} & c_{22} \end{bmatrix} \quad (5-5)$$

where,

$$c_{11} = \frac{\rho+1}{\rho-1} \cos \theta = c_{22} \quad (5-6)$$

$$c_{12} = -\frac{j}{2} \left[\frac{4\rho Z_o \cos^2 \theta}{\rho-1 \sin \theta} - (\rho-1) Z_o \sin \theta \right] \quad (5-7)$$

$$c_{21} = j \frac{2}{(\rho-1) Z_o} \sin \theta \quad (5-8)$$

The term ρ in the above expressions are the ratio of even-mode to odd-mode characteristic impedance, $\rho = Z_e / Z_o$.

Now, using two-port network theory Y_{in} can be written as:

$$Y_{in} = \frac{c_{21} Z_s + c_{22}}{c_{11} Z_s + c_{12}} \quad (5-9)$$

Substituting (5-5) - (5-8) into (5-9) and subsequent simplification results into a complex form of $Y_{in} = M + jN$ with:

$$M = \frac{4Z_s(\rho-1)^2}{4\left[Z_s^2(\rho+1)^2 - 2\rho(\rho-1)^2 Z_o^2\right] \cos^2 \theta + (\rho-1)^4 Z_o^2 \sin^2 \theta + 16\rho^2 Z_o^2 \cos^4 \theta / \sin^2 \theta} \quad (5-10)$$

$$N = \frac{\rho+1}{Z_o} \frac{\left[4Z_s^2 - (\rho-1)^2 Z_o^2\right] \sin(2\theta) + 8\rho Z_o^2 \cos^3 \theta / \sin \theta}{4\left[Z_s^2(\rho+1)^2 - 2\rho(\rho-1)^2 Z_o^2\right] \cos^2 \theta + (\rho-1)^4 Z_o^2 \sin^2 \theta + 16\rho^2 Z_o^2 \cos^4 \theta / \sin^2 \theta} \quad (5-11)$$

The following observations can be made from (5-10) - (5-11):

- 1) In (5-10), there is no frequency dependent term in the numerator. However, the presence of only even powers of $\sin \theta$ and $\cos \theta$ in the denominator ensures that the values of M will repeat with a period of π . In addition, M will not change its sign due to even powers of sine and cosine terms as the frequency switches from f_1 to f_2 .
- 2) Numerator of (5-11) also has a period of π but the sign of N will change as the frequency switches from f_1 to f_2 due to terms containing 2θ or odd powers of sine and cosine terms.

Therefore, it can be deduced that $Y_{in}|_{f_1} = (Y_{in}|_{f_2})^*$ holds true, if the value of θ is given by (5-12).

$$\theta = \frac{(1+q)\pi}{1+r}, \quad \text{where } r = f_2/f_1 \text{ and } q \in \text{integer} \quad (5-12)$$

To summarize:

“if θ is chosen as defined by (5-12), then the input admittance looking into a coupled-line terminated into a purely real impedance is complex conjugate of each other at the two frequencies. Since, impedance is simply inverse of the admittance, the same property also holds true for the input impedance.

Interestingly, this property was also shown to hold good for single-section transmission line in chapter 3. It is highly interesting and useful property and its applic-

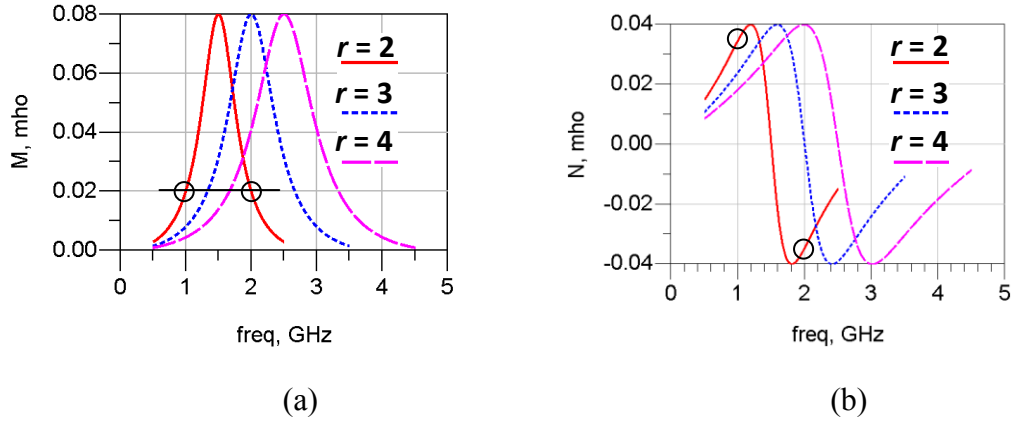


Figure 5.4 Variation of (a) real and (b) imaginary parts of Y_{in} with frequency.

ation in novel dual-frequency impedance matching networks will be demonstrated shortly.

To demonstrate that indeed the values of Y_{in} are complex conjugate of each other at the two frequencies, a coupled-line having $\rho=3$ and $Z_o=25\Omega$ is considered. It is also assumed that $f_1=1\text{GHz}$ and $Z_s=50\Omega$. Simulations are performed for three values of second frequency $f_2=2\text{GHz}$, 3GHz and 4GHz and this correspond to $r=2$, 3 and 4 respectively. The corresponding values of θ can be calculated from (5-12) by setting $q=0$ to get compact size. Simulations are performed using the Keysight ADS to find the profile of Y_{in} and the obtained results are depicted in Fig. 5.4.

To understand the meaning of the plots in Fig. 5.4, consider the case of $r=2$ and focus on the values of M and N at frequencies 1GHz and 2GHz . It is evident from these values highlighted using small circles that the values of M are the same at 1GHz and 2GHz , where as that of the N changes its sign. Similar observation can be readily made for the other values of r as well. Therefore, it is apparent that the real part of Y_{in} remains the same and the imaginary part just changes its sign as the frequency switches from f_1 to f_2 .

5.2 DC-Isolated Dual-Frequency Impedance Transformer for Real Load Impedance

The two proposed configurations for matching a real load impedance to a real source impedance are depicted in Fig. 5.5. It can be seen that the only difference between these two configurations is in the placement of stub. The design with stub on the load side is named as configuration-I, whereas the design with stub on the source side is named as configuration-II. The analysis of both these configurations is given in subsequent subsections.

5.2.1 Analysis of Configuration-I

The configuration-I is shown in Fig. 5.5(a). It is apparent that it consists of parallel coupled lines (Section A), and a short or an open stub (Section B). In section A, Z_e is the even-mode impedance, Z_o is the odd-mode impedance, and θ_1 is the electrical length of the coupled lines whereas Z_2 and θ_2 are the characteristic impedance and electrical length of the stub. Y_{in1} denotes the admittance looking into Section A while Y_{in2} is the admittance looking into Section B. The physical dimensions l (length), w (width) and s (separation between coupled lines) of respective transmission line segments are also shown in the figure. All electrical lengths are defined at the first frequency, f_1 .

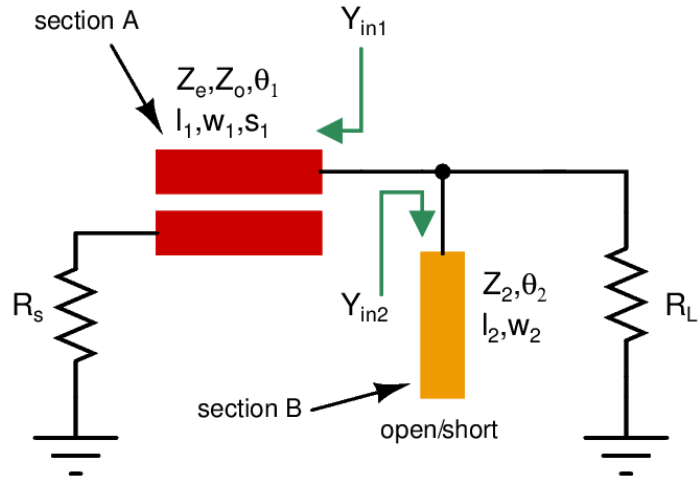
As shown in the previous section, the value of Y_{in1} may be expressed as follows:

$$Y_{in1} = P + jQ \quad (5-13)$$

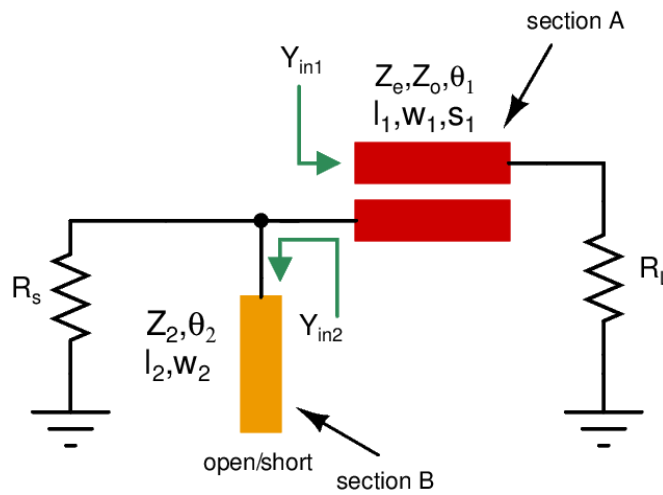
Where, P and Q are given by (5-14) and (5-15):

$$P = \frac{4R_s(\rho-1)^2}{4\left[R_s^2(\rho+1)^2 - 2\rho(\rho-1)^2 Z_o^2\right] \cos^2 \theta_1 + (\rho-1)^4 Z_o^2 \sin^2 \theta_1 + 16\rho^2 Z_o^2 \cos^4 \theta_1 / \sin^2 \theta_1} \quad (5-14)$$

$$Q = \frac{\rho+1}{Z_o} \frac{\left[4R_s^2 - (\rho-1)^2 Z_o^2\right] \sin(2\theta_1) + 8\rho Z_o^2 \cos^3 \theta_1 / \sin \theta_1}{4\left[R_s^2(\rho+1)^2 - 2\rho(\rho-1)^2 Z_o^2\right] \cos^2 \theta_1 + (\rho-1)^4 Z_o^2 \sin^2 \theta_1 + 16\rho^2 Z_o^2 \cos^4 \theta_1 / \sin^2 \theta_1} \quad (5-15)$$



(a)



(b)

Figure 5.5 Dual-frequency matching networks (a) Configuration-I: Stub on the load side (b) Configuration-II: Stub on the source side [60].

Using the dual-frequency admittance property shown in the previous section, one can express $Y_{in1}|_{f_1} = P + jQ$ and $Y_{in1}|_{f_2} = P - jQ$ and vice-versa if the value of θ_1 is given by:

$$\theta_1 = \frac{(1+q)\pi}{1+r} \quad (5-16)$$

where, q is an integer and r is the band-ratio f_2/f_1 .

The section A is designed in such a manner that:

$$P = 1 / R_L \quad (5-17)$$

The imaginary part of Y_{in1} , which is $+Q @ f_1$ and $-Q @ f_2$, is cancelled by a dual-frequency susceptance, section B, having the following property:

$$Y_{in2} |_{f_1} = -jQ \quad (5-18)$$

$$Y_{in2} |_{f_2} = +jQ \quad (5-19)$$

The following equations should hold true if an open stub is used as a dual-frequency susceptance:

$$-jQ = j(1 / Z_2) \tan \theta_2 \quad (5-20)$$

$$+jQ = j(1 / Z_2) \tan(r \theta_2) \quad (5-21)$$

Simplification of (5-20)-(5-21) yields,

$$\theta_2 = \frac{(1+s)\pi}{1+r}, \quad \text{where } s \text{ is an Integer} \quad (5-22)$$

$$Z_2 = -\tan \theta_2 / Q \quad (5-23)$$

Similarly, for a short stub to work as a dual-frequency susceptance, the following equations need to be satisfied.

$$-jQ = -j(1 / Z_2) \cot \theta_2 \quad (5-24)$$

$$+jQ = -j(1 / Z_2) \cot(r \theta_2) \quad (5-25)$$

Further simplification of (5-24)-(5-25) results into:

$$\theta_2 = \frac{(1+s)\pi}{1+r}, \quad \text{where } s \text{ is an Integer} \quad (5-26)$$

$$Z_2 = \cot \theta_2 / Q \quad (5-27)$$

5.2.2 Analysis of Configuration-II

Analysis of this configuration is similar to that of the configuration-I with the exception of the following changes.

1. R_S in equations (5-13) and (5-14) needs to be replaced by R_L .
2. The coupled line is now designed such that

$$P = 1/R_S \quad (5-28)$$

5.2.3 Design Procedure

Design steps for the proposed network are as follows:

- 1) For a given value of r , R_L and R_S and assuming an appropriate value of Z_o , say 25Ω , the value of ρ is calculated with the help of (5-14), (5-16) and (5-17). A realizable value of ρ lies anywhere between 2 and 4 [53]. Alternatively, assuming a suitable value for ρ , the value of Z_o can be determined using the same equations [59]. It is reiterated that $P = 1/R_L$ or $P = 1/R_S$ needs to be set depending upon whether the configuration-I or the configuration-II is being used. Thus, the corresponding value of Z_e is $\rho * Z_o$. If the obtained parameters for section A are not physically realizable then one needs to choose a different value for ρ and repeat the calculations. It should be apparent from this step that one of the advantages of this proposed L-network is the availability of the free variable. It must be noted that such flexibility is not available in the transmission line based L-type matching networks reported in [30].
- 2) Subsequently, the value of Q is evaluated with the help of (5-15), and using the design procedure of dual-frequency stubs as described previously, a suitable section B may be designed. Practically, θ_2 is either greater or less than 90° . Furthermore, it is to be noticed that the value of integer s depends on the sign of Q . Now, there are four possible cases in such a scenario:
 - a) The value of Q is positive /negative and open /short stub is to be used in section B: it follows from (5-23) / (5-27) that $\tan\theta_2$ / $\cot\theta_2$ must be negative

to ensure a positive value of Z_2 . This implies that the integer s must be chosen such that θ_2 comes out to be greater than 90° in (5-23) / (5-27).

- b) The value of Q is positive/negative and short/open stub is to be used in section B: it follows from (5-27) / (5-23) that $\cot\theta_2 / \tan\theta_2$ must be positive as well to ensure a positive value of Z_2 . This implies that the integer s must be chosen such that θ_2 comes out to be less than 90° in (5-27) / (5-23).

Furthermore, the requirement to obtain physically realizable design parameters for stubs also affects the choice of the integer s . Lastly, if using open stub as section B does not yield a physically realizable l_2 and w_2 , then one should try a short stub and vice versa.

A design example shall make the procedure more clearer. Suppose $R_L = 100\Omega$ is to be matched to $R_S = 50\Omega$ at $f_1 = 1\text{GHz}$ and $f_2 = 2\text{GHz}$. This implies $r = 2$, and thus $\theta_1 = 60^\circ$ from (5-16) considering $q = 0$ for compact board size. Furthermore, a value of $Z_o = 25\Omega$ is assumed. Since, $P = 0.01\text{mho}$ from (5-17), the value of ρ is found from (5-14) which comes out to be 2.1332 after omission of the unreasonable values. The value of Q corresponding to $\rho = 2.1332$ is found to be 0.04639 mho from (5-15). Next, since the value of Q is positive, s is set as 1 in (5-22) so that $\theta_2 = 120^\circ$ and $\tan\theta_2$ becomes negative to ensure a positive value of Z_2 . The value of Z_2 then evaluates to 37.34Ω from (5-23). This completes the design.

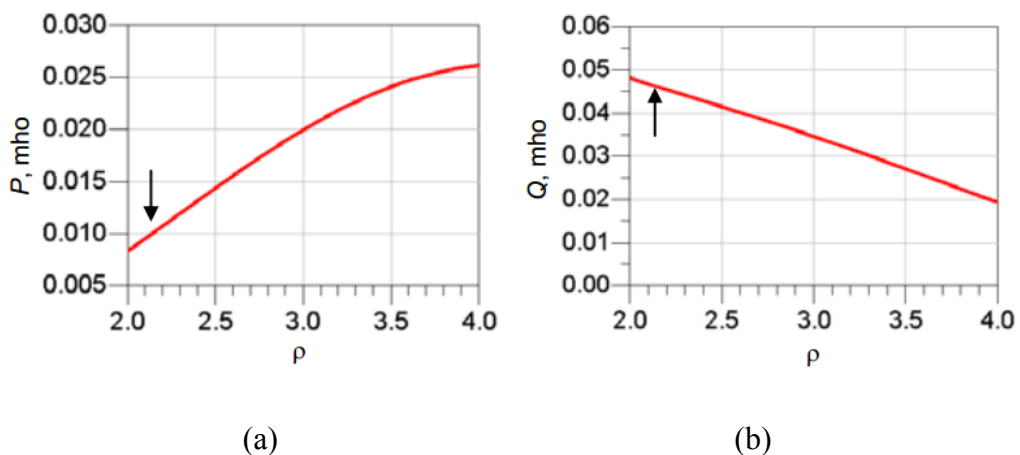


Figure 5.6 Variation of P and Q (@ f_1) with ρ in the above example (a) Plot of P : Arrow indicates the value of ρ ($= 2.1332$) where the value of $P = 0.01\text{mho}$ (b) Plot of Q : Arrow indicates the value of Q corresponding to $\rho = 2.1332$.

Although, equation (5-17) along with (5-14) and (5-16) can be solved by algebraic means but a plot such as the one shown in Fig. 5.6 is very useful for a quick estimation of ρ and Q and for the intuition it may provide. For example, to check if a match for $R_L=20\Omega$ can be obtained in the above example can be quickly and easily assessed with the help of Fig. 5.6(a). It clearly shows that the match is not possible as the plot does not touch $P = 1/R_L = 0.05\text{mho}$ point.

5.2.4 Results and Discussions

A series of simulation were carried out to show the flexibility of the proposed circuits in matching different load and source impedances. The source side impedance (R_S) is assumed to be 50Ω during all these simulations.

First, the configuration-I is considered for various cases given in TABLE 5.1. Here, the

Table 5-1 Configuration-I, $f_1= 1\text{GHz}$, $Z_o=25 \Omega$, $R_L=100\Omega$

Cases	f_2 (GHz)	Z_e (Ω)	θ_1 (deg)	Z_2 (Ω)	θ_2 (deg)
1	2	53.33	60	37.34	120, OC
2	2.5	68.36	51.43	145.19	102.86, OC
3	3	85.36	45	44.334	45, SC
4	3.3	97.05	41.86	56.52	41.86, SC

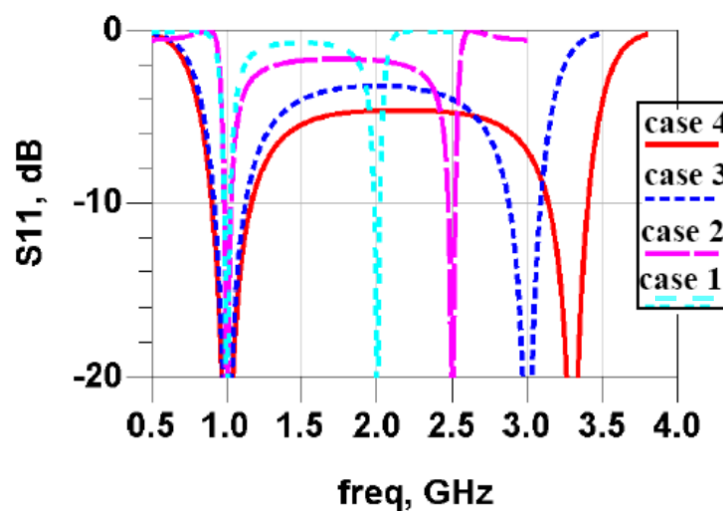


Figure 5.7 The simulated return-loss for the designs cases listed in TABLE 5.1.

load impedance and f_1 are kept fixed while the value of f_2 is varied. The term OC denotes the use of an open circuit stub as section B whereas the term SC denotes the use of a short circuit stub. It is noticed from TABLE 5-1 that one cannot go beyond $f_2 = 3.3$ GHz as the value of required ρ will be greater than 4 which may pose fabrication challenges [53]. It is clear from the corresponding return loss plots shown in Fig. 5.7 that the proposed topology is capable of achieving very good matching at the two distinct desired frequencies simultaneously.

In TABLE 5-2, the design parameters are given for the case where the load is again fixed but for arbitrarily varying f_1 and f_2 . Fig. 5.8 shows the return loss for this case, which shows a proper matching for this case as well.

Lastly in TABLE 5-3, f_1 and f_2 are both fixed value of $f_1 = 1.5$ GHz and $f_2 = 3$ GHz while the load impedance is swept. A good matching can be observed from return loss plots which appear in Fig. 5.9. Again, it can be seen in TABLE 5-3 that for the increasing value of the load impedance from 40Ω to 80Ω , the required value of Z_e de-

Table 5-2 Configuration-I, $Z_o=25\ \Omega$, $R_L=100\Omega$

Cases	f_1 (GHz)	f_2 (GHz)	Z_e (Ω)	θ_1 (deg)	Z_2 (Ω)	θ_2 (deg)
1	0.9	2.4	73.74	49.10	32.01	49.10, SC
2	1.5	3.5	63.20	54	90.15	108, OC
3	2	4.2	56.24	58.06	48.67	116.13, OC

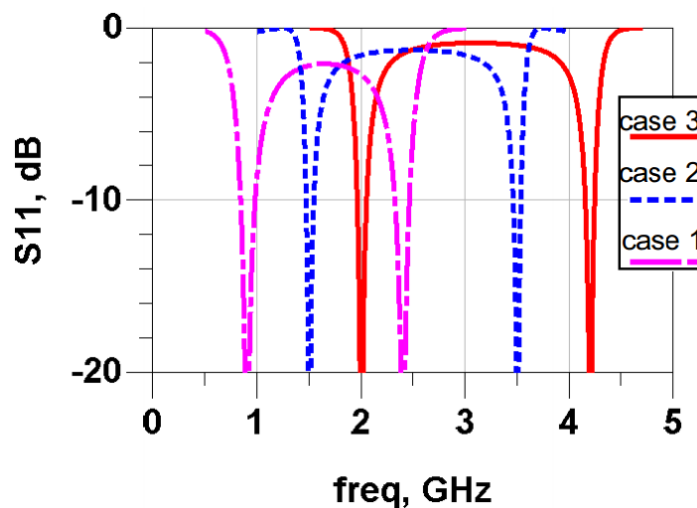


Figure 5.8 The simulated return-loss for the designs cases listed in TABLE 5.2

Table 5-3 Configuration-I, $f_1= 1.5\text{GHz}$, $f_2= 3\text{GHz}$, $Z_o=25 \Omega$

Cases	$R_L (\Omega)$	$Z_e (\Omega)$	$\theta_1 (\text{deg})$	$Z_2 (\Omega)$	$\theta_2 (\text{deg})$
1	40	91.37	60	70.10	120, OC
2	60	67.27	60	44.45	120, OC
3	80	58.48	60	39.69	120, OC

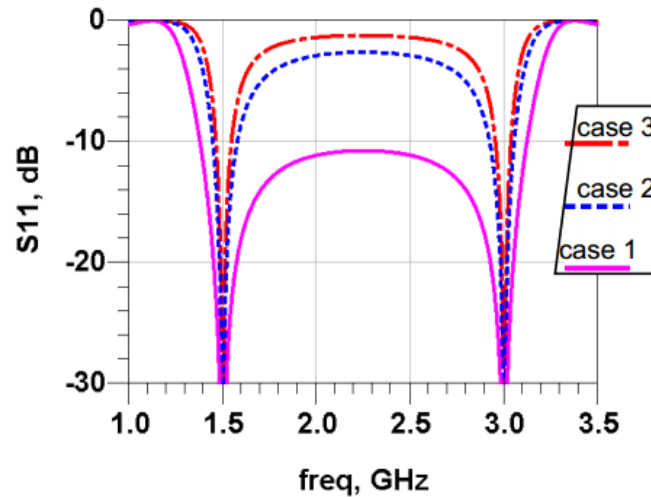


Figure 5.9 The simulated return-loss for the designs cases listed in TABLE 5.3.

creases and ultimately a situation would come, $R_L=100 \Omega$ for example, where the required ρ will be smaller than 2 and this would lead to fabrication challenges [53].

TABLE 5-4 to TABLE 5-6 provide similar computed values for the configuration-II as were done for the configuration-I. Their corresponding simulated results are depicted in Figs. 5.10 to 5.12.

Table 5-4 Configuration-II, $f_1= 1\text{GHz}$, $Z_o=25 \Omega$, $R_L=20\Omega$

Cases	$f_2 (\text{GHz})$	$Z_e (\Omega)$	$\theta_1 (\text{deg})$	$Z_2 (\Omega)$	$\theta_2 (\text{deg})$
1	2	53.11	60	31.37	120, OC
2	2.5	73.28	51.43	108.51	102.86, OC
3	2.9	93.61	46.15	27.60	46.15, SC

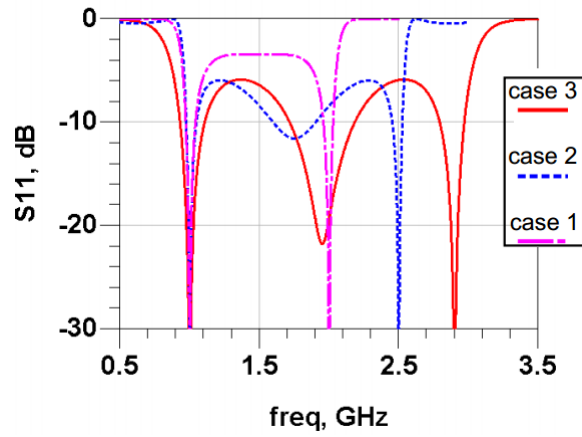


Figure 5.10 The simulated return-loss for the designs cases listed in TABLE 5.4.

Table 5-5 Configuration-II, $Z_o=25 \Omega$, $R_L=20\Omega$

Cases	f_1 (GHz)	f_2 (GHz)	$Z_e(\Omega)$	$\theta_1(\text{deg})$	$Z_2(\Omega)$	$\theta_2(\text{deg})$
1	0.8	1.8	62.50	55.38	57.17	110.76, OC
2	1.3	2.75	57.28	57.78	41.45	115.56, OC
3	2	4.5	62.50	55.38	57.17	110.77, OC
4	1.7	5.1	99.3	45	29.56	45, SC

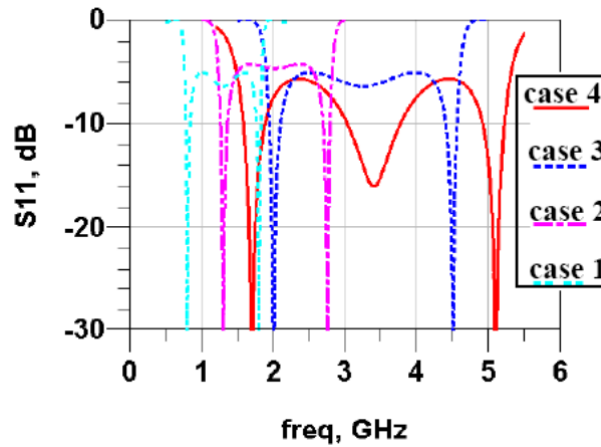


Figure 5.11 The simulated return-loss for the designs cases listed in TABLE 5.5.

Table 5-6 Configuration-II, $f_1= 1\text{GHz}$, $f_2= 2\text{GHz}$, $Z_o=25 \Omega$

Cases	$R_L (\Omega)$	$Z_e(\Omega)$	$\theta_1(\text{deg})$	$Z_2(\Omega)$	$\theta_2(\text{deg})$
1	30	58.69	60	36.80	120, OC
2	45	70.27	60	46.13	120, OC
3	65	93.86	60	67.84	120, OC

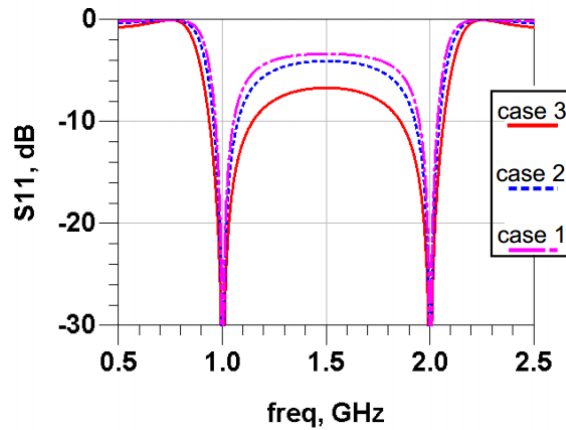


Figure 5.12 The simulated return-loss for the designs cases listed in TABLE 5.6.

All the design parameters listed in TABLES 5.1 to 5.6 are calculated using the design equations derived in the previous section. The simulated results clearly show proper matching in the entire considered scenario. Different bandwidths are obtained for different cases and its value depends on the load as well as on the frequency ratio. A comparison of the simulated results for the two configurations reveals that both of them are capable of matching quite a variety of loads at different frequencies. Perhaps, a preference in choice largely depends on the ease of fabrication.

A prototype was developed to work at $f_1 = 1\text{GHz}$ and $f_2 = 2\text{GHz}$ for the configuration-I using Roger's RO4350B laminate on 1oz copper cladding to show the practical utility of the proposed design. The considered load is a 20.5Ω CRCW series SMD resistor available from Vishay-Dale. The prototype along with the corresponding

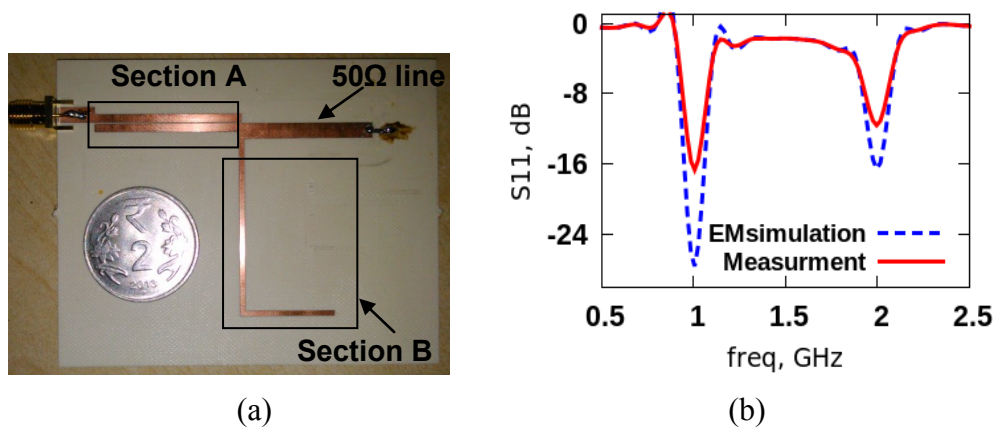


Figure 5.13 (a) The manufactured prototype in our lab. This is a configuration-I type matching network (b) the comparison of measurement and the EM-simulation results.

physical dimensions (in mm), $l_1 = 31.620$, $w_1 = 1.750$, $s_1 = 0.285$, $l_2 = 59.517$ and $w_2 = 1.112$, is depicted in Fig. 5.13(a). The obtained EM simulation and measurement results are compared in Fig. 5.13(b).

Next, to show the practical utility of the configuration-II, a T-junction power divider shown in Fig. 5.14(a) is considered [30]. Its equivalent circuit looking from the port 1 is shown in Fig. 5.14(b). For equal power division, the paths from port1 to port2 and from port1 to port3 are the same and therefore the coupled line impedances as well as the impedance of the right-side termination gets halved in Fig. 5.14(b). The obtained equivalent circuit may readily be recognized as the proposed configuration-II shown in Fig. 5.5(b). Now, here the requirement is to match $R_L = Z_0/2$ to $R_S = Z_0$, where $Z_0 (= 50\Omega)$ is the port impedance. Based on this idea, a dual-frequency T-junction power divider is designed and implemented to work at $f_1 = 1\text{GHz}$ and $f_2 = 2.1\text{GHz}$. The Prototype and the corresponding S-parameters are depicted in Fig. 5.15. It must be noted that this T-junction divider is not matched at all the ports, but only at port 1, therefore, S22 and S33 are not depicted. There is slight anomaly between the EM simulated and the measured results that can be attributed to in-home fabrication and due to difference between the actual design data of the used substrate and that used for simulation.

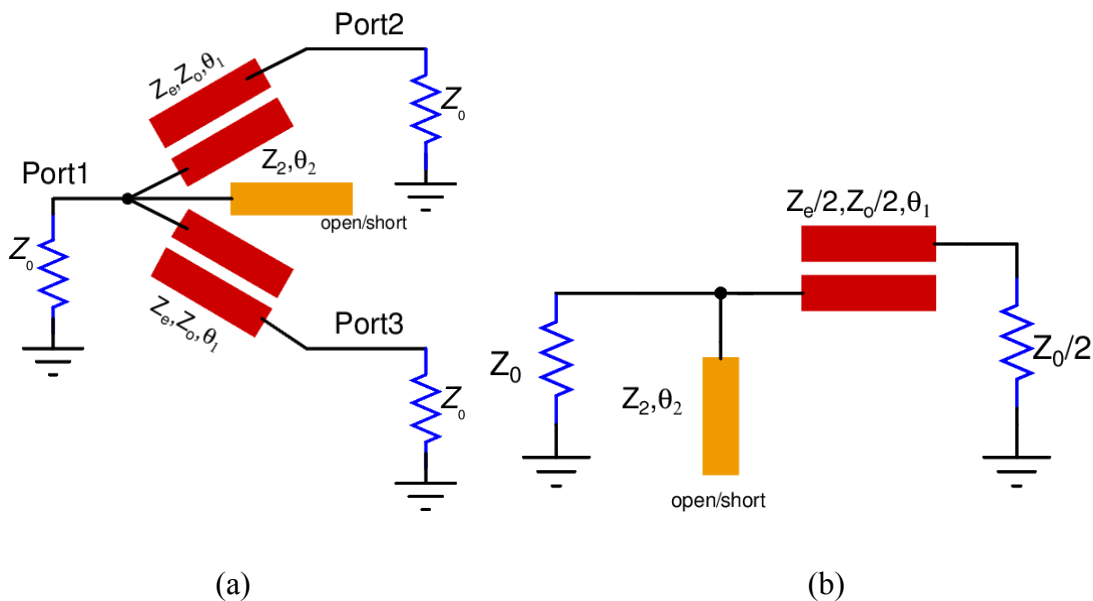


Figure 5.14 (a) A dual-frequency T-junction power divider (b) Equivalent circuit of the divider looking into the port1.

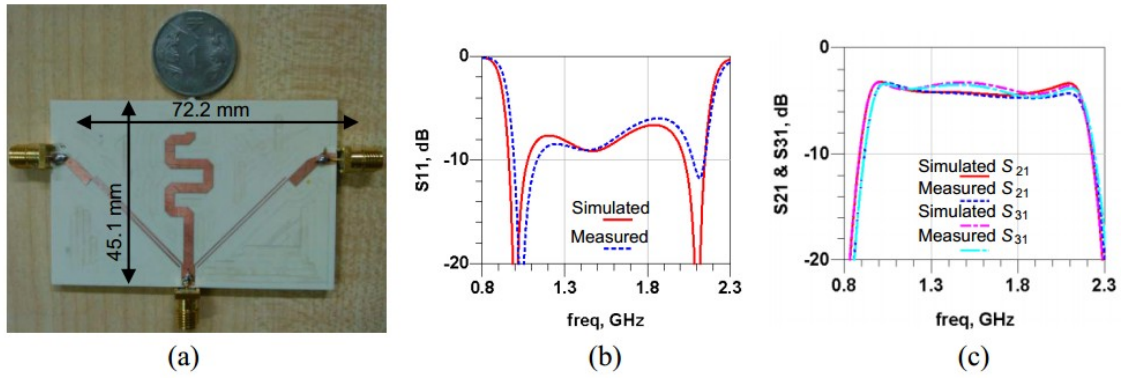


Figure 5.15 (a) Photograph of the designed T-junction divider (b) Simulated/measured Return loss of port 1 (c) Simulated/measured transmissions.

It is observed from the measured results of the divider, Fig. 5.15 (b)-(c), as well as the simulations depicted in Figs. 5.7 to 5.8 that the out-of-the-band performance may deteriorate in some cases depending upon the value of the load impedance or the frequency-ratio. A remedy to circumvent this issue is to use a parallel combination of a short and open stub shown in Fig. 5.16(a) instead of using only either of them. It may be proved in a manner similar to the one discussed in section 2.1 that the value of Z for such a configuration can be given by:

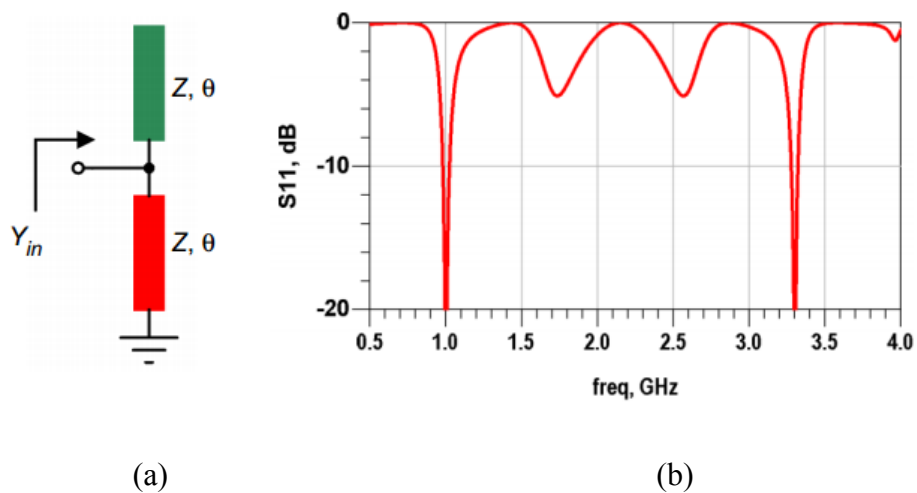


Figure 5.16 (a) A dual-band complex impedance using parallel combinations of open and short stubs to fine-tune out-of-the-band performance (b) Simulated Return loss for the case4 of TABLE 5-1 showing better out-of-the-band performance.

$$Z = \frac{1 - \tan^2 \theta}{Q \tan \theta} \quad (5-29)$$

where, θ has the same expression as that of θ_2 .

Using this parallel stub, case 4 of TABLE 5-1 is redesigned to illustrate the improvement. The value of Z and θ are found to be 34.56Ω and 125.58° respectively. The simulated return loss depicted in Fig. 5.16(b) clearly conveys that the out-of-the-band performance is much better as compared to previous result shown in Fig. 5.7 (case4). This solution would, however, come at a price of increased layout complexity.

A comparison of the proposed matching network with some previously reported designs for real load and source impedances is presented in TABLE 5-7. Apparently, one of the key aspects of this proposed approach is the inherent dc-blocking feature which comes due to the presence of parallel coupled line. As mentioned earlier, this feature could be extremely useful in design of amplifiers.

Table 5-7 Comparison with Some Existing Designs

Technique/Ref. No	Type of Load	Bands	DC Isolation	Experiment
Cascaded Transmission-Lines [29]	Real	Two	No	No
Chebyshev Function [30]	Real	Two	No	No
L-type Network[25]	Real	Two	No	Yes
Stubbed Coupled Lines [52]	Real	Three	No	Yes
Cascaded Coupled Lines [51]	Real	Four*	No	Yes
This work Coupled Line+ Stub	Real	Two	Yes	Yes

5.3 DC Isolated Dual-Frequency Impedance Matching Network for Complex Impedance

A coupled lines based L-type network investigated in the previous section is used for real-to-real impedance transformation. It is apparent from Fig. 3.4 that the same can be utilized to realize the impedance matching network for frequency dependent complex load impedance. The proposed impedance matching network [59] comprises of three sections as shown in Fig. 5.17. Here, Z_s is the source side impedance whereas Z_L is the frequency dependent complex load impedance. Section A consists of a transmission line section having characteristic impedance Z_1 and electrical length θ_1 , while section B consists of coupled lines having even/odd-mode impedances equal to Z_e and Z_o and electrical length θ_2 whereas section C is an open/short stub with characteristic impedance Z_3 and electrical length θ_3 . All these electrical lengths are defined at the first frequency f_1 . The physical dimensions l (length), w (width) and s (separation between coupled lines) of various transmission-lines are also depicted in the figure. The respective admittances (impedances) looking into sections A, B and C are $Y_{in1}(Z_{in1})$, $Y_{in2}(Z_{in2})$ and $Y_{in3}(Z_{in3})$. In this architecture, the overall idea is to first match the real part of Y_{in1} to the real part of Y_{in2} , and then cancel out the ‘leftover’ imaginary part of $Y_{in1} + Y_{in2}$ by the shunt stub Y_{in3} . The design of sections A and B are similar to that used in Fig. 3.5. However, for sake of completeness, their design equations are repeated here as well.

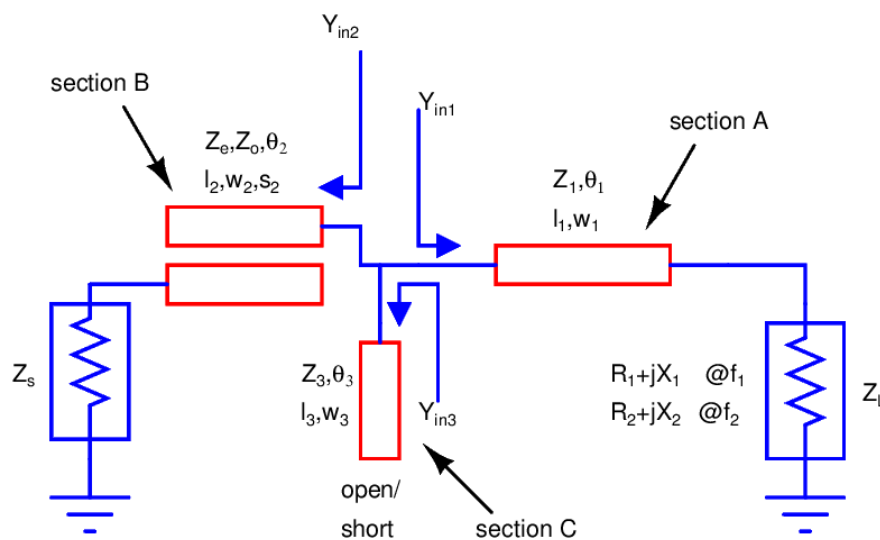


Figure 5.17 A dual-frequency matching network for complex load impedance [59].

5.3.1 Design of Section A

It is assumed that the load impedance at the two arbitrary frequencies f_1 and f_2 are given by:

$$Z_L |_{f_1} = R_1 + jX_1 \text{ and } Z_L |_{f_2} = R_2 + jX_2.$$

As reported in [40], if section A is designed such that:

$$Z_1 = \sqrt{R_1 R_2 + X_1 X_2 + \frac{X_1 + X_2}{R_2 - R_1} (R_1 X_2 - R_2 X_1)} \quad (5-30)$$

$$\theta_1 = \frac{p\pi + \arctan\left(\frac{Z_1(R_1 - R_2)}{R_1 X_2 - R_2 X_1}\right)}{1+r}, \quad \text{where: } p \in \mathbb{I}, \quad r = f_2 / f_1 \text{ with } r \geq 1 \quad (5-31)$$

Then, the impedance looking into section A are complex conjugate of each other at the two frequencies, i.e., $Z_{in1} |_{f_1} = Z_{in1}^* |_{f_2}$. More elaborately, it can be expressed as $Z_{in1} = 1/Y_{in1} = R_{in1} + jX_{in1} @ f_1$ and $Z_{in1} = 1/Y_{in1} = R_{in1} - jX_{in1} @ f_2$ where the values of R_{in1} and X_{in1} are given by [40]:

$$R_{in1} = \frac{R_1 Z_1^2 [1 + \tan^2 \theta_1]}{Z_1^2 - 2Z_1 X_1 \tan \theta_1 + (R_1^2 + X_1^2) \tan^2 \theta_1} \quad (5-32)$$

$$X_{in1} = \frac{(Z_1^2 - R_1^2 - X_1^2) Z_1 \tan \theta_1 + Z_1^2 X_1 [1 - \tan^2 \theta_1]}{Z_1^2 - 2Z_1 X_1 \tan \theta_1 + (R_1^2 + X_1^2) \tan^2 \theta_1} \quad (5-33)$$

Alternatively, Y_{in1} may also be obtained by inverting and simplifying Z_{in1} .

$$Y_{in1} = G_1 - jB_1 @ f_1 \quad (5-34)$$

$$Y_{in1} = G_1 + jB_1 @ f_2 \quad (5-35)$$

where,

$$G_1 = R_{in1} / (R_{in1}^2 + X_{in1}^2) \quad (5-36)$$

$$B_1 = X_{in1} / (R_{in1}^2 + X_{in1}^2) \quad (5-37)$$

5.3.2 Design of Section B

Since the section B shown in Fig. 5.17 is the same as network of Fig. 5.3 and hence $Y_{in2} = M + jN$, where M and N are given by (5-10) and (5-11), respectively.

Now, one can proceed further using either of the following two options after invoking $\text{Re}(Y_{in2}) = \text{Re}(Y_{in1})$:

(a) Assume Z_o to be a free variable and solve for ρ

(b) Assume ρ to be a free variable and solve for Z_o

Option a) leads to a complicated fourth order equation in ρ while option b) leads to a simple quadratic equation in Z_o (of the form $ax^2 - b = 0$). Therefore following value for Z_o is obtained by choosing the option (b):

$$Z_o = \sqrt{4Z_s \frac{[(\rho-1)^2 / G_1] - Z_s (\rho+1)^2 \cos^2 \theta_2}{(\rho-1)^4 \sin^2 \theta_2 + 16\rho^2 \cos^4 \theta_2 / \sin^2 \theta_2 - 8\rho(\rho-1)^2 \cos^2 \theta_2}} \quad (5-38)$$

It is interesting to note that coupled line used in [47] has to achieve the required matching both for real as well as for imaginary parts of Y_{in1} with that of Y_{in2} . It is not easy to achieve this at two different frequencies especially with microstrip coupled line having unequal even/odd mode phase velocities. In the proposed network, only real part of Y_{in1} needs to be matched to the real part of Y_{in2} while their remaining imaginary parts are cancelled by a shunt stub marked as section C. Furthermore, this additional stub also enables the enhancement in the range of load that could be matched.

5.3.3 Design of Section C

This section is utilized to cancel the imaginary part of $Y_{in1} + Y_{in2}$, given by expressions (5-39) and (5-40), at two different frequencies.

$$j \text{Im}(Y_{in1} + Y_{in2}) = -j(B_1 - N) \quad @f_1 \quad (5-39)$$

$$= j(B_1 - N) \quad @f_2 \quad (5-40)$$

As mentioned earlier, section C could either be an open stub or a short stub. For open stub to work at two distinct frequencies, following set of equations must be satisfied:

$$-j \text{Im}(Y_{in1} + Y_{in2})|_{f_1} = j(1/Z_3) \tan \theta_3 \quad (5-41)$$

$$-j \text{Im}(Y_{in1} + Y_{in2})|_{f_2} = j(1/Z_3) \tan(r\theta_3) \quad (5-42)$$

The terms Z_3 and θ_3 can be determined by solving (5-41) and (5-42):

$$\theta_3 = \frac{(1+s)\pi}{1+r}, s \in I \quad (5-43)$$

$$Z_3 = \tan \theta_3 / (B_1 - N) \quad (5-44)$$

A short stub may be shown to work at two frequencies with design equations similar to those given by (5-43)-(5-44), except that the tangent in (5-44) needs to be replaced by cotangent.

It is important to note that $\{p, q, s\} \in I$ and can be chosen as any integer value but usually they are set to zero to get smaller footprints on the board. Furthermore, stubs may not be realizable in some situations and in those cases other techniques to realize complex impedances can be employed [22, 45].

5.3.4 Design Steps

Design steps can be summarized as follows:

- 1) The values of Z_1 and θ_1 are evaluated using (5-30) and (5-31) from the given values of $r, R_1, X_1, R_2,$ and X_2 .
- 2) Then R_{in1} and X_{in1} are determined using (5-32) and (5-33). Subsequently, the values of G_1 and B_1 are calculated from (5-36) and (5-37).
- 3) This step is for Y_{in2} . Here, θ_2 is found using (5-12) and a suitable value of ρ is assumed to compute Z_o from (5-38). Once the value of ρ and Z_o are known, the value for Z_e can be found using $Z_e = \rho Z_o$.
- 4) To design section C, (5-43)-(5-44) is used to get θ_3 and Z_3 after evaluating N from (5-11).

5.3.5 Simulation and Experimental Validation

TABLE 5-8 provides a comparison between the proposed design and the one reported in [47]. It can be noted that θ_c defined in [47] and θ_2 defined in this paper has the same meaning. It can also be seen that the value of Z_o for the chosen specifications and the mentioned frequencies is negative for the design reported in [47] while the proposed design gives realizable values for various parameters.

Table 5-8 Comparison with [47]

Ref.	Frequencies (GHz)	$Z_L(\Omega)$	Section A	Section B	Section C
[47]	$f_1=1.45$	$25-j20$	$Z_1=111.36\Omega$	$Z_o= -32.27\Omega$ $Z_e= 31.04\Omega$ $\theta_c= 64.29^\circ$	NA
This Work	$f_2=2.61$	$24.5+j12.5$	$\theta_1=1.42^\circ$	$\rho= 4, \theta_2= 64.29^\circ$ $Z_o= 29.16\Omega$ $Z_e= 116.64\Omega$	Open stub $Z_3=41.73\Omega$ $\theta_3=128.57^\circ$

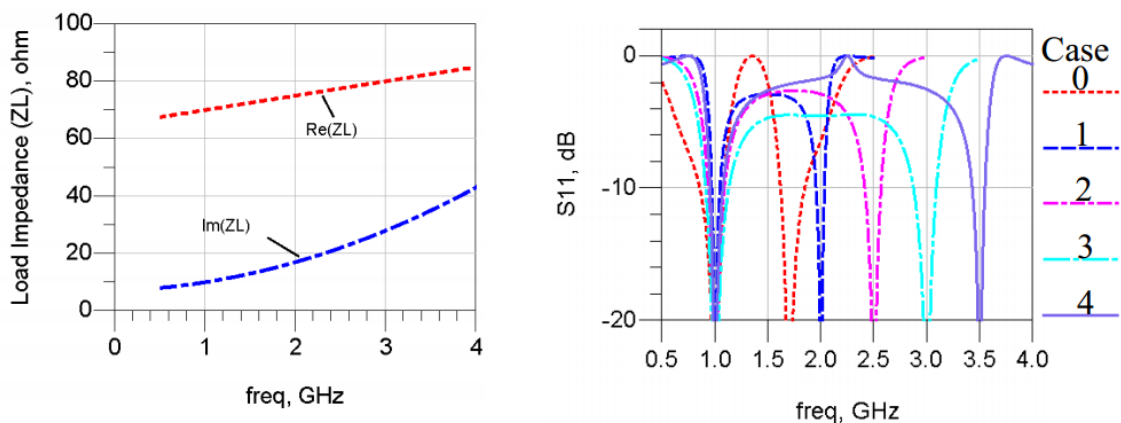


Figure 5.18 (a) Variation of real and imaginary parts of the frequency-dependent complex load (Z_L) (b) S_{11} in dB for different cases listed in TABLE 5-9.

To further study the proposed matching network, an arbitrarily chosen frequency dependent load is considered as depicted in Fig. 5.18(a). The first frequency f_1 is fixed at 1GHz and f_2 is varies to five different values as mentioned in TABLE 5-9. The load impedance along with the design parameters are also mentioned in TABLE 5-9 for five different cases. The simulated results for the designs listed in TABLE 5-9 are shown in Fig. 5.18(b), which validates the derived design equations.

Additionally, few more considered cases are given in TABLE 5-10. Here, the two frequencies are kept fixed for varying load impedances. The simulated results for these

Table 5-9 Design Parameters for Some Cases where f_1 is Fixed and f_2 is Varying.

Case	Frequencies (GHz)	Z_L (Ω)	Section A	Section B	Section C
0	$f_1=1$ $f_2=1.7$	$70 + j10$ $73.5 + j14.5$	$Z_1=85.08\Omega$ $\theta_1=49.29^\circ$	$\rho=4, \theta_2=66.67^\circ$ $Z_o=68.63\Omega$ $Z_e=274.52\Omega$	short stub $Z_3=136.25\Omega$ $\theta_3=133.34^\circ$
1	$f_1=1$ $f_2=2$	$70 + j10$ $75 + j17$	$Z_1=88.29\Omega$ $\theta_1=44.96^\circ$	$\rho=2.2, \theta_2=60^\circ$ $Z_o=51\Omega$ $Z_e=112.2\Omega$	open stub $Z_3=75.20\Omega$ $\theta_3=120^\circ$
2	$f_1=1$ $f_2=2.5$	$70 + j10$ $77.5 + j23$	$Z_1=95.55\Omega$ $\theta_1=39.72^\circ$	$\rho=2.75, \theta_2=51.43^\circ$ $Z_o=35.71\Omega$ $Z_e=98.20\Omega$	short stub $Z_3=39.85\Omega$ $\theta_3=51.43^\circ$
3	$f_1=1$ $f_2=3$	$70 + j10$ $80 + j28$	$Z_1=101.43\Omega$ $\theta_1=34.71^\circ$	$\rho=3.5, \theta_2=45^\circ$ $Z_o=34.44\Omega$ $Z_e=120.54\Omega$	short stub $Z_3=68.12\Omega$ $\theta_3=45^\circ$
4	$f_1=1$ $f_2=3.5$	$70 + j10$ $82.5 + j35$	$Z_1=109.42\Omega$ $\theta_1=31.09^\circ$	$\rho=3.8, \theta_2=40^\circ$ $Z_o=22.67\Omega$ $Z_e=86.15\Omega$	short stub $Z_3=107.60\Omega$ $\theta_3=120^\circ$

designs in TABLE 5-10 are shown in Fig. 5.19. All these examples demonstrate the validity and usefulness of the proposed matching network.

Finally, the proposed matching network implemented on an FR-4 substrate ($\epsilon_r=4.7$, thickness=1.5mm) with 1oz copper is shown in Fig. 5.20(a). It is important to note that the designed prototype is based on simplified equations discussed in [59] and therefore extensive simulation and optimization in Keysight ADS were carried out. The physical

Table 5-10 Design Parameters for Some Cases: f_1 and f_2 Fixed and the Load is Varying.

Cases	Frequencies (GHz)	$Z_L (\Omega)$	Section A	Section B	Section C
0	$f_1=1$ $f_2=2$	$30 - j27$ $47 + j60$	$Z_1=75.81\Omega$ $\theta_1=52.41^\circ$	$\rho=2.5,$ $\theta_2=60^\circ$ $Z_o=57.52\Omega$ $Z_e=143.8\Omega$	short stub $Z_3=88.67\Omega$ $\theta_3=60^\circ$
1		$80 + j15$ $90 + j24$	$Z_1=98.91\Omega$ $\theta_1=39.98^\circ$	$\rho=2.1,$ $\theta_2=60^\circ$ $Z_o=48.06\Omega$ $Z_e=100.93\Omega$	open stub $Z_3=69.46\Omega$ $\theta_3=120^\circ$
2		$50 + j60$ $20 - j30$	$Z_1=43.59\Omega$ $\theta_1=51.39^\circ$	$\rho=2.1,$ $\theta_2=60^\circ$ $Z_o=53.53\Omega$ $Z_e=112.4\Omega$	open stub $Z_3=49.94\Omega$ $\theta_3=120^\circ$

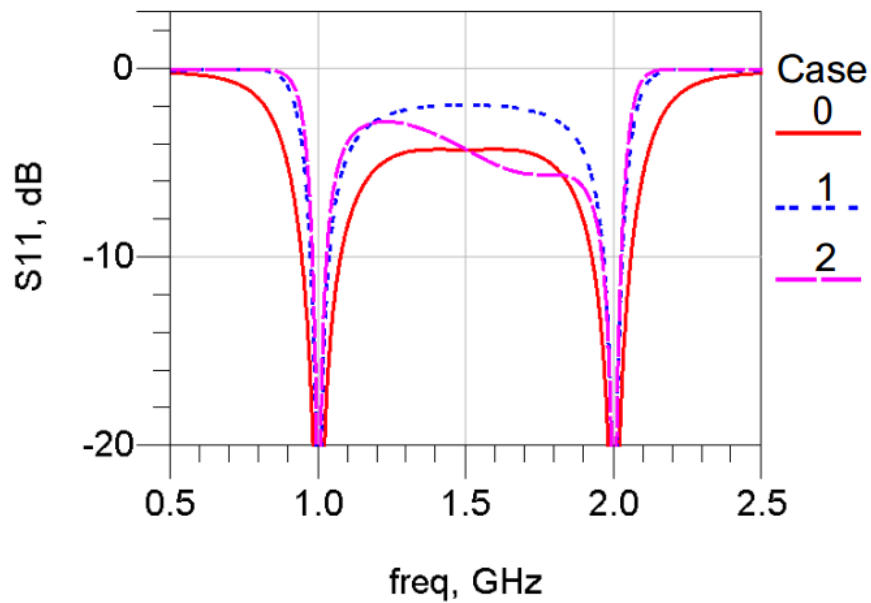


Figure 5.19 S11 in dB for different cases listed in TABLE 5-10.

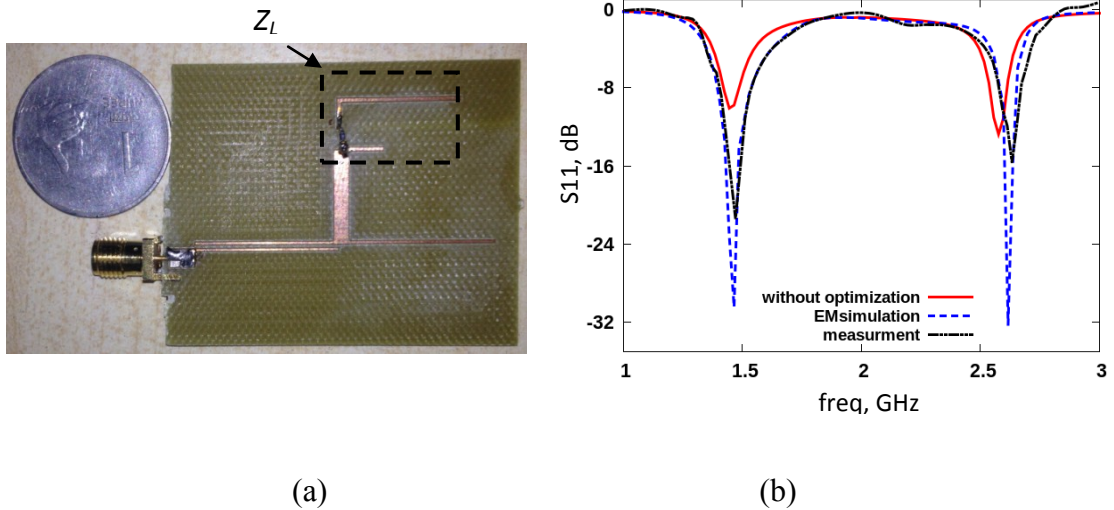


Figure 5.20 (a) Photo of prototype manufactured in our lab and (b) Plot of S_{11} in dB against frequency.

dimensions of the implemented matching network are (dimensions in mm) $l_1=13.91$, $l_2=21.66$, $l_3=21$, $w_1=2.25$, $w_2=0.64$, $w_3=0.76$ and $s_2=0.36$. To verify the operation of the designed impedance transformer, a frequency dependent complex load described in [47] is created. The load uses two open stubs and a Vishay-Dale CRCW series 10 Ω SMD resistor. The values of realized loads at the two frequencies of $f_1 = 1.45\text{GHz}$ and $f_2 = 2.61\text{GHz}$ are as follows: $Z_L(\Omega) = 8.049 - j26.868 @ f_1$ and $114.621 + j190.247 @ f_2$.

The simulated and measured results of the proposed matching network are shown in Fig. 5.20(b). The plot of S_{11} in dB shows dips around the two design frequencies with the measured return loss of approximately 20.5dB @ f_1 and 16dB @ f_2 . A slightly higher deviation is observed around f_2 perhaps due to the more pronounced impact of difference in even/odd-mode velocities. Nevertheless, it is evident from the plot that a good match can be obtained using the proposed circuit.

A comparison with some existing state-of-the-art is shown in TABLE 5-11. It may be noted that since there is no standard definition for a frequency dependent complex load; different reported designs have used different frequency dependency of load, thus it will not be fair to make comparison based on the bandwidth [56]. Moreover, the design reported in [47] also provides DC-blocking, but works for a very limited range of r .

Table 5-11 Comparison with Some Previous Designs.

Ref. No.	Type of Load	Experiment	DC Blocking	Design Equations	Lumped/Distributed
[34]	Real	No	No	Simple	Distributed
[35]	Real	No	No	Simple	Distributed
[38]	Complex (but same @ f_1 & f_2)	No	No	Complex ²	Distributed
[40]	FDCL ¹	No	No	Simple	Distributed
[41]	FDCL	Yes	No	Simple	Distributed
[42]	FDCL	Yes	No	Complex	Distributed
[43]	FDCL	No	No	Simple	Distributed
[22]	FDCL	Yes	No	Complex	Distributed
[44]	FDCL	Yes	No	Simple	Distributed
[50]	FDCL	No	No	Simple	Lumped
[48]	FDCL	Yes	No	Simple	Distributed
This Work	FDCL	Yes	Yes	Simple	Distributed

¹FDCL: frequency-dependent complex load

²Complex: requires computer to solve the design equations

5.4 Conclusion

This chapter of the thesis introduced a very interesting dual-frequency admittance/impedance property of coupled lines terminated into a real impedance. A rigorous mathematical analysis duly backed with graphical illustrations was used to demonstrate the existence of the property. Further, this property was used to propose novel dual-frequency impedance matching networks. The proposed L-type matching network aimed to cater real load impedances, whereas the T-type transformer was

proposed for frequency dependent complex load impedances. While DC blocking feature is inherent to these proposed matching networks due to the used of parallel coupled lines; this also enables the extension of the range of load that could be matched. A dual-band T-junction power divider has been proposed as an example application of the developed impedance transformer. The simulation and experimental results match well thereby validates the design presented in this chapter.

Chapter 6

Admittance Property of Two-Sections Transmission line

Two sections of cascaded transmission lines have been used in many dual-frequency impedance matching networks and their details were also outlined in Chapter 2. For example, the two sections based Monzon transformer that matches a real load to a real source impedance has become a *de facto* for dual-frequency applications. A single section when terminated into a real impedance shows dual-frequency admittance property as demonstrated in Chapter 3. A natural question then arises if the same property would be valid for two sections of transmission line (TSTL) as well? This is the subject of this chapter. Moreover, the current state-of-the-art dual-frequency impedance matching networks are useful, but have one or several of the following constraints:

- 1) complicated design equations/processing steps,
- 2) very limited frequency ratio, and
- 3) limited range of load impedances that can be matched.

Therefore, in this chapter, the concerns mentioned above are addressed by utilizing a novel characteristic of TSTL [94-95]. In addition, as an immediate application, design of a dual-frequency branch line coupler with enhanced band-ratio is also demonstrated [96].

6.1 Dual-Frequency Admittance Property of TSTL Terminated into a Real Impedance

A two section transmission line (TSTL) terminated into a real impedance Z_0 is shown in Fig. 6.1 [94-95]. Let f_1 and f_2 be the two distinct frequencies of interest for du-

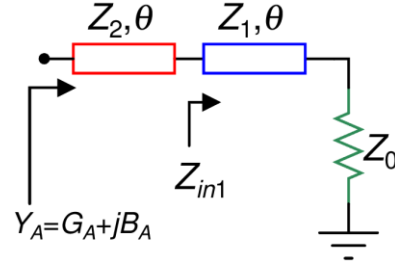


Figure 6.1 A TSTL terminated into a real impedance Z_0 [94-95].

al-frequency applications. Here, Z_1 and Z_2 are the characteristic impedances of the two cascaded transmission line (TL) sections and each of them has an electrical length of θ . It is important to note that each electrical length is defined at the first frequency f_1 unless mentioned otherwise. In Fig. 6.1, the term Y_A is the input admittance looking into the terminated TSTL.

The dual-frequency admittance property of the network of Fig. 6.1 can be stated as follows:

"If the electrical length θ of the TSTL terminated into a real impedance is selected as given in (6-1) then the input admittances are complex conjugate of each other at the two frequencies, i.e., $Y_A|_{f_1} = (Y_A|_{f_2})^$. It means, if $Y_A|_{f_1} = |G_A| + j|B_A|$ then $Y_A|_{f_2} = |G_A| - j|B_A|$ and vice-versa."*

$$\theta = \frac{(1+k)\pi}{1+r}, k \in \text{Integer}, r = f_2/f_1 \quad (6-1)$$

where, G_A and B_A are the real and imaginary parts of Y_A and, r is the frequency-ratio or band-ratio.

This property of the TSTL can be proved as follows. In Fig. 6.1, the expression for Y_A can be expressed as:

$$Y_A = 1 / \left(Z_2 \frac{Z_{in1} + jZ_2 \tan \theta}{Z_2 + jZ_{in1} \tan \theta} \right) \quad (6-2)$$

where, Z_{in1} is the impedance looking into the transmission line section with characteristic impedance Z_1 , and is given by:

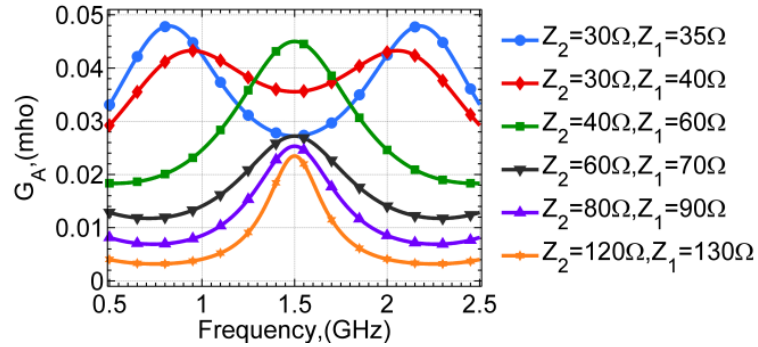
$$Z_{in1} = Z_1 \frac{Z_0 + jZ_1 \tan \theta}{Z_1 + jZ_0 \tan \theta} \quad (6-3)$$

Simplification of (6-2) and (6-3) and separation of the real and imaginary parts of admittance Y_A results into following expressions:

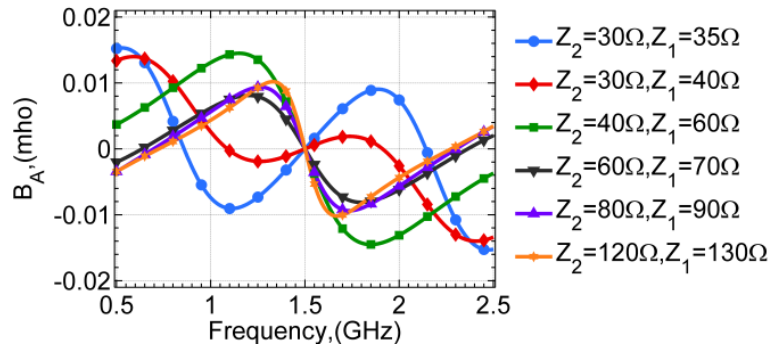
$$G_A = \frac{Z_0 Z_1^2 (1 + \tan^2 \theta)^2}{Z_0^2 (Z_1 - Z_2 \tan^2 \theta)^2 + Z_1^2 (Z_1 + Z_2)^2 \tan^2 \theta} \quad (6-4)$$

$$B_A = \frac{Z_0^2 (Z_1 - Z_2 \tan^2 \theta) - Z_1^2 (Z_2 - Z_1 \tan^2 \theta)}{Z_0^2 (Z_1 - Z_2 \tan^2 \theta)^2 + Z_1^2 (Z_1 + Z_2)^2 \tan^2 \theta} \left(1 + \frac{Z_1}{Z_2}\right) \tan \theta \quad (6-5)$$

It is apparent that only even powers of $\tan \theta$ exist in (6-4) whereas both odd as well as even powers of the same are present in (6-5). It implies that if θ is replaced by $k\pi - \theta$, then the real part G_A will remain the same whereas the imaginary part B_A will change its sign. Considering that electrical length is proportional to the frequency, assigning the lines an electrical length of θ at f_1 and $k\pi - \theta$ at f_2 results into (6-6a,b):



(a)



(b)

Figure 6.2 Plot of admittance, Y_A , for a fixed $r = 2$ and different values of $Z_2 - Z_1$ pair

(a) the real part i.e. G_A and (b) the imaginary part, i.e. B_A .

$$\theta = mf_1 \quad (6-6a)$$

$$k\pi - \theta = mf_2 \quad (6-6b)$$

where, m is some constant with unit of rad/Hz.

Equations (6-6a) and (6-6b) are solved simultaneously to obtain the value of electrical length θ that comes out to be exactly as given in (6-1). Thus, it is concluded that the input admittance Y_A of a TSTL terminated into a real impedance are complex conjugate of each other at two arbitrarily chosen frequencies. Since, impedance is inverse of admittance, the same property also holds good for input impedance.

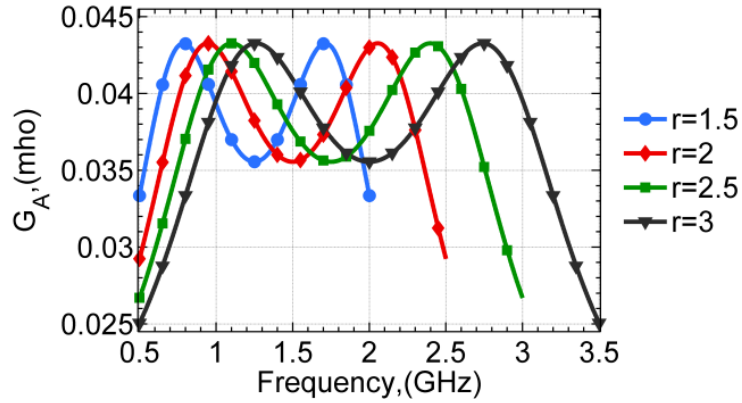
Plots of G_A and B_A as obtained from (6-4) and (6-5) are shown in Fig. 6.2. The plots are for the different pairs of Z_2 and Z_1 but for a fixed value of $r = 2$ (i.e., $\theta=60^\circ$ at $f_1=1\text{GHz}$ from (6-1)). It is clear from these plots that the values of real part (G_A) remains the same at two specified frequencies (at $f_1=1\text{GHz}$ and $f_2=2\text{GHz}$) whereas the imaginary part (B_A) gets flipped for each pair of Z_2 and Z_1 .

Similarly, keeping Z_2 and Z_1 fixed at some values, say 30Ω and 40Ω respectively, and varying r from 1.5 to 3 results into plots shown in Fig. 6.3. To understand this, consider the case of $r = 1.5$ and the frequencies of $f_1=1\text{GHz}$ and $f_2=1.5\text{GHz}$. It is evident that the real-part, G_A , remains the same whereas the imaginary part, B_A , gets flipped. Similar trends are observed for other values of r and for other frequencies of interest as well.

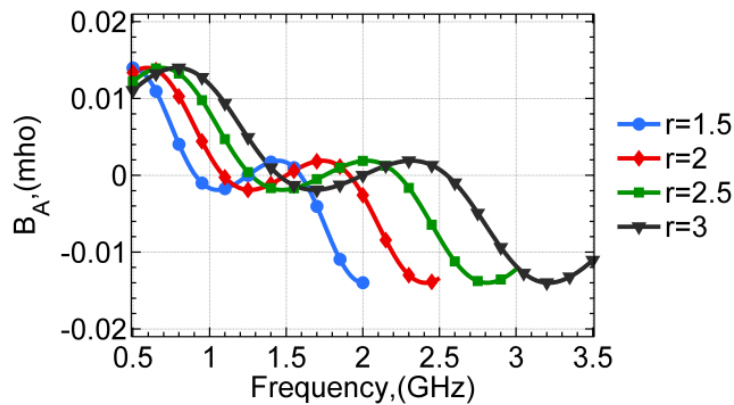
Furthermore, the plots in Figs. 6.2 and 6.3 can be validated by taking appropriate limits. For example, to check whether the values of G_A in Fig. 6.2 make sense or not, one can notice that the value of θ , from (6-1), is $\pi/2$ (assuming $k = 1$) at the center frequency of $f_c=(f_1+f_2)/2$. Therefore, using (6-4), the following simple expression for G_A at f_c can be obtained:

$$G_A|_{f \rightarrow f_c} = G_A|_{\theta \rightarrow \pi/2} = \frac{Z_1^2}{Z_0 Z_2^2} \quad (6-7)$$

As an example, substitution of $Z_0=50\Omega$, $Z_2=40\Omega$, and $Z_1=60\Omega$ in (6-7) yields $G_A=0.045\Omega^{-1}$. It is the same value of G_A obtained from Fig. 6.2(a) as well. Therefore,



(a)



(b)

Figure 6.3 Plot of admittance, Y_A , for different values of r and a fixed value of Z_2 and Z_1 pair ($=30\Omega$ and 40Ω , respectively) (a) the real part i.e. G_A and (b) the imaginary part, i.e. B_A .

the plots in Figs. 6.2 and 6.3 clearly demonstrate the existence of the dual-frequency property of TSTL terminated into real impedance.

6.2 The Monzon Two-sections Transformer

The Monzon two-section transformer, shown earlier in Fig. 2.1 is widely used for matching real load and source impedances at two arbitrary frequencies [34]. It can be shown that Monzon transformer is a special case of the dual-frequency admittance property of TSTL discussed in the previous section. To that end, if the network of Fig. 6.1 is able to match the source impedance Z_0 to the real load Z_L then (6-4)-(6-5)

must lead us to the solutions achieved by Monzon. For this to happen, the following conditions must be satisfied:

$$G_A = 1/Z_L \quad (6-8)$$

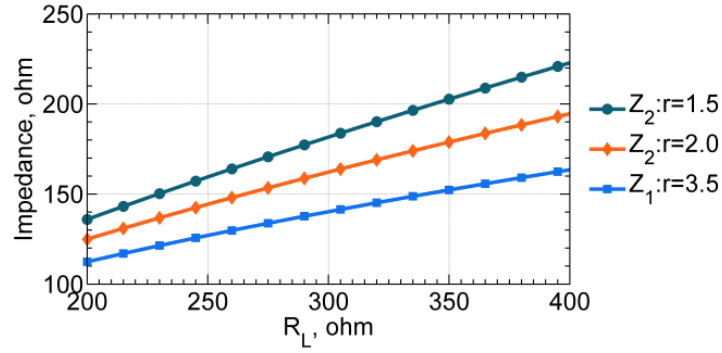
$$B_A = 0 \quad (6-9)$$

Solving (6-8)-(6-9) in conjunction with (6-4)-(6-5) provides the two design equations, A(3) and A(4), listed in the appendix of this chapter. In these expressions, selection of θ as per (6-1) guarantees matching at any two chosen frequencies. These equations, A(3) and A(4), are exactly the same as reported by Monzon [34].

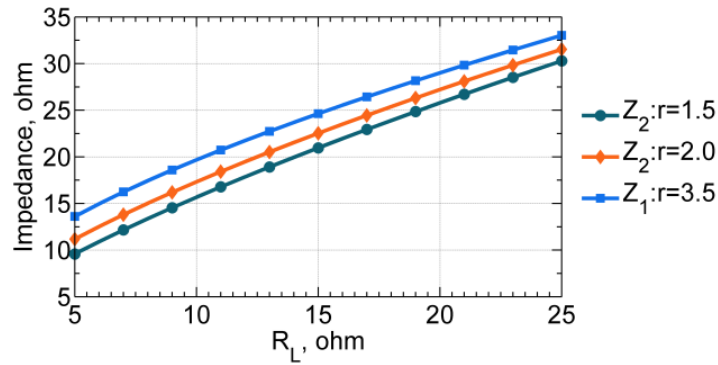
6.3 Limitation of Previous Designs

From A(3) and A(4), it can be deduced that since there is no independent variable in Monzon transformer, the range of load that it can match is limited. To clarify, line impedance for the Monzon transformer for $r = 1.5, 2, \text{ and } 3.5$ are plotted against the load impedance as shown in Fig. 6.4. It is evident from Fig. 6.4 that the required value of Z_1 and/or Z_2 becomes physically unrealizable as R_L/Z_0 (transformation-ratio) increases or decreases significantly. It is assumed here that the characteristic impedance of microstrip lines that can be fabricated lies between 20Ω to 150Ω . Once again, Monzon transformer's usage is also greatly limited as it does not possess any free variable and it is similar to the limitations of the conventional L- and T-type transformers [30], [43].

In a nutshell, incorporating the TSTL in the proposed L- and T-type networks creates free variables and that ultimately results into the enhanced performance. It must be noted that addition of transmission line sections in any random fashion may not result in dual-frequency characteristics. The next section provides the analytical design equations and strategies for the proposed impedance transformers that must be used to achieve dual-frequency characteristics.



(a)



(b)

Figure 6.4 The variation of line impedances with the load impedance in Monzon transformer for $r = 1.5, 2$ and 3.5 for (a) $R_L > Z_0$ and (b) $R_L < Z_0$.

6.4 Proposed Impedance Transformers Employing TSTL

Two types of the dual-frequency impedance matching networks are presented in this section. The first one is an L-type impedance transformer for real source and load impedances whereas the second one is a T-type impedance transformer for matching a real source impedance to a frequency-dependent complex impedance. The proposed transformers are the modification of the conventional single-/dual-frequency L- and T-type networks by incorporation of the TSTL and this leads to huge performance enhancement in terms of the loads that can be matched using them.

6.4.1 Proposed Dual-Frequency L-type Networks Employing TSTL

The proposed L-type impedance transformer has two configurations. The configuration-I, shown in Fig.6.5 (a), comprises of the TSTL and a stub at the load side. In the case of configuration-II, the stub is at the source side as shown in Fig. 6.5(b).

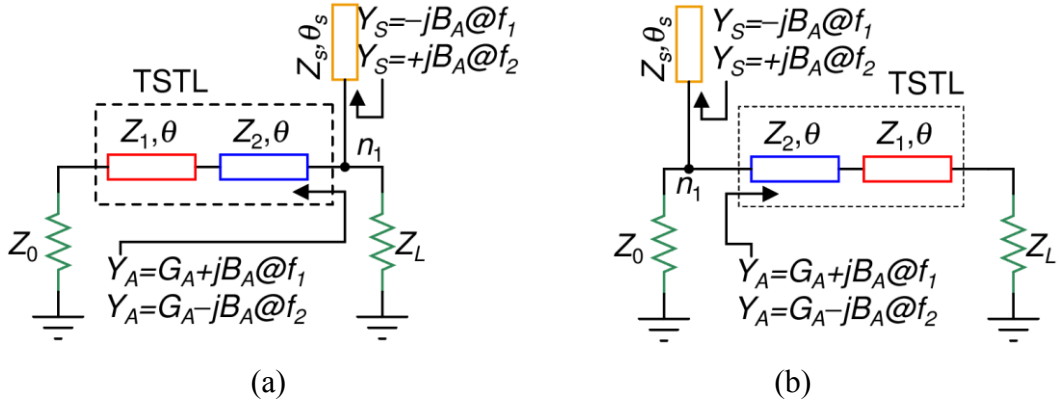


Figure 6.5 Proposed dual-frequency L-type impedance transformers (a) configuration-I: Stub on the load side (b) configuration-II: Stub on the source side.

In essence, now the single section TL[30]/coupled-line [60] of the previously reported L-type dual-frequency impedance transformers are replaced by a TSTL. As per Fig. 6.5(a), Y_A is the admittance of TSTL terminated into the real source impedance Z_0 . The dual-frequency susceptance, Y_S , which can be realized using either a short-circuited or an open-circuited stub or a combination thereof [60], cancels the imaginary part of Y_A at node n_1 . Then, the following condition must be satisfied for matching:

$$G_A = 1/Z_L \equiv Y_L \quad (6-10)$$

Now, (6-10) and (6-4) can be solved to obtain a quadratic equation in Z_2 whose solution is:

$$Z_2 = \frac{-b \pm \sqrt{b^2 - 4ac}}{2a} \quad (6-11)$$

where,

$$a = Y_L Z_0^2 \tan^4 \theta + Y_L Z_1^2 \tan^2 \theta \quad (6-12)$$

$$b = 2Y_L Z_1^3 \tan^2 \theta - 2Y_L Z_0^2 Z_1 \tan^2 \theta \quad (6-13)$$

$$c = -Z_0 Z_1^2 (1 + \tan^2 \theta)^2 + Y_L Z_0^2 Z_1^2 + Y_L Z_1^4 \tan^2 \theta \quad (6-14)$$

It is important to note that a non-positive value of Z_2 in (6-11) has to be discarded. In these expressions, Z_1 is a free variable that can be selected independently to get a physically realizable transformer. Once the value of Z_1 is selected and that of Z_2 and θ are determined using (6-11)-(6-14) and (6-1), the value of B_A is computed using (6-5).

This value of B_A is subsequently used to design the dual-frequency susceptance, Y_S , as follows:

If an open stub is to be used as a dual-frequency susceptance, then the following equations must be satisfied:

$$-jB_A = j \tan \theta_s / Z_s \quad (6-15)$$

$$+jB_A = j \tan r\theta_s / Z_s \quad (6-16)$$

Solving (6-15) and (6-16) simultaneously yields the following expressions of θ_s and Z_s :

$$\theta_s = \frac{(1+m)\pi}{1+r}, \quad m \in \text{Integer}, \quad r = f_2/f_1 \quad (6-17)$$

$$Z_s = -\tan \theta_s / B_A \quad (6-18)$$

where, the integer m is usually chosen as 1 or 2 to achieve compact size and a positive value of Z_s . More details of the dual-frequency stub design can be referred from chapter 5. It is also important to note that the combination of open-short stub is not discussed in [30] and [43], but is more useful in some situations as demonstrated in the next chapter.

For the configuration-II in Fig. 6.5(b), Y_A is the admittance of TSTL terminated into the real load impedance Z_L . Following design equations can be obtained for this configuration:

$$G_A = 1/Z_0 \equiv Y_0 \quad (6-19)$$

Equations (6-19) and (6-4) can be solved to obtain a quadratic equation in Z_2 whose solution is:

$$Z_2 = \frac{-b \pm \sqrt{b^2 - 4ac}}{2a} \quad (6-20)$$

where,

$$a = Y_0 Z_L^2 \tan^4 \theta + Y_0 Z_1^2 \tan^2 \theta \quad (6-21)$$

$$b = 2Y_0 Z_1^3 \tan^2 \theta - 2Y_0 Z_L^2 Z_1 \tan^2 \theta \quad (6-22)$$

$$c = -Z_L Z_1^2 (1 + \tan^2 \theta)^2 + Y_0 Z_L^2 Z_1^2 + Y_0 Z_1^4 \tan^2 \theta \quad (6-23)$$

Once again, Z_1 is a free variable and can be selected by designer within the realizable limits. Subsequently, Z_2 and θ can be determined and this leads to the value of B_A which can then be used to design the dual-frequency susceptance, Y_S , as was shown for the configuration-I.

6.4.2 Proposed Dual-Frequency T-type Network Employing TSTL

The conventional T-network for frequency dependent complex load [43], [59] is modified by incorporating a TSTL as shown in Fig. 6.6. The overall idea is to equate G_A to G_C and cancel the leftover imaginary part at node n_1 with the help of the stub having admittance Y_S . All these steps are depicted in Fig. 6.6 as well.

In this proposed scheme, the transmission line Z_C / θ_C transforms the frequency-dependent complex load, $Z_L = R_1 + jX_1 @f_1$ and $Z_L = R_2 + jX_2 @f_2$, into complex conjugate admittances, $Y_C = G_C - jB_C @f_1$ and $Y_C = G_C + jB_C @f_2$, at the T- junction point n_1 . To accomplish this, the design equations (6-24)-(6-25) must be followed [40], [59].

$$Z_C = \sqrt{R_1 R_2 + X_1 X_2 + \frac{X_1 + X_2}{R_2 - R_1} (R_1 X_2 - R_2 X_1)} \quad (6-24)$$

$$\theta_C = \frac{p\pi + \arctan\left(\frac{Z_C(R_1 - R_2)}{R_1 X_2 - R_2 X_1}\right)}{1+r}, \quad p \in I, \quad r = f_2 / f_1 \geq 1 \quad (6-25)$$

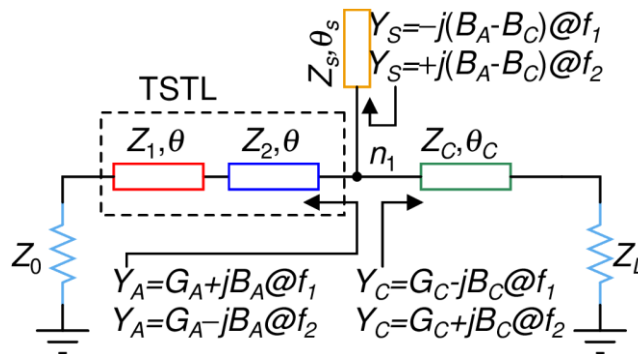


Figure 6.6 Proposed dual-frequency T-type matching network for frequency-dependent complex load, $Z_L=R_1+jX_1$ @ f_1 and $Z_L=R_2+jX_2$ @ f_2 .

Then, the expressions of G_C and B_C are as follows:

$$G_C = R_{in1} / (R_{in1}^2 + X_{in1}^2) \quad (6-26)$$

$$B_C = X_{in1} / (R_{in1}^2 + X_{in1}^2) \quad (6-27)$$

$$R_{in1} = \frac{R_1 Z_C^2 [1 + \tan^2 \theta_C]}{Z_C^2 - 2Z_C X_1 \tan \theta_C + (R_1^2 + X_1^2) \tan^2 \theta_C} \quad (6-28)$$

$$X_{in1} = \frac{(Z_C^2 - R_1^2 - X_1^2) Z_C \tan \theta_C + Z_C X_1 [1 - \tan^2 \theta_C]}{Z_C^2 - 2Z_C X_1 \tan \theta_C + (R_1^2 + X_1^2) \tan^2 \theta_C} \quad (6-29)$$

Now the TSTL for the proposed T-network is designed in such a manner that at node n_1 the real part of Y_A equals that of Y_C i.e.

$$G_A = G_C \quad (6-30)$$

Equations (6-30) and (6-4) can be solved simultaneously to achieve design equation for Z_2 which is similar to (6-11), with the only difference being replacement of Y_L with G_C in (6-12)-(6-14). Then the leftover net imaginary part, $(B_A - B_C)$ @ f_1 and $-(B_A - B_C)$ @ f_2 , at node n_1 is cancelled by the dual-frequency stub such that $Y_S = -j(B_A - B_C)$ @ f_1 and $Y_S = +j(B_A - B_C)$ @ f_2 . Again, the design of dual-frequency stub proceeds as (6-15)-(6-18) and their details can be found in the previous chapter.

At this point, it is important to be able to realize that the proposed T-network shown in Fig. 6.6 is completely different from the earlier reported T-network [45]. Working principles of these two impedance transformers are entirely distinct. In terms of the notations used in Fig.6.6, [45] proposes to cancel B_C using Y_S , and to match the remaining real part G_C to Z_0 using the two section Monzon's transformer. In contrast, the proposed scheme envisages to equate G_A and G_C and cancel the leftover imaginary part with the help of the stub possessing admittance Y_S . The admittance Y_A in the proposed T-network is a complex quantity, owing to the presence of TSTL, whereas it will be purely real if defined in [45] owing to the presence of Monzon's transformer.

Moreover, it is also possible to achieve a '*selectable transmission zero*' in the proposed T-network by incorporating the type of stubs reported in [45].

6.5 Generic Nature of the Proposed Transformers

It is apparent from Fig. 6.5 that setting $\theta_s = 0$ would reduce the proposed networks to a special condition that can be considered as two-section Monzon transformer. Similarly, setting $Z_1=Z_2$ and replacing θ with $\theta/2$ in Fig. 6.5 reduce the proposed networks to a special condition that can be considered as conventional L-networks [30]. Lastly, setting $Z_1=Z_2$ and replacing θ with $\theta/2$ in the TSTL section of Fig. 6.6 reduces the proposed network to a special condition that can be considered as conventional T-network [43]. Therefore, the proposed scheme is more generic and can be used for the range of load impedances which is not possible to handle using Monzon transformer [34] or the conventional L-/T-networks [30], [43], in addition to the range already covered by the original Monzon and L-/T-networks. The key to this performance improvement lies in the presence of a free variable Z_1 that provides the proposed networks the ability to provide dual-frequency impedance matching over a much broader range of load impedances.

6.6 Design Steps for the Proposed Transformers

A flowchart shown in Fig. 6.7 illustrates the systematic design-steps involved in the design of the proposed dual-frequency L-network given in Fig. 6.5(a). It has been assumed that the physically realizable TL segment possess characteristic impedance between 20Ω to 150Ω . Since Z_1 is a free variable, the idea is to select any value of Z_1 in the realizable range and then tune it until calculations lead to realizable values for both Z_2 as well as Z_s .

Moreover, since, the other proposed designs in this chapter have solutions similar to that given by (6-11)-(6-14), therefore, these design steps are directly applicable to all those designs as well. For instance, while designing TSTL for the proposed dual-frequency T-network, Z_2 needs to be calculated using (6-11) but one needs to substitute G_C in place of Y_L in (6-12) - (6-14). The rest of the steps remain the same.

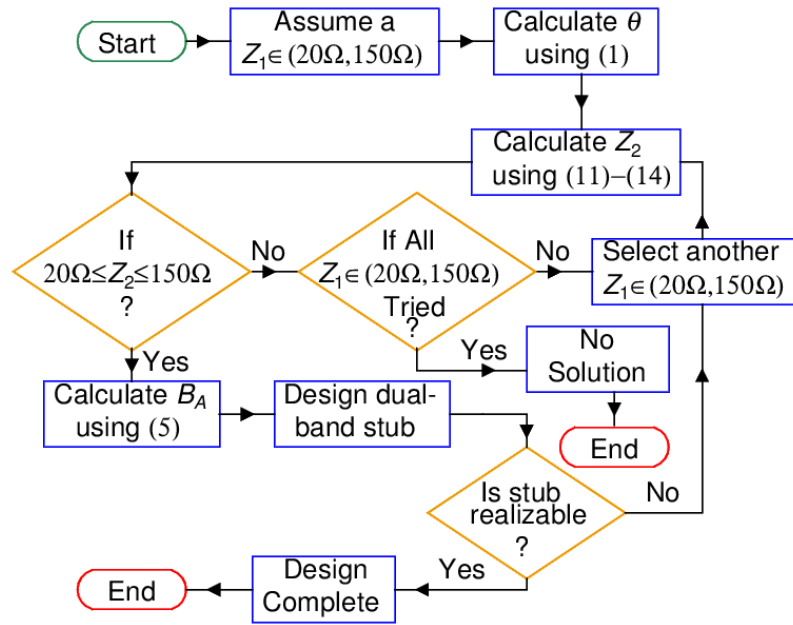
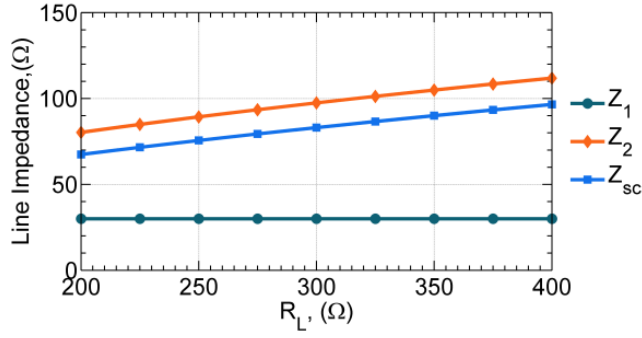


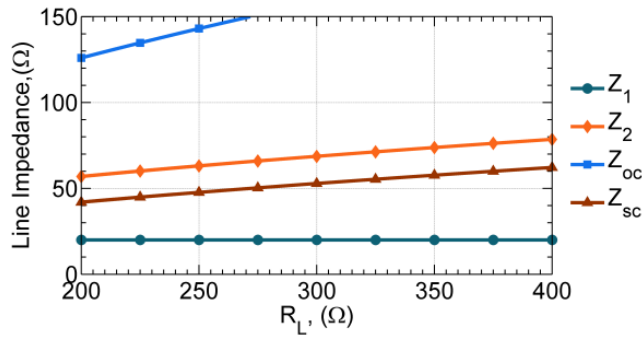
Figure 6.7 Design steps of dual-frequency L-type network of Fig. 6.5(a). Equation (1) mentioned in the flowchart is refers to the equation (6.1) in this chapter, and so on.

6.7 Simulation and Discussion

To begin with, the performance of the proposed L-type transformers is compared with that of the Monzon transformer. It should be noted that the L-type transformer reported in [30] possess limited frequency-/transformation-ratio compared to the Monzon transformer [34]. For the evaluation of the proposed configuration-I, Fig. 6.8 depicts the required line impedance plots as R_L is swept from 200Ω - 400Ω when $r=2$. Here, Fig. 6.8(a) considers the case for $Z_1=30\Omega$ whereas Fig. 6.8(b) presents the case for $Z_1=20\Omega$. Since, Z_1 is free variable; other possible plots may also exist. It is important to note that open stub can also be used for lower values of R_L for the case when $Z_1=20\Omega$. It is evident from these plots that a very high transformation-ratio can be achieved. The subsequent Fig. 6.9 depicts the required line impedance in configuration-II for different values of R_L for the case when $R_L < Z_0$ and $r = 2$. Please note that, in general, Z_1 need not be a fixed value for a given value of r . Instead it can be changed for different value of R_L as can be seen in this example. Similarly, Fig. 6.10 depicts this variation for $r = 1.5$ and $r = 3.5$. If the plots in Figs. 6.8-6.10 are compared with the Monzon transformer's results shown earlier in Fig. 6.4 then, apparently, the proposed transformer offers a more fabrication friendly option.



(a)



(b)

Figure 6.8 The variation of line impedances with the load impedance for the proposed configuration-I for $r=2$, $R_L > Z_0$ (a) $Z_1=30\Omega$ (fixed) and (b) $Z_1=20\Omega$ (fixed).

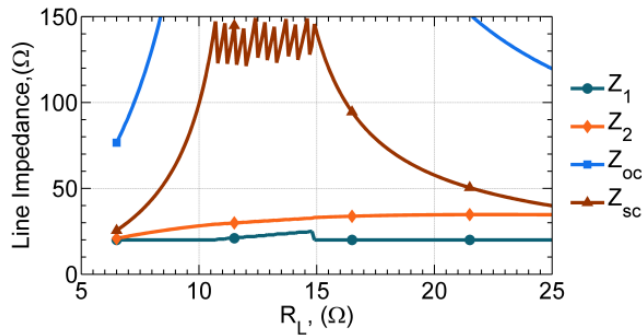


Figure 6.9 The variation of line impedances with the load impedance for the proposed configuration-II for $r=2$, $R_L < Z_0$.

Two design examples with extreme load impedances, R_L , are considered. For this purpose, $R_L=400\Omega$ on the higher side and then another $R_L=6.5\Omega$ on the lower side are assumed to be matched to a source impedance of $Z_0 = 50\Omega$ for $r = 2$. This means that there is a need to realize a 1:8 and 7.7:1 transformers, respectively. Using the proposed scheme, one possible set of design parameters, while considering configuration, for

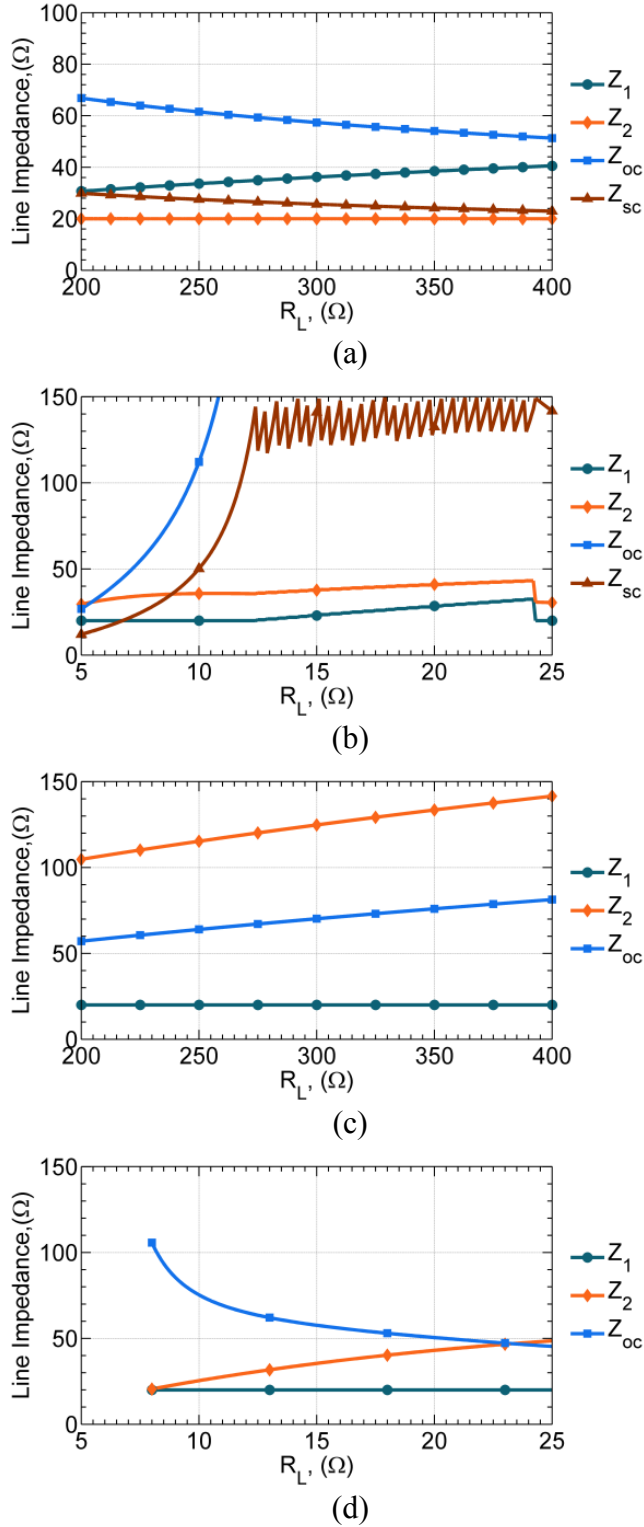


Figure 6.10 The variation of line impedances with the load impedance for the proposed L-type networks for $r = 1.5$ and 3.5 (a) Configuration-I, $R_L > Z_0$, Z_1 : varying, $r = 1.5$ (b) Configuration-II, $R_L < Z_0$, Z_1 : varying, $r = 1.5$ (c) Configuration-I, $R_L > Z_0$, Z_1 : Fixed (20Ω), $r = 3.5$ (d) Configuration-II, $R_L < Z_0$, Z_1 : Fixed (20Ω), $r = 3.5$.

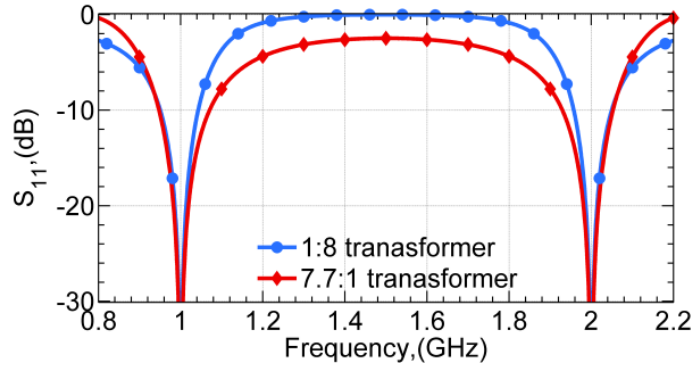


Figure 6.11 Return loss for examples using the proposed L-networks, which cannot be designed using either Monzon or conventional L-networks: Return loss for the 1:8 transformer and 7.7:1 transformer.

$R_L=400\Omega$ comes out to be $Z_1=35\Omega$, $Z_2=126.4\Omega$, $Z_5=115.4\Omega$ (short-circuited stub), $\theta=60^\circ$, and $\theta_5=120^\circ$. Similarly, for $R_L=6.5\Omega$ the parameters are $Z_1=20\Omega$, $Z_2=20.86\Omega$, $Z_5=76.63\Omega$ (open-circuited stub), $\theta=60^\circ$, and $\theta_5=120^\circ$ while considering configuration-II. It is apparent that the proposed designs can be physically realized whereas the conventional Monzon transformer cannot, as can be inferred from Fig. 6.4. The simulated return losses shown in Fig. 6.11 support this argument.

Comparison of the proposed L-networks with the Monzon transformer is also summarized in TABLE 6-1 for different frequency-ratios. Again, it is apparent that compared with the Monzon transformer the proposed transformer clearly offers a better design for $R_L>Z_0$ as well as for $R_L<Z_0$.

Now for the sake of completeness, the proposed L-type networks are also compared with the conventional L-type transformer reported in [30]. Few examples are worked out in TABLE 6-2 where scheme of [30] is compared with the proposed L-type network incorporating TSTL. It is apparent that the design [30] is highly limited as the

Table 6-1 Comparison of Transformation- Ratio with Previous Design

r	This Work		[34]	
	Z_0/R_L	Z_0/R_L	Z_0/R_L	Z_0/R_L
1.5	>1:30	11.11:1	1:4.6	3.57:1
2.0	1:30	7.7:1	1:5.2	3.85:1
3.5	1:9	5.9:1	1:6.8	5:1

Table 6-2 Design Parameters for Proposed L-type Impedance Network as Compared with the Design Parameters of [30]

Case	f_1 (GHz)	f_2 (GHz)	R_L (Ω)	Proposed L-type Configuration-I		Conventional L-type Designs [30]			
				$Z_1/Z_2/\theta$	Z_S / θ_S	Fig.1a		Fig.1b	
1	1	2	40	$Z_1=65 \Omega$ $Z_2=36.40 \Omega$ $\theta=60^\circ$	Open stub $Z_S=86.60 \Omega$ $\theta_S=120^\circ$	$Z_1=46.15\Omega, \theta_0=60^\circ$		$Z_2=42.82\Omega, \theta_0=60^\circ$	
						Open stub $Z_{S1}=692.22\Omega$ $\theta_{S1}=60^\circ$	Short stub $Z_{S1}=230.75\Omega$ $\theta_{S1}=120^\circ$	Open stub $Z_{S2}=512.24\Omega$ $\theta_{S2}=120^\circ$	Short stub $Z_{S2}=171.26\Omega$ $\theta_{S2}=60^\circ$
2	1	2	60	$Z_1=75 \Omega$ $Z_2=48.54\Omega$ $\theta=60^\circ$	Open stub $Z_S=130.22 \Omega$ $\theta_S=120^\circ$	$Z_1=52.9\Omega, \theta_0=60^\circ$		$Z_2=56.27\Omega, \theta_0=60^\circ$	
						Open stub $Z_{S1}=793.7\Omega$ $\theta_{S1}=120^\circ$	Short stub $Z_{S1}=264.5\Omega$ $\theta_{S1}=60^\circ$	Open stub $Z_{S2}=1012.9\Omega$ $\theta_{S2}=60^\circ$	Short stub $Z_{S2}=337.64\Omega$ $\theta_{S2}=120^\circ$
3	1	3	100	$Z_1=45 \Omega$ $Z_2=88.08\Omega$ $\theta=45^\circ$	Open stub $Z_S=136.98 \Omega$ $\theta_S=45^\circ$	$Z_1=0, \theta_0=60^\circ$		$Z_2=86.6\Omega, \theta_0=45^\circ$	
						N.A	N.A	Open stub $Z_{S2}=173.2\Omega$ $\theta_{S2}=60^\circ$	N.A

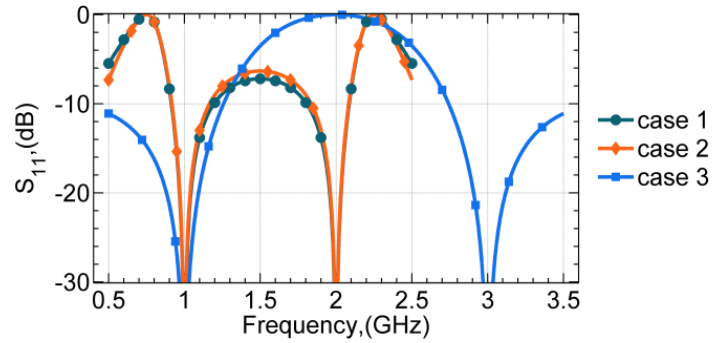


Figure 6.12 Simulated return-loss for the proposed design cases given in TABLE 6-2.

required line impedances cannot be realized physically whereas the same cases can be handled easily by the proposed scheme. The corresponding simulated results shown in Fig. 6.12 clearly support this argument.

TABLES 6-3 and 6-4 provide some design examples for the proposed L-type impedance transformer configurations-I and II respectively. In TABLE 6-3, f_1 and R_L are fixed whereas f_2 is varied to some discrete values. In contrast, TABLE 6-4 shows the cases where both the frequencies are varied and the load is fixed. It may be noted that for the dual-frequency stub design, wherever possible, the open-circuit stub has been preferred to avoid via to the ground plane. The corresponding simulated return-loss plots are shown in Figs. 6.13 and 6.14 and they show the proper working of the proposed networks.

Table 6-3 Design Parameters for Proposed L-type Network Configuration-I, $f_1=1\text{GHz}$ (fixed), and f_2 Varying, $R_L=100\Omega$

Case	f_2 (GHz)	$Z_1/Z_2/\theta$	Z_S / θ_S
1	2	$Z_1=105 \Omega$ $Z_2=57.26 \Omega$ $\theta=60^\circ$	Open stub $Z_S=116.24 \Omega$ $\theta_S=120^\circ$
2	2.5	$Z_1=35 \Omega$ $Z_2=75.03 \Omega$ $\theta=51.43^\circ$	Open stub $Z_S=119.42 \Omega$ $\theta_S=51.43^\circ$
3	3	$Z_1=45 \Omega$ $Z_2=88.076 \Omega$ $\theta=45^\circ$	Open stub $Z_S=136.98 \Omega$ $\theta_S=45^\circ$
4	3.5	$Z_1=50 \Omega$ $Z_2=92.47 \Omega$ $\theta=40^\circ$	Open stub $Z_S=131.11 \Omega$ $\theta_S=40^\circ$

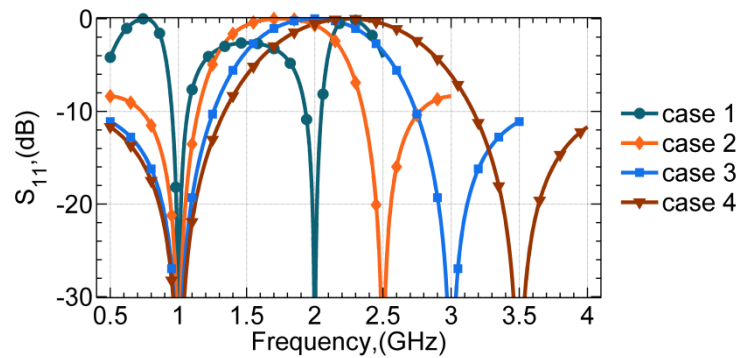


Figure 6.13 Simulated return loss corresponding to TABLE 6-3.

Table 6-4 Design Parameters for Proposed L-type

Case	f_1 (GHz)	f_2 (GHz)	$Z_1/Z_2/\theta$	Z_S / θ_S
1	0.9	2.4	$Z_1=72.24 \Omega$ $Z_2=55 \Omega$ $\theta=49.01^\circ$	Open stub $Z_S=114.39 \Omega$ $\theta_S=49.01^\circ$
2	1.2	3.5	$Z_1=45 \Omega$ $Z_2=74.82 \Omega$ $\theta=45.96^\circ$	Open stub $Z_S=67.16 \Omega$ $\theta_S=45.96^\circ$
3	2	4.5	$Z_1=47.33 \Omega$ $Z_2=35 \Omega$ $\theta=55.38^\circ$	Open stub $Z_S=55.29 \Omega$ $\theta_S=55.38^\circ$

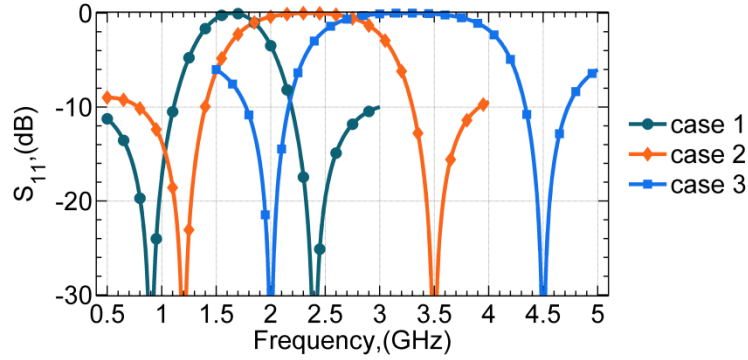


Figure 6.14 Simulated return loss corresponding to TABLE 6-4.

Next, the performance of the proposed T-type network is evaluated. To that end, some design examples are presented in the TABLE 6-5 where f_1 is fixed whereas f_2 and Z_L are assumed to be varying. As listed in the table, the design parameters are again physically realizable. The corresponding return loss shown in Fig. 6.15 exhibits good matching and thereby validates the considered scenario. One aspect to be understood here is that the impedance Z_L is frequency dependent and complex for T-type networks and therefore it is not suitable to draw plots like Fig. 6.9 or Fig. 6.10 as Z_L/Z_0 will be complex. Instead, for comparison purpose, some examples are mentioned in TABLE 6-6 which are either difficult or impossible to implement using the conventional T-network design [43], but can be easily implemented using the proposed network. It is thus apparent from the table that the design parameters for the design of [43] are unrealizable whereas that of the proposed design are realizable. It is due to the presence of the free variable in the proposed scheme. The corresponding simulated results are shown in Fig. 6.16 which exhibit proper matching.

At this juncture, a comment on bandwidth is appropriate. As far as the bandwidth of various networks are concerned, unfortunately, so far there has not been any rigorous study of bandwidths in dual-band matching networks using distributed components. So, it is difficult to make any direct comparisons. The explanation given in [24] is only qualitative rather than quantitative. Nevertheless, it is apparent from all the plots in this section that the 10-dB bandwidth achieved in most of the cases are adequate as per comparison done in [22]. Moreover, it is important to reiterate that the bandwidth is not that critical requirement in multi-frequency networks as needed in wide-band networks.

Table 6-5 Design Parameters for Proposed T-type Impedance Transformer, $f_1 = 1\text{GHz}$,
 f_2 : Varying and, Z_L :Varying

Case	Frequency (GHz)	$Z_L(\Omega)$	Z_C/θ_C	$Z_1/Z_2/\theta$	Z_S/θ_S
1	$f_1=1$ $f_2= 1.5$	$41.040+j9.469$ $42.091+j14.254$	$Z_C =77.91\Omega$ $\theta_C =62.51^\circ$	$Z_1=135 \Omega$ $Z_2=122.50 \Omega$ $\theta =72^\circ$	Open Stub $Z_S = 132.1 \Omega$ $\theta_S =144^\circ$
2	$f_1=1$ $f_2= 2$	$41.040+j9.469$ $43.622+j19.095$	$Z_C =77.92 \Omega$ $\theta_C =50.50^\circ$	$Z_1=35 \Omega$ $Z_2=70.71 \Omega$ $\theta =60^\circ$	Open Stub $Z_S = 126.4 \Omega$ $\theta_S =60^\circ$
3	$f_1=1$ $f_2=2.5$	$41.040+j9.469$ $45.696+j24.003$	$Z_C =77.93\Omega$ $\theta_C =41.91^\circ$	$Z_1=75 \Omega$ $Z_2=73.82 \Omega$ $\theta =51.43^\circ$	Short Stub $Z_S = 49.62 \Omega$ $\theta_S =102.86^\circ$
4	$f_1=1$ $f_2=3$	$41.040+j9.469$ $48.403+j28.98$	$Z_C =77.96\Omega$ $\theta_C =35.46^\circ$	$Z_1=45 \Omega$ $Z_2=85.48 \Omega$ $\theta =45^\circ$	Open Stub $Z_S = 68.49 \Omega$ $\theta_S =45^\circ$
5	$f_1=1$ $f_2=3.5$	$41.040+j9.469$ $52.863+j34.008$	$Z_C =78.00\Omega$ $\theta_C =30.44^\circ$	$Z_1=45 \Omega$ $Z_2=86.64 \Omega$ $\theta =40^\circ$	Open Stub $Z_S = 53.10 \Omega$ $\theta_S =40^\circ$

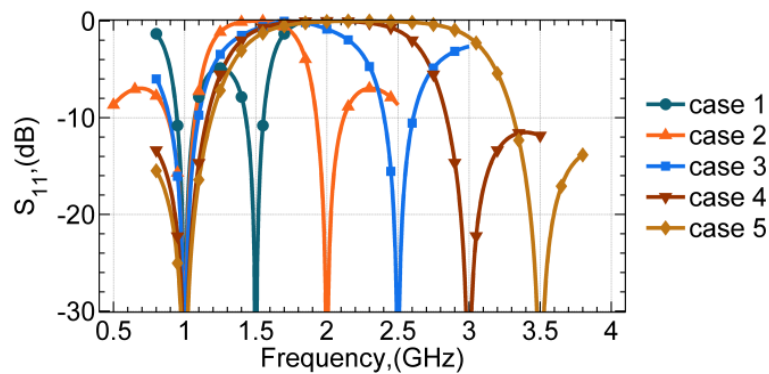


Figure 6.15 Simulated return loss corresponding to TABLE 6-5.

Furthermore, please note that theoretically the insertion loss (transmission) is direct function of the return loss (reflection) assuming no radiation and no conductive and dielectric losses exist in structure. These losses are often negligible at low RF frequencies and for transmission line based structures built properly in low loss dielect-

Table 6-6 Design Parameters for Proposed T-type Impedance Transformer. These are just some examples where conventional T-type network [43] cannot be realized.

Case	Frequency (GHz)	$Z_L(\Omega)$	Nikravan's Design[43]				Proposed T-type Network		
			Z_a/θ_a	Z_b/θ_b		Z_c/θ_c	$Z_1/Z_2/\theta$	Z_c/θ_c	Z_S/θ_S
1	$f_1=1$ $f_2=2$	10.272+j11.866 11.061+j24.374	$Z_a=167.78\Omega$ $\theta_a=60^\circ$	Open Stub	Short stub	$Z_c=76.64\Omega$ $\theta_c=51.03^\circ$	$Z_1=33\Omega$	$Z_c=76.64\Omega$ $\theta_c=51.03^\circ$	Open Stub
				$Z_b=166.3\Omega$ $\theta_b=60^\circ$	$Z_b=55.4\Omega$ $\theta_b=120^\circ$		$Z_2=126.75\Omega$ $\theta=60^\circ$		$Z_S=138.93\Omega$ $\theta_S=60^\circ$
2	$f_1=1$ $f_2=2.5$	155.921-j27.021 130.383-j54.805	$Z_a=73.09\Omega$ $\theta_a=51.53^\circ$	Open Stub	Short stub	$Z_c=75.62\Omega$ $\theta_c=45.42^\circ$	$Z_1=100\Omega$	$Z_c=75.62\Omega$ $\theta_c=45.42^\circ$	Open stub
				$Z_b=838.2\Omega$ $\theta_b=102.86^\circ$	$Z_b=152.56\Omega$ $\theta_b=51.43^\circ$		$Z_2=32.06\Omega$ $\theta=51.43^\circ$		$Z_S=125.18\Omega$ $\theta_S=102.86^\circ$
3	$f_1=1.5$ $f_2=2.5$	86.547+j13.384 90.133+j21.835	$Z_a=94.97\Omega$ $\theta_a=67.5^\circ$	Open Stub	Short stub	$Z_c=121.68\Omega$ $\theta_c=55.29^\circ$	$Z_1=135\Omega$	$Z_c=121.68\Omega$ $\theta_c=55.29^\circ$	Open Stub
				$Z_b=524.8\Omega$ $\theta_b=67.5^\circ$	$Z_b=217.39\Omega$ $\theta_b=135^\circ$		$Z_2=107.54\Omega$ $\theta=67.5^\circ$		$Z_S=136.98\Omega$ $\theta_S=135^\circ$

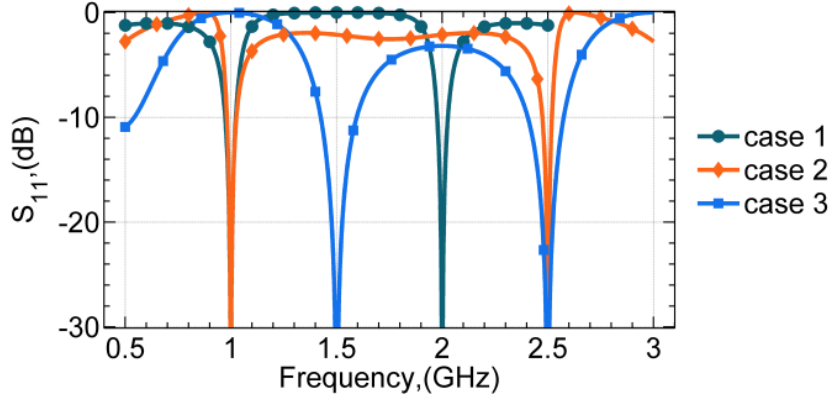


Figure 6.16 Simulated return loss corresponding to TABLE 6-6.

ric substrate as demonstrated in the next chapter. Therefore, the vast majority of existing literature of dual-frequency matching does not include the insertion-loss result and this thesis has also followed this pattern. Moreover, as shown in the next section, the fabricated prototype is essentially also a single-port network.

6.8 Prototype and Measurement

To validate the proposed design, a prototype of T-type matching network, of Fig. 6.6, has been fabricated on FR4 substrate with $\epsilon_r = 4.7$, 1.5 mm dielectric height, and 35 μm copper cladding. A length of TL segment in series with a 19.1 Ω SMD resistor (Part# CRCW060319R1FKTA by Vishay-Dale) is used to create a frequency-dependent complex load, $Z_L=20.08+j11.54\Omega$ @ f_1 and $Z_L=21.55+j23.61\Omega$ @ f_2 , to be matched to $Z_0=50\Omega$ at 1GHz/2GHz. The design values of various TL sections are $Z_1 = 40\Omega$, $Z_2 = 98.68\Omega$, $Z_C = 71.5\Omega$, $Z_S = 132.74\Omega$ (open stub), $\theta = \theta_S = 60^\circ$, and $\theta_C = 50.23^\circ$. The fabricated prototype along with various dimension are shown in Fig. 6.17. An Agilent Fieldfox VNA (N9926A) is used to measure the return loss of this single-port prototype.

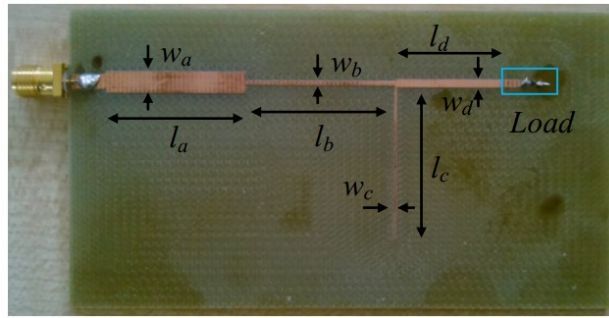


Figure 6.17 The fabricated dual-frequency T-type matching network of Fig. 6.6. Dimensions (mils): $l_a = 1037$, $w_a = 160$, $l_b = 1120$, $w_b = 30$, $l_c = 1141.6$, $w_c = 15$, $l_d = 897.1$, $w_d = 58.7$.

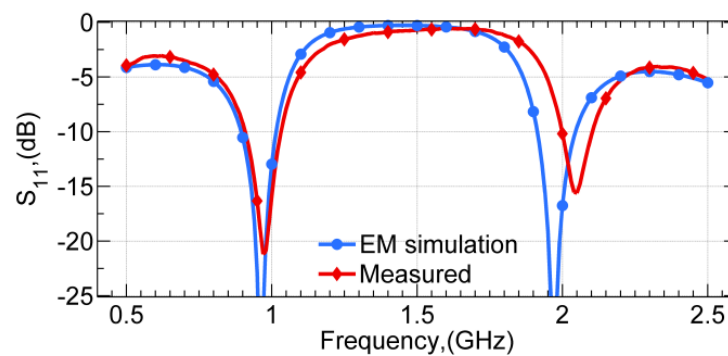


Figure 6.18 EM simulated and measured return loss of the fabricated T-type matching network.

As shown in Fig. 6.18, the measured return loss is better than 15dB at both the frequencies. A small shift in these results can be attributed to in-home fabrication of the prototypes and due to the use of less stable FR4 substrate as well as the anomaly in the models used for the resistor and the via.

6.9 Application in Port-Extended Branch-Line Coupler

Branch-line couplers (BLCs) are key components in hosts of communication and instrumentation applications. Therefore, there has always been huge research interest in its design and development. The current research is focused in many directions such as miniaturization [97-98], bandwidth extension [99-100] along with harmonic suppression [101], and arbitrary port termination capabilities [102-104]. However, with the ever growing interests in the software-defined/cognitive radios (SDRs/CRs) [13, 63], the current decade has also seen huge interest in the design of dual-frequency

BLCs [85-87, 102, 105-116].

A number of interesting approaches to design dual-band BLC have been reported in the literature and they can be classified into the following three categories.

- 1) *Dual-band quarter-wave blocks based*: In this approach, a dual-band BLC is obtained by simple replacement of all the quarter-wave lines of a single-band BLC with equivalent dual-band quarter-wave blocks. For example, the composite right-/left-hand (CRLH) transmission-lines [87], Pi-networks [85, 105], T-networks [86, 106], and stepped-impedance with open/short stub lines [107-108] come into this category. These reported designs have either limited band-ratio or complex design procedure or they provide a means of obtaining only equal power division. There have been reports of modified dual-band BLCs for obtaining tunability around the two frequencies [109-110], and arbitrary phase with arbitrary power division [111], but they have limited utility due to design complexities.
- 2) *Unique dual-band structures based*: In this technique, the structure is chosen and analyzed to assess their suitability for dual-band operation. The coupled-line based BLCs [112-114] and the cross line coupler [115] are examples of this approach. However, achieving good performance at two frequencies from coupled line based designs is difficult due to inherent unequal even/odd-mode velocities in microstrip technology whereas cross-line coupler realization requires a larger board area.
- 3) *Based on port extension technique*: This technique, essentially an impedance matching technique, matches the input impedance of a branch-line structure to the port impedance using a matching network [5]. An interesting graphical explanation of this technique using Mobius transformation provides easier interpretation [117]. There is no detailed and intuitive analysis of dual-band port extended couplers, perhaps first introduced in [6], and such dual-band port-extended couplers [102, 115] also possess limited frequency-ratio.

It is thus apparent that the literature is replete with design techniques for dual-band BLCs. However, it is also important to note that the major limitation in the current state-of-the-art dual-band BLCs is their limited band-ratio and/or power division ratio. This chapter deliberates on improved designs of dual-band BLCs based on port extension concept. The approach is very simple in terms of their design equations and

significantly advances the current state-of-the-art in terms of band-ratio and/or power division ratio.

6.9.1. The BLC Core

A BLC core, shown in Fig. 6.19, is considered where Z_{1c} and Z_{2c} are characteristic impedances of the vertical and horizontal TL sections whereas θ_1 are the electrical lengths of each TL sections. Here a term α is defined such that:

$$\alpha = Z_{1c} / Z_{2c} \quad (6-31)$$

Riblet [5] showed that the equivalent port admittance of such a BLC core, $Y_{eq,BLC}$, is given by:

$$Y_{eq,BLC} = G_{BLC} + jB_{BLC} \quad (6-32)$$

Where,

$$G_{BLC} = \frac{\sqrt{\alpha^2 - 1}}{Z_{1c} \sin \theta_1} \quad (6-33)$$

$$B_{BLC} = -\frac{(1 + \alpha) \cot \theta_1}{Z_{1c}} \quad (6-34)$$

Where the term α is basically related to the power division ratio k as follows:

$$k^2 = \left| \frac{S_{21}}{S_{31}} \right|^2 = \alpha^2 - 1. \quad (6-35)$$

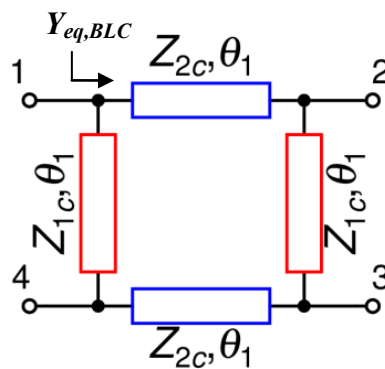
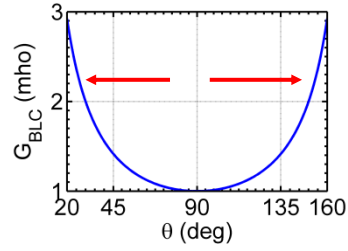
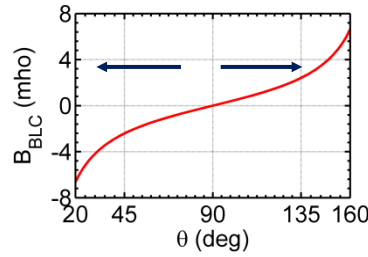


Figure 6.19 A Branch-Line Coupler (BLC) Core.



(a)



(b)

Figure 6.20 The real and the imaginary parts of equivalent admittance of BLC core.

It can be observed that the only frequency dependent term in the right-hand side of (6-33) and (6-34) is θ_1 . Now the interest is in the behavior of $Y_{eq,BLC}$ at two frequencies, namely f_1 and f_2 , with $r=f_2/f_1$ defined as the band-ratio and $f_2>f_1$. Now, if θ_1 is chosen such that [59]:

$$\theta_1|_{f_1} = \frac{m\pi}{1+r}, m \in Integer \quad (6-36)$$

then $G_{BLC}|_{f_1} = G_{BLC}|_{f_2}$ and $B_{BLC}|_{f_1} = -B_{BLC}|_{f_2}$, that is, the equivalent admittance of BLC core at the two frequencies are complex conjugate of each other.

For illustration of this behavior of $Y_{eq,BLC}$, the normalized real and imaginary parts of the equivalent port admittance are plotted in Fig. 6.20 with the assumption of $Z_{1c}=1$, $\alpha=\sqrt{2}$ and $m=1$ (usually, for compact size). The complex conjugate property of $Y_{eq,BLC}$ is apparent from Fig. 6.20. This is a very important result and it will be used in the design of dual-band port extended couplers in the subsequent sections.

6.9.2. Conventional Coupler from Riblet's View-point

The port extended dual-band coupler reported in [115] is redrawn in Fig. 6.21 for convenience. Here, a TL segment having characteristic impedance of Z_{ex} and electrical

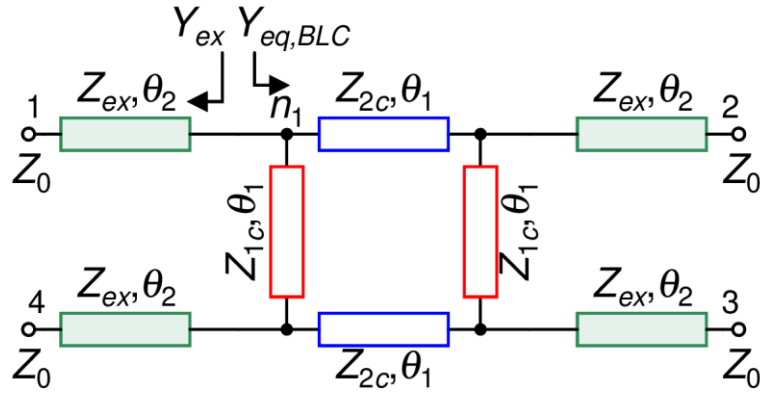


Figure 6.21 Conventional port extended dual-band coupler [115].

length θ_2 is attached to all the four ports of the BLC to match $Y_{eq,BLC}$ with the port impedance Z_0 . The electrical lengths θ_1 and θ_2 are assumed to be distinct. For conjugate matching, it is required that:

$$Y_{ex} = Y_{eq,BLC}^* \quad (6-37)$$

The admittance Y_{ex} can be expressed as:

$$Y_{ex} = 1 / \left(Z_{ex} \frac{Z_0 + jZ_{ex} \tan \theta_2}{Z_{1x} + jZ_0 \tan \theta_2} \right) = G_{ex} + jB_{ex} \quad (6-38)$$

where,

$$G_{ex} = \frac{Z_0 (1 + \tan^2 \theta_2)}{Z_0^2 + Z_{ex}^2 \tan^2 \theta_2} \quad (6-39)$$

$$B_{ex} = \frac{(Z_0^2 - Z_{ex}^2) \tan \theta_2}{Z_{ex} (Z_0^2 + Z_{ex}^2 \tan^2 \theta_2)} \quad (6-40)$$

Due to the presence of tangent squared terms in (6-39) and the unity power of tangent in (6-40), it can be concluded that if θ_2 is selected equal to θ_1 as given by (6-36) then $Y_{ex}|_{f_1} = (Y_{ex}|_{f_2})^*$ [59]. It means that $G_{ex}|_{f_1} = G_{ex}|_{f_2}$ and $B_{ex}|_{f_1} = -B_{ex}|_{f_2}$. This result was detailed in Chapter 3 as well. Now, using (6-37), i.e., setting $G_{ex} = G_{BLC}$ and $B_{ex} = -B_{BLC}$, equations (6-41)-(6-42) can be achieved:

$$\frac{Z_{ex}}{Z_0} = \frac{1}{2} \left[\sqrt{\frac{\alpha+1}{\alpha-1} \frac{1}{\sin^2 \theta_0} + 4} - \sqrt{\frac{\alpha+1}{\alpha-1} \frac{1}{\sin \theta_0}} \right] \quad (6-41)$$

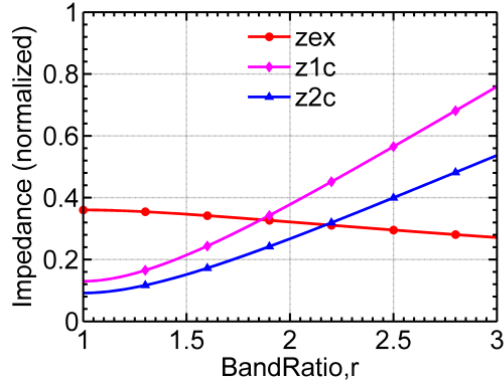


Figure 6.22 Normalized impedance variation with the band-ratio for $\alpha = \sqrt{2}$. This is the same as reported in [115].

$$\frac{Z_{1c}}{Z_0} = \frac{\sqrt{\alpha^2 - 1} (Z_0^2 + Z_{ex}^2 \tan^2 \theta_0)}{Z_0^2 \sin \theta_0 (1 + \tan^2 \theta_0)} \quad (6-42)$$

where $\theta_0 = \theta_1 = \theta_2$. Now setting $\alpha = \sqrt{2}$ (this value of α corresponds to equal power division, $k=0$ dB) in (6-41) and (6-42) provides expressions which are exactly the ones reported in [115]. In fact, it is clear that the port-matching technique results into more generic design equations in terms of power division ratio, α . The variation of line impedances with band-ratio for the port extended coupler is shown in Fig. 6.22 and it has similar profile as the one shown in the Fig. 3 of [115]. It clearly demonstrates that the dual-band port-extended BLC can be analyzed using Riblet's approach.

6.9.3 Limitation of the Conventional Approach

Following two discernible limitations could be seen in the even-odd mode analysis of the conventional coupler [115]:

- a) It is only valid for equal power division scenario.
- b) It is less amenable to implementation in microstrip. It can be deduced from the de-normalized plots of various line impedances, shown in Fig. 6.23, of the conventional coupler that the required line impedances are very low even if the minimum characteristic impedance that can be fabricated easily and with accuracy is assumed to be 20Ω . In fact, Z_{ex} is always lesser than 20Ω (that is why it is not visible in Fig. 6.23) and this explains the use of very thick TLs in [115].

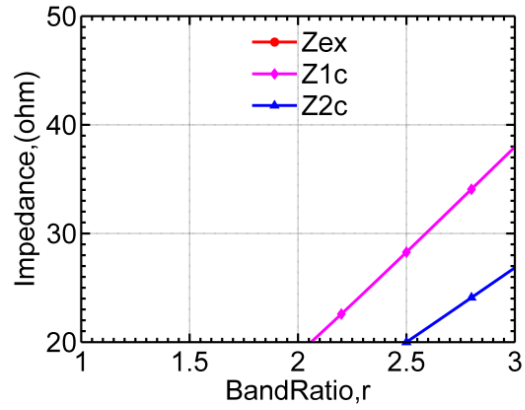


Figure 6.23 De-normalized impedance variation with the band-ratio for $\alpha = \sqrt{2}$. As is apparent, Z_{ex} is always less than 20Ω .

6.9.4 The Proposed Dual-Frequency Port Extended Coupler

It became apparent in the last section that the port extended coupler shown in Fig. 6.21 can also be analyzed as an impedance matching problem. For this, the conventional idea is to synthesize the real part of Y_{ex} to be equal to the real part of $Y_{eq,BLC}$ and the imaginary part of Y_{ex} equal but opposite in sign to imaginary part of $Y_{eq,BLC}$. This process is highly constrained as the design parameters must be chosen to satisfy these two requirements and that eventually results in extremely limited realizable TL impedances. The two novel configurations proposed in this paper takes alternative approach of analysis through Riblet's technique and that allows flexible design equations in terms of realizable TL impedances and extended band-ratio.

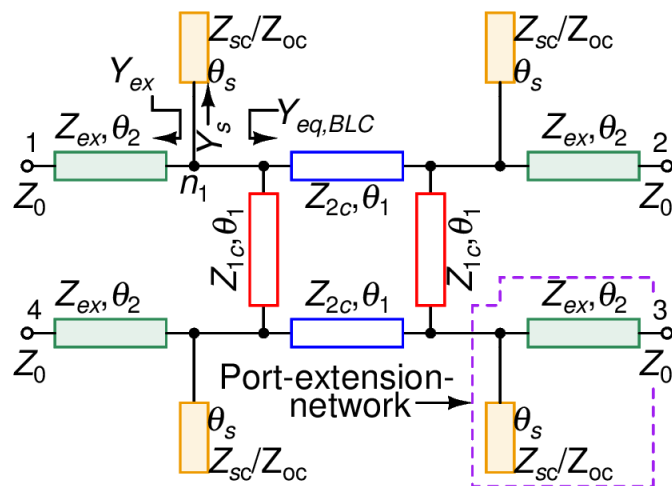


Figure 6.24 The proposed port-extended dual-frequency coupler: Configuration-I.

Configuration-I: In the first proposed dual-frequency port extended coupler, shown in Fig. 6.24, Z_{ex} and Z_s are the characteristic impedance of port extension transmission line and the stub respectively, and Z_0 denotes the port termination. The term $Y_{ex} = G_{ex} + jB_{ex}$ is the admittance looking into the TL section with characteristic impedance Z_{ex} while $Y_s = jB_s$ denotes the admittance of the stub.

Now the port matching at the port n_1 can be achieved as follows:

1) Equate the real part of Y_{ex} to real-part of $Y_{eq, BLC}$, that is:

$$G_{ex} = G_{BLC} \quad (6-43)$$

2) Cancel the leftover net imaginary parts, $j(B_{ex} + B_{BLC})$, of Y_{ex} and $Y_{eq, BLC}$ at port n_1 with the help of dual-frequency stub of admittance Y_s . Therefore, for its cancellation:

$$B_s = -(B_{ex} + B_{BLC}) \quad (6-44)$$

Where, G_{ex} and B_{ex} are given by (6-39) and (6-40). Now, substitution of G_{ex} from (6-39) into (6-43) yields following expression for Z_{ex} :

$$Z_{ex} = \sqrt{\frac{Z_0(1+t^2 - G_{BLC}Z_0)}{G_{BLC}t^2}} \quad (6-45)$$

Where, $t = \tan \theta_2 = \tan \theta_1$, and G_{BLC} is given by (6-33). This value of Z_{ex} can then be substituted in (6-40) to find B_{ex} .

A dual-frequency stub can help enforce (6-44) and their design details were given in Chapter 5 and in [60]. It can be inferred that an open stub can work as dual-frequency stub to satisfy (6-44) provided the following equations are satisfied:

$$Z_s \tan \theta_s = -(B_{ex} + B_{BLC}) \quad (6-46)$$

$$Z_s \tan r\theta_s = +(B_{ex} + B_{BLC}) \quad (6-47)$$

Where, the fact that the electrical length θ_s defined at f_1 becomes $r\theta_s$ at f_2 with $r=f_2/f_1$. In addition, if $\theta_2 = \theta_1$ are chosen according to (6-36) then the term $B_{ex} + B_{BLC}$ just changes its sign at the two frequencies. Solving (6-46) and (6-47) simultaneously yields Z_s given in (6-48).

given as:

$$Z_{ex2} = \frac{-b \pm \sqrt{b^2 - 4ac}}{2a} \quad (6-51)$$

with,

$$a = G_{BLC} t^2 (Z_0^2 t^2 + Z_{ex1}^2) \quad (6-52)$$

$$b = 2G_{BLC} Z_{ex1} t^2 (Z_{ex1}^2 - Z_0^2) \quad (6-53)$$

$$c = -Z_0 Z_{ex1}^2 (1 + t^2)^2 + G_{BLC} Z_0^2 Z_{ex1}^2 + G_{BLC} Z_{ex1}^4 t^2 \quad (6-54)$$

In these expressions, Z_{ex1} is a free variable that can be selected independently to get a physically realizable coupler. Once the value of Z_{ex1} is selected, and that of Z_{ex2} is determined using (6-51)-(6-54) and (6-33), the value of B_{ex} is computed using (6-50). This value of B_{ex} is subsequently utilized to design the dual-frequency stub using (6-48). More details about dual-frequency stub design can be obtained from [60].

6.9.5 Design Steps

A simple design flowchart for the configuration-I of the proposed BLC is shown in Fig. 6.26. It is assumed that Z_{2c} is a free design variable and thus the design process begins with the selection of a realizable value of $Z_{2c} \in (30\Omega, 120\Omega)$. As $Z_{1c} = \alpha Z_{2c}$, the value Z_{2c} must be selected such that Z_{1c} is also $\in (30\Omega, 120\Omega)$ for a required α . Then all the elements of port extension network are designed using the design equations. A different value of Z_{2c} needs to be considered and the design steps repeated if any of the TL-section is physically not realizable. This flexibility in the proposed technique distinguishes it from the reported design of [115].

The design steps for the configuration-II are similar except that it possesses more flexibility owing to the presence of the two design variables Z_{2c} and Z_{ex1} . In the first round, suitable value of these free design variables are assumed. If any of the TL-sections is found unrealizable then either Z_{2c} or Z_{ex1} or both can be modified. Both these configurations have free bounded design variables, in the range of $(30\Omega, 120\Omega)$, and therefore a simple computer program involving loop statement can be employed to quickly obtain the design parameters.

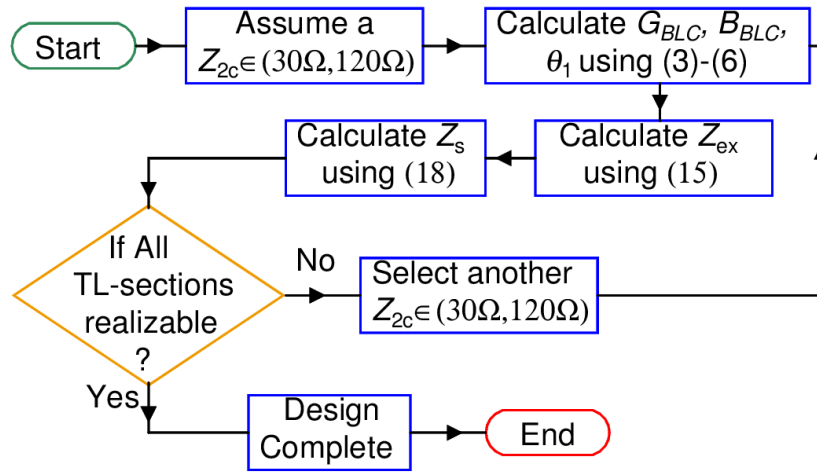


Figure 6.26 Flowchart for the design of proposed coupler with configuration-I. Equations (3)-(6) refers to the equation (6-33)-(6-36) in this chapter, and equation (15) and (18) refers to (6-45) and (6-48), respectively.

6.9.6 Simulation and Discussion

In this section, the capabilities and limitations of the proposed BLC configurations are assessed. In this regard, Fig. 6.27 depicts the variation of the characteristic impedances with band-ratio ($r = f_2/f_1$) in the configuration-I for equal power division ratio ($\alpha = \sqrt{2}$, $k = 0\text{dB}$). Here, Z_{2c} is the free design variable and therefore various design parameters have been plotted for different values of Z_{2c} . It is apparent from Fig. 6.27(a) that for $Z_{2c} = 30\Omega$, Z_{ex} is within the realizable limits of fabrication ($30\Omega, 120\Omega$) from $r = 1$ to 2.65. However, it can also be seen in the same figure that a short stub could only be realized from $r = 1.4$ to 1.85 and an open stub from $r = 1.65$ to 3. Since, a designer would choose either a short or an open stub depending upon the required band-ratio, therefore, the net band-ratio in this case is 1.4 -2.65, obtained from $(1-2.65) \cap \{(1.4-1.85) \cup (1.65-3)\}$. It can be concluded from Fig. 6.27 that the achievable band-ratio depends on the choice of Z_{2c} . For example, it lies in the range 1.4 – 2.65 for $Z_{2c} = 30\Omega$ while it changes to 1.55 – 3.35 for $Z_{2c} = 80\Omega$. It must be noted that for $\alpha = \sqrt{2}$, the maximum allowed value for $Z_{2c} = (\text{maximum allowed value of } Z_{1c}) / \sqrt{2} = 120\Omega / \sqrt{2} = 84.85\Omega$. Apparently the required value of Z_{ex} increases with the increase in the value of Z_{2c} . This phenomenon can be understood by considering (6-33) and (6-45). From (6-33) it is clear that the increase in the value of Z_{2c} , and hence that of the Z_{1c} , decreases the value of G_{BLC} and this in turn increases Z_{ex} according to (6-45). Ideally, a higher value of Z_{2c} should be preferred as it will result into thinner extended

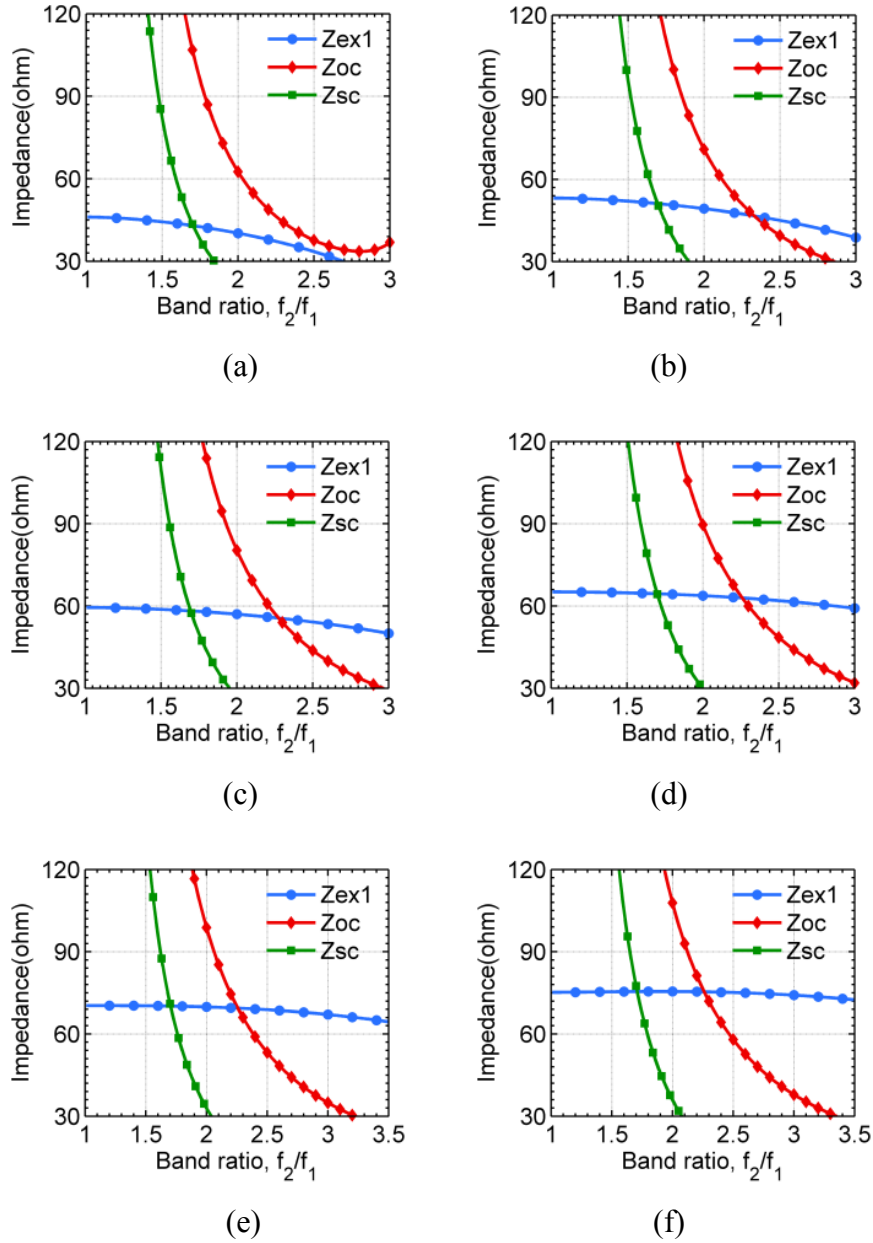


Figure 6.27 Impedance variation with band-ratio in configuration-I ($Z_{ex1}=Z_{ex}$) with $k=0$ dB, when $Z_{2c}=(a) 30\Omega$, (b) 40Ω , (c) 50Ω , (d) 60Ω , (e) 70Ω , and (f) 80Ω .

lines that can be folded easily for size reduction.

The unequal power division cases for the configuration-I are depicted in Fig. 6.28. The values of Z_{2c} for each case are chosen to meet the maximum allowed value of Z_{1c} . It is apparent that the proposed port-extended coupler is capable of providing unequal power division but with reduced band-ratio as the power division ratio increase.

It can be deduced from Fig. 6.28 that the achievable band-ratios are 1.55 - 3.4 and

1.55 - 2.95 for 2dB and 8dB BLC respectively. It should be noted that the maximum power division ratio considered here is for $\alpha_{\max} = (Z_{1c})_{\max}/(Z_{2c})_{\min} = 120/30 = 4$, and this corresponds to $k = 11.76\text{dB}$. The achievable band-ratio for this case is merely 1.65 - 2.05 as can be seen in Fig. 6.29.

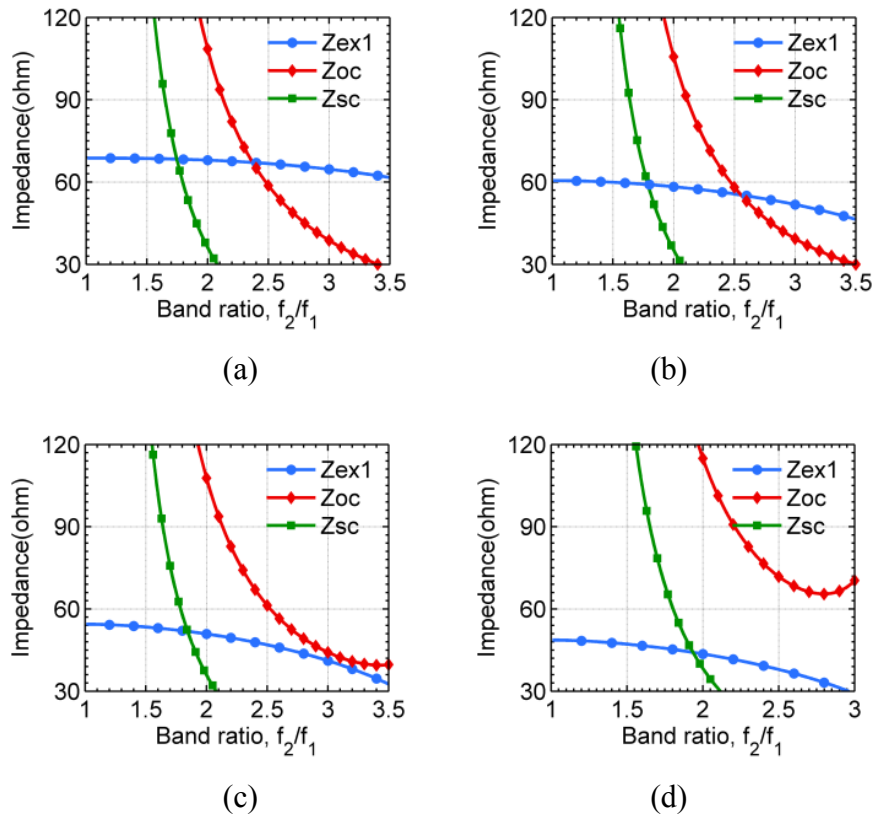


Figure 6.28 Impedance variation with band-ratio in configuration-I ($Z_{ex1} = Z_{ex}$) for (a) $k = 2\text{dB}$, $Z_{2c} = 74\Omega$, (b) $k = 4\text{dB}$, $Z_{2c} = 62\Omega$, (c) $k = 6\text{dB}$, $Z_{2c} = 53\Omega$, (d) $k = 8\text{dB}$, $Z_{2c} = 44\Omega$.

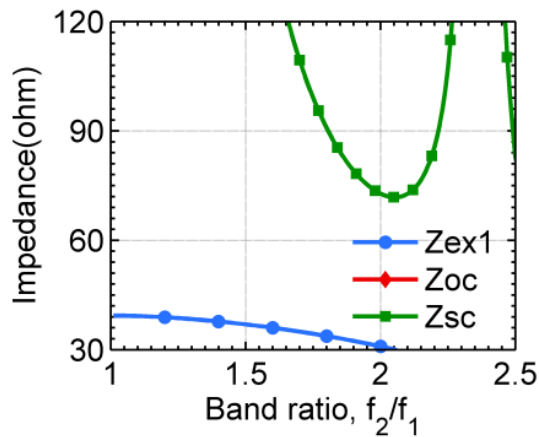


Figure 6.29 Impedance variation with band-ratio in configuration-I ($Z_{ex1} = Z_{ex}$) for maximum allowed power division ratio, $k = 11.76\text{dB}$ (and, $Z_{2c} = 30\Omega$).

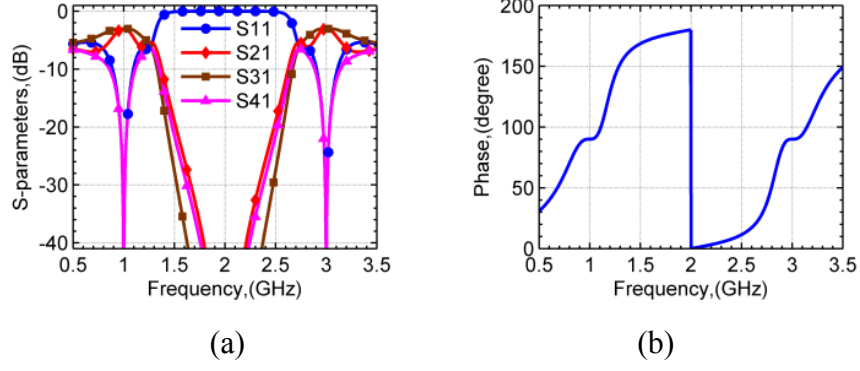


Figure 6.30 S-parameters and phase difference of the proposed BLC configuration-I for equal-power division ($k = 0\text{dB}$).

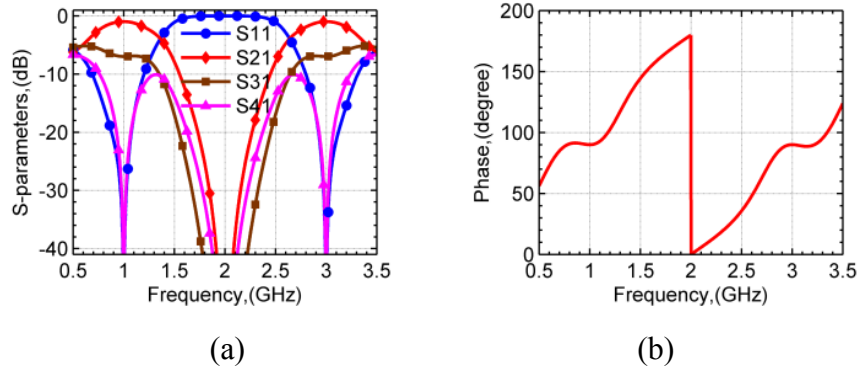


Figure 6.31 S-parameters and phase difference of the proposed BLC configuration-I for $k = 6\text{dB}$.

Figs. 6.30 and 6.31 show the S-parameters and differential phase ($= \angle(S21/S31)$) for $r = 3$ of an equal power division BLC and 6dB BLC respectively. The design parameters for equal division BLC are $Z_{2c} = 80\Omega$, $Z_{1c} = 113.14\Omega$, $Z_{ex} = 74.16\Omega$, $Z_s = 37.89\Omega$, and $\theta_1 = \theta_2 = \theta_s = 45^\circ$, while for 6dB BLC are $Z_{2c} = 53.5\Omega$, $Z_{1c} = 119.4\Omega$, $Z_{ex} = 41.61\Omega$, $Z_s = 44.05\Omega$, and $\theta_1 = \theta_2 = \theta_s = 45^\circ$. All these lines are convenient to fabricate and the corresponding simulation results also confirms proper working.

Essentially, the overall idea of configuration-I is based on matching and therefore it may be extremely tempting to extend this concept to unequal port terminations [102]. The design steps remain the same except that, now, the four port-extension network will be different depending on the value of port termination impedances. Fig. 6.32 shows simulation result, for configuration-I, for $r = 2.5$ ($f_1 = 1.5\text{ GHz}$, $f_2 = 3.75\text{GHz}$) while considering unequal ports impedances. The computed design parameters in this case are:

$$Z_{2c} = 70\Omega, Z_{1c} = 98.995\Omega, \theta_1 = \theta_2 = \theta_s = 51.428^\circ.$$

Port1($Z_0=50\Omega$): $Z_{ex} = 68.86\Omega$, $Z_s = 53.17\Omega$,
 Port2($Z_0=100\Omega$): $Z_{ex} = 79.39\Omega$, $Z_s = 75.93\Omega$,
 Port3($Z_0=90\Omega$): $Z_{ex} = 79.03\Omega$, $Z_s = 70.43\Omega$, and
 Port4($Z_0=47\Omega$): $Z_{ex} = 67.43\Omega$, $Z_s = 52.05\Omega$.

The simulated results are otherwise good except that the phase differences at the two frequencies are 87.12° and 92.88° . These must be 90° considering that ideal transmission lines are used during simulation. To get more insight, the structure reported in [102] was implemented and simulated for unequal impedance condition mentioned above. The corresponding design parameters were obtained from Fig. 5(a) of [102]. The simulated results depicted in Fig. 6.33, interestingly enough, provide the phase differences of 91.11° and 88.89° at the design frequencies. The variation reported in design [102] is smaller as compared to the proposed configuration-I. However, it should be noted that the value of Z_{2c} is 70Ω in [102] while the corresponding value of Z_{2c} is 51.15Ω here and therefore direct comparison may not be appropriate.

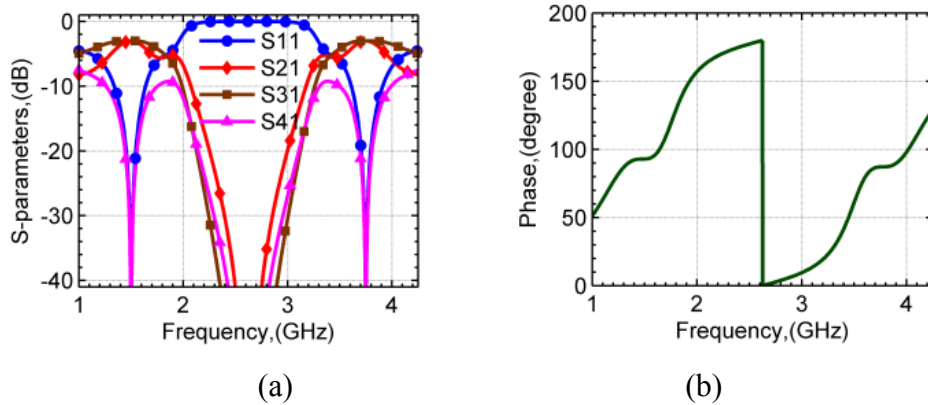


Figure 6.32 S-parameters and phase difference of the proposed BLC configuration-I for $k=0\text{dB}$ and unequal port terminations.

Essentially the deviation in the phases can be attributed to Riblet's theory in Section II of [5]. It is clearly stated that all the four port-matching networks must be identical so that this process does not alter the symmetry of the BLC core. This basic requirement of symmetry is defied when the Riblet's port-matching technique is applied to unequal port terminations scenario and this effectively leads to anomaly in the phase difference. Nevertheless, the idea presented in [102] is interesting, and can be extended to the proposed design considering that many applications may allow for 4° - 5° differential phase difference tolerances.

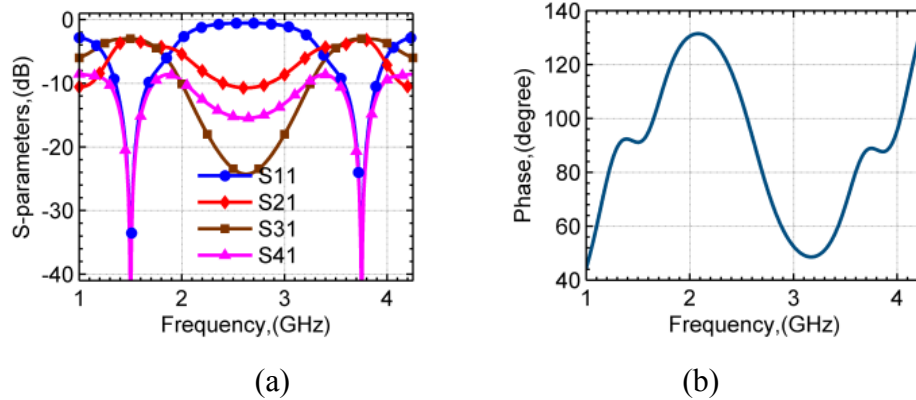


Figure 6.33 S-parameters and phase difference of the conventional BLC [102] for $k = 0\text{dB}$ and unequal port terminations.

Even with all the good features, the configuration-I is limited to smaller band-ratio for higher power division case as can be seen in Fig. 6.29. In this situation, configuration-II could fulfill the requirements. Under similar impedance conditions to the one used for configuration I, the configuration-II is capable of providing band-ratio of 1.5 - 3 for maximum power division as can be seen in Fig. 6.34. The reported design [102] can provide a band-ratio of 1 - 1.93 for maximum power division ratio. The configuration-II can be combined to the design [102] to achieve an overall band-ratio of 1.0 - 3.0 for maximum power division of 11.76dB. It can thus be concluded that the proposed BLC enhances the current state-of-the-art significantly.

Lastly, to show a design example using the proposed configuration-II, a BLC is designed for $k = 11.76\text{dB}$ (maximum power division) and $r = 2.5$. The design parame-

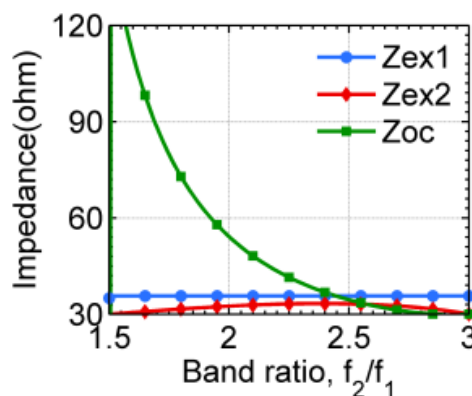


Figure 6.34 Impedance variation with band-ratio in configuration-II for maximum allowed power division ratio, $k = 11.76\text{dB}$ (and, $Z_{2c} = 30\Omega$).

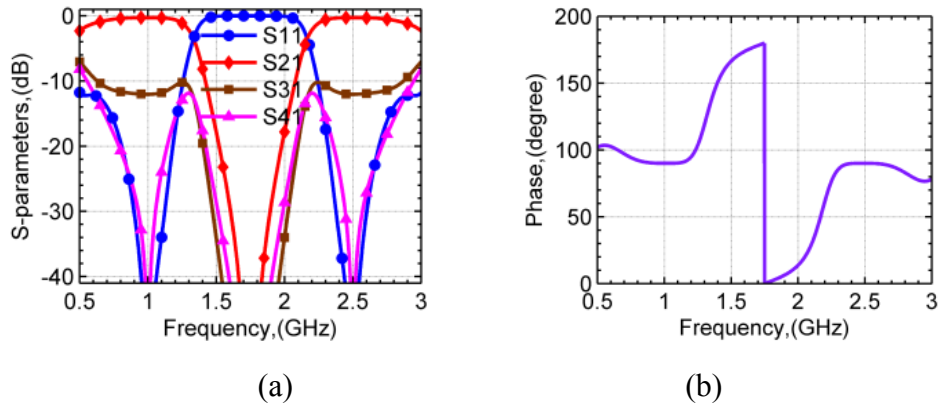


Figure 6.35 S-parameters and phase difference of the proposed BLC configuration-II for $k=11.76\text{dB}$.

ters in this situation are $Z_{2c} = 30\Omega$, $Z_{1c} = 120\Omega$, $Z_{ex1} = 35\Omega$, $Z_{ex2} = 33.5\Omega$, $Z_s = 33.11\Omega$, and $\theta_1 = \theta_2 = \theta_s = 51.43^\circ$. The simulated results depicted in Fig. 6.35 confirm the proper operation as predicted by the proposed theory.

Two prototypes, one for each configuration, have been implemented to validate the proposed BLC configurations on Rogers RO4003C substrate having dielectric constant $\epsilon_r=3.55$, dissipation factor $\tan\delta=0.002$, substrate height= 0.813mm, and copper cladding of 35um on both sides. The prototype-I, for configuration-I, shown in Fig. 6.36 is designed for a non-integer band-ratio $r = 2.1$ and $k = 6\text{dB}$. The first chosen frequency is $f_1=1.2\text{GHz}$ and therefore $f_2=2.52\text{ GHz}$. The design parameters for this prototype are $Z_{2c} = 53\Omega$, $Z_{1c} = 118.29\Omega$, $Z_{ex} = 50.22\Omega$, $Z_s = 93.80\Omega$ (open stub), and $\theta_1 = \theta_2 = \theta_s = 58.06^\circ$. It may be noted that during prototyping the corners need to be properly modeled using either two cascaded MTEEs or a MCROSOs, both of these elements are available in Keysight[®] Advanced Design System (ADS) library, and therefore their presence necessitates optimization. The former option is used in this work. The final physical dimensions are also mentioned in Fig. 6.36. The prototypes are measured using an N5230A PNA-L 13.5 GHz vector network analyzer as shown in Fig. 6.37. The EM simulated and the measured results are compared in Fig. 6.38. It is apparent from Fig. 6.38 that the return loss and isolations are better than 20dB. For a 15dB reference, the return loss bandwidth are found to be $298\text{MHz}@f_1 / 380\text{MHz}@f_2$ and the isolation bandwidth $262\text{MHz}@f_1 / 300\text{MHz}@f_2$ and these are significantly higher than the ones reported in [102]. Moreover, the transmissions S21 and S31 are found to be $-1.4\text{dB}@f_1 / -1.6\text{dB}@f_2$ and $-6.8\text{dB}@f_1 / -6.4\text{dB}@f_2$, respectively. The corresponding

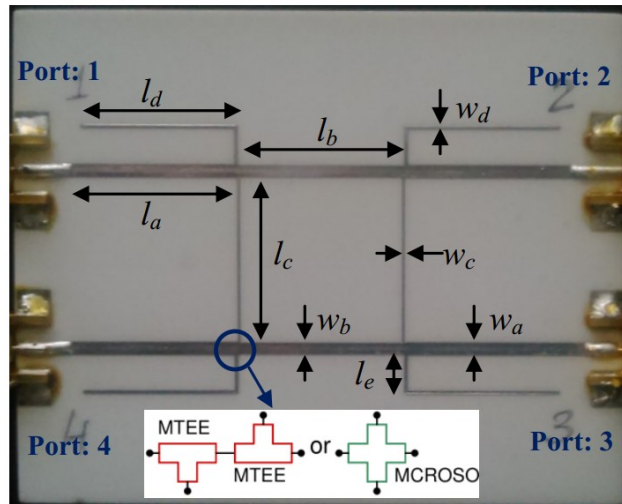


Figure 6.36 The prototype-I based on configuration-I. Dimensions (mm): $l_a=25.752$, $w_a=1.823$, $l_b=22.945$, $w_b=1.620$, $l_c=23.274$, $w_c=0.288$, $l_d=21.565$, $w_d=0.448$, $l_e=5.080$.

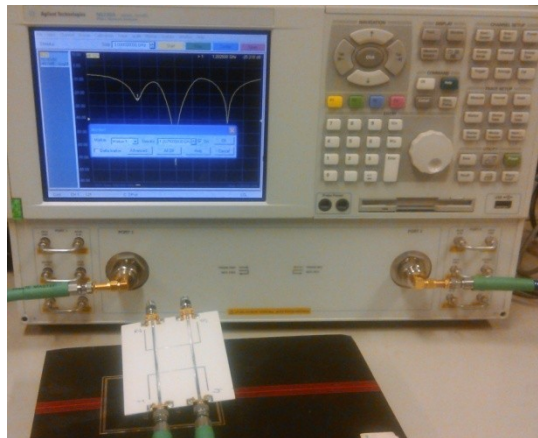
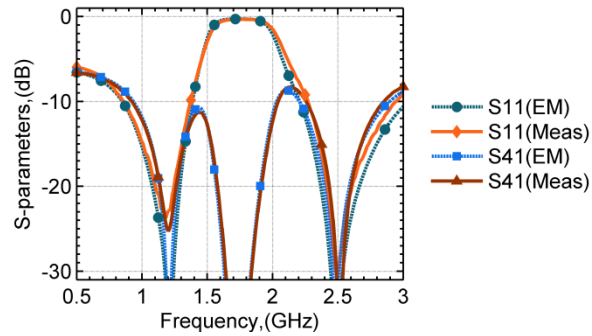


Figure 6.37 Measurement Setup: an Agilent VNA being used for S-parameter measurement.

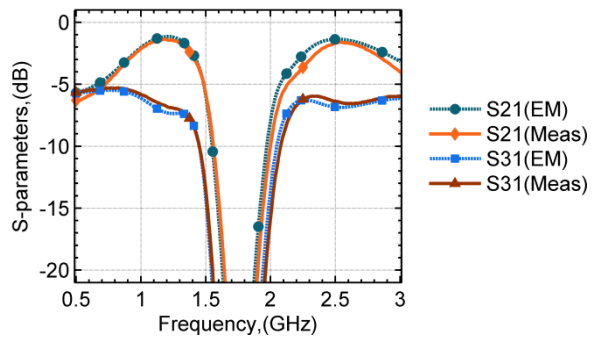
EM simulated values of these parameters are $-1.2\text{dB}@f_1/-1.4\text{dB}@f_2$ and $-7.3\text{dB}@f_1/-6.9\text{dB}@f_2$. The measured phase differences are found to be $88.85^\circ@f_1/-88.9^\circ@f_2$ and could be said to be within the permissible tolerance.

The second prototype is for configuration-II with $k=2\text{dB}$ for an integer band-ratio of $r=2$ and $f_1=1\text{GHz}$, and therefore $f_2=2\text{GHz}$, with the physical dimensions is depicted in Fig. 6.39 and the corresponding EM simulated and the measured responses are shown in Fig. 6.40. The design parameters calculated using the proposed design equations are $Z_{2c}=60\Omega$, $Z_{1c}=96.47\Omega$, $Z_{ex1}=58.45\Omega$, $Z_{ex2}=45\Omega$, $Z_s=84.57\Omega$ (open-circuit), and $\theta_1=\theta_2=\theta_s=60^\circ$. It is apparent from Fig. 6.40 that the return loss and

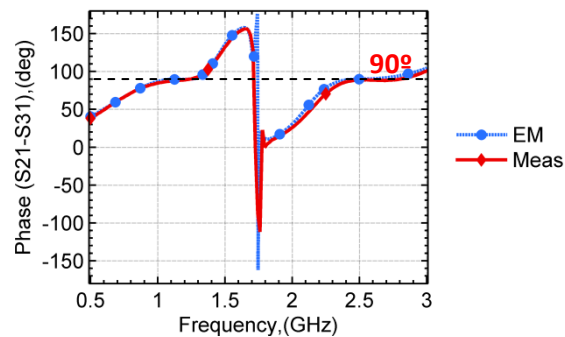
isolations are better than 20dB. Again, for a 15dB reference, the return loss bandwidth at are found to be 115MHz@ f_1 / 180MHz@ f_2 and the isolation bandwidth 110MHz@ f_1 / 165MHz@ f_2 and these are once again higher than the ones reported in [102]. Moreover, the measured transmission parameters S21 and S31 are found to be $-2.7\text{dB}@f_1 / -2.8\text{dB}@f_2$ and $-4.2\text{dB}@f_1 / -4.5\text{dB}@f_2$, respectively. The corresponding EM simulated values of these parameters are $-2.4\text{dB}@f_1 / -2.5\text{dB}@f_2$ and $-4.5\text{dB}@f_1 / -4.6\text{dB}@f_2$, and



(a)



(b)



(c)

Figure 6.38 S-parameters and phase difference of the prototype-I (configuration-I) for $k=6\text{dB}$, $f_1=1.2\text{GHz}$, $f_2=2.52\text{GHz}$ ($r=1.2$). (a) return loss S11 and Isolation S41 (b) transmissions S21 and S31, and (c) phase difference (S21-S31).

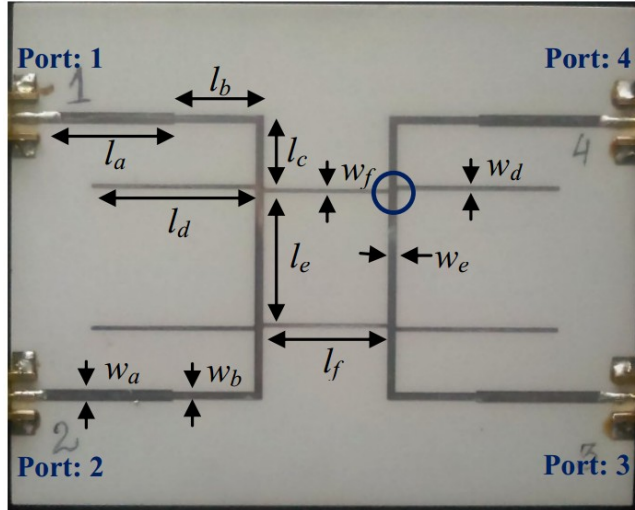


Figure 6.39 The prototype-II based on configuration-II. Dimensions (mm): $l_a=26.563$, $w_a=2.312$, $l_b=16.770$, $w_b=1.564$, $l_c=12.7$, $l_d=33.155$, $w_d=0.787$, $l_e=27.038$, $w_e=1.654$, $l_f=25.287$, $w_f=0.643$.

differs only slightly from the respective measured values. The ideal values of these parameters are -2.1dB and -4.1dB . The measured phase differences are found to be $91.7^\circ@f_1 / -92.8^\circ@f_2$ and could be said within the permissible tolerance. Overall measured response of the prototypes compare quite well to those obtained from EM simulation.

A comparison of the proposed designs with the previously reported dual-frequency port-extended designs is summarized in Table I. Since the required line impedances in [115] are less than 20Ω , its band-ratio is very limited. In contrast, the proposed BLC with configuration-I significantly improves the band-ratio and caters to the need of arbitrary power-divisions / port terminations. Moreover, use of the proposed BLC configuration-II significantly enhances the band-ratio for achieving the maximum power-division ratio, especially towards the upper band-ratio. Furthermore, the design equations to be solved are all in closed-form; and none of them are beyond second-degree polynomial. Thus, the design simplification of proposed techniques should be evident. In a nutshell, the proposed design techniques successfully enhance the current-state-of-the-art.

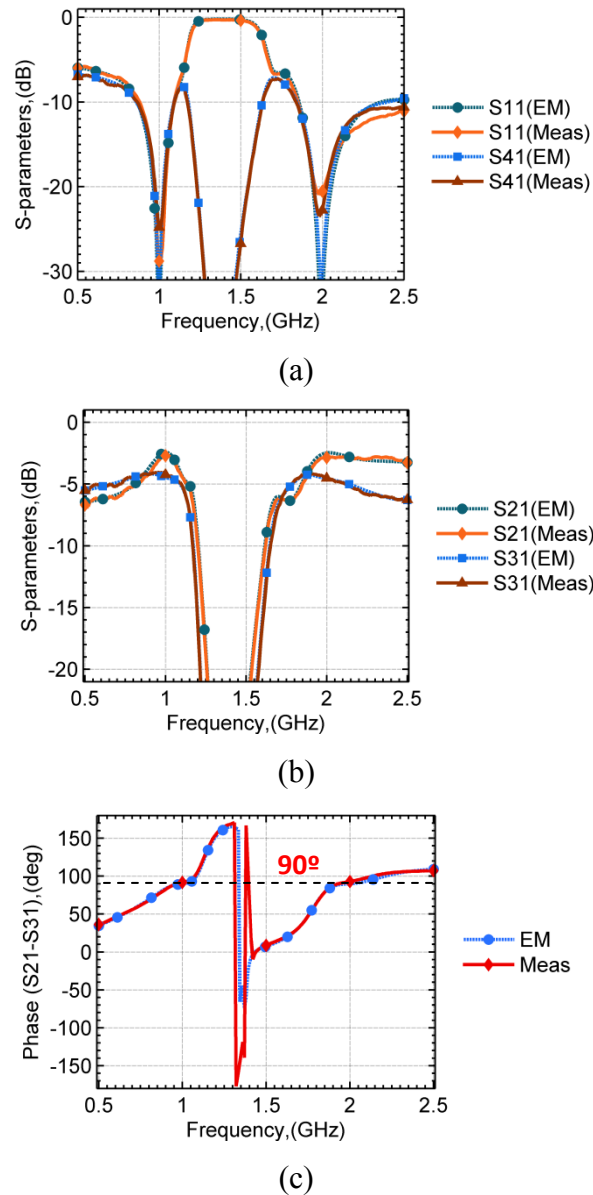


Figure 6.40 S-parameters and phase difference of the prototype-II (configuration-II) for $k=6\text{dB}$, $f_i=1\text{GHz}$, $f_i=2\text{GHz}$ ($r=2$). (a) return-loss S11 and Isolation S41 (b) transmissions S21 and S31, and (c) phase difference (S21-S31).

6.10 Conclusion

This chapter started by proposing interesting complex conjugate admittance property of two cascaded sections of transmission lines terminated into a real impedance. The discovered result is established through rigorous mathematical analysis, and is duly demonstrated graphically. It has been proved in this chapter that the popular Monzon transformer is, in fact, a special case obtained from this property.

Table 6-7 Comparison with Previous Port-extended Designs

Ref.		Power Division	Band-Ratio	Port-terms
[115]		equal	very limited	equal: Z_0
[102]		arbitrary	1- 1.93 for $k=11.76\text{dB}$	arbitrary
This Work	Conf-I	arbitrary	1.4-3.35 for $k=0\text{dB}$ 1.55-3.4 for $k=2\text{dB}$ 1.55-2.95 for $k=8\text{dB}$ 1.65-2.05 for $k=11.76\text{dB}$	arbitrary
	Conf-II		1.5- 3 for $k=11.76\text{dB}$	

Moreover, by incorporating TSTL in the conventional L- and T-type matching networks, significant performance improvement is observed. Author's initial efforts to enhance the frequency-ratio of branch-line couplers by providing a generalized analytical approach are detailed in [118]. The idea was to replace two of the four arms of single frequency unequal length branch-line coupler with either a T- or Pi-networks. The methodology was successful; however, the characteristic of the reported dual-frequency branch-line coupler was narrow-band, just like its single frequency counterpart. The concept of single-section introduced in Chapter 3, and the two-section introduced in this chapter has been used to port-extended branch-line couplers to enhance their frequency-ratio. The proposed techniques analysed in this chapter has been verified from measurement results as well. The present techniques are intuitive and possess a great deal of flexibility, owing mainly to the presence of one or more free design variables.

Appendix

Simplification leading to the Monzon's equations

Using (6-5) into (6-9) results into the following equation.

$$Z_0^2 (Z_1 - Z_2 \tan^2 \theta) - Z_1^2 (Z_2 - Z_1 \tan^2 \theta) = 0 \quad \text{A(1a)}$$

This implies:

$$\tan^2 \theta = \frac{Z_1 Z_0^2 - Z_2 Z_1^2}{Z_2 Z_0^2 - Z_1^3} \quad \text{A(1b)}$$

Furthermore, using (6-4) into (6-8) gives the following expression.

$$\frac{Z_0 Z_1^2 (1 + \tan^2 \theta)^2}{Z_0^2 (Z_1 - Z_2 \tan^2 \theta)^2 + Z_1^2 (Z_1 + Z_2)^2 \tan^2 \theta} = \frac{1}{Z_L} \quad \text{A(2)}$$

Substituting the expression of $\tan^2 \theta$ from A(1b) into A(2) and doing some lengthy algebraic manipulations results into the first design equation of Monzon:

$$Z_2 = \frac{Z_0 Z_L}{Z_1} \quad \text{A(3)}$$

Finally, substituting Z_2 from A(3) into A(1b) gives the second equation of Monzon:

$$Z_1 = \sqrt{\frac{Z_0(Z_L - Z_0)}{2\alpha} + \sqrt{\left(\frac{Z_0(Z_L - Z_0)}{2\alpha}\right)^2 + Z_L Z_0^3}} \quad \text{A(4)}$$

with, $\alpha = \tan^2 \theta$.

Chapter 7

Load Healing in Dual-Frequency Matching Networks

It was revealed in Chapter 2 that while numerous dual-frequency matching networks have been reported but the major challenges are their limited frequency-ratio and transformation-ratio. It can be inferred from discussions in the previous chapters that for a given frequency-ratio, the transformation-ratio is limited and vice versa. In most of the practical scenarios, especially in the case of amplifiers, the load impedance is complex as well as frequency-dependent and as such the limited frequency-ratio and transformation-ratio is really a problematic issue. The reason for this limitation will be clear soon. For implementation in microstrip technology, the limit of characteristic impedance that could normally be fabricated is usually in the range of 20Ω to 140Ω . However, there always exist some load values that result into practically unrealizable values of the constituent TL elements of a particular matching topology. It is due to the fact that the load (to the matching network), $Z_L=R_1+jX_1 @f_1$ and $Z_L=R_2+jX_2 @f_2$, can take any value depending on the design frequencies, the biasing conditions, and the transistor being used. For example, TABLE 7-1 lists some examples that cannot be realized using the conventional T-network [43].

It is apparent that the matching network is practically unrealizable for all the three cases. It is due to one or more constituent elements having characteristic impedance that is beyond the limit of fabrication. In such scenarios, one can either switch to some other reported matching network topologies or can use multiple stages [22]. In order to address this concern, a novel and very simple technique, called **load-healing**, for dual-frequency matching networks has been introduced in this chapter and this was also reported in [119]. In a nutshell, the idea is to tune the load itself such that the matching network effectively sees a load impedance that is realizable. This concept is illustrated in this chapter using the conventional T-network but the idea remains valid for other designs as well.

Table 7-1 Some Cases where Conventional T-Type Network [43] Cannot Be Realized

Case	Frequency (GHz)	$Z_L(\Omega)$	Nikravan's Design[43]			
			Z_a/θ_a	Z_b/θ_b		Z_c/θ_c
1	$f_1=1$ $f_2=2$	$10.27 + j11.87$ $11.06 + j24.37$	$Z_a=167.78\Omega$ $\theta_a=60^\circ$	Open Stub $Z_b=166.3\Omega$ $\theta_b=60^\circ$	Short stub $Z_b=55.4\Omega$ $\theta_b=120^\circ$	$Z_c=76.64\Omega$ $\theta_c=51.03^\circ$
2	$f_1=1$ $f_2=2.5$	$155.92 - j27.02$ $130.38 - j54.80$	$Z_a=73.09 \Omega$ $\theta_a=51.53^\circ$	Open Stub $Z_b=838.2\Omega$ $\theta_b=102.86^\circ$	Short stub $Z_b=152.56\Omega$ $\theta_b=51.43^\circ$	$Z_c=75.62\Omega$ $\theta_c=45.42^\circ$
3	$f_1=1.5$ $f_2=2.5$	$86.54 + j13.38$ $90.13 + j21.83$	$Z_a=94.97 \Omega$ $\theta_a=67.5^\circ$	Open Stub $Z_b=524.8\Omega$ $\theta_b=67.5^\circ$	Short stub $Z_b=217.39\Omega$ $\theta_b=135^\circ$	$Z_c=121.68\Omega$ $\theta_c=55.29^\circ$

7.1 Proposed Scheme: Analysis and Design

The proposed dual-frequency impedance matching network scheme is illustrated in Fig. 7.1. The task is to match a frequency-dependent complex load, $Z_L=R_1+jX_1 @f_1$ and $Z_L=R_2+jX_2 @f_2$, to a real source impedance of Z_0 (usually 50Ω). A **load-healing** element is embedded between the conventional T-network and the load. In fact, the load-healer could be as complex as another T-network itself but a fair requirement of the load-healer is to be as simplistic as possible. Therefore, two simple load-healers named as type-1, which is a simple transmission line (TL) section, and type-2, which is an open circuited stub, is used here to illustrate the whole idea. A short circuited stub is also feasible as load healer but at the cost of increased step of digging a via to the ground.

In this proposed network, the load-healing element modifies the load and transforms Z_L into another frequency dependent complex load, $Z_{Lx}=R_{1x}+jX_{1x} @f_1$ and $=R_{2x}+jX_{2x} @f_2$, which is a function of Z_x , θ_x , and $r = f_2/f_1$. Now, section A of the T-network transforms Z_{Lx} into admittance, Y_{2n} , which is related by complex conjugate relation at the two frequencies i.e. $Y_{2n}|_{f_1} = Y_{2n}^*|_{f_2}$. Similarly, section B is used to transform the source impedance, Z_0 , into an admittance Y_{1n} such that $Y_{1n}|_{f_1} = Y_{1n}^*|_{f_2}$. To achieve complex conjugate matching, the real part of Y_{1n} is equated that to the real part of Y_{2n} and the remaining net imaginary part at the node N is cancelled by section C, a

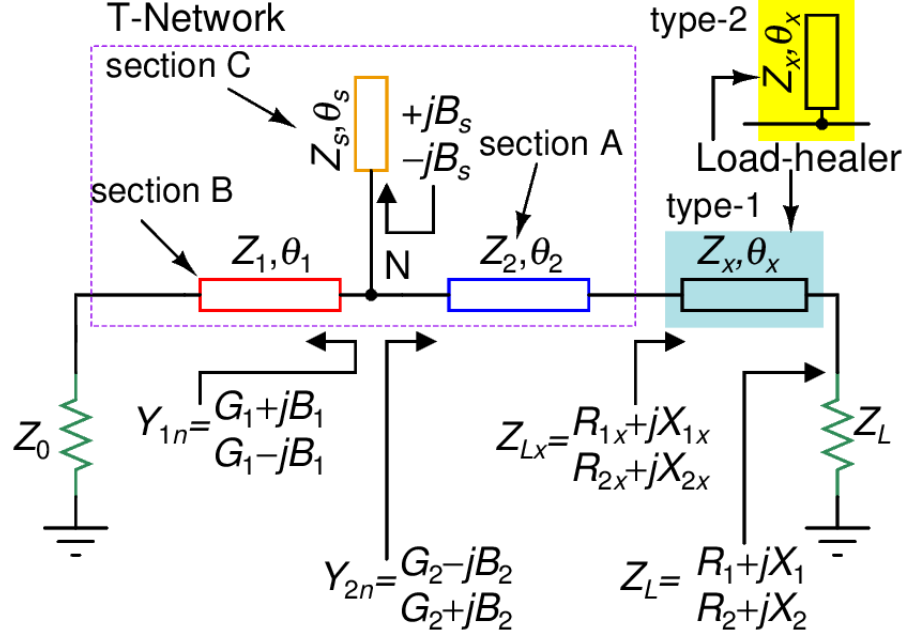


Figure 7.1 Proposed matching scheme incorporating lead-healing element.

dual-frequency stub. Design equations of the proposed matching network are discussed in the next section.

7.1.1 The Load-Healer

Considering the type-1 load-healer first, Z_{Lx} is found by using the formula of input impedance of a loaded TL section.

$$Z_{Lx} = Z_x \frac{Z_L + jZ_x \tan \theta_x}{Z_x + jZ_L \tan \theta_x} \quad (7-1)$$

Now, simplifying and separating the real and imaginary parts yields R_{1x} and X_{1x} as:

$$R_{1x} = \frac{R_1 Z_x^2 \sec^2 \theta_x}{(Z_x - X_1 \tan \theta_x)^2 + (R_1 \tan \theta_x)^2} \quad (7-2)$$

$$X_{1x} = Z_x \frac{(X_1 + Z_x \tan \theta_x)(Z_x - X_1 \tan \theta_x) - R_1^2 \tan \theta_x}{(Z_x - X_1 \tan \theta_x)^2 + (R_1 \tan \theta_x)^2} \quad (7-3)$$

Since electrical length is proportional to frequency, the terms θ_x defined at f_1 becomes $r\theta_x$ at f_2 . Thus, R_{2x} and X_{2x} are given by:

$$R_{2x} = \frac{R_2 Z_x^2 \sec^2 r\theta_x}{(Z_x - X_2 \tan r\theta_x)^2 + (R_2 \tan r\theta_x)^2} \quad (7-4)$$

$$X_{2x} = Z_x \frac{(X_2 + Z_x \tan r\theta_x)(Z_x - X_2 \tan r\theta_x) - R_2^2 \tan r\theta_x}{(Z_x - X_2 \tan r\theta_x)^2 + (R_2 \tan r\theta_x)^2}. \quad (7-5)$$

It can be easily comprehended from (7-2) - (7-5) that:

$$\lim_{\theta_x \rightarrow 0} Z_{Lx} = Z_L. \quad (7-6)$$

And, thus, the strength of the proposed scheme is clearly evident. It can be used for all those impedances normally handled by the conventional T-type matching network in addition to what cannot be handled by the same.

Now, for the type-2 load-healer, Z_{Lx} is given by the following expression:

$$Z_{Lx} = Z_L \parallel -jZ_x \cot \theta_x = \frac{-jZ_x Z_L \cot \theta_x}{Z_L - jZ_x \cot \theta_x} \quad (7-7)$$

Following the same procedure opted for type-1 load-healer; the following expressions are obtained in this case.

$$R_{1x} = \frac{R_1 Z_x^2 \cot^2 \theta_x}{R_1^2 + (X_1 - Z_x \cot \theta_x)^2} \quad (7-8)$$

$$X_{1x} = \frac{Z_x \cot \theta_x \left[R_1^2 + X_1 (X_1 - Z_x \cot \theta_x) \right]}{R_1^2 + (X_1 - Z_x \cot \theta_x)^2} \quad (7-9)$$

$$R_{2x} = \frac{R_2 Z_x^2 \cot^2 r\theta_x}{R_2^2 + (X_2 - Z_x \cot r\theta_x)^2} \quad (7-10)$$

$$X_{2x} = \frac{Z_x \cot r\theta_x \left[R_2^2 + X_2 (X_2 - Z_x \cot r\theta_x) \right]}{R_2^2 + (X_2 - Z_x \cot r\theta_x)^2} \quad (7-11)$$

Condition given by (7-6) also holds true for the type-2 load-healer.

7.1.2 Design of Section A

The role of this section is to transform Z_{Lx} into an admittance Y_{2n} , such that $Y_{2n}|_{f_1} = Y_{2n}^*|_{f_2}$

. Therefore, this section is designed using the following equations [40]:

$$Z_2 = \sqrt{R_{1x}R_{2x} + X_{1x}X_{2x} + \frac{X_{1x} + X_{2x}}{R_{2x} - R_{1x}}(R_{1x}X_{2x} - R_{2x}X_{1x})} \quad (7-12)$$

$$\theta_2 = \frac{p\pi + \arctan\left(\frac{Z_{1x}(R_{1x} - R_{2x})}{R_{1x}X_{2x} - R_{2x}X_{1x}}\right)}{1+r}, p \in \text{integer}. \quad (7-13)$$

With the section A designed using (7-12) - (7-13), the value of G_2 and B_2 are given by the following relations [40, 59]:

$$G_2 = \frac{a}{a^2 + b^2} \quad (7-14)$$

$$B_2 = \frac{b}{a^2 + b^2} \quad (7-15)$$

Where, a and b are given by (7-16) - (7-17):

$$a = \frac{R_{1x}Z_2^2[1 + \tan^2 \theta_2]}{Z_2^2 - 2Z_2X_{1x} \tan \theta_2 + (R_{1x}^2 + X_{1x}^2) \tan^2 \theta_2} \quad (7-16)$$

$$b = \frac{(Z_2^2 - R_{1x}^2 - X_{1x}^2)Z_2 \tan \theta_2 + Z_2^2X_{1x}(1 - \tan^2 \theta_2)}{Z_2^2 - 2Z_2X_{1x} \tan \theta_2 + (R_{1x}^2 + X_{1x}^2) \tan^2 \theta_2} \quad (7-17)$$

7.1.3 Design of Section B

Applying the formula of input impedance, Y_{1n} can be expressed as $G_1 + jB_1$ with G_1 and B_1 given by:

$$G_1 = \frac{Z_0(1 + \tan^2 \theta_1)}{Z_0^2 + Z_1^2 \tan^2 \theta_1} \quad (7-18)$$

$$B_1 = \frac{(Z_0^2 - Z_1^2) \tan \theta_1}{Z_1(Z_0^2 + Z_1^2 \tan^2 \theta_1)} \quad (7-19)$$

It is apparent from (7-18)-(7-19) that G_1 remains the same whereas B_1 just changes its sign if θ_1 is replaced by $\pi - \theta_1$. Therefore, if θ_1 is selected according to (7-20) then $Y_{1n}|_{f_1} = Y_{1n}^*|_{f_2}$, i.e., if $Y_{1n} = G_1 + jB_1 @f_1$, then $Y_{1n} = G_1 - jB_1 @f_2$ and vice-versa.

$$\theta_1 = \frac{q\pi}{1+r}, q \in \text{integer}. \quad (7-20)$$

Now setting $G_1 = G_2$ leads to the expression of Z_1 :

$$Z_1 = \frac{1}{\tan \theta_1} \sqrt{\frac{Z_0(1 + \tan^2 \theta_1)}{G_2} - Z_0^2} \quad (7-21)$$

7.1.4. Design of Section C

Having designed the sections A and B, the last step is to cancel the remaining imaginary parts of Y_{1n} and Y_{2n} at the junction N. The net sum of imaginary parts are $+(B_1 - B_2) @f_1$ and $-(B_1 - B_2) @f_2$. Since admittance sums at a junction, the task therefore is to synthesize an admittance using section C that is equal to $-(B_1 - B_2) @f_1$ and $+(B_1 - B_2) @f_2$. There are three simple options to synthesize these admittances as shown in Fig. 7.2. Noting that θ_s defined at f_1 becomes $r\theta_s$ at f_2 , an open stub needs to satisfy the following equations:

$$(B_2 - B_1) = Y_s|_{f_1} = \tan \theta_s / Z_s \quad (7-22)$$

$$-(B_2 - B_1) = Y_s|_{f_2} = \tan r\theta_s / Z_s \quad (7-23)$$

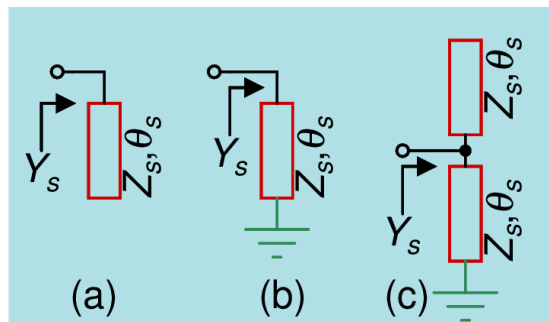


Figure 7.2 Dual-frequency stubs to be used as section C (a) open, (b) short, and (c) open-short combination.

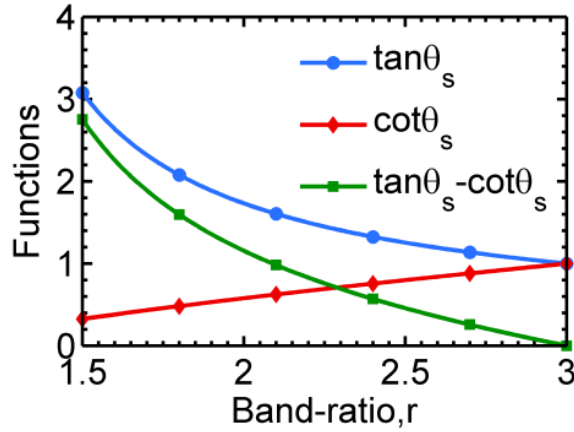


Figure 7.3 Numerators of stub design equations against the band-ratio.

Solving (7-22) and (7-23) simultaneously gives the following design equations:

$$Z_s = \tan \theta_s / (B_2 - B_1) \quad (7-24)$$

$$\theta_s = \frac{m\pi}{1+r}, m \in \text{integer}. \quad (7-25)$$

Design equations for a short stub shown in Fig. 7.2(b) remains the same except that $-\cot\theta_s$ needs to be used in (7-24) instead of $\tan\theta_s$ [60]. Moreover, if an open-short stub combination, Fig. 7.2(c), is to be used then the designs equations are:

$$Z_s = (\tan \theta_s - \cot \theta_s) / (B_2 - B_1) \quad (7-26)$$

While details of these dual-frequency stubs were provided in Chapter 5, and in [60], but it is interesting to consider the open-short combination a little further in order to understand its other features. For this purpose, three functions namely the numerators of the design equations of the three stubs, $\tan\theta_s$, $\cot\theta_s$, and $\tan\theta_s - \cot\theta_s$, are plotted in Fig. 7.3. It is apparent that for $r > 2.3$, $\tan\theta_s - \cot\theta_s$ is lesser than the other two functions. An implication of this fact is that the open-short combination may yield a realizable value of Z_s while the other two may not. For example, if $r = 2.7$ and $B_2 - B_1 = 0.0025$ then the required values of Z_s are 454.5Ω , 352Ω and 102.5Ω respectively for the open, short, and open-short combination. The first two are unrealizable whereas the third is realizable in microstrip technology. And, thus the advantage of using the open-short stub type is evident in such a scenario.

7.1.5. Design Procedure

The flowchart of design procedure is illustrated in Fig. 7.4. The design begins with assuming suitable values of Z_x and θ_x . Ideally, θ_x should be selected as small as possible and Z_x must lie within the range of 20Ω to 140Ω . Moreover, during the design cycle, characteristics impedance of each of the TL section of T-network must be ensured within the fabrication limit otherwise one needs to change Z_x or θ_x or both. While designing section C, all the three types of stub should be designed to find the most suitable one, unless there is design restriction on using short stub. The integers, p , q , and m are usually selected either equal to 1 or 2 to achieve compact size and to ensure positive value of various TL sections [60].

7.2 Design Examples, Prototypes and Measurement Results

The design cases listed in TABLE 7-1 that cannot be realized using the conventional T-network are chosen as the design examples. The corresponding design parameters of the proposed technique are listed in TABLE 7-2 with type-1 load-healer and in TABLE 7-3 with type-2 load-healer. It is apparent that none of the parameters are beyond the impedance limit of 20Ω to 140Ω . Moreover, it is interesting to observe how addition of very small length of TL section turns otherwise unrealizable design into realizable

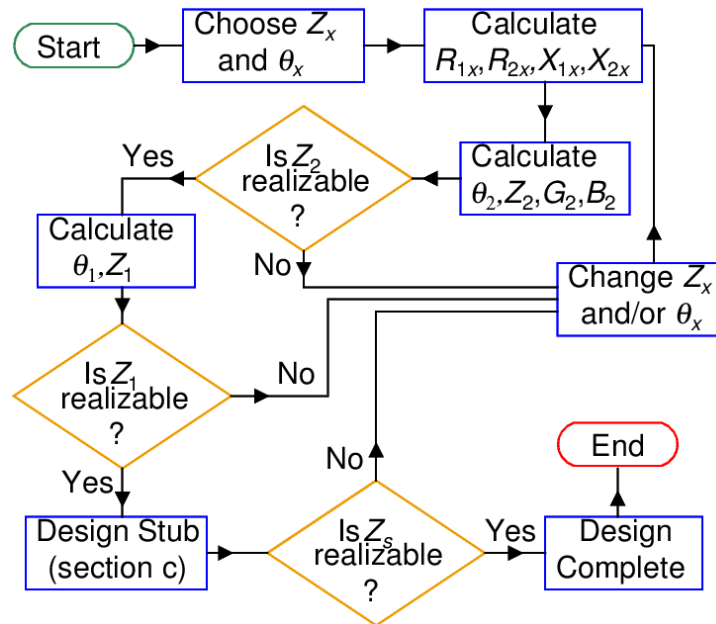


Figure 7.4 Flowchart illustrating the design procedure.

ones. It must be noted that since Z_x and θ_x are free variables, the examples in TABLE 7-2 / TABLE 7-3 is just one possible value for each case out of several possibilities. Figs. 7-5 and 7-6 show the return and insertion losses of the design cases listed in TABLES 7-2 and 7-3 respectively. A good matching and insertion loss performance is evident from these plots. The simulation results have been obtained using ideal transmission lines as well as their implementation in FR4 ($\epsilon_r=4.6$, height=1.5mm, copper cladding =35 μ m, and loss-tangent=0.02) and in Roger's RO5880[®] ($\epsilon_r=2.2$, height=1.5mm, copper cladding =35 μ m, and loss-tangent=0.0009) microstrip substrates. The correspo-

Table 7-2 Proposed Network (Type-1) Parameters for Cases of TABLE 7-1

Case	Z_x/θ_x	Z_2/θ_2	Z_1/θ_1	Z_s/θ_s
1	$Z_x=40\Omega$ $\theta_x=10^\circ$	$Z_2=49.3\Omega$ $\theta_2=37.03^\circ$	$Z_1=105.9\Omega$ $\theta_1=60^\circ$	$Z_s=113.8\Omega$ $\theta_s=60^\circ$ Open Stub
2	$Z_x=60\Omega$ $\theta_x=5^\circ$	$Z_2=64.2\Omega$ $\theta_2=41.26^\circ$	$Z_1=69.52\Omega$ $\theta_1=51.43^\circ$	$Z_s=88.33\Omega$ $\theta_s=51.43^\circ$ Short Stub
3	$Z_x=60\Omega$ $\theta_x=30^\circ$	$Z_2=46.5\Omega$ $\theta_2=54.3^\circ$	$Z_1=40.48\Omega$ $\theta_1=67.5^\circ$	$Z_s=53.84\Omega$ $\theta_s=135^\circ$ Open Stub

Table 7-3 Proposed Network (Type-2) Parameters for Cases of TABLE 7-1

Case	Z_x/θ_x	Z_2/θ_2	Z_1/θ_1	Z_s/θ_s
1	$Z_x=30\Omega$ $\theta_x=5^\circ$	$Z_2=41.2\Omega$ $\theta_2=42.22^\circ$	$Z_1=87.4\Omega$ $\theta_1=60^\circ$	$Z_s=100.8\Omega$ $\theta_s=60^\circ$ Open Stub
2	$Z_x=80\Omega$ $\theta_x=4^\circ$	$Z_2=45.77\Omega$ $\theta_2=45.88^\circ$	$Z_1=64.87\Omega$ $\theta_1=51.43^\circ$	$Z_s=42.48\Omega$ $\theta_s=51.43^\circ$ Short Stub
3	$Z_x=120\Omega$ $\theta_x=4^\circ$	$Z_2=99.25\Omega$ $\theta_2=46.5^\circ$	$Z_1=92.9\Omega$ $\theta_1=135^\circ$	$Z_s=84.4\Omega$ $\theta_s=67.5^\circ$ Short Stub

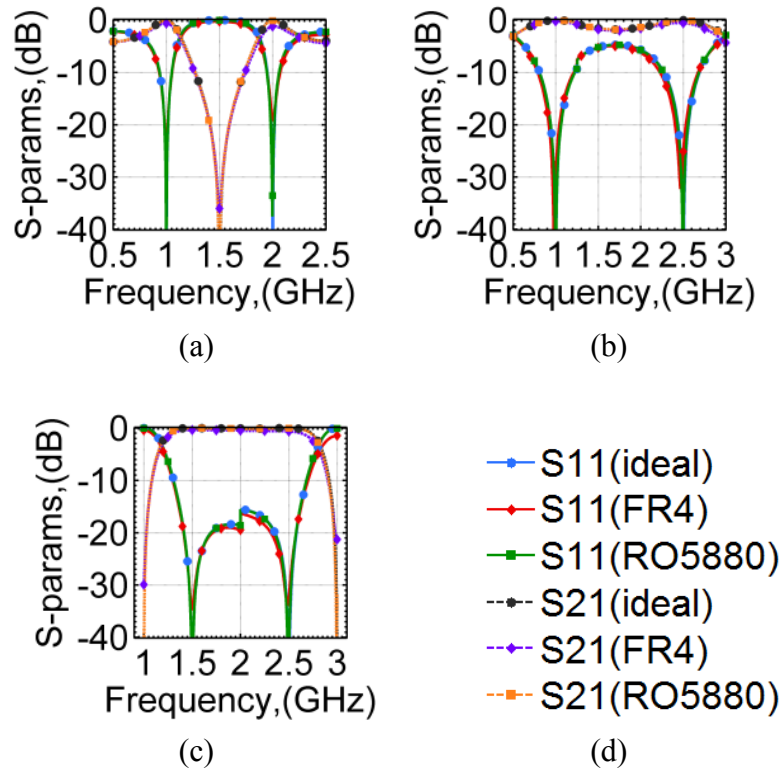


Figure 7.5 Simulated return and insertion-losses corresponding to the Table II designs

(a) Case 1 (b) Case 2 (c) Case 3, and (d) legend.

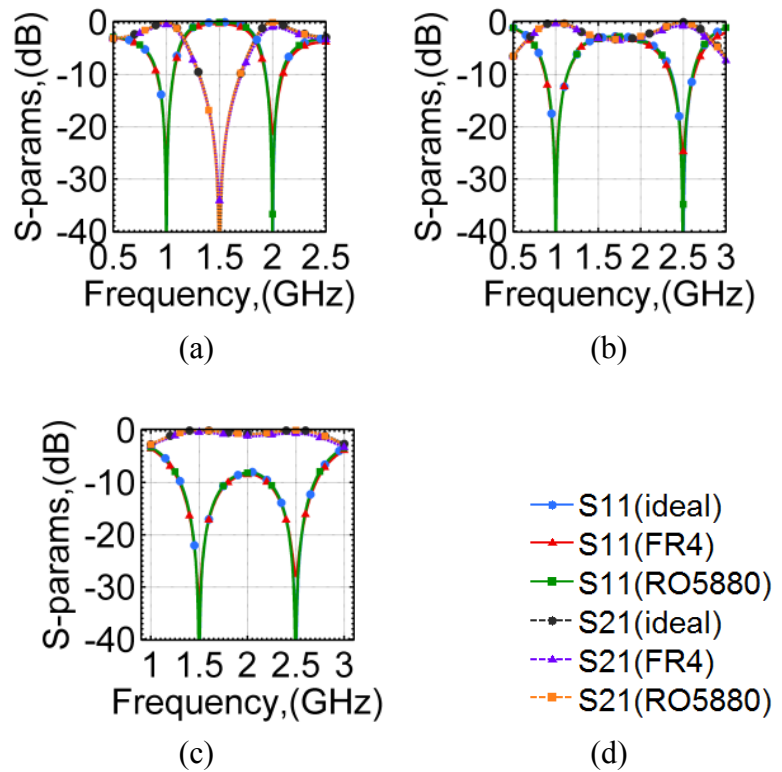


Figure 7.6 Simulated return and insertion-losses corresponding to the Table III designs

(a) Case 1 (b) Case 2 (c) Case 3, and (d) legend.

ding dimensions can easily be calculated using any line calculator software, such as ADS LineCalc[®]. Moreover, since RO5880[®] is a very low loss and more frequency stable material, therefore, performance obtained using this substrate is significantly better than the corresponding results obtained using FR4.

To validate the ongoing discussion, two prototypes for $Z_L = 92.971 - j15.784\Omega$ @ 1GHz and $Z_L = 78.816 - j21.529\Omega$ @ 2GHz have been designed corresponding to the two types of the load-healers. These designs, depicted in Fig. 7.7, are implemented on FR4 substrate ($\epsilon_r = 4.6$, height = 1.5mm, copper = 35 μ m). The frequency dependent load is a TL section in series with a 100 Ω resistor. Their calculated design parameters are given in TABLES 7-4 and 7-5 respectively for the two types of the load-healers. The final designs need a little optimization, for example, to take junction discontinuity into

Table 7-4 Design Parameters of Prototype with Type-1 Load-Healer

Params.	Z_x/θ_x	Z_2/θ_2	Z_1/θ_1	Z_s/θ_s
Ideal	$Z_x=40\Omega$ $\theta_x=10^\circ$	$Z_2=50.7\Omega$ $\theta_2=39.8^\circ$	$Z_1=45.4\Omega$ $\theta_1=60^\circ$	$Z_s=105.3\Omega$ $\theta_s=120^\circ$ Open Stub
W/L(mm)	$W=3.98$	$W=2.71$	$W=3.26$	$W=0.51$
Calc.	$L=4.41$	$L=17.89$	$L=26.73$	$L=57.21$
W/L(mm)	$W=3.62$	$W=2.91$	$W=3.74$	$W=0.48$
Optm.	$L=4.35$	$L=17.65$	$L=25.98$	$L=56.85$

Table 7-5 Design Parameters of Prototype with Type-2 Load-Healer

Params.	Z_x/θ_x	Z_2/θ_2	Z_1/θ_1	Z_s/θ_s
Ideal	$Z_x=90\Omega$ $\theta_x=10^\circ$	$Z_2=49.37\Omega$ $\theta_2=46.45^\circ$	$Z_1=45\Omega$ $\theta_1=60^\circ$	$Z_s=99\Omega$ $\theta_s=120^\circ$ Open Stub
W/L(mm)	$W=0.80$	$W=2.83$	$W=3.30$	$W=0.61$
Calc.	$L=4.72$	$L=20.83$	$L=26.72$	$L=56.93$
W/L(mm)	$W=0.73$	$W=3.00$	$W=3.77$	$W=0.51$
Optm.	$L=4.18$	$L=21.34$	$L=27.92$	$L=58.84$

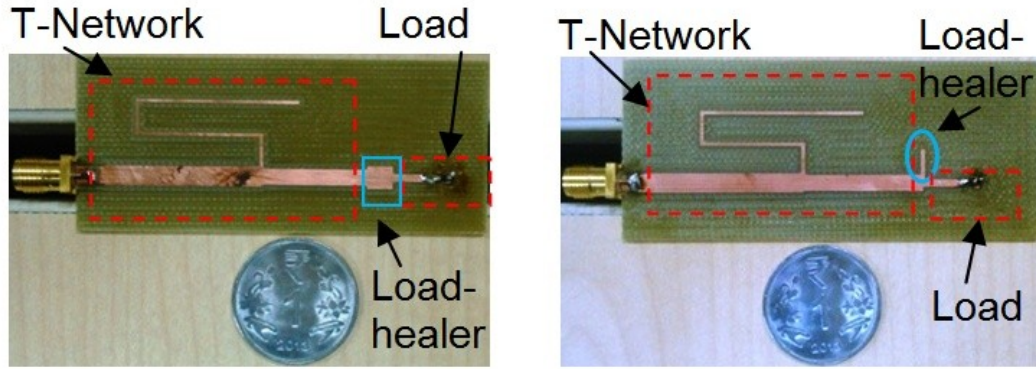


Figure 7.7 Fabricated prototypes with (a) type-1 and (b) type-2 load-healers.

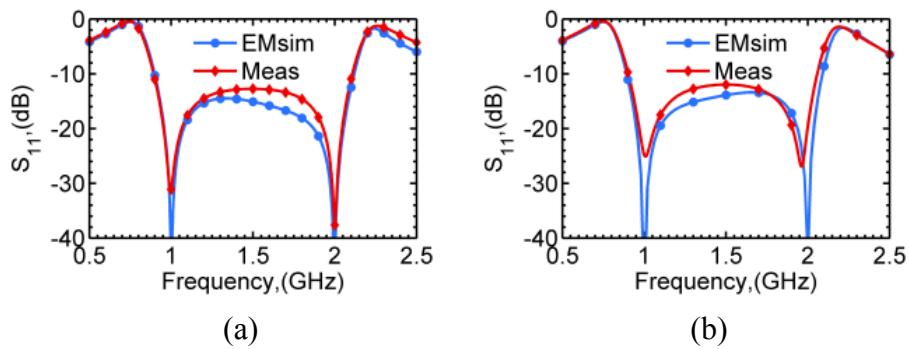


Figure 7.8 EM simulated and the measured return loss of the prototype with (a) type-1 load-healer and (b) type-2 load-healer.

account. TABLES 7-4 and 7-5 also provide the calculated and optimized design dimensions (in mm) for various parameters (params.). The corresponding electromagnetic simulated (EMsim) and measured (Meas) return losses depicted in Fig. 7.8 are in good agreement of each other and thereby validates the proposed load-healing concept.

7.3 Discussion

The limited load-range of the design reported in [5] is partly due to the fact that section A comes directly after the load. The load being complex and distinct at the two frequencies puts a heavy burden on the section A for transforming the same to a complex conjugate relation. The same limitation is also apparent in the designs reported in [21, 24, 40-41]. Therefore, the technique presented here can also be extended for those scenarios as well. Moreover, Y_{in} in Fig. 1 of [23] must be equal to $Y_0 (=1/Z_0)$

while no such restriction is present in the proposed design here due to the presence of section B. This clearly provides an additional flexibility to the proposed load-healing technique while handling frequency dependent complex loads. Furthermore, in general, the load-healer will also modify the band-width but since the load itself is frequency dependent so defining band-width in such a case is a vague idea as intuitively explained in [24].

7.4 Conclusion

This Chapter is based on author's work reported in [119]. A novel concept of dual-frequency impedance matching incorporating load-healing has been explained in this chapter. An example circuit of conventional T-type network was analyzed in presence of two simple types of load-healers. Type-1 load healer adds (although most often very little) to the total length of the network but may be preferable in cases where the type-2 load-healer would be difficult to incorporate during the layout. It is demonstrated through a number of examples that an otherwise unrealizable dual-frequency matching network could easily be realized by incorporating the load-healers. The presented scheme is generic in nature and could potentially be applied in other conventional dual-frequency impedance matching networks as well as in the tri-frequency matching network to be discussed in Chapter 9. Moreover, a combination of type-1 and type-2 load-healers may also be a potential candidate but at the cost of increased number of free variables and complexity.

Chapter 8

Dual-Frequency Admittance Property of Multi-Section Commensurate Transmission Lines

The dual-frequency admittance property of single-section transmission line was explained thoroughly in Chapter 3. It was shown in Chapter 6 that cascade of two sections of transmission lines also showed similar behavior. It was demonstrated that these properties are highly useful in the design of dual-frequency components with enhanced band-ratio.

In this chapter, a rigorous mathematical analysis will be presented to prove the existence of the dual-frequency conjugate admittance property of multi-section commensurate transmission lines. Moreover, their potential application in dual-frequency impedance matching problem is also discussed and demonstrated.

8.1 The Property and its Proof

A multi-section commensurate transmission line (TL) structure is shown in Fig.8.1. Here, Z_{ini} is the characteristic impedance of i^{th} TL-section while θ is the electrical length of each section, $i \in [1, k]$ beginning from the right, and k is the total number of TL sections.

The dual-frequency impedance property of this multi-section structure can be stated as follows:

"The impedance, Z_{ink} , looking into the multi-section line is complex conjugate of each other at the two frequencies f_1 and f_2 , that is, $Z_{ink}|_{f_1} = (Z_{ink}|_{f_2})^$, and vice-versa, if the value of θ is selected as follows:*

$$\theta = \frac{m\pi}{(1+r)}, m \in \text{Integer}, r = f_2 / f_1. \quad (8-1)$$

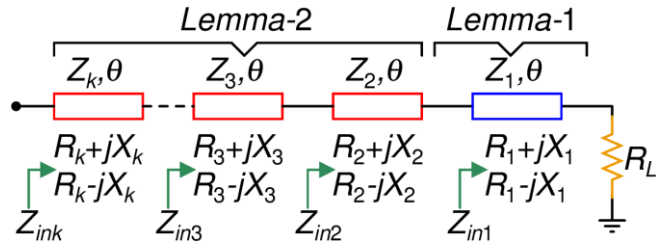


Figure 8.1 Multi-section TL terminated into a real impedance.

Moreover, since admittance is just the inverse of impedance, the above dual-frequency property also holds true for the input admittance. The proof of the above property is based on the following two lemmas.

Lemma-1: consider Fig. 8.2(a), where a TL-section having characteristic impedance Z_x and electrical length θ_x is terminated into a real impedance R_s . The term Z_{inx} is the input impedance looking into this structure. Then, the lemma-1 can be stated as:

"If θ_x is chosen as θ , that is, the same as given in (8-1), then $Z_{inx}|_{f_1} = (Z_{inx}|_{f_2})^*$, and vice-versa."

Proof: Applying the formula of input impedance for a transmission-line in Fig. 8.2(a), Z_{inx} can be expressed as:

$$Z_{inx} = Z_x \frac{R_s + jZ_x \tan \theta_x}{Z_x + jR_s \tan \theta_x} = R_x + jX_x \quad (8-2)$$

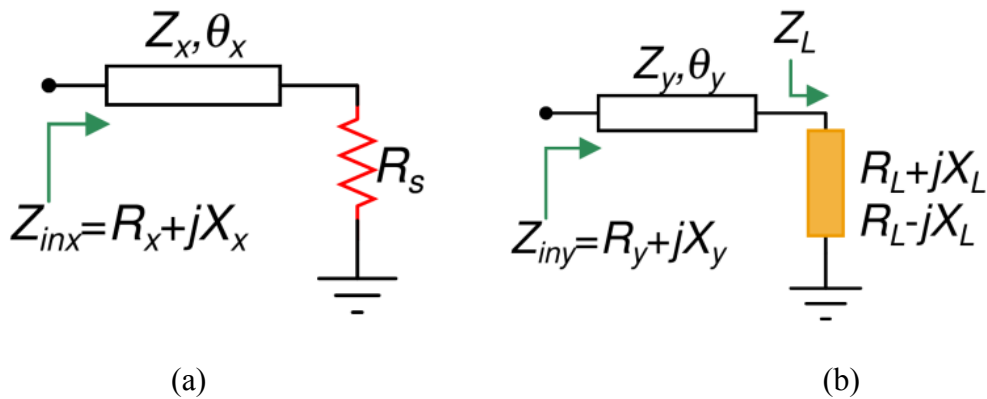


Figure 8.2 A TL section terminated into (a) a real impedance (b) complex conjugate impedance.

where,

$$R_x = \frac{R_s Z_x^2 (1 + \tan^2 \theta_x)}{Z_x^2 + R_s^2 \tan^2 \theta_x} \quad (8-3)$$

$$X_x = \frac{Z_x (Z_x^2 - R_s^2) \tan \theta_x}{Z_x^2 + R_s^2 \tan^2 \theta_x} \quad (8-4)$$

A quick look at the above expression reveals that if θ_x is replaced by $m\pi - \theta_x$, then R_x remains the same whereas just the sign of X_x gets changed. Therefore, if θ_x is the electrical length assigned to the TL at the first frequency, f_1 , and it is chosen in such a manner that the corresponding electrical length at the second frequency, f_2 , is $m\pi - \theta_x$, then the following expressions can be written while considering that electrical length is proportional to frequency:

$$\theta_x = k_1 f_1 \quad (8-5)$$

$$m\pi - \theta_x = k_1 f_2 \quad (8-6)$$

where, k_1 is some constant with unit of rad/Hz.

Solving (8-5) and (8-6) for θ_x gives the following expression:

$$\theta = \frac{m\pi}{(1+r)}, m \in \text{Integer}, r = f_2 / f_1 \quad (8-7)$$

Lemma-2: consider Fig. 8.2(b), where a TL-section having characteristic impedance Z_y and electrical length θ_y is terminated into an impedance Z_L , which has complex conjugate relation at two frequencies, that is, $Z_L|_{f_1} = (Z_L|_{f_2})^*$. The term Z_{iny} is the input impedance looking into this structure. Then, the lemma-2 can be stated as:

"If θ_y is chosen as θ , that is, the same as given (8-1), then $Z_{iny}|_{f_1} = (Z_{iny}|_{f_2})^*$, and vice-versa."

Proof: Applying the formula of input impedance for a transmission-line in Fig. 8.2(b) and after subsequent simplification the following expressions are obtained.

$$R_y|_{f_1} = \frac{R_L Z_y^2 (1 + \tan^2 \theta_y)}{(Z_y - X_L \tan \theta_y)^2 + (R_L \tan \theta_y)^2} \quad (8-8)$$

$$X_y|_{f_1} = Z_y \frac{(X_L + Z_y \tan \theta_y)(Z_y - X_L \tan \theta_y) - R_L^2 \tan \theta_y}{(Z_y - X_L \tan \theta_y)^2 + (R_L \tan \theta_y)^2} \quad (8-9)$$

Now, considering the fact that an electrical length θ defined at f_1 becomes $r\theta$ at f_2 ; $R_y|_{f_2}$ and $X_y|_{f_2}$ are obtained from (8-8) and (8-9) by replacing θ_y with $r\theta_y$ and X_L with $-X_L$. Then, it is apparent from (8-8) and (8-9) that for $Z_{iny}|_{f_1} = (Z_{iny}|_{f_2})^*$ to hold true, one must ensure $\tan r\theta_y = -\tan \theta_y$, and this requires that θ_y should be given by:

$$\theta = \frac{m\pi}{(1+r)}, m \in \text{Integer}, r = f_2 / f_1 \quad (8-10)$$

Now, use of the lemma-1 and lemma-2 in Fig. 8.1 proves the dual-frequency impedance property of the multi-section line.

8.2 Application of the Property

The classic two-section Monzon transformer [34], which can be considered as a special case of the proposed multi-section transformer, has no independent (free) variable as is apparent from (19) - (20) of [34]. This fact limits the range of load (and thus, the transformation-ratio $K=Z_0/R_L$) that can be matched using the same. Here, R_L is the load impedance whereas $Z_0=50\Omega$ is the source impedance. To illustrate this aspect, plots of the line impedances of the Monzon transformer against the load impedance are shown in Fig. 8.3 for $r = 1.5, 2,$ and 3.5 . Two scenarios are considered, first the load impedance is smaller as compared to the source impedance ($K >1$, Fig. 8.3(a)), and second the load impedance is larger as compared to the source impedance ($K <1$, Fig. 8.3(b)). It is evident from Fig. 8.3 that as R_L moves below 15Ω or beyond 240Ω , the required values of either or both of the line impedances are less than 20Ω or greater than 150Ω . Typically, the realizable characteristic impedance of microstrip lines that can be fabricated lies between 20Ω to 150Ω . Thus, it is clear that Monzon two-section transformer is very limited in many scenarios. And, therefore, in the next subsections potential of the dual-frequency impedance property to mitigate this limitation is investigated.

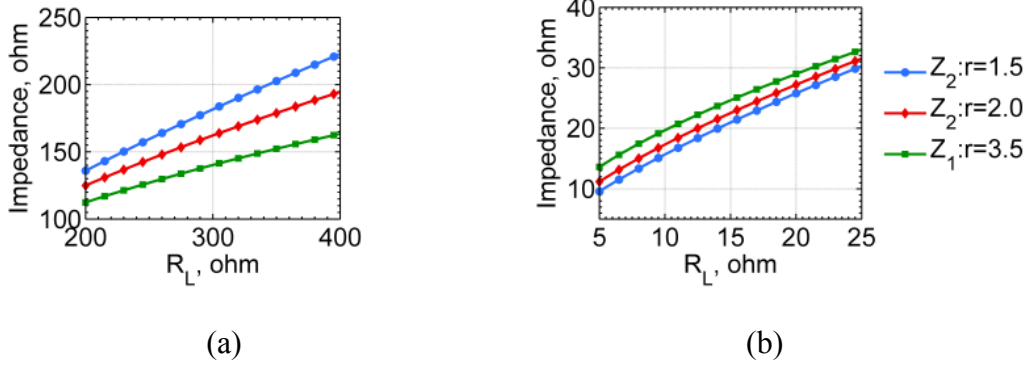


Figure 8.3 The variation of line impedances with the load impedance in Monzon transformer for $r=1.5, 2$ and 3.5 , when (a) $R_L > Z_0$ (b) $R_L < Z_0$.

8.2.1 Proposed Tri-Section Dual-Frequency Transformer

The proposed tri-section dual-frequency impedance transformer is shown in Fig. 8.4. As depicted, Z_{ini} , where $i=\{1,2,3\}$, is the input impedance looking into the i^{th} transmission line beginning from the right. Moreover, since θ is to be chosen according to (8-1), therefore Z_{ini} , $i = \{1,2,3\}$, has the complex conjugate relation at the two frequencies. The expression of R_1 and X_1 can be obtained using (8-3) and (8-4).

Following expressions for the shown tri-section network can be deduced.

$$Z_{in2} = Z_2 \frac{R_1 + jX_1 + jZ_2 \tan \theta}{Z_2 + j(R_1 + jX_1) \tan \theta} \quad (8-11)$$

$$Z_{in3} = Z_3 \frac{Z_{in2} + jZ_3 \tan \theta}{Z_3 + jZ_{in2} \tan \theta} \quad (8-12)$$

Eliminating Z_{in2} from (8-11) and (8-12) and invoking $Z_{in3}=Z_0$, the following equations are obtained. The term a in the following expressions refers to $\tan \theta$.

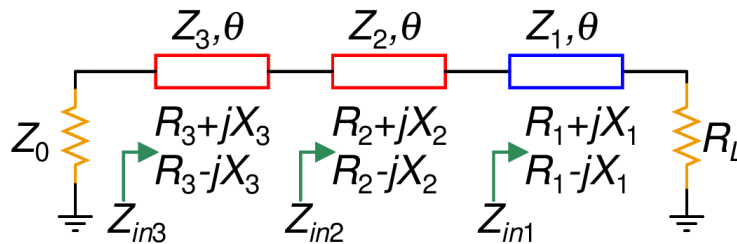


Figure 8.4 Proposed tri-section dual-frequency impedance transformer.

$$Z_0 a^2 Z_2^2 + [Z_0 X_1 a + Z_3 (R_1 - Z_0)] Z_2 + [Z_3 Z_0 X_1 a - Z_3^2 R_1 a^2] = 0 \quad (8-13)$$

$$Z_3 a Z_2^2 + [Z_3 X_1 - R_1 Z_0 a + Z_3^2 a] Z_2 - [Z_3 Z_0 R_1 a + Z_3^2 X_1 a^2] = 0 \quad (8-14)$$

Elimination of Z_2 from (8-13) and (8-14) results into a 4th-order equation in Z_3 :

$$AZ_3^4 + BZ_3^3 + CZ_3^2 + DZ_3 + E = 0 \quad (8-15)$$

where:

$$A = \frac{R_1^2 a^4}{Z_0} - p_1 (R_1 - Z_0) \frac{R_1 a}{Z_0} - R_1 p_1^2 a^2 \quad (8-16)$$

$$B = p_1 X_1 (R_1 - Z_0) (1 + a^2) + p_1^2 Z_0 X_1 a - p_1 X_1 R_1 a^2 - 2 X_1 R_1 a^3 (1 + a^2) \quad (8-17)$$

$$C = Z_0 X_1^2 a^2 (1 + a^2)^2 - 2 Z_0 R_1^2 a^4 + 2 p_1 Z_0 R_1^2 a^3 + R_1^2 (R_1 - Z_0) a^2 + p_1 Z_0 X_1^2 a (1 + a^2) + p_1 R_1 Z_0 (R_1 - Z_0) a \quad (8-18)$$

$$D = 2 Z_0^2 R_1 X_1 a^3 (1 + a^2) + R_1^2 X_1 a^3 - Z_0 R_1 X_1 (R_1 - Z_0) a (1 + a^2) - p_1 Z_0^2 R_1 X_1 a^2 \quad (8-19)$$

$$E = Z_0^3 R_1^2 a^4 - Z_0^2 R_1 X_1^2 a^2 (1 + a^2) - Z_0^2 R_1^2 (R_1 - Z_0) a^2 - Z_0^2 R_1^3 a^4 \quad (8-20)$$

$$p_1 = a + \frac{1}{a} \left(1 - \frac{R_1}{Z_0}\right) \quad (8-21)$$

This 4th order equation (8-15) can be solved for Z_3 and subsequently Z_2 can be obtained from (8-13) and (8-14).

$$Z_2 = \frac{Z_0 R_1 a Z_3 + X_1 (1 + a^2) Z_3^2 - \frac{R_1 a}{Z_0} Z_3^3}{p_1 Z_3^2 - Z_0 R_1 a} \quad (8-22)$$

Regarding the proposed tri-section dual-frequency transformer, following aspects can be mentioned.

- 1) Solution of (8-15) and (8-22) depends on R_1 and X_1 which in turn depends on Z_1 . Therefore, Z_1 is a free variable which provides flexibility to the proposed tri-section transformer. This free variable is not present in the Monzon two-section transformer. In fact, the proposed tri-section transformer is a more generic form of

Monzon transformer. Specifically, when the length of the line having characteristic impedance Z_1 tends to zero, the proposed transformer reduces to the Monzon transformer since $X_1=0$ and $R_1=R_L$ in this scenario.

- 2) Z_1 is a free yet a bounded variable and its value is selected appropriately in the range 20Ω to 150Ω until realizable values of Z_2 and Z_3 are obtained.

8.2.2 Generic Multi-Section Transformer Design

After discussing working of the proposed tri-section dual-frequency impedance transformer, it is now easier to extend the same to multi-section transformer. The following guidelines can be used to assess the design equations.

For the proposed tri-section dual-frequency impedance transformer Z_3 and Z_2 are the variable to be determined and Z_1 is assumed to be a free variable. On a similar line, for quad-section transformer Z_4 and Z_3 are to be determined and Z_2 and Z_1 can be assumed to be free variables. In general, for k -section transformer of Fig. 1, Z_k and Z_{k-1} are to be determined and Z_{k-2} , Z_{k-3} , ..., and Z_1 are assumed to be free variables. Now, in order to determine Z_k and Z_{k-1} , one simply needs to replace Z_3 and Z_2 in (8-15) and (8-22) by Z_k and Z_{k-1} respectively. The required values of R_1 and X_1 in (8-15)-(8-29) are now functions of Z_{k-2} , Z_{k-3} , ..., and Z_1 , and they can readily be obtained using (8-3)-(8-4), and recursive use of (8-8)-(8-9).

8.2.3 Simulation and Discussion

Fig. 8.5 depicts the line impedance variations for the proposed three-section transformer for different values of $r = 1.5, 2$ and 3.5 for the case $R_L > Z_0$ in Figs. 8.5(a) to (c) and for the case $R_L < Z_0$ in Figs. 8.5(d) to (f). These plots are obtained by using the equations derived in the previous section and letting Z_1 to assume any value between 20Ω - 150Ω . Comparing these plots with the Monzon two-section transformer response shown earlier in Fig. 8.3, it is apparent that the required line impedances fall within the realizable impedance limit. Specifically, it must be noted that the required characteristics impedances are neither below 20Ω nor above 150Ω . Please also note Fig. 8.5 just shows one of the possible profiles for each scenario considering that Z_1 is a free variable and there can be several such scenarios. .

Next, since there are more than one free variable for quad-/higher-section transformer, it is more meaningful to show their potential using few examples. To that end, TABLE 8-1 shows few example of the proposed quad-section transformer with their corresponding simulation results in Fig. 8.6. The proper dual-frequency behavior is apparent. Thanks to the availability of two free design variables (Z_1 and Z_2) now, the parameters of quad-section transformer can be more easily realized in microstrip.

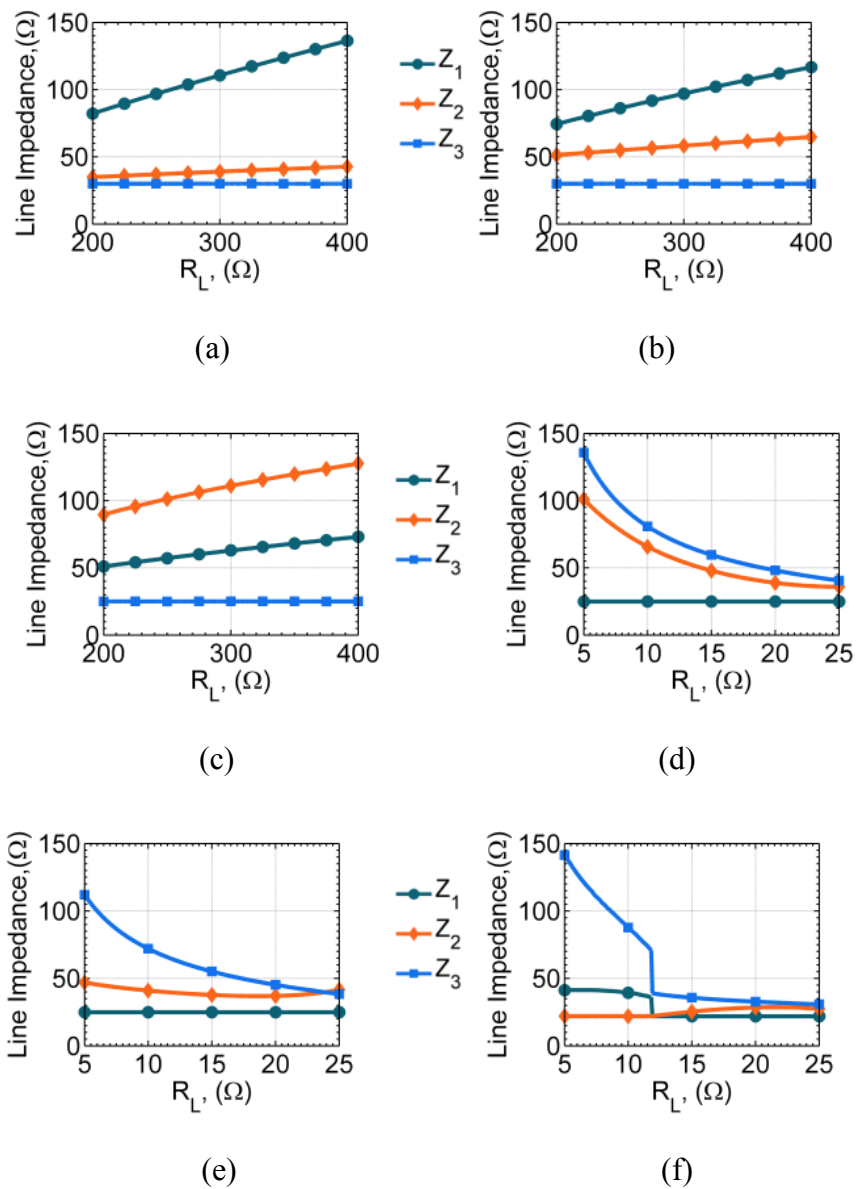
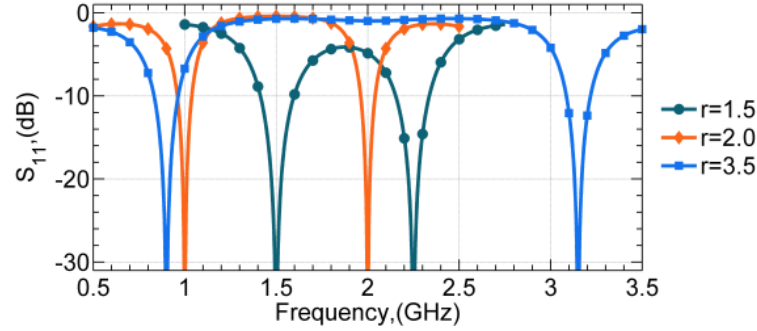


Figure 8.5 Line impedance variation for the proposed tri-section dual-frequency impedance transformer, when $R_L > Z_0$ and (a) $r = 1.5$, (b) $r = 2$, and (c) $r = 3.5$, and, when $R_L < Z_0$ and (d) $r = 1.5$, (e) $r = 2$, and (f) $r = 3.5$.

Table 8-1 Line Impedance of Quad-Section Transformer, $R_L=400\Omega$

r	$Z_1(\Omega)$	$Z_2(\Omega)$	$Z_3(\Omega)$	$Z_4(\Omega)$
1.5	100	40	42.34	77.31
2.0	70	60	37.38	99.12
3.5	71.1	105.2	30.05	30.01

**Figure 8.6** Return-loss of the proposed quad-section transformer.

At this juncture, it is relevant to draw the reader's attention to another interesting design reported earlier in [40]. The proposed tri-section transformer is distinctively different from that reported in [40] in the following ways:

- 1) The earlier reported transformer cannot match a real impedance to another real impedance. Specifically, it must be noted that substituting $R_a=R_b=R_L$ in equation (13) of [40] does not yield a realistic solution.
- 2) The concept of the proposed tri-section transformer emanates from a more generalized and easily comprehensible dual-frequency property of multi-section transmission line discussed in Section II. Therefore, it can be extended to, say, a four-section transformer, while [40] cannot.

8.2.4 Prototypes and Measurement Results

Three designs of the proposed tri-section impedance transformers are implemented on Roger's RO4003C substrate having dielectric constant $\epsilon_r=3.55$ and substrate height of 0.8mm on 35 μ m copper cladding as shown in Fig. 8.7(a). Here '1', '2' and '3' denote the design number as well as the port number. l_i and w_i , $i=\{1,2,3\}$, represents the length and width of the i^{th} section for each design. The complete details of each design are

mentioned in TABLE 8-2. A 10Ω resistor has been used for design 2 as any lower value is not available. Each design is a single-port network and their return loss is measured using N5230A PNA-L 13.5GHz network analyzer as depicted in Fig. 8.7(b). The measured return loss of each design is shown in Fig. 8.7(c).

Table 8-2 Design Parameters of the Prototype (Dimensions: Mils)

No.	$r, f_1(\text{GHz})$	$R_L(\Omega)$	l_3/w_3	l_2/w_2	l_1/w_1
1	$r=1.5, f_1=1.5$	402	916.4/211	888.8/154.4	908.4/17.2
2	$r=2.0, f_1=1.0$	10	1246.6/18.2	1170.4/61.6	1063.7/125
3	$r=3.5, f_1=0.9$	402	1734.9/153.5	909.9/17.6	43.57
Part No. for R_L :		CRCW0603402RFKEA (402Ω) CRCW060310R0FKEA (10Ω)			

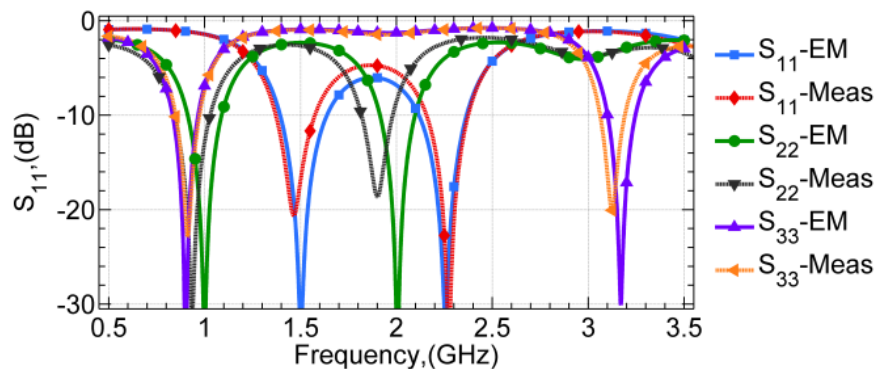
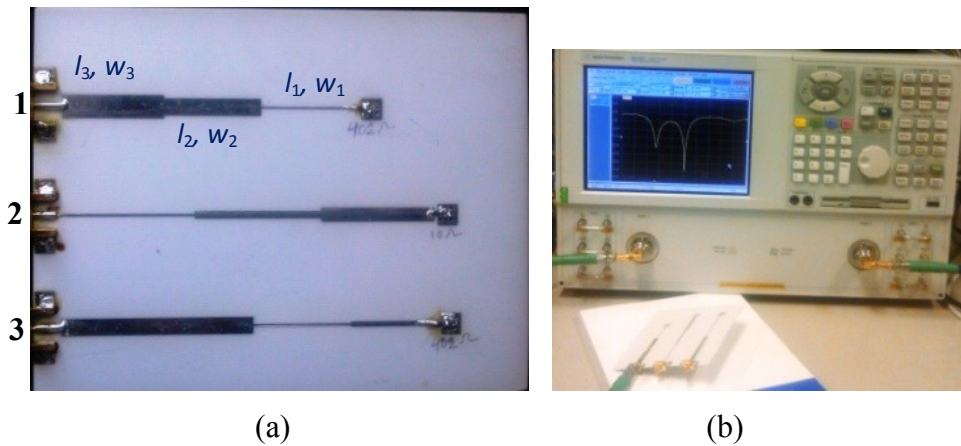


Figure 8.7 (a) The fabricated prototype, (b) measurement setup, and (c) comparison of return losses obtained from EM-simulation and measurement.

It is apparent from the simulated and the measured results that the prototypes are cable of providing the required matching. Slight discrepancy between the simulation and measured data may be attributed to inaccurate model of resistors and via effects.

Now for 15dB reference, the minimum achievable bandwidth of 61MHz occurs for the design 3 at f_2 . This bandwidth is a good figure for dual-frequency applications [22]. It should also be noted that insertion loss is direct function of the return loss assuming that no radiation/conductive/dielectric losses exist in structure. As discussed in [119], these losses are often negligible at low RF frequencies and for transmission line based structures built properly in low loss dielectric substrate.

8.3 Conclusion

In this chapter, theory and application of dual-frequency impedance property of multi-section commensurate transmission-line was presented. Rigorous mathematical analysis was carried out to derive the design equations. Interestingly, this property holds true for single section (Chapter 3) and two sections of transmission lines (Chapter 6). So, it was natural that this property should also exist for multi-section lines as well. Therefore, the material of this chapter can be seen as a generalization of the materials presented in Chapter 3 and Chapter 6. The presented theory can potentially be applied to overcome the limited transformation-/frequency-ratios of the current-state-of-the-art designs.

Chapter 9

Tri-Frequency Matching Network

A tri-frequency matching network should be able to provide concurrent impedance matching at three arbitrary frequencies. Such impedance matching network is of very high value in the multi-frequency circuits and systems [55].

However, a detailed survey of multi-frequency impedance matching network presented in Chapter 2 clearly reveals that there is lack of systematic synthesis approach for tri-frequency matching networks. The existing approaches, albeit very few, are limited because of either being a lumped element approach based, coupled lines based, or limited to only real load impedances. In fact, the tri-frequency impedance matching network used in [55] is a brute-force technique.

Therefore, it is of paramount importance that a generic distributed element based technique for systematic synthesis and design to achieve concurrent impedance matching at three arbitrary frequencies is invented and this is the topic of current chapter. Specifically, the developed matching network discussed in this chapter is cascade of a dual-band matching network, which has been discussed extensively in the previous eight chapters, and a novel dual-to-tri-band transformer [121]. Analysis of the proposed network provides closed form design equations that enable physically realizable solution owing to the presence of a free design variable. The presented theory is demonstrated through two example prototypes on Roger's RO4350B substrate.

9.1 Proposed Tri-Frequency Matching Network

Illustration of the proposed tri-frequency impedance transformer is shown in Fig. 9.1. Its aim is to match the load impedance R_L (shown at the extreme right) to the source impedance, Z_0 ($=50 \Omega$, shown at the extreme left), at three arbitrary frequencies, say, f_1 , f_2 , and f_3 such that, $f_1 < f_2 < f_3$. The design utilizes a dual-band impedance transformer (*DBIT*), although any *DBIT* from the existing literature could be selected, the two examples in this chapter make use of the *DBIT* concepts of type-I [30] and

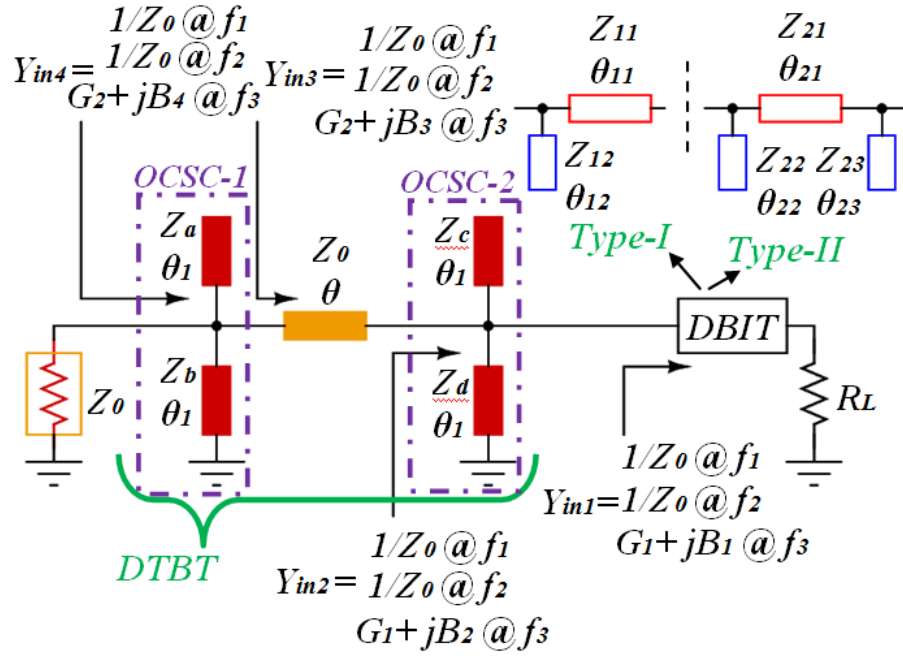


Figure 9.1 The proposed tri-frequency matching network.

type-II [122]. In series with the *DBIT*, there is a *dual to tri-band transformer (DTBT)* as well.

In Fig. 9.1, *OCSC-1*, *OCSC-2*, and a transmission-line (*TL*) segment of electrical length θ and characteristic impedance Z_0 (i.e. same as the source impedance) are the three constituents of the proposed *DTBT*. The constituents *OCSC- i* ($i \in \{1, 2\}$) are parallel combination of open and short stubs with electrical lengths θ_1 and respective characteristic impedances Z_a (Z_c) and Z_b (Z_d). All the electrical lengths are defined at the first frequency, f_1 , and $\forall i: Y_i = 1/Z_i$. It is important to recall that the electrical length is proportional to frequency, for non-dispersive lines [13], and so the electrical length θ defined at f_1 is equal to $u\theta$ at f_3 , for example, with $u=f_3/f_1$.

The working of the proposed tri-frequency transformer, shown in Fig. 9.1, is as follows. Matching at the first two frequencies f_1 and f_2 is established by *DBIT*. The *DTBT* is designed in such a way that it doesn't alter the matching at these two frequencies. The role of *DTBT* comes into picture only at third frequency, f_3 , and, therefore, $Y_{in1} = Y_{in2} = Y_{in3} = Y_{in4} = 1/Z_0 @ f_1 \& @ f_2$ is always valid. In general, the value of $Y_{in1} @ f_3$ will be of the form $G_1 + jB_1$, where G_1 and B_1 depend on whether the *DBIT*

is of type-I or type-II besides the value of R_L . The expressions of G_1 and B_1 are given at the end of this chapter as Appendix.

The *DTBT* is ineffective @ f_1 and f_2 as the *TL*-segment does not alter the matching established by *DBIT* @ f_1 and f_2 considering that the characteristic impedance of the same has been chosen to be equal to source impedance (i.e., Z_0), and the OCSC- i $\{i \in 1, 2\}$ have an infinite input impedance at f_1 and f_2 .

The admittance of OCSC-1, Y_p , is given by:

$$Y_p = \frac{1}{jZ_b \tan \theta_1} - \frac{1}{jZ_a \cot \theta_1} \quad (9-1)$$

Infinite impedance of OCSC-1 requires that Y_p be set to zero and, therefore, the following expression is obtained from (9-1).

$$Z_a = Z_b \tan^2 \theta_1 \quad (9-2)$$

Moreover, for the condition in (9-2) to be simultaneously satisfied @ f_1 and f_2 , a condition for θ_1 is given by [59]:

$$\theta_1 = \frac{(1+s)\pi}{1+r} \quad (9-3)$$

where, s is an integer and $r = f_2 / f_1$.

Similarly, for OCSC-2 to present infinite impedance, Z_a and Z_b can be replaced by Z_c and Z_d respectively in (9-2) and that result into:

$$Z_c = Z_d \tan^2 \theta_1 \quad (9-4)$$

Furthermore, admittance Y_{in3} @ f_3 can be expressed as:

$$Y_{in3}|_{f_3} = \frac{1}{Z_0} \frac{Z_0 + jZ_{in2}|_{f_3} \tan u\theta}{Z_{in2}|_{f_3} + jZ_0 \tan u\theta} = G_2 + jB_3 \quad (9-5)$$

$$\text{where, } G_2 = \frac{G_1(1 + \tan^2 u\theta)}{(1 - Z_0 B_2 \tan u\theta)^2 + (Z_0 G_1 \tan u\theta)^2} \quad (9-6)$$

$$B_3 = \frac{(1 - Z_0 B_2 \tan u\theta)(Z_0 B_2 + \tan u\theta) - Z_0^2 G_1^2 \tan u\theta}{Z_0 [(1 - Z_0 B_2 \tan u\theta)^2 + (Z_0 G_1 \tan u\theta)^2]} \quad (9-7)$$

where, $u = f_3/f_1$, and

$$B_2 = B_1 + Y_c \tan u\theta_1 - Y_d \cot u\theta_1 \quad (9-8a)$$

$$= B_1 + Y_c (\tan u\theta_1 - \tan^2 \theta_1 \cot u\theta_1) \quad (9-8b)$$

Similarly, admittance Y_{in4} @ f_3 can be expressed as follows:

$$Y_{in4}|_{f_3} = G_2 + jB_4 \quad (9-9)$$

where, $B_4 = B_3 + Y_a \tan u\theta_1 - Y_b \cot u\theta_1 \quad (9-10a)$

$$= B_3 + Y_a (\tan u\theta_1 - \tan^2 \theta_1 \cot u\theta_1) \quad (9-10b)$$

And, therefore, the matching is achieved at f_3 , if the following constraints are imposed:

$$G_2 = 1/Z_0 \quad (9-11)$$

$$B_4 = 0 \quad (9-12)$$

Equations (9-6) and (9-11) can be solved simultaneously to arrive at:

$$\tan u\theta = \frac{Z_0 B_2 \pm \sqrt{(Z_0 B_2)^2 - (1 - Z_0 G_1)(Z_0^2 B_2^2 + Z_0^2 G_1^2 - Z_0 G_1)}}{(Z_0^2 B_2^2 + Z_0^2 G_1^2 - Z_0 G_1)} \quad (9-13)$$

Once the value of θ is known from (9-13), the equations (9-2), (9-7), (9-8a-b), (9-10a-b), and (9-12) can be simplified to find the admittance, Y_a , given by:

$$Y_a = -\frac{B_3}{\tan u\theta_1 - \tan^2 \theta_1 \cot u\theta_1} \quad (9-14)$$

It is obvious from (9-7) and (9-8a-b) that B_3 depends on B_2 which in turn depends on Z_c . This is one extremely important parameter of the proposed tri-band matching network. The term Z_c can be considered a free variable that can be selected appropriately to get a physically realizable transformer. In practice, for realizable microstrip, the value of Z_c lies between 30Ω to 150Ω .

9.2 Design Procedure

The design steps are summarized as follows:

Step-I: For a given R_L , calculate the parameters Z_{11} , θ_{11} , Z_{12} , θ_{12} for type-I *DBIT* or Z_{21} , θ_{21} , Z_{22} , θ_{22} , Z_{23} , θ_{23} for type-II *DBIT* using the equations given in [30] or [122]. This design should be validated through simulation.

Step-II: Calculate $Y_{in}|_{f_3} = G_1 + jB_1$ using the formula (A1a) and (A1b) or (A2a) and (A2b) given in Appendix depending upon the type of *DBIT* or preferably by simulation.

Step-III: In some cases, OCSC-2 may not be required (thus, $B_2=B_1$). Hence, all the tri-band design should start with this assumption. Value of Z_a is evaluated using (9-13) and (9-14). Out of the two values from (9-13), only that value of θ is used which gives physically realizable transformer. Impedance Z_b is then calculated from (9-2).

Step-IV: If values of *TLs* of *DTBT* are not within the realizable limits of 30Ω to 150Ω , then the design procedure is repeated by considering use of OCSC-2 assuming a suitable value for Z_c . It will be useful to write a MATLAB program incorporating various design equations and then sweep the value of Z_c from 30Ω to 150Ω . Then choose only that value of Z_c which gives physically realizable transformer parameters. It may be noted that the side stub of *DBIT* may be combined with stubs of OCSC-2 as done here in the example-II of the next section.

9.3 Design Examples

As a case study, two design examples, while assuming f_1 , f_2 , and f_3 as 1GHz, 2GHz and 2.5GHz respectively, are given to demonstrate the effectiveness of the proposed matching network. The first example makes use of type-I *DBIT* whereas the second uses a type-II *DBIT*. Both the designs have been prototyped on RO4350B substrate of thickness 1.524 mm and a copper cladding of 35 μm .

9.3.1 Design Example-I with type-I *DBIT*

In this example, $R_L=100\Omega$ is taken. Using the design procedure, the values of

various lines for the *DBIT* are found to be $Z_{11}=57.735 \Omega$, $\theta_{11}=60^\circ$, and $Z_{12}=57.735 \Omega$, $\theta_{12}=60^\circ$. The admittance Y_{in3} @ $f_3=0.012+j0.024 \Omega^{-1}$ is found through simulation. Using the design equations, the design values of *DTBT* are found to be $Z_a=141.42 \Omega$, $Z_b=47.14 \Omega$, $\theta_1=60^\circ$, and $\theta=60.166^\circ$. Apparently OCSC-2 is not required in this case as the design values are physically realizable. The fabricated board is shown in Fig. 9.2(a) and the corresponding EM simulated and the measured results are shown in Fig. 9.3(a). The agreements of simulated and measured results at the three frequencies demonstrate the effectiveness of the proposed design.

9.3.2 Design Example-II with type-II DBIT

In this example, $R_L=20 \Omega$ is taken to match $Z_0=50 \Omega$. Once again the design procedure provides $Z_{21}=36.5 \Omega$, $\theta_{21}=60^\circ$, $Z_{22}=109.54 \Omega$, $\theta_{22}=60^\circ$, and $Z_{23}=109.54 \Omega$,

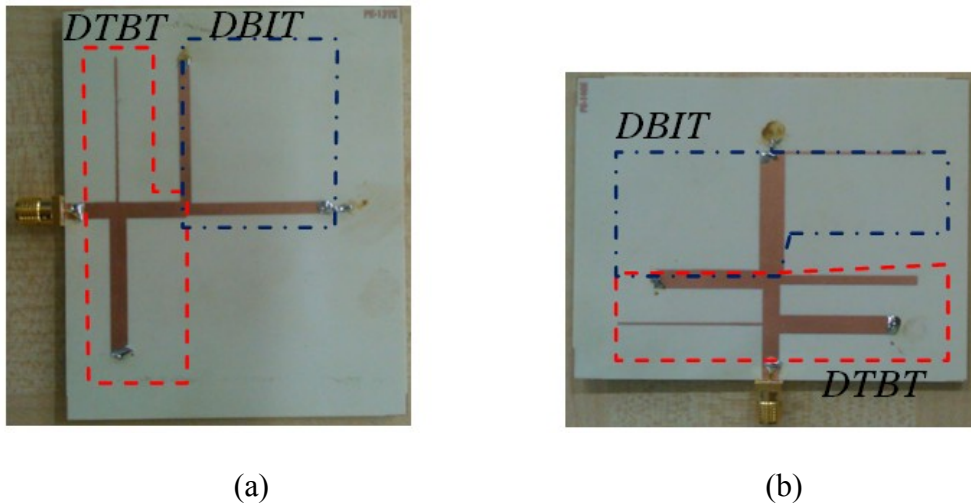


Figure 9.2 Fabricated devices (a) example-I (b) example-II [121].

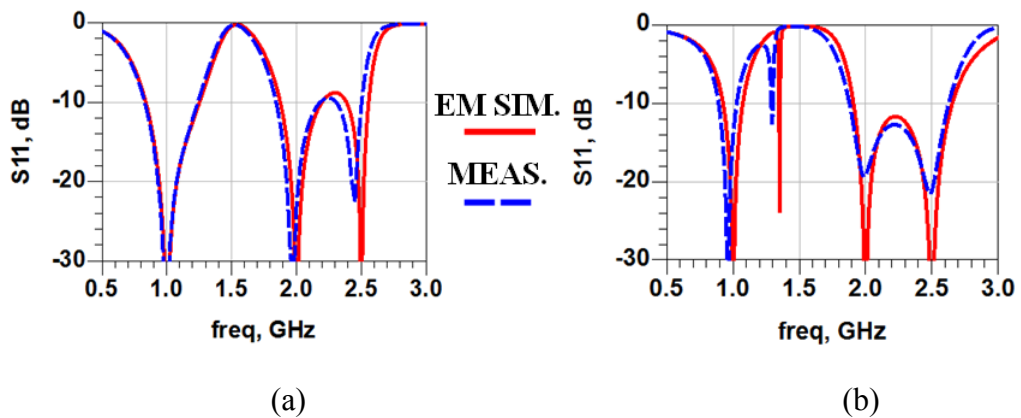


Figure 9.3 Simulation and measurement results (a) example-I (b) example-II.

$\theta_{23}=60^\circ$ for various segments of type-II *DBIT*. Since, instead of 20Ω resistor, a slightly different CRCW series SMD resistor of value $19.6\ \Omega$ is available commercially, the designed *DBIT* needed a little optimization. The value of admittance Y_{in3} @ f_3 is found to be $0.053259+j0.009097\ \Omega^{-1}$. However, for this value of Y_{in3} , the *DTBT* turns out to be physically unrealizable. Therefore, the *DTBT* was redesigned by incorporating the OCSC-2. The impedance Z_c , the free variable, is chosen to be equal to $100\ \Omega$. From the design equations $Z_a=116.82\ \Omega$, $Z_b=38.94\ \Omega$, $Z_d=33.33\ \Omega$, $\theta_1=60^\circ$, and $\theta=13.45^\circ$ are found. The fabricated implemented board is shown in Fig. 9.2(b) whereas the corresponding EM simulated and measured results given in Fig. 9.3(b) perfectly demonstrate the tri-frequency matching capabilities of the proposed design.

The slight anomaly in the measurement and simulation values, of both prototypes, can be overcome by using frequency stable substrate such as RO5880 with $\epsilon_r=2.2$ and using high quality fabrication facilities.

The comparison of the proposed work with the current state-of-the-art is given in TABLE 9-1. The novelty of the proposed tri-band matching scheme is apparent as it significantly advances the tri-band matching techniques and will therefore find definite applications where the earlier techniques could not be applied.

Table 9-1 Comparison with Current State-of-the-Art

Ref.	operation	load type	frequencies	compensation^b
[60]	dual-band	real	arbitrary	required
[23]	dual-band	complex	arbitrary	not required
[54]	tri-band	real	arbitrary	required
[55]	tri-band	real	restricted	not required
This Work	tri-band	complex ^a	arbitrary	not required

^aDepends on the type of *DBIT*.

^bFor different even-odd mode velocities in microstrip.

9.4. Conclusion

In this chapter, a generic scheme to synthesize a tri-frequency matching network has been discussed. To verify the concepts, a real and fixed load was assumed in the design examples. However, the presented tri-frequency matching technique is also extendable to frequency dependent complex load if appropriate complex to real type DBIT such as reported in reference [40], or others discussed in the previous chapters are used. For example, in the following schematic, depicted in Fig. 9.4, the design of a tri-frequency matching network is shown that matches **three distinct complex impedances** to $Z_0=50$ ohm, at three arbitrarily chosen frequencies. The DBIT discussed in [40] is used to illustrate the idea. The three loads are modeled by an if-else statement as shown. A proper matching is evident from Fig. 9.4 (bottom). Thus, it is clear that the proposed scheme can also be applied for frequency dependent complex loads.

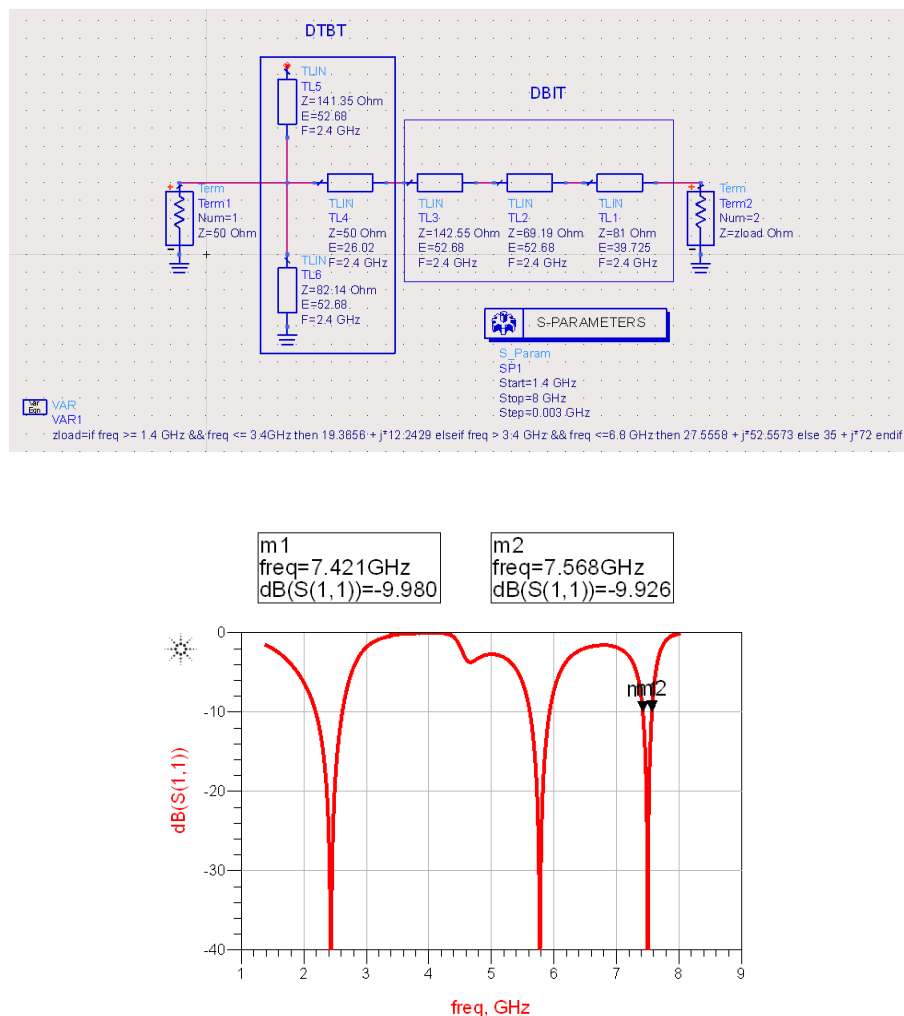


Figure 9.4 Tri-frequency matching network (top) and simulated return loss (bottom).

Appendix

A. Type-I DBIT

$$G_1 = \frac{R_L(1 + \tan^2 u\theta_{11})}{R_L^2 + Z_{11}^2 \tan^2 u\theta_{11}} \quad (\text{A1a})$$

$$B_1 = \frac{R_L^2 \tan u\theta_{11} - Z_{11}^2 \tan u\theta_{11} + R_L^2 B_L Z_{11} + B_L Z_{11}^3 \tan^2 u\theta_{11}}{Z_{11}(R_L^2 + Z_{11}^2 \tan^2 u\theta_{11})} \quad (\text{A1b})$$

where, $B_L = -Y_{12} \cot u\theta_{12}$ for SC stub and $B_L = -Y_{12} \tan u\theta_{12}$ for an OC stub with $\theta_{ij}, \forall i, j$ are similar as θ_1 .

B. Type-II DBIT

$$G_1 = \frac{R_L(1 + \tan^2 u\theta_{21})}{(1 - B_p Z_{21} \tan u\theta_{11})^2 + (R_L Z_{21} \tan u\theta_{21})^2} \quad (\text{A2a})$$

$$B_1 = \frac{D_1 - D_2}{Z_{21}((1 - B_p Z_{21} \tan u\theta_{11})^2 + (R_L Z_{21} \tan u\theta_{21})^2)} \quad (\text{A2b})$$

where, $D_1 = 2Z_{21}B_p + \tan u\theta_{21} - Z_{21}^2 R_L^2 \tan u\theta_{21} - 3Z_{21}^2 B_p^2 \tan u\theta_{21}$

$$D_2 = Z_{21}B_p \tan^2 u\theta_{21} + Z_{21}^3 B_p^3 \tan^2 u\theta_{21} + R_L^2 B_p Z_{21}^3 \tan^2 u\theta_{21}$$

$B_p = -Y_{22} \cot u\theta_{22}$ for SC stub and $B_p = -Y_{22} \tan u\theta_{22}$ for an OC stub with $\theta_{ij}, \forall i, j$ are similar as θ_1 .

Chapter 10

A Theorem for Multi-Frequency DC-Feed Network Design

A DC-feed is an extremely important component, as it blocks the interactions of RF signal with DC bias source [3]. A DC-feed could also be seen a special case of impedance transformation circuit with the requirement of establishing infinite input impedance at the design frequency. A look at Fig. 1.9 conveys that a dual-frequency amplifier needs a dual-frequency DC-feed. In general, realization of a multi-frequency amplifier requires a multi-frequency DC-feed (MFDCF) network [22, 55]. Moreover, concept of the presented MFDCF could also be extended to create short-circuit at the input of multi-frequency baluns during their even-mode operation [123].

The analysis, design, prototypes, and applications of the MFDCF were presented in [55, 124]. However, the design equations, (1)-(3) of [124], are approximate and necessitate optimization even for implementation using ideal transmission lines. Furthermore, the optimization requirements get severe with the increase in the number of frequency bands considering that the number of variables to be optimized increases. Since, prototypes of MFDCF were already shown in [124] and utilized in [55], the main focus and contribution of this chapter is to prove a novel, interesting, and useful theorem pertaining to synthesis of MFDCF [125]. It is also demonstrated that the combination of the proposed theorem and CAD tools drastically reduce the complexity of MFDCF design.

10.1 The Statement of the Theorem

The schematic of the conventional MFDCF of [124] is redrawn in Fig. 10.1. It comprises of multiple L-networks into cascade with k being the total number of frequency bands. Apparently, each L-network consists of a horizontal transmission line (TL) section and a vertical open stub. Here, " Z_{i^t} " is the characteristic impedance of the i^{th} TL section and " Z_{i^s} " is the characteristic impedance of the i^{th} stub, with $i= 1, 2, \dots, k$.

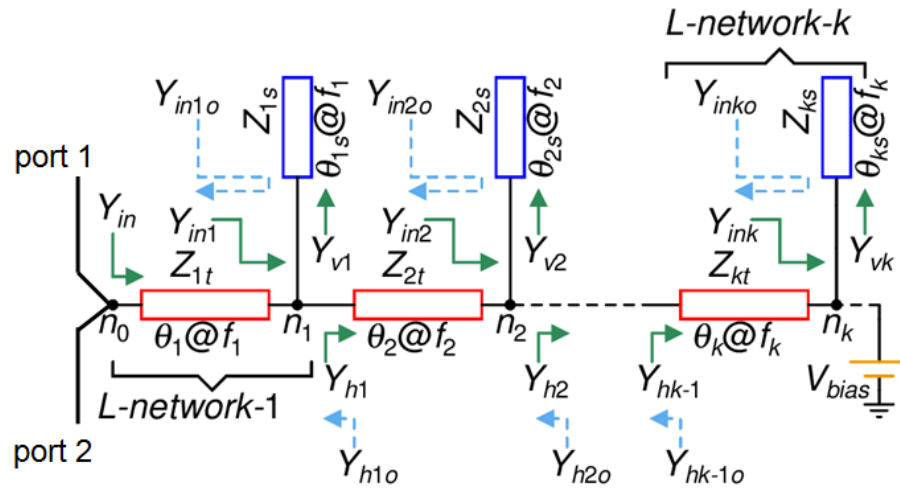


Figure 10.1 Multi-frequency DC-feed network (MFDCF): the subscript 'o' - in $Y_{x.zo}$ means in the opposite direction of $Y_{x.z}$. port 1 connects to the drain (FET), whereas port 2 connects to the output matching network.

Similarly, θ_i and θ_{is} are the electrical length (in degrees) of TL sections and the stubs respectively defined at f_i , with $i= 1, 2, \dots, k$. Usually, the values of " Z_{is} " $\forall i$ are chosen on higher side so that the resulting stubs are thin and could be folded easily and that aids in design miniaturization. However, the value of " Z_{it} " $\forall i$ may be chosen on lower side considering that these lines have to carry large DC currents. Therefore, $Z_{it} = 50\Omega$ and $Z_{is}=100\Omega \forall i$ are chosen here for validation of the concept. Moreover, $\theta_{is}=90^\circ @ f_i \forall i$ is chosen and thus the design objective is to find θ_i .

The DC bias voltage is applied at the k^{th} node, as shown in Fig. 10.1. The term Y_{in} is the admittance at the RF input port, n_0 , looking towards the right and its ideal value must be zero. Equivalently the input impedance, $Z_{in}=1/Y_{in}$, offered to the RF input should be infinite i.e., an open-circuited condition. The frequencies are assumed such that $f_i > f_{i+1} \forall i$. Furthermore, $Y_{m,n}$ is defined as, $Y_{m,n}=1/Z_{m,n}$, with $m= \{1, 2, \dots, k\}$ and $n= \{t, s\}$.

Now, following theorem for the evaluation of θ_i is proposed:

"Cotangent of electrical length of any horizontal TL section ($\cot\theta_i$) is equal to the net imaginary-part of the admittance of the preceding stages while looking towards the left, divided by the characteristic admittance of that horizontal TL section. The input RF port, n_0 , remains open circuited during this evaluation."

10.2 Proof of the Theorem

Proof of the theorem is based on the following lemma.

Lemma: For both the structures shown in Fig. 10.2, if $Y_s = Y_i^*$, then $Y_o = Y_l^*$. It conveys that if there exists a complex conjugate admittance relationship at one end then the same exists at the other end as well.

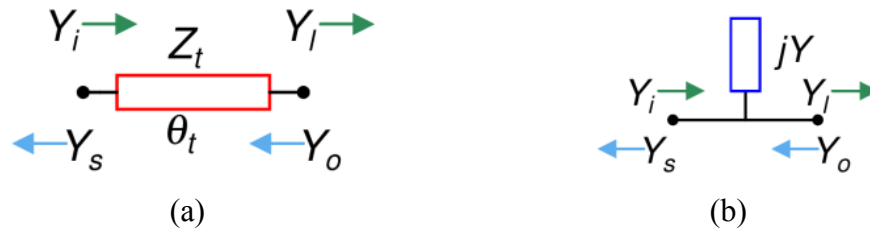


Figure 10.2 (a) A transmission-line and (b) a shunt admittance.

10.2.1. Proof of the Lemma

In Fig. 10.2(a):

$$Y_i = Y_t \frac{Y_l + jY_t \tan \theta_t}{Y_t + jY_l \tan \theta_t} \quad (10-1)$$

$$Y_o = Y_t \frac{Y_s + jY_t \tan \theta_t}{Y_t + jY_s \tan \theta_t} \quad (10-2)$$

$$Y_s = Y_i^* = Y_t \frac{Y_l^* - jY_t \tan \theta_t}{Y_t - jY_l^* \tan \theta_t} \quad (10-3)$$

Substitution of Y_s from (10-3) into (10-2) yields $Y_o = Y_l^*$.

Furthermore, in Fig. 10.2(b):

$$Y_i = jY + Y_l \quad (10-4)$$

$$Y_s = Y_i^* = -jY + Y_l^* \quad (10-5)$$

$$Y_o = jY + Y_s \quad (10-6)$$

Now substitution of Y_s from (10-5) into (10-6) yields $Y_o = Y_l^*$.

As an extension to the above lemma, if the two networks in the Fig. 10.2 are

combined to make an L-network, then the lemma holds true for the L-network as well. Subsequently, it can also be concluded that if a complex conjugate relationship for admittance exists at node n_0 of Fig. 10.1 then the same holds true for all the nodes of Fig. 10.1.

10.2.2 Proof of the theorem

Consider the problem of finding any general $\theta_k @f_k$ for the k^{th} L-network shown in Fig. 10.3. Please note that the notation $Y_{xy..zo}$, with an 'o' in subscript means the value of $Y_{xy..z}$ looking towards the left. Since, $Y_{in}|_{f_k} = 0$ is desired and opening the RF input port implies $Y_{ino}|_{f_k} = 0$, so a complex conjugate relationship exists at the input. Therefore, application of the above discussed lemma to Fig. 10.3, gives $Y_{ink-1}|_{f_k} = (Y_{ink-1o}|_{f_k})^*$.

The input port is open, so $Y_{ink-1o}|_{f_k}$ is purely imaginary, and therefore, following expression at node n_{k-1} can be obtained:

$$Y_{ink-1o}|_{f_k} = -Y_{ink-1}|_{f_k} = -(Y_{vk-1}|_{f_k} + Y_{hk-1}|_{f_k}) \quad (10-7)$$

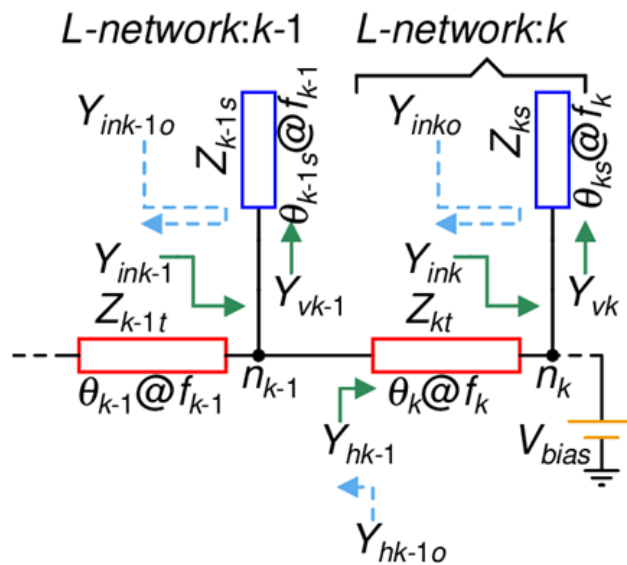


Figure 10.3 The k^{th} - and $k-1^{\text{th}}$ -L-networks. The remaining stages are not shown for the sake of clarity. The task is to determine $\theta_k @f_k$.

However, since $\theta_{ks}=90^\circ@f_k$, the node n_k is at ac ground. Thus,

$$Y_{hk-1}|_{f_k} = -jY_{kt} \cot \theta_k \quad (10-8)$$

Simplification of (10-7) with the help of (10-8) results into (10-9).

$$\cot \theta_k = \frac{Y_{ink-1o}|_{f_k} + Y_{vk-1}|_{f_k}}{jY_{kt}} \quad (10-9)$$

Furthermore, in the notation with subscript 'o', one can express (10-9) by (refer Fig. 10.3):

$$\cot \theta_k = \frac{\left(Y_{hk-1o}|_{f_k} \right) / j}{Y_{kt}} \quad (10-10)$$

The numerator in (10-10) is the net imaginary-part of the admittance of the preceding $k-1$ stages that the k^{th} TL section effectively sees towards the left. This completes the proof.

10.3 CAD Assisted Design Methodology

The proposed theorem makes the task much easier if the concept is utilized in combination with any commercial CAD tool. For example, Fig. 10.4 shows a simu-

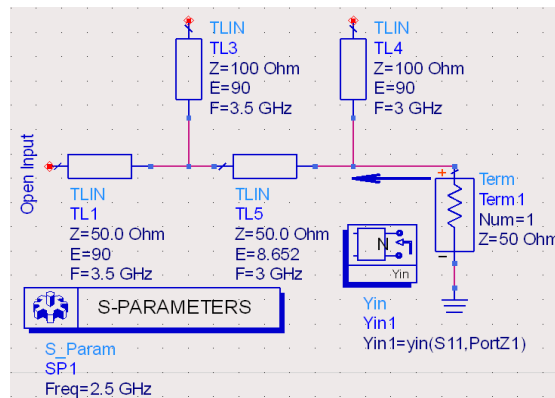


Figure 10.4 Simulation setup in ADS for determination of the admittance Y_{in1} (to the left) at 2.5GHz; the design frequencies are 3.5GHz/3GHz/2.5GHz. $\theta_3@2.5\text{GHz}$ for 3rd L-network is obtained by dividing Y_{in1} by $j(1/50)\Omega^{-1}$.

on setup in Keysight ADS[®] that can be used to quickly find the input admittance, Y_{in1} , looking towards the left (in the direction of the arrow). In this network, therefore, the electrical length of horizontal line of the 3rd L-network (@ 2.5GHz) can simply be found by dividing the obtained Y_{in1} by $j(1/50)\Omega^{-1}$.

10.4 Design and Comparison

The design parameters θ_1 , θ_2 , and θ_3 of a tri-frequency DC-feed obtained using the proposed theorem are given in TABLE 10-1. It also lists the ones obtained using approximate equations of [124]. It is important to note that θ_i in Fig. 2(a) in [124] are obtained using the design equations while Fig 2(b) in [124] are obtained using subsequent optimizations.

Table 10-1 Comparison of Obtained Design Parameters for Tri-Band Case

Freq (GHz)	θ_i [124]	θ_i PROPOSED	Phase S ₁₁ (Simulation)	
			[124]	PROPOSED
$f_1=2.65$	$\theta_1=90^\circ$	$\theta_1=90^\circ$	@ f_1 , 0°	@ f_1 , 0°
$f_2=2.15$	$\theta_2=17^\circ$	$\theta_2=11.51^\circ$	@ f_2 , 1.1°	@ f_2 , 0°
$f_3=1.49$	$\theta_3=27.6^\circ$	$\theta_3=15.53^\circ$	@ f_3 , -99°	@ f_3 , 0°

The simulation results obtained for the proposed technique are compared in Fig. 10.5. Apparently, the phase of S_{11} found using the design equations of [124] is far off from the ideal value of zero, whereas the proposed theorem gives exact result. As per TABLE 10-1, the parameters of the prototype shown in Fig. 2(b) of [124] obtained after intensive optimization comes closer to the values obtained using the proposed theorem. The proposed theorem also provides exact insertion-loss profile as can be seen in Fig 10.5. Due to the approximate nature of the design equations of [124], even with ideal elements the insertion-loss is non-zero at the design frequencies, especially at f_3 , whereas the proposed theorem leads to correct parameters.

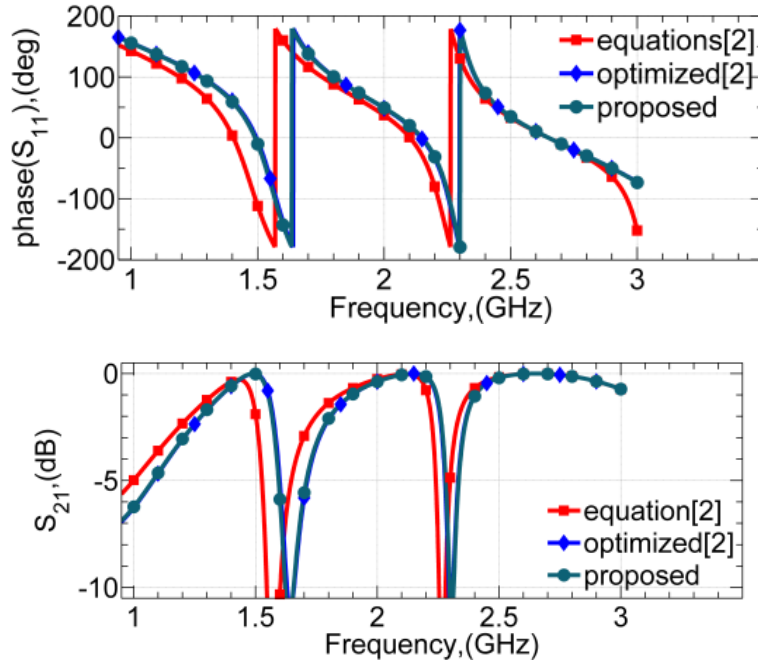


Figure 10.5 Phase of S11 for tri-frequency DC-feed (top) and S21 (bottom). Ref. [2] in this figure refers to the Ref. [124] in this thesis.

To demonstrate the scalability of the proposed technique, a simulation was carried out for penta-frequency using the proposed theorem and was compared with the technique reported in [124]. The obtained results are listed in TABLE 10-2 and plotted in Fig. 10.6. It is apparent that the parameters found using the proposed theorem provide ideal value of zero for phase of S_{11} at all the design frequencies whereas the corresponding results obtained using technique [124] are far off from ideal values and requires intensive tuning/optimization. Moreover, for a 0.3dB reference, the minimum S_{21} bandwidth for the design using proposed theorem happens at f_5 and is equal to 84MHz and this is adequate for multi-frequency applications [22].

Table 10-2 Comparison of Obtained Design Parameters for Penta-Band Case

Freq (GHz)	θ_i [124]	θ_i PROPOSED	Phase S11 (Simulation)	
			[124]	PROPOSED
$f_1=3.5$	$\theta_1=90^\circ$	$\theta_1=90^\circ$	@ $f_1, 0^\circ$	@ $f_1, 0^\circ$
$f_2=3.0$	$\theta_2=12.86^\circ$	$\theta_2=8.67^\circ$	@ $f_2, -23.4^\circ$	@ $f_2, 0^\circ$
$f_3=2.5$	$\theta_3=15^\circ$	$\theta_3=7.89^\circ$	@ $f_3, -106^\circ$	@ $f_3, 0^\circ$
$f_4=2.0$	$\theta_4=18^\circ$	$\theta_4=8.2^\circ$	@ $f_4, \text{undefined}$	@ $f_3, 0^\circ$
$f_5=1.5$	$\theta_5=22.5^\circ$	$\theta_5=9.64^\circ$	@ $f_5, \text{undefined}$	@ $f_3, 0^\circ$

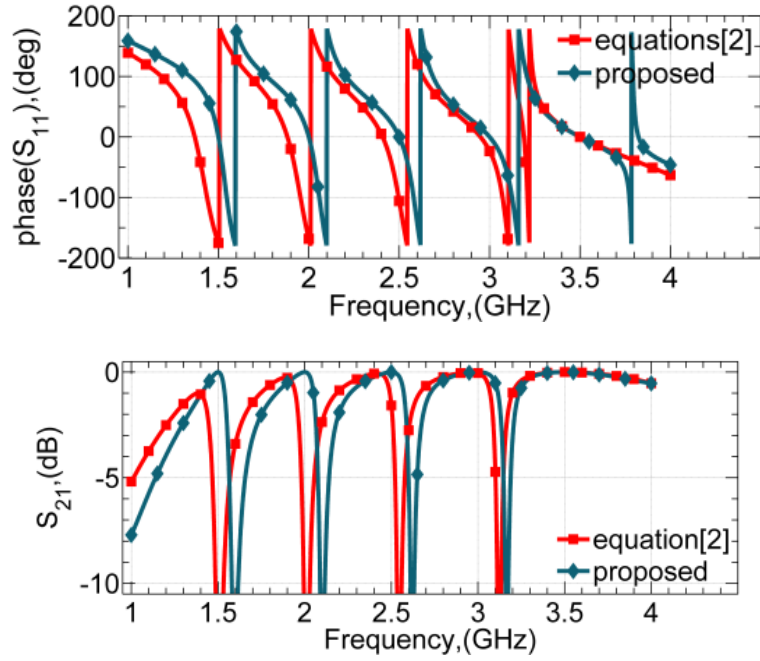


Figure 10.6 Phase of S_{11} for penta-frequency DC-feed (top) and S_{21} (bottom). Ref. [2] in this figure refers to the Ref. [124] in this thesis.

Lastly, comparison with some previous design is summarized in TABLE 10-3. It can be observed that the proposed theorem helps overcome the limitations and constraints of the existing techniques.

Table 10-3 Comparison with Previous DC Feed Techniques

Ref.	Bands	Design	CAD Integration
[13]	Two	Exact	No
[55]/[124]	multiple	Highly approximate	No
This Work	multiple	Exact	Possible

10.5 Conclusion

In this chapter, a novel and rigorous analytical synthesis approach formulated as theorem that yields the exact design of arbitrary MFDCF networks was presented. The most distinguishing feature of the proposed theorem is its effectiveness to quickly

provide the exact design parameters of MFDCF networks without the need to use any circuit optimization tool. The use of an EM simulation tool in conjunction with the proposed theorem is recommended to compensate for any circuit impairments due to material or layout related matters.

Conclusion and Future Directions

Research in utterly sophisticated, modern wireless communication systems with high-end capabilities is at the peak; thanks to the continuously growing user needs. This complexity puts huge burden on the circuits and systems design engineers as it brings about new design challenges each day. Especially, due to the rapid developments in multi-frequency/multi-standard wireless communication systems during the last decade, the design of RF front-ends has become a very challenging affair while designing wideband components, especially those requiring adequate operation over multi-octave bandwidth has always been considered difficult. However, the alternative architecture employing multi-frequency components is also by no means an easier task. Whether wideband or multi-frequency; the vast majority of RF front-end components employ impedance matching networks as a key component, and therefore their analysis and design is of the paramount importance.

In this thesis, the main goal was divided into two major categories, namely the design and performance improvement of dual-frequency impedance matching network and to come up with a systematic design methodology for tri-frequency impedance matching networks.

To that end, the first important contribution of this thesis work has been the proposal of interesting dual-frequency admittance property of a single section transmission line terminated into a real impedance. As described in Chapter 3, this property proved to be greatly useful as it provided a clear insight into the working of dual-frequency matching networks employing single section transmission lines terminated into real impedances, such as a T-type matching network. Using the discovered property, two flavors of dual-frequency impedance matching network for frequency dependent complex load impedance was presented in Chapter 3 with significantly improved performance due to two possible ways in which the L-type network can be used. In addition, the discovered property was also applied for the design and development of the port-extended dual-frequency Wilkinson power divider (WPD). The advantage of the proposed WPD is apparent from the fact that only one isolation resistor is required, that too, is independent of the frequency-ratio. The

achievable frequency-ratio is in the range of 1.5-4 and this is fairly good considering the other advantages as outlined in TABLE 3-5.

In Chapter 4, use of quarter wave-block was described for the design of dual-frequency impedance transformation networks. The advantage of this technique lies in its flexibility to employ any dual-frequency quarter-wavelength block from a large number of those reported in the literature. The Simulation and measurement results exhibited proper matching capabilities. Besides, the technique is very simple and even an asymmetric looking block, such as an L-network, could be employed with proper orientation to suit during layout phase.

Coupled lines are very important for matching network design as they facilitate miniaturization. Therefore, Chapter 5 was devoted to novel dual-frequency matching networks employing parallel coupled lines. A unique dual-frequency admittance property was shown to exist when such coupled lines are terminated with a real impedance. The discovered property was utilized to the analysis and design of dual-frequency impedance matching networks. Specifically, the modified L-type network can be used for the real load impedances whereas the modified T-type network could be used for frequency dependent complex networks. An immediate application of the introduced matching networks would be highly desirable in the design of dual-frequency amplifiers where coupling capacitors will no more be required owing to inherent DC-isolation present in the described matching networks.

Two cascaded sections of transmission lines are one of the most commonly used topologies for dual-frequency matching networks. In Chapter 6, the dual-frequency admittance property is also shown to exist for them when termination is a real impedance. The discovered property is more generic as it paves way for the intuitive design of dual-frequency impedance transformation networks. Specifically, not only all the earlier reported two section designs such as Monzon transformer could be better explained using the discovered property; novel topologies with improved frequency- and transformation-ratios can also be designed. The modified L-type networks and the modified T-type networks have been described in Chapter 6 that caters to the real and frequency dependent complex loads respectively. In fact, the earlier reported designs could be considered as special cases of the proposed dual-frequency matching networks. The dual-frequency coupler proposed by the author utilizing unequal arm

length based single frequency coupler was a good attempt at enhancing the frequency ratio. However, the design also possesses small bandwidth just like its single frequency counterpart. Therefore, the discovered properties of single section line described in Chapter 3 and that of the two sections lines has been applied in port-extended couplers to enhance its frequency- and power-division ratios as outlined in TABLE 6-7.

A very troublesome scenario in dual-frequency impedance matching network is the limited load of range that could be matched to a real source impedance. Since, a circuit designer has no control over the input/output impedances of a transistor or other active device at given set of frequencies, the existing dual-frequency matching networks may not yield a physically realizable design. For a physically realizable design, the line impedance of transmission lines must typically lie between 20Ω - 150Ω . If any of the constituting line impedance is beyond this range, there is no other way except to change the matching network topology or to use multiple stages of matching networks. Therefore, Chapter 7 recommends applying an interesting load-healing concept. By employing a very small trace of series or shunt transmission lines in front of the load, a physically realizable dual-frequency matching networks could be designed as described in the chapter.

The dual-frequency admittance property that holds true for single- and two-sections of transmission lines terminated into a real impedance is generalized to multi-section scenario. This generalization was described and proved after a rigorous mathematical analysis in Chapter 8. The multi-section dual-frequency transformer offers higher degree of independent variables and this result in manifold increase in the transformation-ratio. It was demonstrated in the same chapter, duly backed by closely matched simulation and measured results.

In Chapter 9, a generic and systematic design methodology for tri-frequency matching networks has been described. The technique used a conventional dual-band impedance transformer (DBIT) in conjunction with novel dual-to-tri-band transformer (DTBT) to achieve concurrent tri-frequency functionality. Two design examples were demonstrated to show the usefulness of the proposed technique. Moreover, the technique is generic and perfectly capable of handling frequency dependent complex loads, when a DBIT for frequency dependent complex load is utilized.

A much related problem to impedance matching is the concept of DC-feed. The idea is to create infinite input impedance for the RF signal at the frequency of interest. Design of multi-frequency amplifiers necessitates a multi-frequency DC-feed. In Chapter 10, a synthesis procedure for multi-frequency DC-feed network has been presented. While the procedure is formulated in terms of a simple theorem, the real advantage of the proposed theorem is when it is used along with a commercial CAD tool. The theorem helps calculate the required electrical lengths of the involved transmission lines very quickly without any limitations on the number of frequencies.

While a large number of design scenarios have been considered in this thesis but still there could be many directions for future works. Some of the topics worth examining would be:

a) ***Development of multi-frequency matching networks:*** the major focus of this work has been to mitigate the limited frequency- and transformation ratios of dual-frequency networks by advanced network topologies. In addition, the tri-frequency impedance matching network puts forward a scheme to establish matching at three arbitrary frequencies concurrently. The same technique could be extended to multi-frequency scenarios. The advanced dual-frequency schemes demonstrated in this thesis such as ones with the inherent DC isolation could be incorporated in the tri- and multi-frequency matching networks to get rid of the requirement of coupling capacitors. However, multi-frequency stubs would be required if the proposed tri-frequency matching network has to be extended to multi-frequency scenario. In this regard, the concept of multi-frequency DC-feed networks establishing infinite input impedance at the frequencies of interest should be greatly useful.

b) ***Impedance transformation circuit miniaturization:*** The impedance matching networks in this thesis require a particular electrical length to be fulfilled by the constituting transmission line elements. The circuit size of these transformers often becomes large, especially at the low frequencies. While meandering could definitely be used to reduce the overall footprint, but still a circuit miniaturization technique can be explored for area efficient realization. The slow-wave technique could be integrated into the impedance matching networks described in this thesis as a way to achieve systematic miniaturization.

c) ***Incorporation of built-in harmonic matching:*** the advanced network topologies discussed in this thesis are fully capable of establishing impedance matching at fundamental frequencies; harmonic matching networks could be integrated into these networks to cater to the needs of PA designers. Especially, the second and third harmonic control circuit would be very attractive. As mentioned in the introduction chapter, it is possible to include harmonic networks which can be de-embedded for an independent fundamental frequency matching network design. However, finding a technique for doing this that is built-in into the fundamental matching network itself in a systematic and analytical way would be worth examining as this could automate the complete matching network design from measured or simulated load pull data.

Bibliography

- [1]. W. H. Hayt, J. E. Kemmerly, and S. M. Durbin, *Engineering Circuit Analysis*, 6th ed., New Delhi: TMH, 2003.
- [2]. D. M. Pozar, *Microwave Engineering*, 3rd ed., New Delhi: J. Wiley & Sons, 2010.
- [3]. G. Gonzalez, *Microwave Transistor Amplifiers: Analysis and Design*. 2nd ed., Englewood Cliffs, NJ: Prentice Hall, 1996, chap. 2 and 3, pp. 92–175.
- [4]. L. Wu, Z. Sun, H. Yilmaz, and M. Berroth, "A dual-frequency Wilkinson power divider," *IEEE Trans. Microw. Theory Tech.*, vol.54, no.1, pp.278–284, Jan. 2006.
- [5]. R. P. Gordon, "A directional coupler with very flat coupling," *IEEE Trans. Microw. Theory Tech.*, vol.26, no.2, pp.70–74, Feb. 1978.
- [6]. I. Ohta and T. Kawai, "Design of quadrature hybrids and directional couplers based on the equivalent admittance approach," *IEICE transaction*, vol.E88-C, no.1, 2005.
- [7]. Methods of patch antenna feed (online), Accessed: May 04, 2015: URL: <http://www.antenna-theory.com/antennas/patches/patch3.php>
- [8]. M. Pinuela, P. D. Mitcheson, and S. Lucyszyn, "Ambient RF energy harvesting in urban and semi-urban environments," *IEEE Trans. Microw. Theory Tech.*, vol.61, no.7, pp.2715–2726, Jul. 2013.
- [9]. Z. Liu, Z. Zhong, and Y.-X. Guo, "Enhanced dual-band ambient RF energy harvesting with ultra-wide power range," *IEEE Microw. Wireless Compon. Lett.*, vol. 25, no. 9, pp. 630–632, Sept. 2015.
- [10]. K. Niotaki, A. Georgiadis, A. Collado, and J. S. Vardakas, "Dual-band resistance compression networks for improved rectifier performance," *IEEE Trans. Microw. Theory Tech.*, vol. 62, no. 12, pp. 3512–3521, Nov. 2015.
- [11]. N. Shariati, W. S. T. Rowe, J. R. Scott, and K. Ghorbani, "Multi-service highly sensitive rectifier for enhanced RF energy scavenging," *Nature Sci. Rep.*, vol. 5, p. 9655, 2015.
- [12]. N. Nallam and S. Chatterjee, "Multi-band frequency transformations, matching networks and amplifiers," *IEEE Trans. Circuits Syst. I, Reg. Papers*, vol. 60, no. 6, pp. 1635–1647, Jun. 2013.
- [13]. K. Rawat, M. S. Hashmi, and F. M. Ghannouchi, "Dual-band RF circuits and components for multi-standard software defined radios," *IEEE Circuits Syst. Mag.*, vol. 12, No. 1, pp.12–32, Feb. 2012.
- [14]. P. B. Kenington, *RF and Baseband Techniques for Software Defined Radio*. Boston: Artech House, 2005.
- [15]. K. Kawai, T. Furuta, H. Okazaki, and S. Narahashi, "Multi-band radio frequency circuits for mobile terminals," *NTT Docomo Technical Journal*, vol. 13, No.3, 2011. [Accessed: June 06, 2016] URL: https://www.nttdocomo.co.jp/english/binary/pdf/corporate/technology/rd/technical_journal/bn/vol13_3/vol13_3_023en.pdf
- [16]. H. Hashemi and A. Hajimiri, "Concurrent multiband low-noise amplifiers—Theory, design, and applications," *IEEE Trans. Microw. Theory Tech.*, vol. 50, no. 1, pp. 288–301, Jan. 2002.
- [17]. H. W. Bode, *Network Analysis & Feedback Amplifier Design*, Van Nostrand, 1945
- [18]. R. M. Fano, "Theoretical limitations on the broadband matching of arbitrary impedances," *Journal of the Franklin Institute*, vol. 249, No. 2, pp. 139–154, Feb. 1950.
- [19]. R. M. Fano, "Theoretical limitations on the broadband matching of arbitrary impedances," *Massachusetts Inst. Technol., Res. Lab. Electron., Rep. 41*, pp. 1–48. Jan. 1948, [Accessed: June 06, 2016] URL: <http://hdl.handle.net/1721.1/5007>.

- [20]. J. Pang, S. He, C. Huang, Z. Dai, C. Li and J. Peng, "A novel design of concurrent dual-band high efficiency power amplifiers with harmonic control circuits", *IEEE Microw. Wireless Compon. Lett.*, vol. 26, no. 2, pp.137–139, Feb. 2016.
- [21]. Y. Wu, L. Jiao and Y. Liu, "Comments on "novel dual-band matching network for effective design of concurrent dual-band power amplifiers"," *IEEE Trans. Circuits Syst. I, Reg. Papers*, vol. 62, no. 9, pp. 2361–2361, Aug. 2015.
- [22]. K. Rawat and F.M. Ghannouchi, "Dual-band matching technique based on dual-characteristic impedance transformers for dual-band power amplifiers design," *IET Microwaves, Antennas & Propagation*, vol.5, no.14, pp.1720–1729, Nov. 2011.
- [23]. O. Manoochehri, A. Asoodeh, and K. Forooraghi, "Pi -model dual-band impedance transformer for unequal complex impedance loads," *IEEE Microw. Wireless Compon. Lett.*, vol.25, no.4, pp.238–240, Apr. 2015.
- [24]. M. A. Maktoomi, M. S. Hashmi, and V. Panwar, "A dual-frequency matching network for FDCLs using dual-band $\lambda/4$ -lines," *Progr. Electromagn. Res. L*, vol. 52, pp. 23–30, 2015.
- [25]. B. Becciolini, "Impedance matching networks applied to RF power transistors," *Freescale Semiconductor, Appl. Note AN721, Rev. 1.1*, [Accessed: June 06, 2016] URL: http://cache.freescale.com/files/rf_if/doc/app_note/AN721.pdf.
- [26]. C. Bowick, J. Blyler, and C. Ajluni, *RF Circuit Design*, 2nd ed., Newnes: USA, Chap. 4, pp. 63–102.
- [27]. D. Youla, "A new theory of broad-band matching," *IEEE Trans. Circuit Theory*, vol. 11, no. 1, pp. 30–50, Jan. 1964.
- [28]. H. J. Carlin and P. J. Crepeau, "Theoretical limitations on the broadband matching of arbitrary impedances," *IRE Trans. Circuit Theory*, vol. 8, no. 2, pp. 165–165, June 1961.
- [29]. H. J. Carlin and R. C. Shen, "Gain-bandwidth theory for optimizing transmission through a prescribed lossless two-port," *IEEE Trans. Circuit Theory*, vol. 19, no. 1, pp. 98–100, Jan. 1972.
- [30]. M. J. Park, and B. Lee, "Dual band design of single stub impedance matching networks with application to dual band stubbed T junctions," *Wiley Microw. & Opt. Tech. Lett.*, vol. 52, No. 6, 1359–1362, 2010.
- [31]. K. Rawat, M. S. Hashmi, and F. M. Ghannouchi, "Double the band and optimize," *IEEE Microw. Mag.*, vol.13, no.2, pp.69–82, Mar. 2012.
- [32]. K. -A. Hsieh, H. -S. Wu, K. -H. Tsai, C. -K. C Tzuang, "A dual-band 10/24-GHz amplifier design incorporating dual-frequency complex load matching," *IEEE Trans. Microw. Theory Tech.*, vol.60, no.6, pp.1649–1657, Jun. 2012.
- [33]. Y. L. Chow and K. L. Wan, "A transformer of one-third wavelength in two sections-for a frequency and its first harmonic," *IEEE Microw. Wireless Comp. Lett.*, vol. 12, no. 1, pp. 22–23, Jan. 2002.
- [34]. C. Monzon, "A small dual-frequency transformer in two sections," *IEEE Trans. Microw. Theory Tech.*, vol. 51, no. 4, pp. 1157–1161, Apr. 2003.
- [35]. J. Sophocles and A. Orfanidis, "Two-section dual-band Chebyshev impedance transformer," *IEEE Microw. Wireless Compon. Lett.*, vol.13, no. 9, pp. 382–384, Sep. 2003.
- [36]. G. Castaldi, "An exact synthesis method for dual-band Chebyshev impedance transformers", *Prog. Electromagn. Res.*, pp. 305–319, 2008.
- [37]. P. Colantonio, F. Giannini, and L. Scucchia, "A new approach to design matching networks with distributed elements," *Proc. 15th International Conference on Microwaves, Radar and Wireless Communications*, MIKON-2004, vol. 3, 811–814, 2004.
- [38]. Y. Wu, Y. Liu, and S. Li, "A dual-frequency transformer for complex impedances with two unequal sections," *IEEE Microw. Wireless Comp. Lett.*, vol. 19, no. 2, pp. 77–79, Feb. 2009.
- [39]. S. C. D. Roy, "Comment on "A dual-frequency transformer for complex impedances with two unequal sections"," *IEEE Microw. Wireless Comp. Lett.*, vol.19, no.9, pp.602, Sept. 2009.

- [40]. X. Liu, Y. Liu, S. Li, F. Wu, and Y. Wu, "A three-section dual-band transformer for frequency-dependent complex load impedance," *IEEE Microw. Wireless Compon. Lett.*, vol. 19, no. 10, pp. 611–613, Oct. 2009.
- [41]. Y. Wu, Y. Liu, S. Li, C. Yu, and X. Liu, "A generalized dual-frequency transformer for two arbitrary complex frequency-dependent impedances," *IEEE Microw. Wireless Compon. Lett.*, vol. 19, no. 12, pp. 792–794, Dec. 2009.
- [42]. M. -L. Chuang, "Dual-band impedance transformer using two-section shunt stubs," *IEEE Trans. Microw. Theory Tech.*, vol. 58, no. 5, pp. 1257–1263, May 2010.
- [43]. M. A. Nikravan and Z. Atlasbaf, "T-section dual-band impedance transformer for frequency-dependent complex impedance loads," *IET Electron. Lett.*, vol. 47, no. 9, pp. 551–553, Apr. 2011.
- [44]. X. Zheng, Y. Liu, S. Li, C. Yu, Z. Wang, and J. Li, "A dual-band impedance transformer using pi-section structure for frequency-dependent complex loads," *Prog. Electromagn. Res. C*, vol. 32, pp. 11–26, 2012.
- [45]. M. -L. Chuang, "Analytical design of dual-band impedance transformer with additional transmission zero," *IET Microwaves, Antennas & Propagation*, vol. 8, No. 13, pp. 1120–1126, Oct. 2014.
- [46]. X. Fu, D. T. Bepalko, and S. Boumaiza, "Novel dual-band matching network for effective design of concurrent dual-band power amplifiers," *IEEE Trans. Circuits Syst. I, Reg. Papers*, vol. 61, no. 1, pp. 293–301, Jan. 2014.
- [47]. Y. Wu, Y. Liu, S. Li and C. Yu, "New coupled-line dual-band dc-block transformer for arbitrary complex frequency-dependent load impedance," *Wiley Microw. & Opt. Tech. Lett.*, vol. 54, no. 1, pp. 139–142, Jan. 2012.
- [48]. Y. Wu, W. Sun, S. -W. Leung, Y. Diao and K. -H. Chan, "A novel compact dual-frequency coupled-line transformer with simple analytical design equations for frequency-dependent complex load impedance," *Prog. Electromagn. Res.*, vol. 134, pp. 47–62, 2013.
- [49]. S. Li, B. Tang, Y. Liu, S. Li, C. Yu, and Y. Wu, "Miniaturized dual-band matching technique based on coupled-line transformer for dual-band power amplifiers design," *Prog. Electromagn. Res.*, vol. 131, pp. 195–210, 2012.
- [50]. B. -T. Moon and N. -H. Myung, "A dual-band impedance transforming technique with lumped elements for frequency-dependent complex loads," *Prog. Electromagn. Res.*, vol. 136, pp. 123–139, 2013.
- [51]. M. Chongcheawchamnan, S. Patisang, M. Krairiksh and I. Robertson, "Tri-band Wilkinson power divider using a three-section transmission line transformer," *IEEE Microw. Wireless Compon. Lett.*, vol. 16, no. 8, pp. 452–454, Aug. 2006.
- [52]. Z. Wang and W. C. Park "Concurrent tri-band GaN HEMT power amplifier using resonators in both input and output matching networks," *Proc. IEEE WAMICON Conf.*, pp. 1–4, 2012.
- [53]. Y. -F. Bai, X. -H. Wang, C. -J. Gao, Q. -L. Huang, and X. -W. Shi, "Design of compact quad frequency impedance transformer using two-section coupled line," *IEEE Trans. Microw. Theory Tech.*, vol. 60, no. 8, pp. 2417–2423, Aug. 2012.
- [54]. X. H. Wang, L. Zhang, Y. Xu, Y. F. Bai, C. Liu, and X. -W. Shi, "A tri-band impedance transformer using stubbed coupling line," *Prog. Electromagn. Res.*, vol. 141, pp. 33–45, 2013.
- [55]. X. A. Nghiem, J. Guan, T. Hone, and R. Negra "Design of concurrent multiband Doherty power amplifiers for wireless applications," *IEEE Trans. Microw. Theory Tech.*, vol. 61, no. 12, pp. 4559–4568, Dec. 2013.
- [56]. Y. Liu, Y. Zhao, S. Liu, Y. Zhou, and Y. Chen, "Multi-frequency impedance transformers for frequency-dependent complex loads," *IEEE Trans. Microw. Theory Tech.*, vol. 61, no. 9, pp. 3225–3235, Sept. 2013.
- [57]. M. A. Maktoomi, R. Gupta, and M. S. Hashmi, "A dual-band impedance transformer for frequency dependent complex loads incorporating an L-type network," *Proc. 2015 Asia-Pacific Microwave Conference (APMC'2015)*, Nanjing, China, December 2015.

- [58]. M. A. Maktoomi and M. S. Hashmi, "A novel enhanced band-ratio dual-band Wilkinson power divider with option of partial port extension," *IEEE Trans. Microw. Theory Tech.* (*under review*).
- [59]. M. A. Maktoomi, M. S. Hashmi, and F. M. Ghannouchi, "A T-section dual-band matching network for frequency-dependent complex loads incorporating coupled line with DC-block property suitable for dual-band transistor amplifiers," *Progr. Electromagn. Res. C*, vol. 54, pp. 75–84, 2014.
- [60]. M. A. Maktoomi and M. S. Hashmi, "A coupled-line based L-section DC isolated dual-band real to real impedance transformer and its application to a dual-band T-junction power divider," *Progr. Electromagn. Res. C*, vol. 55, pp. 95–104, 2014.
- [61]. U. T. Ahmed and A. M. Abbosh, "Modified Wilkinson power divider using coupled microstrip lines and shunt open-ended stubs," *IET Elect. Lett.*, vol. 51, no. 11, pp. 838–839, May 2015.
- [62]. R. Gómez-García, R. Loeches-Sanchez, D. Psychogiou, and D. Peroulis, "Single/multi-band Wilkinson-type power dividers with embedded transversal filtering sections and application to channelized filters," *IEEE Trans. Circuits Syst. I, Reg. Papers*, vol. 62, no. 6, pp. 1518–1527, Jun. 2015.
- [63]. R. Gómez-García, F. M. Ghannouchi, N. B. Carvalho, and H. C. Luong, "Advanced circuits and systems for CR/SDR applications," *IEEE J. Select. Emerging Topics Circuits Syst.*, vol. 3, no. 4, pp. 485–488, Dec. 2013.
- [64]. X. Wang, I. Sakagami, K. Takahashi, and S. Okamura, "A generalized dual-band Wilkinson power divider with parallel L, C, and R components," *IEEE Trans. Microw. Theory Techn.*, vol. 60, no. 4, pp. 952–964, Apr. 2012.
- [65]. X. Wang, I. Sakagami, Z. Ma, A. Mase, M. Yoshikawa, and M. Ichimura, "Miniaturized dual-band wilkinson power divider with self-compensation structure," *IEEE Trans. Compon., Packag., Manuf. Technol.*, vol. 5, no. 3, pp. 389–397, Mar. 2015.
- [66]. N. Gao, G. Wu, and Q. Tang, "Design of a novel compact dual-band Wilkinson power divider with wide frequency ratio," *IEEE Microw. Wireless Compon. Lett.*, vol. 24, no. 2, pp. 81–83, Feb. 2014.
- [67]. A. Genc and R. Baktur, "Dual- and triple-band Wilkinson power dividers based on composite right- and left-handed transmission lines," *IEEE Trans. Compon., Packag., Manuf. Technol.*, vol. 1, no. 3, pp. 327–334, Mar. 2011.
- [68]. K.-K. M. Cheng and F.-L. Wong, "A new Wilkinson power divider design for dual band application," *IEEE Microw. Wireless Compon. Lett.*, vol. 17, no. 9, pp. 664–666, Sep. 2007.
- [69]. K.-K.M Chang and C. Law, "A novel approach to the design and implementation of dual-band power divider," *IEEE Trans. Microw. Theory Techn.*, vol. 56, no. 2, pp. 487–492, Feb. 2008.
- [70]. M.-J. Park and B. Lee, "A dual-band Wilkinson power divider," *IEEE Microw. Wireless Compon. Lett.*, vol. 18, no. 2, pp. 85–87, Feb. 2008.
- [71]. Y. Shin, B. Lee, and M. -J. Park, "Dual-band Wilkinson power divider with shifted output ports," *IEEE Microw. Wireless Compon. Lett.*, vol. 18, no. 7, pp. 443–445, Jul. 2008.
- [72]. Y. Wu, Y. Liu, Y. Zhang, J. Gao, and H. Zhao, "A dual band unequal Wilkinson power divider without reactive components," *IEEE Trans. Microw. Theory Techn.*, vol. 57, no. 1, pp. 216–222, Jan. 2009
- [73]. G. Wu, L. Yang, Y. Zhou and Q. Xu, "Wilkinson power divider design for dual-band applications," *IET Electron. Lett.*, vol. 50, no. 14, pp. 1003–1005, July 2014.
- [74]. M.-J. Park, "Two-section cascaded coupled line Wilkinson power divider for dual-band applications," *IEEE Microw. Wireless Compon. Lett.*, vol. 19, no. 4, pp. 188–190, Apr. 2009.
- [75]. Y. Wu, Y. Liu, and Q. Xue, "An analytical approach for a novel coupled line dual-band Wilkinson power divider," *IEEE Trans. Microw. Theory Techn.*, vol. 59, no. 2, pp. 286–294, Feb. 2011.
- [76]. X. Tang and K. Mouthaan, "Compact dual-band power divider with single allpass coupled lines sections," *IET Electron. Lett.*, vol. 46, no. 10, pp. 688–689, May 2010.

- [77]. M. -J. Park, "Dual-band Wilkinson divider with coupled output port extensions," *IEEE Trans. Microw. Theory Techn.*, vol. 57, no. 9, pp. 2232–2237, Sept. 2009.
- [78]. W. -H. Chen, Y. -C. Liu, X. Li, Z. -H. Feng, and F. M. Ghannouchi, "Design of reduced-size unequal power divider for dual-band operation with coupled lines," *IET Electron. Lett.*, vol. 47, no. 1, pp.59–60, Jan. 2011.
- [79]. Y. -C. Liu, W. -H. Chen, X. Li and Z. -H. Feng, "Compact design of dual-band power divider with coupled-line shunt elements," *IET Electron. Lett.*, vol. 47, no. 4, pp.262–263, Feb. 2011.
- [80]. I. Sakagami, X. Wang, K. Takahashi, and S. Okamura, "Generalized two way two-section dual-band Wilkinson power divider with two absorption resistors and its miniaturization," *IEEE Trans. Microw. Theory Techn.*, vol. 59, no. 11, pp. 2833–2847, Nov. 2011.
- [81]. Y. Liu, W. Chen, X. Li, and Z. Feng, "Design of compact dual band power dividers with frequency-dependent division ratios based on multisection coupled line," *IEEE Trans. Compon., Packag., Manuf. Technol.*, vol. 3, no. 3, pp. 467–475, Mar. 2013.
- [82]. M. -J. Park and B. Lee, "Wilkinson power divider with extended ports for dual-band operation," *IET Electron. Lett.*, vol. 44, no. 15, pp. 916–917, Jul. 2008.
- [83]. Q. -X. Chu, F. Lin, Z. Lin, and Z. Gong, "Novel design method of tri-band power divider," *IEEE Trans. Microw. Theory Techn.*, vol. 59, no.9, pp. 2221–2226, Sep. 2011.
- [84]. G. L. Matthaei, L. Young, and E.M.T. Jones, *Microwave Filters, Impedance-Matching Networks, and Coupling Structures*, Artech House, 1980.
- [85]. K. K. M. Cheng and F. L. Wong, "A novel approach to the design and implementation of dual-band compact planar 90° branch-line coupler," *IEEE Trans. Microwave Theory Tech.*, vol. 52, no. 11, pp. 2458–2463, Nov. 2004.
- [86]. H. Zhang and K. J. Chen, "A stub tapped branch-line coupler for dual-band operations," *IEEE Microw. Wireless Compon. Lett.*, vol.17, no.2, pp.106–108, Feb. 2007.
- [87]. I. -H. Lin, M. D. Vincentis, C. Caloz, and T. Itoh, "Arbitrary dual-band components using composite right/left-handed transmission lines," *IEEE Trans. Microwave Theory Tech.*, vol. 52, pp. 1142–1148, Apr. 2004.
- [88]. C. -L. Hsu, J. T. Kuo, and C. W. Chang, "Miniaturized dual-band hybrid couplers with arbitrary power division ratio," *IEEE Trans. Microw. Theory Tech.*, vol. 57, pp. 149–156, Jan. 2009.
- [89]. K. Rawat and F. M. Ghannouchi, "A design methodology for miniaturized power dividers using periodically loaded slow wave structure with dual-band applications," *IEEE Trans. Microw. Theory Tech.*, vol. 57, pp.3330–3338, Dec. 2009.
- [90]. Z. Lin and W. Wu, "A novel approach to the design of dual-band power divider with variable power dividing ratio based on coupled-lines," *Prog. Electromagn. Res.*, vol. 103, pp. 271–284, 2010.
- [91]. B. Li, X. Wu, N. Yang and W. Wu, "Dual-band equal/unequal Wilkinson power dividers based on coupled-line section with short circuited stub," *Prog. Electromagn. Res.*, vol. 111, pp. 163–178, 2011.
- [92]. M. A. Maktoomi, V. Panwar, M. S. Hashmi, and F. M. Ghannouchi, "A dual-band matching network for frequency-dependent complex loads suitable for dual-band RF Amplifiers," in *IEEE MTT-S IMaRC'2014*, Bangalore, India, Dec. 2014.
- [93]. R. K. Mongia, I. J. Bahl, P. Bhartia, and J. Hong, *RF and Microwave Coupled Line Circuits*, 2nd ed., Norwood: Artech House, 2007, Chap. 12.
- [94]. M. A. Maktoomi, A. P. Yadav, M. S. Hashmi, and F. M. Ghannouchi, "Performance enhancement of dual-frequency impedance matching networks using dual-frequency property of two-section transmission-line terminated into a real impedance," *IET Microwaves, Antennas and Propagation*. (*under review*).
- [95]. M. A. Maktoomi, M. H. Maktoomi, Ajay P. Yadav, M. S. Hashmi, and F. M. Ghannouchi, "Dual-frequency admittance property of two sections transmission-line and application," 2016 *IEEE 59th Midwest Symposium on Circuits and Systems (MWSCAS2016)*. (*Accepted*).

- [96]. M. A. Maktoomi, M. S. Hashmi, and F. M. Ghannouchi, "A dual-band port extended branch-line coupler and mitigation of the band-ratio and power division limitations," *IEEE Transactions on Components, Packaging and Manufacturing Technology*. (*under review*)
- [97]. S. -C. Jung, R. Negra, and F. M. Ghannouchi, "A design methodology for miniaturized 3-dB branch-line hybrid couplers using distributed capacitors printed in the inner area," *IEEE Trans. Microw. Theory Techn.*, vol. 56, no. 12, pp. 2950–2953, Dec. 2008.
- [98]. H. Okabe, C. Caloz, and T. Itoh, "A compact enhanced-bandwidth hybrid ring using an artificial lumped-element left-handed transmission line section," *IEEE Trans. Microw. Theory Techn.*, vol. 52, no. 3, pp. 798–804, Mar. 2004.
- [99]. J. -H. Cho, H. -Y. Huang, and S. -W. Yun, "A design of wideband 3-dB coupler with N-section microstrip tandem structure," *IEEE Microw. Wireless Compon. Lett.*, vol. 15, no. 2, pp. 113–115, Feb. 2005.
- [100]. L. Chiu and Q. Xue, "Investigation of a wideband 90 hybrid coupler with an arbitrary coupling level," *IEEE Trans. Microw. Theory Techn.*, vol. 58, no. 4, pp. 1022–1029, Apr. 2010.
- [101]. K. A. Alshamaileh, V. K. Devabhaktuni, and N. I. Dib, "Impedance-varying broadband 90° branch-line coupler with arbitrary coupling levels and higher order harmonic suppression," *IEEE Trans. Compon., Packag., Manuf. Technol.*, vol. 5, no. 10, pp. 1507–1515, Oct. 2015.
- [102]. Y. Wu., S. Y. Zheng, S.-W. Leung, Y. Liu, and Q. Xue, "An analytical design method for a novel dual-band unequal coupler with four arbitrary terminated resistances," *IEEE Trans. Ind. Electron.*, vol.61, no.10, pp.5509–5516, Oct. 2014.
- [103]. H. -R. Ahn, *Asymmetric Passive Components in Microwave Integrated Circuits*. New York:Wiley, 2006.
- [104]. Y. L. Wu, J. Y. Shen, Q. Liu, L. M. Liang, and Y. Liu, "An asymmetric arbitrary branch-line coupler terminated by one group of complex impedances," *Journal of Electromagnetic Wave and applications*, vol. 26, no. 8-9, pp. 1125–1137, Jul. 2012.
- [105]. K. -K. M. Cheng and S. Yeung, "A novel dual-band 3-dB branch-line coupler design with controllable bandwidths," *IEEE Trans. Microw. Theory Techn.*, vol.60, no.10, pp.3055–3061, Oct. 2012.
- [106]. H. Ren, J. Shao, M. Zhou, B. Arigong, J. Ding, and H. Zhang, "Design of dual-band transmission line with flexible phase shifts and its applications," *IET Electron. Lett.*, vol.51, no.3, pp. 261–262, Feb. 2015.
- [107]. K.-S. Chin, K.-M. Lin, Y. -H. Wei, T.-H. Tseng, and Y.-J. Yang, "Compact dual-band branch-line and rat-race couplers with stepped-impedance-stub lines," *IEEE Trans. Microw. Theory Techn.*, vol.58, no.5, pp.1213–1221, May 2010.
- [108]. C.-L. Hsu, J.-T. Kuo, and C.-W. Chang, "Miniaturized dual-band hybrid couplers with arbitrary power division ratios," *IEEE Trans. Microw. Theory Techn.*, vol. 57, no. 1, pp. 149–156, Jan. 2009.
- [109]. E. E. Djoumessi, E. Marsan, C. Caloz, M. Chaker, and K. Wu, "Varactor-tuned dual-band quadrature hybrid coupler," *IEEE Microw. Wireless Compon. Lett.*, vol.16, no.11, pp.603–605, Nov. 2006.
- [110]. Q. Liu, Y. Liu, Y. Wu, J.-Y. Shen, S. Li, C. Yu, and M. Su, "Generalized impedance-transforming dual-band branch-line couplers for arbitrary coupling levels," *Progr. Electromagn. Res. B*, vol. 53, pp. 399–415, 2013.
- [111]. P.-L. Chi and K. -L. Ho, "Design of dual-band coupler with arbitrary power division ratios and phase differences," *IEEE Trans. Microw. Theory Techn.*, vol.62, no.12, pp.2965–2974, Dec. 2014.
- [112]. L. K. Yeung, "A compact dual-band 90° coupler with coupled-line sections," *IEEE Trans. Microw. Theory Techn.*, vol.59, no.9, pp.2227–2232, Sept. 2011.
- [113]. C. -H. Yu and Y. -H. Pang, "Dual-band unequal-power quadrature branch-line coupler with coupled lines," *IEEE Microw. Wireless Compon. Lett.*, vol.23, no.1, pp.10–12, Jan. 2013.

- [114]. X. Wang, W. -Y. Yin, and K. -L. Wu, "A dual-band coupled-line coupler with an arbitrary coupling coefficient," *IEEE Trans. Microw. Theory Techn.*, vol.60, no.4, pp.945–951, Apr. 2012.
- [115]. M.-J. Park and B. Lee, "Dual-band, cross coupled branch line coupler," *IEEE Microw. Wireless Compon. Lett.*, vol. 15, no. 10, pp. 655–657, Oct. 2005.
- [116]. H. Kim, B. Lee, and M.-J. Park, "Dual-band branch-line coupler with port extensions," *IEEE Trans. Microw. Theory Techn.*, vol.58, no.3, pp.651–655, Mar. 2010.
- [117]. H. Mextorf and R. Knochel, "The intrinsic impedance and its application to backward and forward coupled-line couplers," *IEEE Trans. Microw. Theory Techn.*, vol.62, no.2, pp.224–233, Feb. 2014.
- [118]. M. A. Maktoomi, M. S. Hashmi, and F. M. Ghannouchi, "Systematic design technique for dual-band branch-line coupler using T- and Pi-networks and a novel wide band-ratio crossover," *IEEE Transactions on Components, Packaging and Manufacturing Technology*, vol. 6, No. 5, pp. 784–795, Apr. 2016.
- [119]. M. A. Maktoomi, M. S. Hashmi, and F. M. Ghannouchi, "Improving load range of dual-band impedance matching networks using novel load-healing concept," *IEEE Transactions on Circuits and Systems II: Express Briefs*, 2016 (Accepted, available online in the IEEExplore).
- [120]. M. A. Maktoomi, M. Akbarpour, M. S. Hashmi, and F. M. Ghannouchi, "On the dual-frequency impedance/admittance characteristic of multi-section commensurate transmission-line," *IEEE Transactions on Circuits and Systems II: Express Briefs*. (Accepted, available online in the IEEExplore)
- [121]. M. A. Maktoomi, M. S. Hashmi, A. P. Yadav, and V. Kumar, "A generic tri-band matching network," *IEEE Microwave Wireless Components Letters*, vol. 26, No. 5, pp. 316–318, Apr. 2016.
- [122]. Y. Wu, Y. Liu, and S. Li, "A compact Pi-structure dual band transformer," *Prog. In Electromag. Research*, vol. 88, pp.121–134, 2008.
- [123]. M. Zhou, J. Shao, B. Arigong, H. Ren, J. Ding, and H. Zhang, "Design of microwave baluns with flexible structures," *IEEE Microw. Wireless Compon. Lett.*, vol. 24, no. 10, pp. 695–697, Oct. 2014.
- [124]. X. A. Nghiem and R. Negra, "Design of concurrent multiband biasing networks for multiband RF power amplifier," *Proc. 42nd Eur. Microw. Conf.*, Amsterdam, the Netherlands, Oct. 2012, pp. 1–4.
- [125]. M. A. Maktoomi, M. Akbarpour, M. S. Hashmi, and F. M. Ghannouchi, "A theorem for multi-frequency DC-feed network design," *IEEE Microwave Wireless Components Letters*, 2016 (Accepted)

Biography and Curriculum Vitae



Mohammad A. Maktoomi was born in Sasauli– a remote village in India in 1985. He received the B.Tech. degree in electronics engineering from Aligarh Muslim University (AMU), Aligarh, India, in 2009, and is currently working toward the Ph.D. degree in electronics and communication engineering at the Indraprastha Institute of Information Technology Delhi, New Delhi, India.

He has served with the Hindustan College of Science and Technology, Mathura, India, as an Assistant Professor, and AMU as a Guest Faculty Member. From October 2015 to April 2016, He was with the iRadio Laboratory, University of Calgary, Canada, as a Visiting Ph.D. Student. He has published in many international conferences and reputed journals. He is a regular reviewer for many esteemed journals, and has been invited to many workshops to present tutorials. His current research interests include multiband RF/microwave circuits and current-mode analog circuits.

Mr. Maktoomi was a recipient of the Best Student Paper Award at the IEEE IMPACT, India, in 2013, in the RF/microwave category. He was the winner in the Keysight IEEE MTT-S Student Design Contest on Microstrip Filter Design.

When he is not doing research, he enjoys making tutorials.

Mohammad A. Maktoomi, PhD Candidate, IIIT Delhi, India

CONTACT INFORMATION

University:
PhD Lab 3A (old), IIIT Delhi
Okhla Industrial Estate, Phase III
Near Govindpuri Metro
New Delhi 110020
India
E-mail: ayatullahm@iiitd.ac.in

Home:
E-86 (2nd Floor)
Shaheen Bagh
Jamia Nagar, Okhla
New Delhi 110025
India
Voice: (+91) 9990730806

NATIONALITY

Indian

RESEARCH INTERESTS

Multi-Band/Wideband RF/Microwave Active and Passive Components, RF Power Amplifier Design, RF Energy Harvesting, Wireless Power Transfer, Analog Electronics

EDUCATION

Indraprastha Institute of Information Technology Delhi (IIITD), New Delhi, India

Ph.D. Candidate in RF/Microwave Engineering Since February 2013
(Thesis submitted: July 2016; Expected Graduation: August 2016)

- Dissertation Topic: “Analytical Formulations for Systematic Design of Dual-/Tri-Frequency Impedance Transformation Networks Required in Software-Defined Radios (SDRs) and Energy Harvesting Applications.”
- Advisor: Dr. Mohammad S. Hashmi, Assistant Professor, IIITD

Indraprastha Institute of Information Technology Delhi (IIITD), New Delhi, India

Master of Technology (M.Tech.), Electronics and Communication Engineering,
(Thesis submitted: June 2016; Expected Graduation: July 2016)

- Dissertation Topic: “High Bandwidth Planar Power Divider.”
- Advisor: Dr. Mohammad S. Hashmi, Assistant Professor, IIITD

Aligarh Muslim University, Aligarh, U.P., India

Bachelor of Technology (B.Tech.), Electronics Engineering, July 2005 - May 2009

HONORS AND AWARDS

- IIIT Delhi Overseas Research Fellowship
- **Winner** of the Keysight IEEE MTT-S International Microwave and RF Conference (IMaRC) Filter Design Competition 2015
- **Best paper award** in the technical session of microwave at the IEEE International Conference on Multimedia, Signal Processing and Communication Technologies (IMPACT) 2013

RESEARCH INTERNSHIP

iRadio Lab, University of Calgary, Alberta, Canada

Visiting PhD Student

October 2015 - April 2016

Worked with Prof. Fadhel M. Ghannouchi on the design of Multi-Band RF Active and Passive Components

ACADEMIC EXPERIENCE

Indraprastha Institute of Information Technology Delhi (IIITD), New Delhi, India

Teaching Assistant

August 2013 - September 2015

Duties at various times have included office hours for undergraduate and graduate student projects and leading weekly tutorial and lab exercises in Analog Circuit Design and Electromagnetism

Aligarh Muslim University, Aligarh, U.P., India

Guest Faculty

August 2011 - June 2012

Taught undergraduate level courses: Basic Electronics, Digital Electronics, SPICE Simulation and associated labs.

Hindustan College of Science and Technology, Mathura, U.P., India

Assistant Professor

July 2009 - May 2011

Taught undergraduate level courses: Analog Integrated Electronics, Semiconductor Devices, SPICE Simulation and associated labs.

RESEARCH AND
PUBLICATIONS

Under Review Articles

M. A. Maktoomi, M. Akbarpour, M. S. Hashmi, and F. M. Ghannouchi, "On the dual-frequency impedance/admittance characteristic of multi-section commensurate transmission-line," *IEEE Transactions on Circuits and Systems II: Express Briefs*.

M. A. Maktoomi, M. S. Hashmi, and F. M. Ghannouchi, "A dual-band port extended branch-line coupler and mitigation of the band-ratio and power division limitations," *IEEE Transactions on Components, Packaging and Manufacturing Technology*.

M. A. Maktoomi, A. P. Yadav, M. S. Hashmi, and F. M. Ghannouchi, "Performance enhancement of dual-frequency impedance matching networks using dual-frequency property of two-section transmission-line terminated into a real impedance," *IET Microwaves, Antennas and Propagation*.

M. A. Maktoomi and M. S. Hashmi, "A novel enhanced band-ratio dual-band Wilkinson power divider with option of partial port extension," *IEEE Transactions on Microwave Theory and Techniques*.

M. A. Maktoomi, M. H. Maktoomi, Ajay P. Yadav, M. S. Hashmi, and F. M. Ghannouchi, "Dual-frequency admittance property of two sections transmission-line and application," *2016 IEEE 59th Midwest Symposium on Circuits and Systems (MWSCAS'2016)*.

R. Gupta, **M. A. Maktoomi**, and M. S. Hashmi, "A new high frequency balun with simplified impedance matching technique," *2016 Asia-Pacific Microwave Conference (APMC'2016)*.

Peer-Reviewed Journal Articles

M. A. Maktoomi, M. S. Hashmi, and F. M. Ghannouchi, "Theory and design of a novel wide-band DC isolated Wilkinson power divider," *IEEE Microwave Wireless Components Letters*, 2016 (Accepted)

M. A. Maktoomi, M. Akbarpour, M. S. Hashmi, and F. M. Ghannouchi, "A theorem for multi-frequency DC-feed network design," *IEEE Microwave Wireless Components Letters*, 2016 (Accepted)

M. A. Maktoomi, M. S. Hashmi, and F. M. Ghannouchi, "Improving load range of dual-band impedance matching networks using novel load-healing concept," *IEEE Transactions on Circuits and Systems II: Express Briefs*, 2016 (Accepted).

M. A. Maktoomi, M. S. Hashmi, and F. M. Ghannouchi, "Systematic design technique for dual-band branch-line coupler using T- and Pi-networks and a novel wide band-ratio crossover," *IEEE Transactions on Components, Packaging and Manufacturing Technology*, vol. 6, No. 5, pp. 784-795, Apr. 2016.

M. A. Maktoomi, M. S. Hashmi, A. P. Yadav, and V. Kumar, "A generic tri-band matching

network,” *IEEE Microwave Wireless Components Letters*, vol. 26, No. 5, pp. 316-318, Apr. 2016.

M. A. Maktoomi, M. S. Hashmi, and V. Panwar, “A dual-frequency matching network for FDCLs using dual-band $\lambda/4$ -lines,” *Progress In Electromagnetics Research L*, vol. 52, pp. 23-30, 2015.

M. A. Maktoomi and M. S. Hashmi, “A coupled-line based l-section DC-isolated dual-band real to real impedance transformer and its application to a dual-band T-junction power divider,” *Progress In Electromagnetics Research C*, vol. 55, pp. 95-104, 2014.

M. A. Maktoomi, M. S. Hashmi, and F. M. Ghannouchi, “A T-section dual-band matching network for frequency-dependent complex loads incorporating coupled line with DC-block property suitable for dual-band transistor amplifiers,” *Progress In Electromagnetics Research C*, vol. 54, pp. 75-84, 2014.

Conference Proceedings

S. Kumar, S. Kaushik, R. Gupta, **M. A. Maktoomi**, and M. S. Hashmi, “A new L-shaped phase inverter design utilizing a loaded transmission line,” in *IEEE MTT-S IWS 2016*, Shanghai, China, March 2016. (Accepted)

M. A. Maktoomi and M. S. Hashmi, “A CAD assisted design methodology for wideband arbitrary power division coupler implemented in microstrip technology,” in *IEEE 22nd NCC 2016*, IIT Guwahati, India, March 2016. (Accepted)

M. A. Maktoomi and M. S. Hashmi, “A novel power divider structure using the Gysel and Wilkinson power dividers with only one grounded resistor,” in *IEEE MTT-S IMArc’2015*, Hyderabad, India, December 2015. (Accepted)

M. A. Maktoomi, R. Gupta, M. S. Hashmi, “A dual-band impedance transformer for frequency-dependent complex loads incorporating an L-type network,” in *2015 Asia-Pacific Microwave Conference (APMC’2015)*, Nanjing, China, December 2015. (Accepted)

M. A. Maktoomi, V. Panwar, M. S. Hashmi, and F. M. Ghannouchi, “A dual-band matching network for frequency-dependent complex loads suitable for dual-band RF amplifiers,” in *IEEE MTT-S IMArc’2014*, Bangalore, India, December 2014.

Z. N. Zafar, **M. A. Maktoomi**, and M. S. Hashmi, “New adjustable square/triangular-wave generators using CCH/CCCII and OTA,” *IEEE ICM*, Qatar, December 2014.

P. Aggarwal, V. Mittal, **M. A. Maktoomi**, and M. S. Hashmi, “A CMOS digitally controlled floating positive resistor using translinear cells,” in *IEEE RAECS*, Chandigarh, India, March 2014.

A. Jain, **M. A. Maktoomi**, and M. S. Hashmi, “A new circuit to measure resistance variation suitable for strain gauge,” in *IEEE SPIN*, Noida, India, February 2014.

M. A. Maktoomi, A. M. Zaidi, and M. S. Hashmi, “A dual-band Bagley power divider using modified -Network,” in *IEEE IMPACT*, Aligarh, India, November 2013.

M. A. Maktoomi, M. A. Siddiqi, S. A. Rahman, and R. K. Mishra, “An interface circuit for measuring small as well as large resistance changes,” in *IEEE ICATE*, Mumbai, India, January 2013.

M. A. Maktoomi, M. Singh, and M. A. Siddiqi, “High bandwidth circuits for the measurement of small resistance changes,” in *IEEE ICPCES*, Allahabad, India, December, 2012.

M. A. Maktoomi, M. A. Siddiqi, and M. P. Pyari, “FVF based CDTA and its application,” in IEEE ICCICT, Mumbai, India, October 2012.

M. A. Maktoomi, R. K. Mishra, M. A. Siddiqi, and M. P. Pyari, “CDTA based logarithmic amplifier,” in IEEE ISPCC, Solan, India, March 2012.

MEMBERSHIP IEEE MTT-S Graduate Student Member

RELEVANT SKILLS

- EDA Packages: Keysight ADS, HFSS, SPICE, MATLAB/octave, gnuplot.
- Language: C.
- Applications: Xcircuit, L^AT_EX, spreadsheet, and presentation software.
- Operating Systems: Unix/Linux, Windows.
- Speaking and Writing level skills in English, Hindi and Urdu languages

REFERENCES

Dr. Mohammad S. Hashmi, Assistant Professor, Electronics and Communication Engineering, IIITD, Okhla Phase-3, New Delhi -110020, India, mshashmi@iiitd.ac.in

Dr. Fadhel M. Ghannouchi, Professor, Department of Electrical and Computer Engineering, University of Calgary, Alberta, Canada, fghannou@ucalgary.ca

Dr. S. A. Rahman, Professor, Electronics Engineering, Aligarh Muslim University, Aligarh-202002, U.P., India, atiqamu@gmail.com

Dr. Ekram Khan, Professor, Electronics Engineering, Aligarh Muslim University, Aligarh-202002, U.P., India, ekhan67@gmail.com